

# SAP2023

Proceedings of the  
14<sup>th</sup> Symposium on Accelerator Physics

第十四届加速器物理学学术交流会议  
*The 14<sup>th</sup> Symposium on Accelerator Physics (SAP2023)*



# PROCEEDINGS

## Editorial Board:

Wenhui Huang (TUB), Xueqing Yan (PKU), Lu Li (IMP),  
Chuanxiang Tang (TUB), Volker RW Schaa (GSI)

Dec 2024

ISBN 978-3-95450-265-3

Copyright © 2024 by JACoW — cc Creative Commons Attribution 4.0

DOI:10.18429/JACoW-SAP2023



# SAP2023 Committees

## Chairmen

*Huang, Wenhui (TUB)*

*Yan, Xueqing (PKU)*

## Scientific Programme Committee

*Tang, Chuanxiang (TUB), Chair*

*Fan, Kuanjun (HUST)*

*Li, Weimin (USTC)*

*Liu, Kexin (PKU)*

*Wang, Dong (SINAP, CAS)*

*Xu, Gang (IHEP, CAS)*

*Zhang, Tianjue (CIAE)*

## Organizing Committee

*Huang Wenhui, Yan Xueqing, An Shizhong, Chen Min, Deng Haixiao, Feng Guangyao,  
He Xiaozhong, Huang Senlin, Jiang Bocheng, Jiao Yi, Li Haohu, Li Jingshen, Li Renkai,  
Li Zhihui, Liu Bo, Mao Lijun, Qin Bin, Su Ping, Wang Lin, Wang Sheng, Wang Wentao,  
Wu Dai, Xiang Dao, Yang Jiancheng, Zhang Weiqing, Zhou Weimin*

## Local Organizing Committee

*Zeng Zhi (Chair), Yu Tong, Zhou Jie, Liu Jianhua*

## Editorial Team

*Lu Li (IMP)*

*Lin Bian (IHEP)*

*Daheng Ji (IHEP)*

*Hongfei Ji (IHEP)*

*Zhichu Chen (SARI)*

*Volker RW Schaa (GSI)*

# Contents

<b>Preface</b>	<b>i</b>
Committees . . . . .	iii
Contents . . . . .	iv
<b>Papers</b>	<b>1</b>
MOCXA02 – Beam-Beam Interaction with Longitudinal Impedance and Its Application in TMCI Study . . . . .	1
MOIBA01 – Research on Beam Dynamics of a 2 GeV 6 MW Isochronous FFA . . . . .	4
MOCYA01 – Study of the Key Physics Problems in 10mA-class High Current Cyclotron . . . . .	9
MOPB001 – Terahertz-Driven MeV Electron Bunch Compression and Streaking . . . . .	14
MOPB003 – Study on a Polarization Controllable Undulator for High-Gain Free Electron Lasers . . . . .	18
MOPB004 – Lowest Longitudinal and Transverse Resistive-wall Wake and Impedance for Nonultra-relativistic Beams	21
MOPB005 – Design of Beam Dynamics for a High-Power DC Proton Accelerator at the MeV Level . . . . .	24
MOPB008 – Approximation of Space Charge Effect in the Presence of Longitudinal Magnetic Fields . . . . .	27
MOPB010 – Impact of NEG Coating Thickness and Resistivity on Beam Coupling Impedance . . . . .	30
MOPB014 – Development of a Vlasov Solver for Arbitrary Sub-optimal Lengthening Conditions in Double-RF System	34
MOPB016 – Matching Section Optics Design for the MeV Ultrafast Electron Beam Experimental Facility . . . . .	37
MOPB017 – Analysis of the Fluctuation of Resonance Driving Terms for Nonlinear Lattice Optimization . . . . .	41
MOPB018 – Longitudinal Beam Dynamics Design for Super Tau-Charm Facility . . . . .	45
MOPB019 – Development Status of Beam Dynamics Software APES for CEPC . . . . .	49
MOPB026 – Physical Design for EEHG Beamlines at S3FEL . . . . .	55
MOPB027 – A Scheme of Fully Coherent X-Ray Free Electron Laser for the Shine Based on Fresh-Slices . . . . .	59
MOPB028 – Investigation on the Trapped Modes of CPMU at HEPS . . . . .	62
MOPB029 – Multi-bunch Operation Mode for Simultaneously Serving SASE and Seeding FEL Beamlines . . . . .	66
MOPB030 – Physical Design of an S-Band Cold Cathode RF Gun . . . . .	70
MOPB031 – Studies on Beam Injection System for Wuhan Advanced Light Source Storage Ring . . . . .	73
MOPB034 – Start to End Simulation for A Compact THz-FEL . . . . .	76
MOPB035 – Beam Dynamics Study of a Photo-Injector at Wuhan Light Source . . . . .	79
MOPB036 – Compact Accelerator Light Source for Industrial Applications . . . . .	82
MOPB037 – Generalized Longitudinal Strong Focusing: A Ring-Based Beam Manipulation Technique . . . . .	85
MOPB039 – Low-Alpha Storage Ring Design for Steady-State Microbunching to Generate EUV Radiation . . . . .	88
TUPB006 – Study on XiPAF Synchrotron Nonlinear Dynamics . . . . .	92
TUPB008 – Evaluation of Field Quality for Elliptical and Curved Magnets . . . . .	96
TUPB009 – General Design of 180 MHz RFQ for BNCT . . . . .	99
TUPB010 – Dynamics Design on 70–250MeV Proton Linac . . . . .	102
TUPB012 – Control of CAFe Beam Energy Using Linear Accelerator Simulation Software AVAS and Beam Line Calibration Technology . . . . .	105
TUPB013 – Multipole Field Optimization of X-Band High Gradient Structure . . . . .	108
TUPB014 – Design of a Large Momentum Acceptance Gantry Based on AG-CCT for Lightweight Proton Therapy Facility	111
TUPB015 – Research on First Harmonic Shimming Method of Cyclotron Based on Least Norm Square Solution . . . . .	114
TUPB016 – High-Fidelity Modeling and Transmission Optimization for the Beamline of HUST-PTF . . . . .	117
TUPB017 – Calibration Experiment of Equivalent Area of Induction Coil for Magnetic Field Measurement of Supercon- ducting Cyclotron . . . . .	120
TUPB018 – The Design of Nonlinear Regenerative Extraction in 250MeV Proton Superconducting Synchrocyclotron . . . . .	123
TUPB019 – Beam Dynamics in Superconducting Proton Linac . . . . .	126
TUPB021 – The Design of a Proton-Heavy Ion Hybrid Synchrotron Upgraded from XiPAF Proton Ring . . . . .	129
TUPB024 – Electron Cooling for Future High-energy Hadron Accelerators . . . . .	133
TUPB025 – Influence of Transverse Distribution of Electron Beam on the Distribution of Proton Beam in the Process of Electron Cooling . . . . .	137
TUPB026 – Design of a Synchrotron for Proton FLASH Radiotherapy Based on Fast Variable-Energy Bunch Splitting . . . . .	141
TUPB027 – New Progress of the Miniaturized Microwave Ion Source at Peking University . . . . .	144
TUPB029 – Wakefield Studies for the Step Structure and the Skin Depth of Coated Dielectric Tubes . . . . .	147
TUPB033 – Heating Estimation of Undulator Vacuum Chamber at S3FEL . . . . .	151
TUPB035 – Recent Progress of the Beam Background Experiment in the BEPCII . . . . .	155

<b>Appendices</b>	<b>159</b>
List of Authors . . . . .	159
List of Institutes . . . . .	162
List of Participants . . . . .	165



# BEAM-BEAM INTERACTION WITH LONGITUDINAL IMPEDANCE AND ITS APPLICATION IN TMCI STUDY

Chuntao Lin\*, Institute of Advanced Science Facilities, Shenzhen, Guangdong, 518107, China  
Kazuhito Ohmi, KEK, Tsukuba, Ibaraki 305-0801, Japan  
Yuan Zhang, Institute of High Energy Physics, Beijing 100049, China

## Abstract

Simulations have showed a novel coherent head-tail instability induced by beam-beam interaction with a large Piwinski angle. The localized cross-wake force has been introduced to explain the instability. The longitudinal impedance would cause coherent and incoherent synchrotron tune shift and distort the particle's trajectories in longitudinal phase space. Further beam-beam simulation revealed that the longitudinal impedance has strong impacts on the beam stability, squeezing the horizontal stable tune area seriously. The instability has become an important issue during the designs of CEPC and FCC-ee. In this paper, we develop a transverse mode coupling analysis method that could be used to study beam-beam instability with and without longitudinal impedance. This method can also be applied in synchrotron light sources to study transverse mode coupling instability (TMCI) with longitudinal impedance and harmonic cavity. Some preliminary results at Shenzhen Innovation Light Source (SILF) are also shown.

## INTRODUCTION

Beam-beam interaction with a crossing angle has been studied for many years. Usually, it is believed that the horizontal oscillation of colliding bunch would be very stable. However, during the study of FCC-ee, the simulations [1] showed that there exists a coherent head-tail instability (X-Z instability) in collision with a large Piwinski angle. The "cross-wake force" induced by beam-beam interaction has been introduced to successfully explain this newfound instability [2, 3].

The stability of horizontal motion is sensitive to the longitudinal dynamics. The longitudinal impedance would modify the beam distribution, distort the longitudinal phase space trajectory, and produce incoherent synchrotron tune shift. Strong-strong simulation [4] showed that the stable tune area would be shifted, and the width would be squeezed when the longitudinal impedance is included in the simulation. It is interesting to study how the longitudinal impedance influences the X-Z instability analytically.

The ordinary transverse mode coupling instability (TMCI) theory [5] is derived as a perturbed Vlasov equation. In this theory, the transverse impedance, a perturbation source, represents the averaged wake force around the circumference of the ring. The TMCI is based on the solution of Sacherer's integral equation, only a few analytic solutions are known for some specific beam distributions so far. Some transverse

mode coupling analytical methods have been developed to treat the localized wake force [2, 3]. However, the distortion of longitudinal phase space trajectory and the incoherent synchrotron tune shift were not considered in these papers. In this paper, we will develop a new transverse mode coupling method where the effects of longitudinal phase space trajectory distortion and incoherent synchrotron tune shift induced by longitudinal impedance could be considered.

## LONGITUDINAL MOTION WITH WAKEFIELD

We use  $s = z + v_0 t$  with  $s$  the longitudinal Serret-Frenet coordinate, representing the arc length measured along the closed orbit from an initial point,  $v_0 \approx c$  the synchronous velocity and  $t$  clock time.  $z$  is the longitudinal distance from the synchronous particle and  $z > 0$  is the bunch head. In the following, we will use  $s$  as the timelike variable and  $z$  as the longitudinal coordinate.

As the particle moves along the beamline, the head of the bunch will act as a source of an electromagnetic field that kicks the tail. In one revolution, the relative longitudinal momentum kick  $\Delta\delta(z)$  received by a particle at  $z$  can be expressed by a wake function [5],

$$\Delta\delta(z) = -\frac{N_0 r_e}{\gamma} \int_{-\infty}^{\infty} W_z(z-z') \rho(z') dz'. \quad (1)$$

$W_z(z)$  is the ordinary longitudinal wake function with the property  $W_z(z) = 0$  ( $z > 0$ ).  $N_0$  represents the single bunch population,  $r_e$  is the classical radius of the electron,  $\gamma$  is the relativistic factor and  $\rho(z)$  is normalized line density.

Including the longitudinal wakefield, the Hamiltonian of the particle then reads,

$$-H = \frac{\eta_p}{2} \delta^2 + \frac{\mu_z^2}{2\eta_p L^2} z^2 - \frac{1}{L} \frac{N_0 r_e}{\gamma} \int_0^z dz'' \int_{-\infty}^{\infty} dz' W_z(z''-z') \rho(z') \quad (2)$$

where  $L$  represents the circumference of the ring,  $\nu_s$  is the synchrotron tune,  $\mu_z = 2\pi\nu_s$ ,  $\eta_p$  is the slippage factor.

For electron machine, due to the synchrotron radiation, the stationary distribution should have a Gaussian distribution with the RMS value  $\sigma_\delta$  in  $\delta$ ,

$$\psi(z, \delta) = \frac{1}{\sqrt{2\pi}\sigma_\delta} \exp\left(-\frac{\delta^2}{2\sigma_\delta^2}\right) \rho(z). \quad (3)$$

$\rho(z)$  can be obtained by solving Haissinski equation.

\* linctao@yeah.net

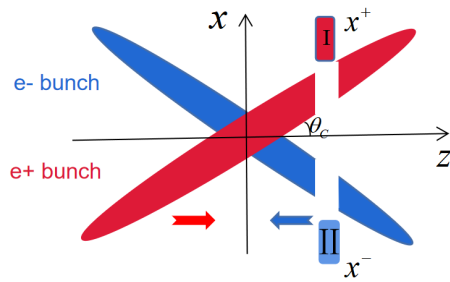


Figure 1: Beam-beam interaction with a crossing angle in Lorentz boost frame.

## CROSS-WAKE FORCE INDUCED BY BEAM-BEAM INTERACTION

Considering electron ( $e^-$ ) and positron ( $e^+$ ) bunches colliding with half crossing angle  $\theta_c$  in the  $x-z$  plane, the two bunches head on each other tilted horizontally by  $\theta_c$  in the Lorentz boost frame shown in Fig. 1. As the collision proceeds from the head of the bunch to the tail, the perturbed momentum kick due to horizontal betatron oscillation experienced by a  $e^\mp$  particle at  $z$  is expressed as follows [3],

$$\Delta p_x^{(\mp)}(z) = - \int_{-\infty}^{\infty} W_x^{(\mp)}(z-z') \rho_x^{(\pm)}(z') dz' \quad (4)$$

where  $\rho_x(z) = \rho(z) \cdot x(z)$  is the dipole moment of bunch, and  $W_x^{(\mp)}(z)$  is the cross-wake function [2, 3] for  $e^\mp$  beams induced by beam-beam interaction.

For symmetric collider, we assume the colliding bunches have the same parameters:  $N_0^+ \gamma^+ = N_0^- \gamma^-$ ,  $\sigma_{xz}^+ = \sigma_{xz}^-$ ,  $\nu_{xz}^+ = \nu_{xz}^-$ . The stability of colliding bunches can be studied separately for the  $\sigma$  mode  $\rho_x^{(+)}(z) = \rho_x^{(-)}(z)$  and  $\pi$  mode  $\rho_x^{(+)}(z) = -\rho_x^{(-)}(z)$ . The momentum kick in Eq. (1) is reduced to a normal wake force for single bunch

$$\Delta p_x(z) = \mp \int_{-\infty}^{\infty} W_x(z-z') \rho_x(z') dz, \quad (5)$$

where the “-” and “+” signs represent  $\sigma$  and  $\pi$  modes, respectively.

## TRANSVERSE MODE COUPLING THEORY WITH LONGITUDINAL IMPEDANCE

We use the normalized coordinates, where  $x$  and  $p_x$  are normalized by

$$x/\sqrt{\beta_x} \rightarrow x, \quad p_x\sqrt{\beta_x} \rightarrow p_x. \quad (6)$$

Since the dipole amplitudes  $x(J, \phi), p_x(J, \phi)$  are periodic functions of  $\phi$  with period  $2\pi$  in the longitudinal phase space, we expand them as Fourier series,

$$x(J, \phi) = \sum_{l=-\infty}^{\infty} x_l(J) e^{il\phi}, \quad p_x(J, \phi) = \sum_{l=-\infty}^{\infty} p_l(J) e^{il\phi}. \quad (7)$$

In the arc section, the synchro-betatron motion for the vector  $(x_l(J), p_l(J))$  is described by the matrix,

$$M_0 = e^{-2\pi i l \nu_s(J)} \begin{pmatrix} \cos \mu_x & \sin \mu_x \\ -\sin \mu_x & \cos \mu_x \end{pmatrix}. \quad (8)$$

Note that the synchrotron tune  $\nu_s(J)$  is a function of  $J$ .

At IP, the change of dipole moment, which is induced by cross-wake force, can be expressed as:

$$\Delta p_x(J, \phi) = \mp \beta_x \int W_x(z-z') x(J', \phi') \rho(z') dz'. \quad (9)$$

Using  $\rho(z') = \int \psi(J', \phi') d\delta'$ , we can rewrite the equation

$$\Delta p_x(J, \phi) = \mp \beta_x \int W_x(z-z') x(J', \phi') \psi(J') dJ' d\phi', \quad (10)$$

Substituting the expansions in Eq. (7) into Eq. (10), we obtain the momentum change for each azimuthal mode

$$\Delta p_l(J) = \mp \frac{\beta_x}{2\pi} \sum_{J'} \int dJ' W_{ll'}(J, J') \psi(J') x_{l'}(J'), \quad (11)$$

where

$$W_{ll'}(J, J') = \iint d\phi d\phi' e^{-il\phi + il'\phi'} W_x(z-z'). \quad (12)$$

Next we truncate  $l$  at  $\pm l_{max}$ , and discretize  $J$  at  $J_1, J_2, \dots, J_{n_j}$ . The momentum kick of Eq. (11) is converted to

$$\begin{aligned} \Delta p_l(J_i) &= \mp \frac{\beta_x}{2\pi} \sum_{J'} \sum_{J'_i} \Delta J_{i'} W_{ll'}(J_i, J'_i) \psi(J'_i) x_{l'}(J'_i) \\ &\equiv \beta_x M_{ll'i'i'} x_{l'}(J'_i). \end{aligned} \quad (13)$$

The transformation at IP, therefore, can be written in a more condensed matrix form,

$$M_W = \begin{pmatrix} 1 & 0 \\ \beta_x M_{ll'i'i'} & 1 \end{pmatrix}. \quad (14)$$

Finally, the stability of the colliding beams is determined by the eigenvalues ( $\lambda'$ s) of the revolution matrix  $M_0 M_W$ .

## APPLICATIONS

We use the CEPC-Z mode parameters [6] to study beam-beam interaction with and without longitudinal impedance. Figure 2 shows growth rate versus horizontal tune without longitudinal impedance obtained by our action discretization method and the conventional radial mode expansion method [5]. The two methods agrees well. We can see there are stable tune areas for both  $\sigma$  and  $\pi$  mode. Figure 3 shows the growth rate for various horizontal tunes where the longitudinal impedance is included. Comparing to the results without impedance shown in Fig. 2, the gap  $\Delta\nu$  between two neighboring peaks is reduced from 0.014 to 0.011. Besides the change of gap  $\Delta\nu$ , the once-stable working tune has turned unstable for both  $\sigma$  and  $\pi$  modes when we consider the influence of impedance.

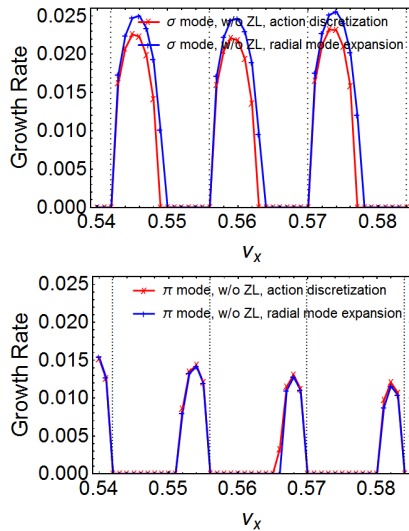


Figure 2: Growth rate vs. horizontal tune without longitudinal impedance (ZL). The upper and lower plots show the results of  $\sigma$  mode and  $\pi$  mode, respectively. The vertical lines are synchro-betatron sidebands  $\nu_x = 0.5 + n\nu_s$ ,  $\nu_s = 0.014$ .

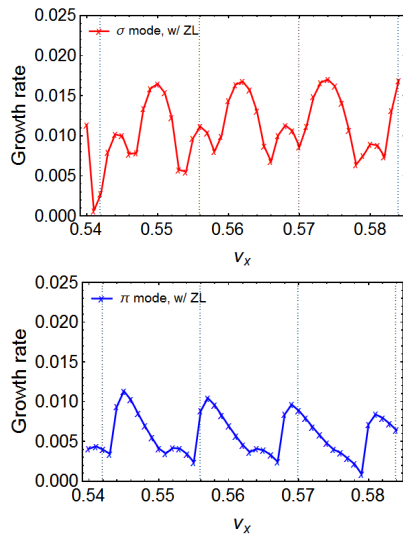


Figure 3: Growth rate vs. horizontal tune with longitudinal impedance (ZL). The red and blue points represent the  $\sigma$  and  $\pi$  modes, respectively.

The action discretization method can also be used to study TMCI with the replacement of cross wake force  $W_x(z)$  in Eq. (5) by the ordinary beam-environment coupling wake function. Here we use SILF parameters [7] without harmonic cavity to study TMCI. As shown in Fig. 4, with the longitudinal impedance, the eigentunes of each azimuthal mode as a spread, and this spread becomes larger as the beam intensity increases. This spread makes the growth rate appear at very low beam intensity.

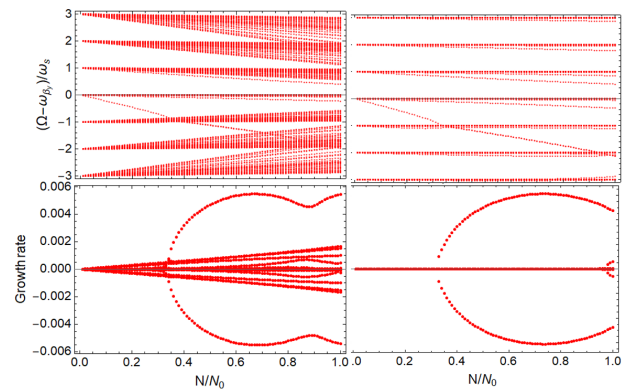


Figure 4: Eigentune and growth rate versus normalized beam intensity with (left) and without (right) longitudinal impedance.

## CONCLUSIONS

The beam-beam coherent head-tail instability in collision with a large crossing angle is strongly dependent on the longitudinal beam dynamics. In the absence of longitudinal impedance, distinct stable regions with horizontal working tunes, separated by  $\nu_s$ , can be observed. However, when considering the longitudinal impedance, these stable regions experience a considerable reduction. The conventional TMCI appears a growth rate at a relative low beam intensity when the longitudinal impedance is included. However we should keep in mind, in the above analysis, the nonlinear part of the force and other damping mechanisms are not included.

## REFERENCES

- [1] K. Ohmi, “Beam-beam and electron cloud effects in cecp/fcc-ee,” *International Journal of Modern Physics A*, vol. 31, no. 33, p. 1644014, 2016.
- [2] K. Ohmi, N. Kuroo, K. Oide, D. Zhou, and F. Zimmermann, “Coherent beam-beam instability in collisions with a large crossing angle,” *Phys. Rev. Lett.*, vol. 119, p. 134801, Sep 2017.
- [3] N. Kuroo, K. Ohmi, K. Oide, D. Zhou, and F. Zimmermann, “Cross-wake force and correlated head-tail instability in beam-beam collisions with a large crossing angle,” *Phys. Rev. Accel. Beams*, vol. 21, p. 031002, Mar 2018.
- [4] Y. Zhang, N. Wang, C. Lin, D. Wang, C. Yu, K. Ohmi, and M. Zobov, “Self-consistent simulations of beam-beam interaction in future  $e^+e^-$  circular colliders including beamstrahlung and longitudinal coupling impedance,” *Phys. Rev. Accel. Beams*, vol. 23, p. 104402, Oct 2020.
- [5] A. Chao, *Physics of Collective Beam Instabilities in High Energy Accelerators*. Wiley-Interscience Publication, New York, 1993, and references therein.
- [6] C. Lin, K. Ohmi, and Y. Zhang, “Coupling effects of beam-beam interaction and longitudinal impedance,” *Phys. Rev. Accel. Beams*, vol. 25, p. 011001, Jan 2022.
- [7] T. He, Z. Sun, T. Zhang, G. Liu, R. Ji, and C. Lin, “Physics design of the shenzhen innovation light source storage ring,” *Journal of Instrumentation*, vol. 18, no. 05, p. P05037, 2023.

# RESEARCH ON BEAM DYNAMICS OF A 2 GeV 6 MW ISOCHRONOUS FFA\*

Tianjue Zhang<sup>†</sup>, Wei Fu<sup>1</sup>, Chuan Wang<sup>1</sup>, Tianjian Bian<sup>1</sup>, Shilun Pei<sup>1</sup>, Zhiguo Yin<sup>1</sup>, Hongji Zhou<sup>1</sup>,  
Ziye Yin<sup>2</sup>, Suping Zhang<sup>1</sup>, Jingyuan Liu<sup>1</sup>, Xiaofeng Zhu<sup>1</sup>, Zhichao Chu<sup>1</sup>, Hao Le<sup>1</sup>

<sup>1</sup>China Institute of Atomic Energy, Beijing 102413, P R China

<sup>2</sup>FRIB, East Lansing, Michigan

## Abstract

CIAE has proposed an innovative design for a 2 GeV, 6 MW isochronous FFA in 2019. This study aims to present the results of beam dynamics research, demonstrating the feasibility to accelerate the intense proton beam with the energy beyond 1 GeV limitation of isochronous cyclotrons. By introducing 1st - 3rd radial gradient of peak magnetic field to simulate the quadrupole to octupole component of the isochronous machine, three different lattice designs are obtained. Adjusting the radial gradient of the peak field allows an option to avoid or cross integer resonances. Various inherent and coupled resonances are investigated subsequently, with a focus on the destructive effects of the  $\nu_r=3$  on the transverse phase space. Based on PIC method, we simulate the vortex motion caused by space charge in a large-scale alternating gradient field. Results indicated that the radial size of beam is  $\sim 10$  mm, which is expected to be improved after considering the effects of neighboring bunches. Additionally, high-Q RF cavities and precession extraction further enlarge the turn separation to 30 mm, ensuring efficient beam extraction in the extraction region.

## INTRODUCTION

High energy and high current proton accelerators are widely applied in frontier research fields such as nuclear physics and particle physics, national economic fields such as public health and advanced energy, and even national defence industry and national security [1][2]. Proton accelerator with an average beam power of 5-10 MW is the world's dream machine for more than 30 years [3][4]. Cyclotrons can provide continuous wave beam but are restrict by energy limitation  $\sim 1$  GeV [5]. Beyond the traditional solutions for high intensity machines such as superconducting linac and rapid cycling synchrotron, CW FFA which is non-scaling and nonlinear was considered as an attractive proposal for several megawatts machine [6]. To utilize strong focusing optics and fixed frequency for CW acceleration, a 2 GeV/6 MW FFA concept design was proposed in 2019 [7]. In this machine, the F-D-F lattice design has been adopted to realize strong focusing. Each focusing and defocusing magnet has a third-order magnetic field gradient in the radial direction, which can achieve the effect of the dipole to octupole magnets, and thereby balance the isochronism and focusing. Based on this principle of adjusting gradient to provide strong focusing, higher-order nonlinear magnetic field components were added (such as quadrupole, hexapole, octupole, etc) to avoid important resonance crossings, resulting in a "radial local achromatic" effect. Three different lattice schemes (2019, 2020,

2022) are designed to achieve the goal of the isochronous acceleration for 2 GeV proton. The basic parameters of the three schemes are listed in Table 1. In this paper, beam dynamics of the 2 GeV/6 MW FFA is summarized for better comprehension of non-scaling and nonlinear FFA machines.

Table 1: Basic Parameters of 2 GeV CW FFA Machine

Parameters	Scheme 1	Scheme 2	Scheme 3
Extracted energy	2 GeV	2 GeV	2 GeV
Focusing magnet radius*	23.3~26.8 m	18.2~20.9 m	17.6~19.4 m
Defocusing magnet radius*	23.3~26.8 m	18.2~20.9 m	17.6~19.4 m
Focusing field	1.5~2.7 T	1.56~2.62 T	1.57~2.66 T
Defocusing field	1.0~2.4 T	1.77~2.51 T	1.15~2.31 T
Number of lattices	10	10	10
RF frequency	44.4 MHz	35.1 MHz	51.6 MHz
Cavity voltage (single cavity)	1.2 MeV	1.5 MeV	1.5 MeV
Harmonic number	26	16	22
Number of cavities	10	15	15
Turn separation for the extraction	$\sim 1.5$ cm	$\sim 1.5$ cm	$\sim 1.5$ cm

\* (From the machining center)

## STATIC ORBITS ANALYSIS

### *Isochronism and Tune*

It is well-known that static beam dynamics results are the basis for one to verify the feasibility of the lattice design. Therefore, the results of phase slip, tune diagram, and static region are introduced first.

The magnetic field of 2 GeV/6 MW machine (CYCIAE-2000) has the characteristics of high order gradient (up to 3<sup>rd</sup>), strong nonlinearity, etc. The physical design and beam dynamics study require higher tracking accuracy of the particle tracking program, especially near the edge field of focusing and defocusing magnets. Besides that, the beam dynamics simulation also needs higher magnetic field interpolation accuracy and more reasonable tracking algorithms which adaptive to wide-range twisty orbits of FFA. Some

improvements of interpolation method are accomplished in closed orbit calculation codes as Cyclops [8].

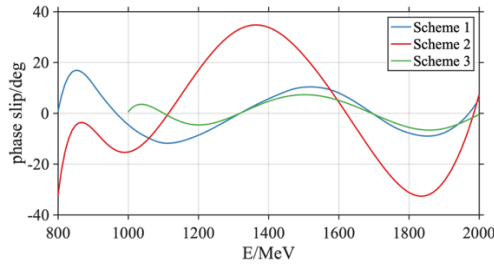


Figure 1: Integral phase slip of different schemes.

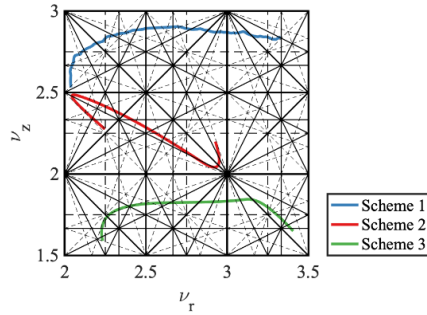


Figure 2: Tune diagram.

In scheme 1 we proposed in 2019, the differential phase slip is controlled below  $\pm 1\%$  and the maximum integral phase slip of three schemes is  $35^\circ$ , as shown in Figure 1. It can be concluded that the magnetic field can well meet the isochronous requirement. The harmonic number is set to 26, and the RF frequency is 44.4 MHz, which equal to 100 MeV compact cyclotron CYCIAE-100.

In scheme 2, the harmonic number is set to 16, and the RF frequency corresponds to 35.1 MHz. The phase slip of the beam during the acceleration process is controlled within  $\pm 40$  degrees, which ensures a specific energy gain per turn. Due to the introduction of local 3<sup>rd</sup> magnetic field distribution to avoid integer resonance, a certain amount of isochronism is sacrificed at the injection and extraction position. Therefore, the corresponding frequency error is about 3%. According to the single-cavity voltage of 1 MV, it takes approximately 91 turns to extract the beam.

In scheme 3, the harmonic number is set to 22, and the RF frequency corresponds to 51.65 MHz. Due to the utilization of an integer resonance suppressor (IRS) [9], it is possible to cross  $\nu_r=3$  integer resonance while controlling beam envelop growth. With the benefit of IRS, the phase slip is better than Scheme 2 and can be controlled within  $\pm 10$  degrees, which is beneficial for clean extraction.

### Stable Region

The stable region both for radial and vertical phase spaces, should be investigated carefully to find the boundary of the linear region and ensure the beam is accelerated stably. Since strong focusing is realized in FFA machines based on alternative fields, the vertical and radial stable region is much bigger than compact cyclotron. For Scheme 2, near injection and extraction, the radial tune is close to 2, 3 respectively.  $\nu_r$  escapes these integer

resonances and provides a certain width away from resonance lines with some sacrifice of isochronism as shown in Figure 2, which is achieved by 3<sup>rd</sup> order magnetic field.

In Scheme 2, the working path is closed to  $\nu_r=2$  and  $\nu_r=3$  resonance lines at injection and extraction respectively. Moreover, the working path moves around the coupled resonance over a wide range, which should be evaluated during resonance analysis. In the stable region, the most important resonance is  $\nu_r=2.5$ , and the corresponding energy is 1270 MeV. The stable regions are shown in Figure 3.

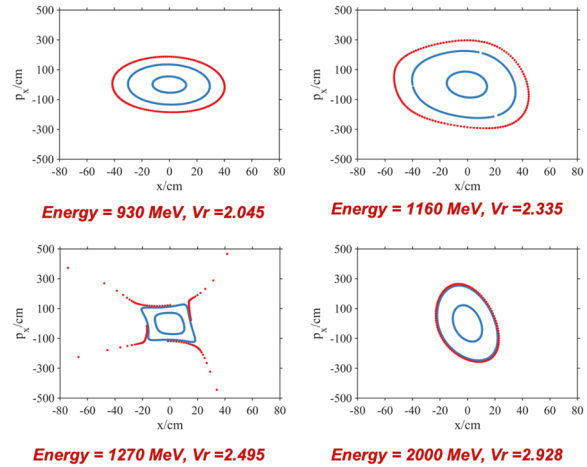


Figure 3: Stable Regions of Scheme 2.

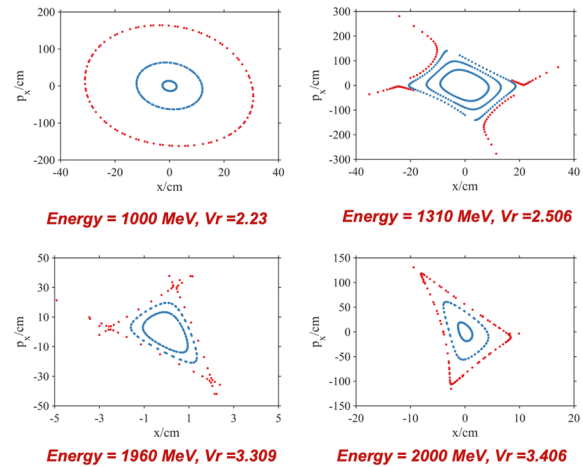


Figure 4: Stable Regions of Scheme 3.

As demonstrated in Figure 4, radial stable region is enough for 3 cm off center non-ideal particles. For Scheme 3,  $\nu_r=3$ , the most important resonance is inhibited using IRS. Besides that, resonances of  $3\nu_r=10$  and  $4\nu_r=10$  are also investigated. Since the highest order of lattice magnetic field is third, the stable region of fourth order resonance is much larger than third order resonance. Moreover, the beam can quickly pass through these two critical inherent resonances with the help of significant energy gain up to 15 MeV per turn based on recent experiments of a scaled RF cavity (Q~42000).

## MULTI-PARTICLE BEAM DYNAMICS

### Resonance Study

For the analysis of Scheme 1, the most important resonance line is  $\nu_r=3$ . To quantify the influence of  $\nu_r=3$  resonance, a  $B_3$  error field is added to the field map of middle plane near the radius of  $\nu_r=3$  (Radial rectangular distribution with radial width 15 cm, phase is fixed at  $45^\circ$ ). The energy gain per turn is 10 MeV/turn, and the gradient of  $\nu_r$  is 0.001/MeV (or 0.01/turn). With 0.5 Gs  $B_3$  amplitude, the radial oscillation increases from  $\sim 6$  mm to  $\sim 15$  mm. With 1 Gs  $B_3$  amplitude, the radial oscillation is about  $\sim 26$  mm. The details are shown in Figure 5.

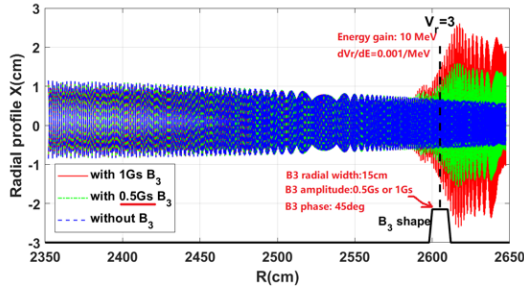


Figure 5: Enlargement of beam envelope caused by  $\nu_r = 3$  integer resonance for Scheme 1.

Resonance study is carried out especially for Scheme 2. We have summarized the crossed resonance lines for the three schemes in the Table 2.

Table 2: Summary of Resonance Study

Reso-nance	Driving term	Scheme 1 Energy	Scheme 2 Energy	Scheme 3 Energy
$\nu_r=2$	$B_2$	800~850	800~900	/
$\nu_r=3$	$B_3$	1640~1680	1850~2000	1690
$2\nu_r=5$	$dB_5/dr$	1280	1280	1320
$\nu_r-\nu_z=0$	$d\bar{B}/dr$	1560	1120	/
$\nu_r+\nu_z=5$	$dB_5/dr$	1030	1640	1870
$\nu_r+2\nu_z=7$	$d^2B_7/dr^2$	/	1390	/
$\nu_r-2\nu_z=-2$	$d^2B_2/dr^2$	/	1250	/
$2\nu_r-\nu_z=2$	$d^2B_2/dr^2$	1230	1030	/
$2\nu_r+\nu_z=8$	$d^2B_8/dr^2$	/	1730	1790
$3\nu_r=7$	$d^2B_7/dr^2$	1150	1160	1170
$3\nu_r=8$	$d^2B_8/dr^2$	1400	1410	1420
$3\nu_r=10$	$d^2B_{10}/dr^2$	2000	/	1960

This table shows that low-order resonances, such as integer resonances, are the main barriers for the higher energy acceleration, especially for the CW FFA machine. Part of numerical simulation results can be found in Ref [10]. It can be concluded that with the benefit of a strong focusing of the alternating radial gradient, the axial envelope is effectively controlled for the coupled resonances. In summary, also through the multi-particle simulation, the beam envelope does not increase significantly when considering

the non-ideal magnetic field, except for the second harmonic field at some particular phases. These simulations show that the lattice structure design of Scheme 2 can tolerate a certain amount of non-ideal magnetic field components and is feasible in magnet construction.

To maintain better isochronism,  $\nu_r=3$  is crossed but suppressed by IRS mentioned before in Scheme 3. In addition, Scheme 3 crosses Walkinshaw resonance when the beam is almost extracted. Since energy gain per turn is relatively large, it can be verified by numerical simulation that the beam envelop grows only slightly when the amount of off-center is about 1 cm, and half envelop increases to 10 mm at the case of 3 cm off-center, which is shown in Figure 6.

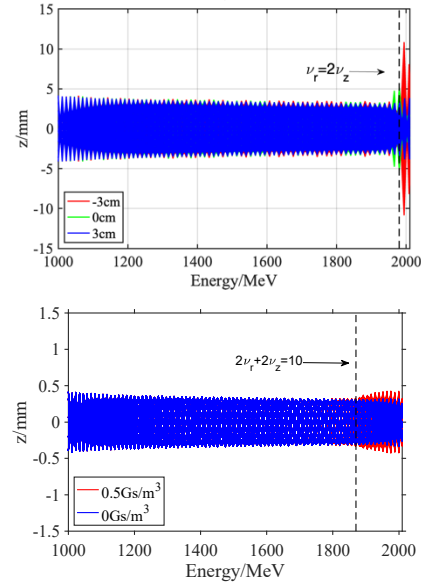


Figure 6: Vertical beam envelop of off-centered beam,  $\nu_r=2\nu_z$  (up),  $2\nu_r+2\nu_z=10$  (down).

Higher order resonance  $2\nu_r+2\nu_z=10$  is also under consideration. It is an inherent resonance in our machine while the highest of magnetic field is 3rd, only small amount of driving term at extraction. Case of 0.5 Gs/m<sup>3</sup> is simulated and the phase of  $B_{10}$  field is random. Figure 6 shows that the beam envelop is growing a little due to this resonance.

### Space Charge Effect in the FFA Machine

In FFA, it is unclear whether the high-current beam, coupled with strong nonlinear, large gradient magnetic field and multi-bunch space charge effects, produces the same beneficial dynamical behavior for beam acceleration and extraction in the high-intensity cyclotron. Its feasibility has to be verified numerically by high-performance parallel computation.

OPAL-CYCL (the cyclotron flavor of the beam dynamics simulation framework OPAL) is a good candidate for CW FFA design since it allows parallel calculations of large-scale particles and uses the first 3D PIC algorithm [11]. In which the code considers the effects of space charge among neighboring bunches. OPAL introduced the AMR (adaptive mesh refinement) algorithm based on the massively parallel computing framework AMReX in version 2.4.0, which can significantly reduce the

computational cost and memory consumption while ensuring computational accuracy. We have modified and verified it, found more in-depth problems related to the mesh accuracy division, and found the direction to optimize the algorithm from the essence. However, there is still room for optimizing the AMR algorithm's domain mapping and resetting the mesh distribution frequency.

After the present analysis, we can conclude that it is reasonable to set a smaller number of grids for directions with smaller beam sizes and more minor variation scales. However, determining the accuracy of such a setting requires larger-scale simulations on a more powerful computer and rigorous theoretical analysis. The isotropic nature of the grid size that the AMR algorithm needs to calculate also makes the ever-changing ratio of the beam size impossible to achieve the best optimization simply by the initial grid size. As shown in Figure 7, for example, when the dimensions or the ratio of the different dimensions of the bundle changes, the dimension that only needs to be divided into two or three grids to maintain the accuracy in the actual region may be mapped to the computational region because the initial setting needs to be divided into four grids, resulting in a waste of computing power.

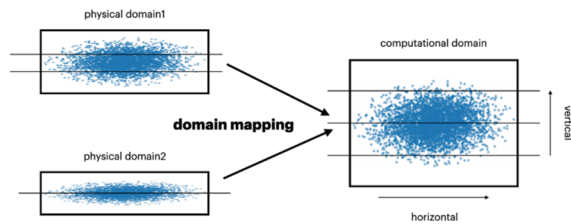


Figure 7: Schematic diagram of the mapping of a beam of varying size scale onto a fixed computational region.

There are also preliminary results from the multi-particle simulations, specifically for Scheme 3. Figure 8 depicts the outcome of the simulation in the horizontal plane and the vortex effect that is seen. The bunch's initial parameters are: Transverse emittance is  $2\pi$  mm·mrad; phase width is  $3^\circ$ ; beam current is 3 mA. In the case of phase width equal to  $3^\circ$ , the vortex motion is incomplete and the initial phase ellipse is not well matched. Moreover, the transverse size of the bunch decreases to around  $\pm 7$  mm at the final turn, making it potentially appropriate for extraction.

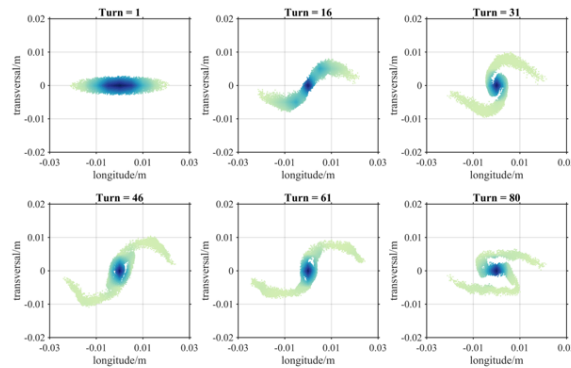


Figure 8: Longitudinal and transverse beam shape variation, from left to right, from top to bottom, 1, 16, 31, 46, 61, 80 turns.

The followings are the compared results with and without the space charge effect, with and without flattop cavity in more detail. As compared in the first and second rows of Figure 9, the beam quality is significantly better without a space charge, demonstrating that the space charge effect is primarily responsible for the vortex effect in the CW FFA. It is also indicated in the second row and the third row in Figure 9 that higher beam current results in a more significant space charge effect, which increases the transverse size near  $\pm 1$  cm. Nevertheless, with higher energy gain provided by RF cavities and properly arranged extraction elements, turn separation is promisingly increased to 30 mm, which is suitable for extraction.

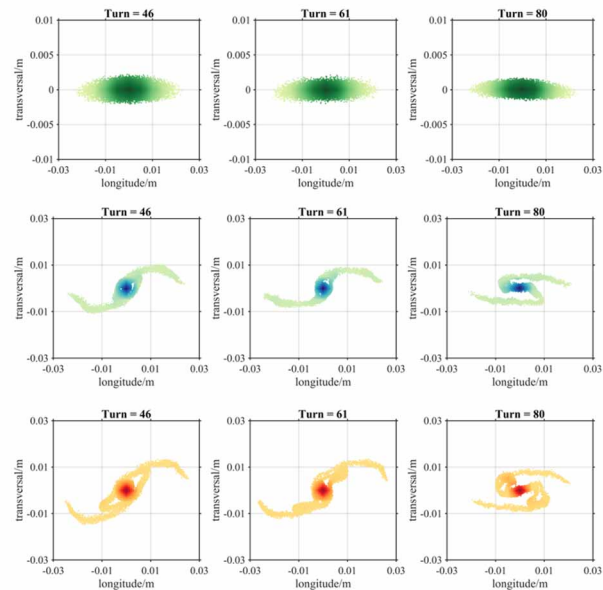


Figure 9: Longitudinal and transverse beam shape variation, from the 1st column to the 3rd column, 46, 61, 80 turns; from the 1st row to the 3<sup>rd</sup> row: 0 mA with space charge (green); 3 mA with space charge (blue-green); 6 mA with space charge (yellow).

## POSSIBLE SOLUTIONS FOR EXTRACTION

### *Extraction by Integer Resonance*

For high-intensity isochronous accelerators, the critical factor limiting a further increase in current intensity is the beam loss around the extraction region. If the extraction efficiency of the accelerator is not high, crucial components such as the accelerator vacuum pipe and deflector will be bombarded during high-power operation, resulting in activation, which will affect the maintenance of the accelerator. Therefore, improving the extraction efficiency of high-current beams by enlarging the turn separation and reducing the bunch size is a critical issue in the research of extraction simulation for high-energy and high-power accelerators.

The 2 GeV FFA adopts the following two methods to increase turn separation: 1) The layout of long drift sections can add a large number of high-frequency cavities to maximize the energy gain; 2) Off-centered injection can produce precession at the extraction position, increasing the separation of the last turn, but integer resonance needs to be carefully considered.

Scheme 2 utilizes integer resonance for extraction, tunes the working path near the extraction area reasonably, and controls  $\nu_r \approx 3$  resonance to drive radial oscillation. Although the second scheme avoids the problem of crossing integer resonance, there are still some challenges in beam extraction. The reason is that due to the adjustment of the local radial gradient of the magnetic field, the beam is on the longitudinal defocusing phase of the high-frequency field in the last thirty circles, increasing the phase width of the beam, which brings a more significant impact on the extraction of the beam and make it more difficult. After the beam with an initial phase width of  $5^\circ$  is accelerated, the phase width is stretched to about  $10^\circ$ . Increase of beam phase width will make the extraction effect of precession worse. As shown on the left side of Figure 10, the results of precession extraction in radial phase space indicated large turn separation but the beam size is growing at extraction region.

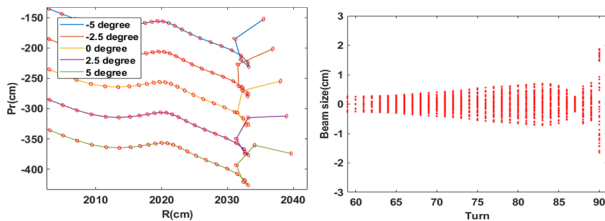


Figure 10: The precession effect of scheme 2 (left) and the growth of the beam envelope (right).

### Extraction by Half Integer Resonance

To avoid growth of beam size and energy dispersion, Scheme 3 is more potential for 3 mA extraction. By adding a  $B_3$  components, radial oscillation of different phases is excited. It realizes a suppression of orbital oscillation and make it possible to cross the integer resonance and utilizing half resonance for extraction. The tolerance of magnetic field error can be improved from 1 Gs to 10 Gs with IRS.

## CONCLUSION

Three feasible schemes for 2 GeV/6 MW FFA are found and beam dynamics is introduced and compared in detail. Scheme 2 avoids  $\nu_r=3$  resonance using adjustment of 3<sup>rd</sup> order radial field, which serves as octupole component.

Resonance study is carried out in detail for Scheme 2 and gives tolerance of magnetic field error. Parallel computing included space charge effect is underway and some results supports high-current extraction while the turn separation is potential to  $\sim 3$  cm. Integer and half-integer resonances extraction is studied and provide some possible methods to enlarge the turn separation from 1.5 cm to 3 cm.

## REFERENCES

- [1] R. Garoby, *et al.*, "Proton drivers for neutrino beams and other high intensity applications", *Journal of Physics: Conference Series*, vol. 408, p. 012016, 2013.
- [2] C. L. Morris, *et al.*, "New Developments in Proton Radiography at the Los Alamos Neutron Science Center (LANSCE)", *Experimental Mechanics*, vol. 56, pp. 111-120, 2016. doi: 10.1007/s11340-015-0077-2
- [3] C. Rubbia, *et al.*, "Conceptual design of a fast neutron operated a high-power energy amplifier", CERN/AT/95-44 (ET).
- [4] Th. Stambach, "High Intensity Problems, Revisited or Cyclotron Operation Beyond Limits", *Proc. of the 15th International Conference on Cyclotrons and their Applications*, Caen, France, 1998, p. 369.
- [5] Johnstone, C., *et al.* "A Compact, GeV, High-Intensity (CW) Racetrack FFAG." *Proceedings of the 20th International Conference on Cyclotrons and Their Applications*, Vancouver, BC Canada, 2010.
- [6] Johnstone, C., *et al.* "Advances in nonlinear non-scaling FFAGs." *International Journal of Modern Physics A*, vol. 26, no. 10-11, pp. 1690-1712, 2011.
- [7] Tianjue Zhang, Ming Li, *et al.*, "A New Solution for Cost Effective, High Average Power (2GeV, 6MW) Proton Accelerator and its R&D Activities", *22st Int. Conf. on Cyclotrons and their Applications*, Cape Town, South Africa, 2019.
- [8] M. Gordon, Computation of closed orbits and basic focusing properties for sector- focused cyclotrons and the design of cyclops, *Particle Accelerators*, vol. 16, p. 39, 1984.
- [9] T. Bian, T. Zhang, *et al.* "Possible solution for the integer resonance crossing problem of gev-class isochronous fixed-field alternating gradient accelerators", *Nuclear Instruments and Methods in Physics Research Section A: Accelerators, Spectrometers, Detectors and Associated Equipment*, vol. 1031, p. 166594, 2022.
- [10] Tianjue Zhang, *et al.* "Innovative research and development activities on high energy and high current isochronous proton accelerator." *Journal of Instrumentation*, vol. 18, no. 03, p.03022, 2023.
- [11] J. J. Yang, *et al.* "Beam dynamics in high intensity cyclotrons including neighboring bunch effects: Model, implementation, and application." *Physical Review Special Topics-Accelerators and Beams*, vol. 13, no. 6, p. 064201, 2010.

# STUDY OF THE KEY PHYSICS PROBLEMS IN 10mA-CLASS HIGH CURRENT CYCLOTRON

Tianjian Bian<sup>†</sup>, Shizhong An, Fengping Guan, Luyu Ji, Sumin Wei  
China Institute of Atomic Energy

## Abstract

10MW-class ultra-high power cyclotron (UHPC) has great application prospects in cutting-edge sciences, neutron source, advanced energy and advanced material, etc. So far, Cyclotron with average beam power of 10 MW still have some bottleneck problems. Beam energy and current of a high-power cyclotron are typically less than 800MeV and 3mA. In this paper, bottleneck problems of UHPC are analysed, and then a preliminary design of UHPC-10MW is presented.

## INTRODUCTION

GeV-class proton beam with an average power of several megawatts has many important applications in particle physics towards the intensity frontier, as well as in the advanced energy and material science. There are three different types of constructed accelerators for high power proton beam production: The cyclotron, linear accelerator and rapid-cycling synchrotron. The highest beam power of these accelerators currently is 1.4 MW. Reference [1] reported the energy efficiency of the three operational accelerators with the highest beam power in the world, which showed that the energy efficiency of the PSI cyclotron is about 2 times of the other types, as shown in Table 1. Weng made a judgement that the beam/grid efficiency should be better than 30%, otherwise the Accelerator Driven subcritical-reactor System(ADS) becomes nonsense 0. Studies have shown that the energy efficiency cyclotron is the highest which is expected to be 60%~65% in superconducting ring cyclotron 0. As cyclotron is a good technical route to develop proton machines with high beam power and high-power efficiency, it shows good prospect in advanced energy.

The beam power of UHPC-10MW aims at 10MW, it composes of two stages. The first stage is a 150MeV/amu injector and the second stage is a 1GeV/amu ring cyclotron. If UHPC-10MW is used to drive a spallation neutron source, the injector and the ring cyclotron can produce thermal neutron flux in the order of  $10^{14}$ n/cm<sup>2</sup>/s and  $10^{15}$ n/cm<sup>2</sup>/s, respectively. UHPC-10MW based spallation neutron source will have higher thermal neutron flux than high-flux reactor based neutron source. Even the 150MeV/amu injector can produce high thermal neutron flux which comparable to middle flux reactor neutron source. Figure 1 shows the history of thermal neutron

flux 0, and UHPC-10MW based spallation neutron sources are marked with stars.

Table 1: Efficiency of Different Types of High-Power Accelerators

Accelerator	Type	Energy (MeV)	Power (MW)	Efficiency
SNS	Linac	1000	1.3	8.6%
JPARC	synchrotron	3000	1.0	3%
SINQ	cyclotron	590	1.4	18%

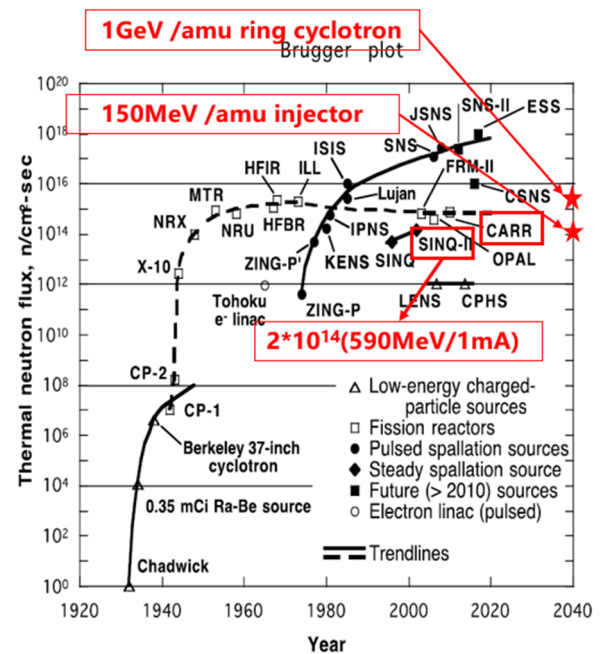


Figure 1: Thermal neutron flux history.

## OVERALL DESIGN AND CONSIDERATION

Figure 2 shows the layout of UHPC-10MW. We choose a 1MeV/amu RFQ as the pre-injector, and a separate sector cyclotron accelerate the beam from RFQ to 150MeV/amu, finally the beam is injected to a 1GeV/amu ring cyclotron.

Superconducting linac is the mainstream of high-power accelerator, due to relative higher technical maturity. So far, no well-approved design of 10MW-class cyclotron is made due to some bottleneck problems. Radial tune is increasing linearly with beam energy in isochronous cyclotron, and thus the integer resonance crossing problem becomes an inevitable problem. Isochronous cyclotron is considered impossible to accelerate particles to a kinetic energy above its rest mass 0, typically 800MeV/amu.

\* This work was supported by the National Natural Science Foundation of China (Grant No. 12105370) and the Scientific Research Program for Young Talent Elite Project of China National Nuclear Corporation (Grant No. FY212406000404).

<sup>†</sup> email address biantianjian@foxmail.com

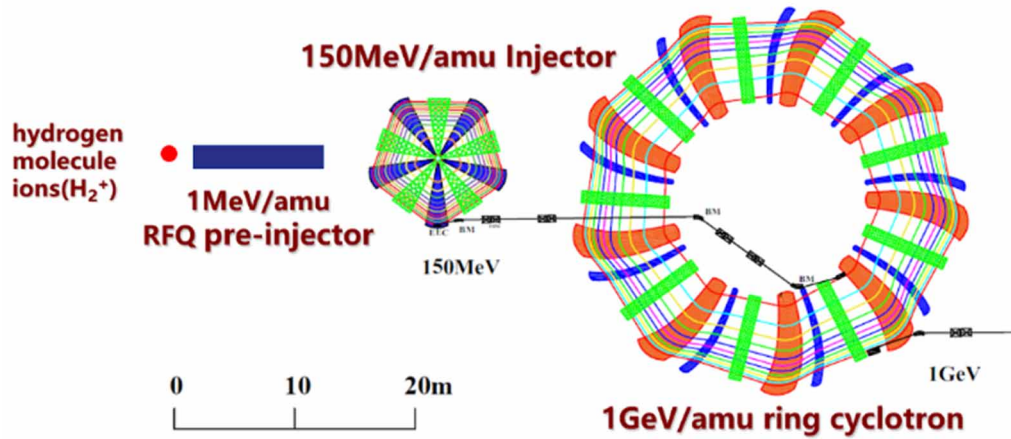


Figure 2: Layout of UHPC-10MW.

Although cyclotron has continuous beam structure, the beam intensity is considered lower than 3mA. The reason is enough clear region is need for beam extraction, otherwise the halo or tail particles will activate the deflector.

In the design phase of UHPC-10MW, those problems need careful consideration and calculation. There are three bottleneck problems and their solutions:

- (1) In low energy region, beam dynamics is dominated by space charge effect, so halo and tail particles are generated by space charge and nonadiabatic acceleration. In our design, we accelerate 5 mA of hydrogen molecule ions ( $H_2^+$ ) instead of 10 mA of protons, which will mitigate the space charge effect 0.
- (2) In high energy region, beam energy is limited by integer resonance. Beam integrates the harmonic field when passing through the integer resonance region, which drives large coherent oscillation. To solve those problems, an idea of integer resonance suppressor (IRS) was proposed 0. IRS introduces the harmonic magnetic field intentionally to reduce the integration of driving harmonic field.
- (3) In extraction region, single turn extraction with very low beam losses is also a very important issue of UHPC. The experience of PSI has shown that the upper limit of power deposition is 200W. For 10MW beam, relative losses should less than  $2E-5$ . IRS can not only inhibit the radial oscillation and beam size blowup caused by integer resonance crossing but also contribute to a controllable coherent oscillation which is helpful to beam extraction with high efficiency 0. With the help of IRS, turn separation can be enlarge to more than 30 mm.

### 150MeV/AMU INJECTOR

Parameters of 150MeV/amu injector are listed in Table 2. 5 sectors scheme is adopted to avoid intrinsic resonance. Generous space between neighboring sectors can be used to install 5 powerful RF cavities. Beam is radially injected by a 1MeV/amu RFQ pre-injector. Electrostatic deflector with a stripper foil placed upstream is used to high efficiency extraction.

To get the matched distribution, we track a coasting beam with 5mA at 1MeV/amu closed orbit until the equipartitioning process has resulted in a stationary distribution. Three cases with different phase width (9, 7, 6 rms degree) are simulated, as shown in Figure 3. For those simulation,  $10^4$  particles and mesh of  $32^3$  grid points is used. In the coasting process, obvious longitudinal-radial coupling occurs and the gradually forms a round, compact distribution in 20 turns.

Track the coasting beam for 50 turns and make statistics on beam parameters. Figure 4(a) and (b) show the relationship of beam parameters with phase width. We can find that both beam size and emittance are increasing with phase width. On the other hand, narrower phase width will develop into more compact distribution and wider phase width will lead to more halo particles, as shown in Figure 4(c) and (d).

Table 2: Parameters of 150MeV/amu Injector

Parameter	value
Accelerating particles	H2+
Extraction particles	H2+
Injection energy	1MeV/amu
Extraction energy	150MeV/amu
Extraction type	Electrostatic deflector
Turn separation at Extraction	~3cm
Magnet sectors	5
Magnetic field of hill	3~3.7T
Radius of pole	4.2m
Cavity number	5
Harmonic number	7
Cavity frequency	~57MHz
Cavity Voltage	~350kV
Energy gain per turn	~3.4MeV

When acceleration is considered, beam halo will also increase due to nonadiabatic acceleration, especially in the low energy region. With contribution of acceleration and precession, turn separation is about 32mm and the second and third to last turn overlap with each other. Beam is well

controlled within  $\pm 6\text{mm}$  in axial direction and septum is placed at the lowest intensity point, as shown in Figure 5. If 0.5mm is chosen as the septum thickness, the beam power at the deflector will be less than 30W.

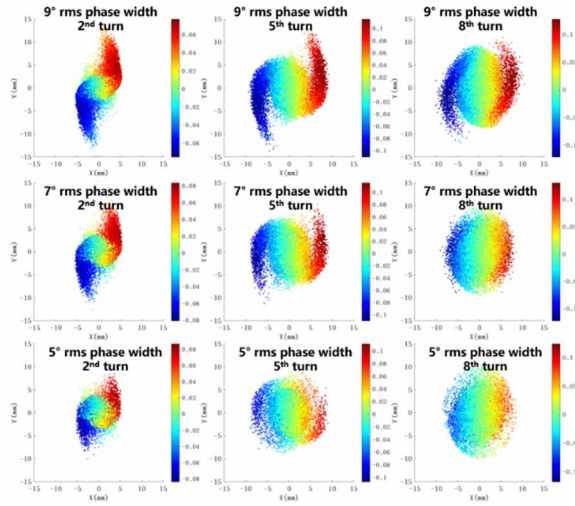


Figure 3: longitudinal-radial coupling in the coasting process. Colour bars stand for energy deviation (MeV).

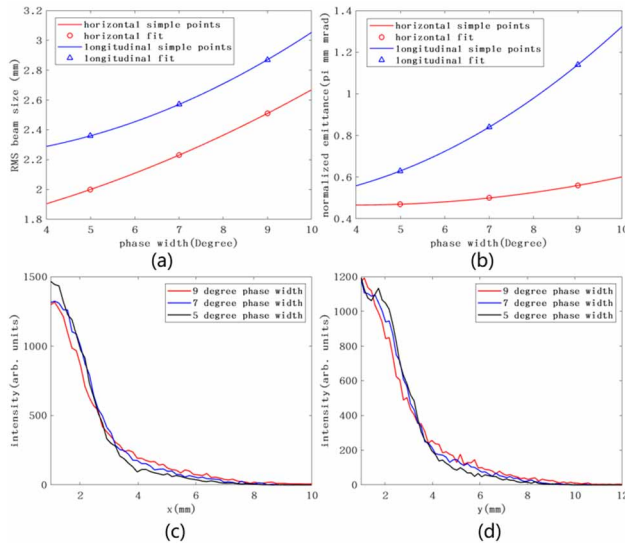


Figure 4: (a) Beam size as function of phase width. (b) Normalized emittance as function of phase width. (c) Distribution of matched beam in x direction. (d) Distribution of matched beam in y direction.

## 1GeV/AMU RING CYCLOTRON

Parameters of 1GeV/amu ring cyclotron are listed in Table 3. 9 high voltage RF cavities are installed in the space between neighboring sectors. Electrostatic deflector with a stripper foil placed upstream is used to high efficiency extraction.

In this ring cyclotron, beam is accelerated to beyond the integer resonance  $\nu_r = 2$ . In the extraction region,  $\nu_r$  extend to nearly 2.5 to enlarge the turn separation. Figure 6 shows the tune diagram.

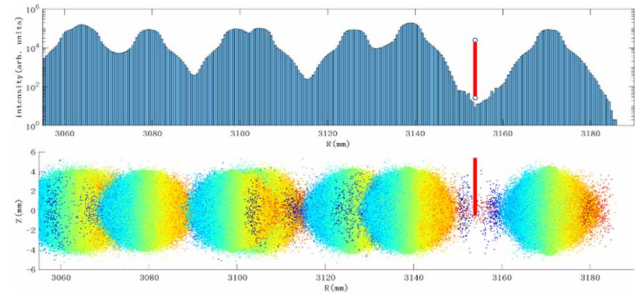


Figure 5: Beam intensity on radial probe.

Table 3: Parameters of 1GeV/amu Injector

Parameter	value
Accelerating particles	H2+
Extraction particles	H2+
Injection energy	150MeV/amu
Extraction energy	1GeV/amu
Extraction type	Electrostatic deflector
Turn separation at Extraction	$\sim 3\text{cm}$
Cell number	9
Magnetic field of hill	2.7~4 T
Radius of pole	$\sim 11.2\text{m}$
Cavity number	9
Harmonic number	14
Cavity frequency	$\sim 57\text{MHz}$
Cavity Voltage	$\sim 1.3\text{MV}$
Energy gain per turn	$\sim 12\text{MeV}$
3 <sup>rd</sup> harmonic Cavity number	3
Voltage of 3 <sup>rd</sup> harmonic Cavity	10% of main cavity Voltage

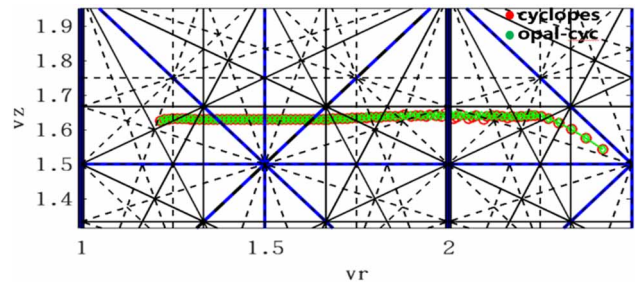


Figure 6: Tune diagram.

Beam integrates the harmonic field when passing through the integer resonance region, which drives large coherent oscillation. Second harmonic field  $B_2$  of only 3Gs will drive coherent oscillation of 70mm, which can be estimated with formula  $\Delta A = \frac{\pi}{\sqrt{Q_r}} \frac{R}{B} \frac{B_2}{Q}$ . Such large coherent oscillation is incompatible with the following resonance  $4\nu_r = 9$  and the beam size is blown up. Figure 7(a) Shows that the radial beam size is increased about 2 times. One of the reasons is that intrinsic resonance  $4\nu_r = 9$  distorts the phase space, as shown in Figure 7(b).

Content from this work may be used under the terms of the CC BY 4.0 licence (© 2023). Any distribution of this work must maintain attribution to the author(s), title of the work, publisher, and DOI

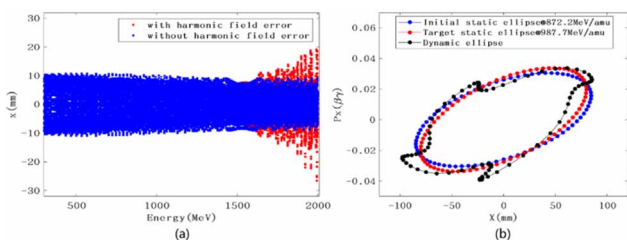


Figure 7: (a) Beam size evolution in the acceleration process. (b) Intrinsic resonance  $4\nu_r = 9$  distorts the phase space.

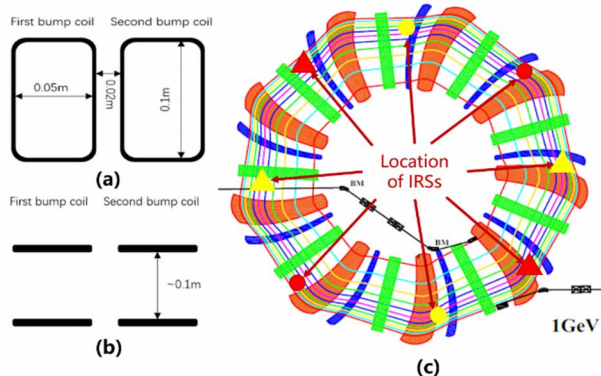


Figure 8: (a) Top view of an IRS. (b) Side view of an IRS. (c) Location of IRS in the ring cyclotron.

IRS method is adopted to correct the large coherent motion before reaching the intrinsic resonance  $4\nu_r = 9$ . Figure 8 shows the structure and location of IRSs in the ring cyclotron. Coil current of IRSs marked by triangle and circle are oppositely directed. Coil current of IRSs marked by same colour have the same current value. Detailed structure and arrangement principle are explained in reference[0]. With the IRSs, radial oscillation is reduced to  $\pm 10$  mm and the beam size will not be blown up, as shown in Figure 9.

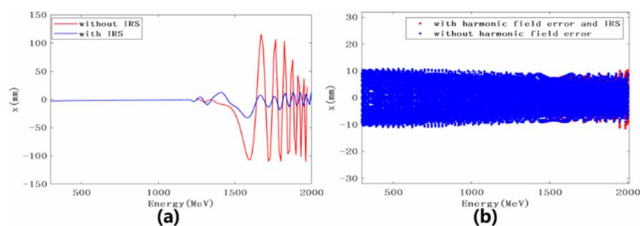


Figure 9: (a) Radial oscillation with and without IRS. (b) Beam size evolution with and without IRS.

With contribution of acceleration and precession, turn separation is about 35mm. The space charge effect also has powerful influence on the beam dynamics. Figure 10 shows beam intensity on radial probe for different phase width. The emittance is  $1 \pi \text{ mm mrad}$  and  $25 \times 10^4$  macro particles and mesh of  $32^3$  grid points is used. For  $2^\circ$  rms phase width, space charge dominates the beam dynamics. A round, compact beam is developed due to vortex motion, but the beam will break up in the integer resonance crossing process. For  $8^\circ$  rms phase width, beam dynamics is dominated by emittance and the turn separation is much

more clear. The case with  $5^\circ$  rms phase width is at the transition between the emittance-dominated and space-charge-dominated. For the optimized case,  $7.5^\circ$  rms phase width and  $2.5 \text{ mm mrad}$  is used and then a clear region is obtained at the extraction point. If 0.5mm is chosen as the septum thickness, the beam power at the deflector will be less than 100W.

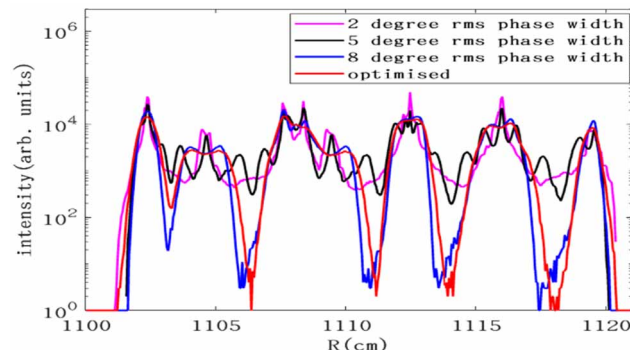


Figure 10: Beam intensity on radial probe for different phase width.

## SUMMARY

This paper presents the preliminary design of UHPC-10MW. Simulation results of beam power deposition on deflector show that the margin is sufficient. In particular, the 1GeV/amu ring cyclotron accelerate the beam to beyond the integer resonance and IRS is used to control the oscillation. Simulations show that IRS can not only reduce the beam size growth rate to less than 5%, but also enlarge the turn separation to 35mm. That is to say, IRS not only acts as integer resonance suppressor, but also plays the role of separation optimizer between the last and second last turn. From our limited knowledge, we do not see any fundamental limits that prevent the construction of a 10MW-class cyclotron.

OPAL 0 and Cyclops 0 are used in the beam dynamics simulation.

## REFERENCE

- [1] Grillenberger, S-H. Kim, M. Yoshii, *et al.*, "The energy efficiency of high intensity proton driver concepts", in *Proc. the 8th International Particle Accelerator Conference*, Copenhagen, Denmark, 2017, pp. 4842-4847.
- [2] W. Weng, "Developments of High Power Proton Accelerators", BNL, 2018.
- [3] L. Calabretta, *et al.* "Cyclotrons and FFAG Accelerators as Drivers for ADS." *Reviews of Accelerator Science & Technology*, vol. 08, pp. 77-97, 2015. J.K.
- [4] John M. Carpenter, "Accelerator-based Neutron Sources: Past, Present, and Future", October 2018.
- [5] Sarkisyan, L.A. "Possibility of accelerating protons to energies above E0 in an isochronous cyclotron". *Soviet Atomic Energy*, vol. 30, pp. 584-586, 1971.
- [6] Alonso, J., *et al.* "The IsoDAR High Intensity H2+ Transport and Injection Tests", *Journal of Instrumentation*, vol. 10, 2015.

- [7] Bian, T., *et al.* “Possible solution for the integer resonance crossing problem of GeV-class isochronous Fixed-Field Alternating Gradient accelerators”, *Nuclear Instruments and Methods in Physics Research Section A: Accelerators, Spectrometers, Detectors and Associated Equipment*, vol. 1031, p. 166594, 2022.
- [8] Bian, T., *et al.* “Inhibition and Utilization of Integer Resonance in GeV/ma Class High Power Circular Accelerator(in Chinese)”, *Atomic Energy Science and Technology*, vol. 009, p. 056, 2022.
- [9] R. Baartman, “Fast crossing of betatron resonances”, in *Proc. of FFAG 2004*, Vancouver, Canada, 2004.
- [10] Gordon, M. M., “Computation of closed orbits and basic focusing properties for sector-focused cyclotrons and the design of 'cyclops'”, *part accel*, 1984.
- [11] Object Oriented Parallel Accelerator Library (OPAL), <https://gitlab.psi.ch/OPAL/src/-/wikis/home>

# TERAHERTZ-DRIVEN MeV ELECTRON BUNCH COMPRESSION AND STREAKING \*

Y. Xu, Y. Song, J. Wang, C. Tsai, K. Fan<sup>†</sup>, Z. Liu<sup>‡</sup>, School of Electric and Electronic Engineering, Huazhong University of Science and Technology, Wuhan, China

## Abstract

Electron bunches with ultra-short bunch length and ultra-high timing stability are crucial for various applications. To achieve these desired characteristics, there is a growing interest in employing Terahertz-driven techniques to manipulate and diagnose electron bunches. This paper presents a method capable of compressing and measuring electron bunch lengths. Theoretical and simulation results demonstrate that the bunch length of 54 fs is reduced to 4 fs by utilizing THz-driven resonant cavity compression, achieving a compression ratio of 13. Furthermore, we also verify the bunch compression using a terahertz-driven streak camera.

## INTRODUCTION

Ultra-short and precisely timed electron bunches are essential for applications such as ultrafast electron diffraction (UED) and free-electron lasers (FELs) [1-3]. In UED, the temporal resolution relies on the quality of the electron bunch used as a probe. Both the bunch length and the timing jitter relative to the laser can impact the overall system resolution. RF deflecting cavities are commonly employed to compress the bunch length while maintaining low emittance [4-5]. However, the phase jitter of the RF resonant field introduces energy instability to the electron bunch, resulting in a time-of-arrival (TOA) jitter typically ranging from tens to hundreds of femtoseconds. THz-driven bunch manipulation enables the generation of electron bunches with femtosecond-scale lengths and high-timing stability.

This all-optical method ensures inherent synchronization between the THz field and the electron bunch, enabling precise manipulation without inducing time jitter [6]. Various demonstrations of THz-driven techniques have been reported. For example, butterfly-shaped resonators compress and diagnose keV-level electron bunches [7], and parallel-plate waveguide structures compress MeV-level electron bunches [8]. The segmented terahertz electron accelerator and manipulator (STEAM) structure offers a multifunctional design for compression and measurement [9]. These studies highlight the potential of strong-field THz techniques for manipulating and diagnosing electron bunches.

This paper presents a method illustrated in Fig. 1 to compress and diagnose electron bunches using THz-driven resonators. A buncher generates a longitudinally polarized field for compressing the electron bunch length, while a slit downstream serves as a THz-driven streak camera to measure the bunch length. Despite the space charge effect

causing continuous expansion in both longitudinal and transverse directions, passing the electron bunch through the THz electric field at the zero-crossing phase achieves opposite momenta for the head and tail electrons, resulting in the minimum bunch length at the sample position. At this position, a transversely polarized THz field generated by the slit converts the electron bunch's longitudinal temporal information into a transverse bunch distribution. Analyzing the measurements from the detector allows us to infer the bunch length and time of arrival. The effectiveness has been verified through theoretical analysis and numerical simulations, demonstrating its capability to compress and evaluate MeV-level electron bunches.

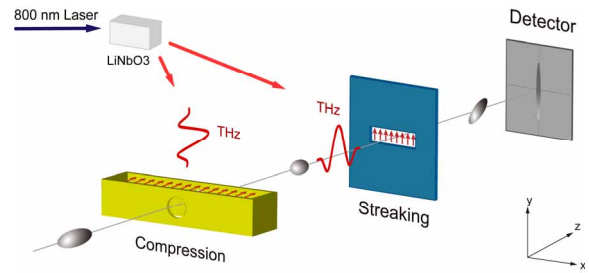


Figure 1: Schematic of the compression and streaking system.

## THz-DRIVEN ELECTRON BUNCH COMPRESSION

Figure 2 illustrates the THz buncher structure along with its equivalent LC circuit model, which can be simplified as a resonator. The driving THz driving pulse, polarized along the z-axis, enters the buncher from the top. As a result of resonance, an enhanced THz field is generated in the gap, with the amplitude and frequency dependent on both the driving THz pulse and the buncher geometric parameters. The THz electric field mainly concentrates near the channel through which the electron beam passes and has a uniform amplitude, as shown in Fig. 2 (b).

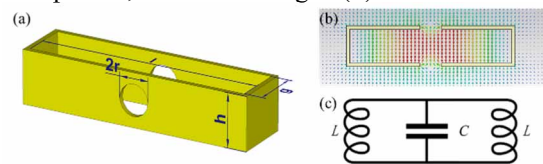


Figure 2: (a) The structure of the THz buncher. (b) The electric field distribution in buncher. (c) The equivalent LC circuit of the buncher.

Due to the structural symmetry, the gap exhibits a strong electric field while having an almost negligible magnetic field. These characteristics make the buncher well-suited for beam compression. When an electron beam passes

\* Work supported by NSFC 12235005 and the State Grid Corporation of China Technology Project 5400-202199556A-0-5-ZN

<sup>†</sup>kjfan@hust.edu.cn, <sup>‡</sup>zzliu@hust.edu.cn

through the buncher, the longitudinal THz electric field will compress the electron beam, reducing its size and duration.

Table 1: Dimensions of the Buncher

Dimensions	Value ( $\mu\text{m}$ )
$l$	454
$h$	100
$g$	100
$r$	30

The structure of the buncher can be described by four parameters, as illustrated in Fig. 2 (a) and Table 1. The resonant frequency of the THz field in the gap can be approximated using an LC resonant circuit, as depicted in Fig. 2 (c). In this circuit model, the planes on either side of the circular aperture are regarded as a parallel-plate capacitor, while the conductor carrying the electron flow is treated as an inductor. Hence, the resonant frequency of the buncher can be calculated using the following expression:

$$f_0 = \frac{c}{s} = \frac{c}{2(l+g)-4r} \quad (1)$$

Here,  $c$  is the speed of light, which represents the propagation velocity of the current in the conductor. Similarly, the distance the current travels in one loop  $s$  can be approximated as the circumference of the inner diameter of the buncher. The parameters ( $l$ ) and ( $g$ ) are the key factors in optimizing the buncher resonant frequency. These parameters primarily control the resonant behavior of the system. Meanwhile, the parameter ( $h$ ) has minimal influence on the charge density distribution around the circular apertures and can be disregarded.

The compression efficiency of the buncher is primarily influenced by two factors: the THz electric field amplitude and the transit time of the electron bunch. Increasing the parameter  $g$  extends the interaction time between the electric field and the electron bunch, thereby improving the compression efficiency. However, it's important to note that increasing  $g$  also leads to drawbacks, including higher radiation power of the THz field, rapid energy decay of the electric field, and a decrease in the quality factor of the buncher. Therefore, when designing a buncher, it is crucial to consider the specific application scenario and strike a balance between compression efficiency and the aforementioned trade-offs.

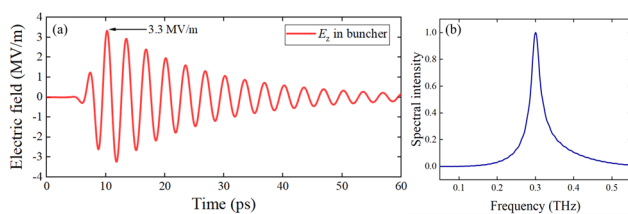


Figure 3: (a) The electric fields at the center of the buncher. (b) The corresponding spectrum.

To generate a larger amplitude THz field, we use a quasi-Gaussian single-pulse THz wave with a central frequency of 0.3 THz, which closely matches the resonance

frequency of the buncher, allowing for effective excitation. CST simulations indicate that the buncher can enhance the THz electric field by a factor of 3.3. The waveform and spectrum are shown in Fig. 3. When the longitudinal center of the beam aligns with the zero-crossing phase of the THz field, two distinct effects occur. The electrons at the head of the beam experience deceleration, while those at the tail experience acceleration. As a result, the overall bunch length decrease after a drift section.

This beam compression dynamics process can be described using a transfer matrix. The coordinates of an individual electron in the longitudinal phase space are defined as  $(\zeta_0, \delta_0)$ , where  $\zeta$  represents the relative position of the electron with respect to the beam center, and  $\delta$  represents the relative energy difference to the reference particle. The coordinates  $(\zeta_1, \delta_1)$  of the electron in the longitudinal phase space after passing through the THz buncher can be described by the following equation:

$$\begin{bmatrix} \zeta_1 \\ \delta_1 \end{bmatrix} = \begin{bmatrix} 1 & L/\beta^2\gamma^2 \\ 0 & 1 \end{bmatrix} \begin{bmatrix} 1 & 0 \\ -k\Delta V/E_{\text{ref}} & 1 \end{bmatrix} \begin{bmatrix} \zeta_0 \\ \delta_0 \end{bmatrix} \quad (2)$$

Here,  $L/\beta^2\gamma^2$  is the momentum compression factor of the drift section,  $k = 2\pi f_0/\beta c$  is the wave number of the THz field,  $E_{\text{ref}}$  is the energy of the electron beam, and  $\Delta V$  is the effective voltage of the THz resonator.

Given a specific THz electric field amplitude, this equation allows us to determine the position where the bunch length is minimized after compression. It is important to highlight that the theoretical model does not account for the space charge effect. Additionally, the buncher is limited to compensate for the linear bunch chirp of the electron beam. Further studies are needed for beams dominated by space charge to address and compensate for the space-charge effect.

## THZ-DRIVEN STREAK CAMERA

The electron beam passes through the buncher, where it undergoes compression to achieve its shortest length at the sample location. A deflection cavity is placed at that location to measure the size of this compressed beam. The slit used for beam length measurement is depicted in Fig. 4 (a), and its geometric parameters are shown in Table 2.

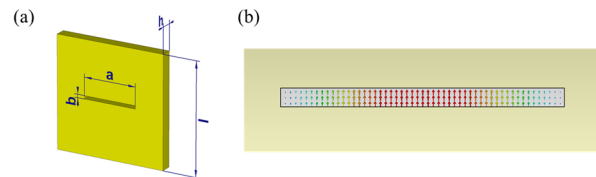


Figure 4: (a) The structure of the slit. (b) The electric field distribution in the slit.

The same slit is also excited by the aforementioned driving THz pulse, with the polarization direction along the  $y$ -axis. Fig. 4 (b) illustrates the electric field distribution generated within the slit gap. Horizontally, the strongest electric field is concentrated in the center, while it gradually weakens towards the sides. In the case of electron bunches with small transverse sizes, the electric field exhibits uniformity.

Table 2: Dimensions of the Slit

Dimensions	Value (μm)
$l$	2000
$b$	30
$a$	480
$h$	100

Figure 5 presents the waveform and spectrum of the THz electric field at the center of the rectangular slit. The field exhibits an enhancement factor of 7.0. In this slit resonator, the enhancement factor of the generated field is primarily influenced by the width of the slit. A narrower slit corresponds to a higher enhancement factor. Theoretical analysis indicates that the enhancement factor can be approximated as the ratio of the longer side to the shorter side of the slit.

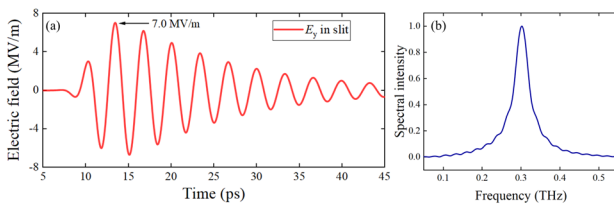


Figure 5: (a) The electric fields at the center of the slit. (b) The corresponding spectrum.

When the electron bunch passes through the THz electric field at the zero-crossing phase, it acquires a net transverse momentum of zero. Although the direction of the bunch motion remains unchanged, the leading and trailing electrons acquire transverse momenta in opposite directions. After a drift section, the longitudinal characteristics of the bunch are transformed into a transverse distribution on the detector. The bunch length can be deduced by utilizing the following formula, which relates it to the transverse size:

$$S = \frac{2e\bar{E}_y}{\sqrt{3}P} \sin\left(\frac{\omega}{2} T_p\right) D\Delta T \quad (3)$$

where  $\omega$  is the angular frequency of the deflecting electric field,  $\bar{E}_y$  is the effective deflecting field strength,  $e$  is the elementary charge,  $P$  is the momentum of the electron bunch,  $D$  is the distance from the second resonator to the detector screen, and  $T_p$  is the time it takes for the electron bunch to pass through the gap.

## PARTICLE-TRACKING SIMULATION RESULTS

Particle tracking simulations are conducted to showcase the evolution of the electron bunch, utilizing the parameters of the HUST-UED beamline [10-12], as shown in Table 3. To achieve longitudinal focusing of the electron beam within 0.45 m, as per the current design parameters of HUST-UED, a peak field of 1141 MV/m is required for the buncher. Considering the field enhancement factor, the driving THz pulse must have an energy of approximately 0.14 mJ. For the slit, the peak field is designed to be 500 MV/m, and the driving THz pulse should have an energy of about 6 μJ. Before the electron beam undergoes

streaking through the slit, it first passes through a vertical aperture with a size of 30 μm to minimize the impact of non-uniformity in the transverse field enhancement factor of the slit on the measurement results.

Table 3: Simulation Parameters

Parameters	Value
Initial bunch length	15 fs
Bunch kinetic energy	3 MeV
Bunch charge	5 fC
Peak THz buncher field	1141 MV/m
Peak THz slit field	500 MV/m

Figure 6 (a) illustrates the imprinting of the bunch after undergoing compression and streaking, which has an initial length of 15 fs. For comparison purposes, the uncompressed bunch imprinting is also shown in Fig. 6(b). The results clearly indicate that the beam is compressed from its original duration of 54 fs to an impressive 4 fs, resulting in a compression ratio of 13. By incorporating the buncher, the temporal resolution of UED can be effectively reduced to approximately 30 fs.

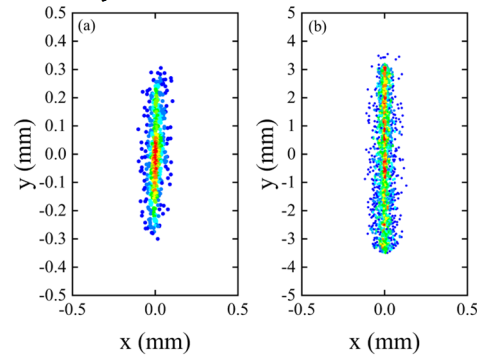


Figure 6: Comparison of bunch imprints for compressed (a) and uncompressed (b).

## CONCLUSION

In summary, the presented approach demonstrates an innovative path towards all-optical bunch length compression and measurement of electron bunches. This method ensures inherent synchronization and eliminates timing jitter, making it ideal for precise electron bunch manipulation and high-resolution diagnostics. The preliminary results demonstrate the successful compression of the electron bunch from 53 fs to 4 fs, which significantly improves the overall time resolution of UED to below 30 fs. The preliminary results highlight the potential of this proposed technique in advancing electron bunch manipulation and achieving ultra-high temporal resolution in applications involving electron-laser-related.

## ACKNOWLEDGEMENTS

The work is supported by the National Natural Science Foundation of China (NSFC 12235005), and the State Grid Corporation of China Technology Project (5400-202199556A-0-5-ZN).

## REFERENCES

- [1] R. J. Dwayne Miller, “Femtosecond Crystallography with Ultrabright Electrons and X-rays: Capturing Chemistry in Action”, *Science*, vol. 343, p. 1108-1116, 2014. doi:10.1126/science.1248488
- [2] G. Sciaini and R. J. Dwayne Miller, “Femtosecond electron diffraction: heralding the era of atomically resolved dynamics”, *Reports on Progress in Physics*, vol. 74, p. 096101, 2011. doi: 10.1088/0034-4885/74/9/096101
- [3] I. Grguraš, A. R. Maier, C. Behrens, et al., “Ultrafast X-ray pulse characterization at free-electron lasers”, *Nature Photonics*, vol. 6, p. 852-857, 2012. doi: 10.1038/nphoton.2012.276
- [4] J. Maxson, et al., “Direct Measurement of Sub-10 fs Relativistic Electron Beams with Ultralow Emittance”, *Phys. Rev. Lett.*, vol. 118, p. 154802, 2017. doi: 10.1103/PhysRevLett.118.154802
- [5] L. Zhao, et al., “Terahertz Streaking of Few-Femtosecond Relativistic Electron Beams”, *Physical Review X*, vol. 8, p. 021061, 2018. doi: 10.1103/PhysRevX.8.021061
- [6] J. Fabiańska, et al., “Split ring resonator based THz-driven electron streak camera featuring femtosecond resolution”, *Scientific Reports*, vol. 4, p. 5645, 2014. doi: 10.1038/srep05645
- [7] C. Kealhofer, et al., “All-optical control and metrology of electron pulses”, *Science*, vol. 352 p. 429-433, 2016. doi: 10.1126/science.aae0003
- [8] E. C. Snively, et al., “Femtosecond Compression Dynamics and Timing Jitter Suppression in a THz-driven Electron Bunch Compressor”, *Phys. Rev. Lett.*, vol. 124, P. 054801, 2020. doi: 10.1103/PhysRevLett.124.054801
- [9] D. Zhang, et al., “Segmented terahertz electron accelerator and manipulator (STEAM)”, *Nat. Photonics*, vol. 12, p. 336-342, 2018. doi: 10.1038/s41566-018-0138-z
- [10] Y. Xu, et al., “Towards precise diagnosis time profile of ultrafast electron bunch trains using orthogonal terahertz streak camera”, *Opt. Express*, vol. 31, p. 19777-19793, 2023. doi: 10.1364/OE.488132
- [11] C.-Y. Tsai et al., “Low-energy high-brightness electron beam dynamics based on slice beam matrix method”, *Nucl. Instrum. Methods. Phys. Res. A*, vol 937, pp. 1-20, Sep. 2019. doi:10.1016/j.nima.2019.05.035
- [12] C.-Y. Tsai and K. Fan. “A Semi-Analytical Approach to Six-Dimensional Path-Dependent Transport Matrices With Application to High-Brightness Charged-Particle Beam Transport”, in *Proc. 2019 North American Particle Acc. Conf. (NAPAC2019)*, Lansing, MI, US, Sep. 2019, pp. 792-795. doi:10.18429/JACoW-NAPAC2019-WEPLS12

# STUDY ON A POLARIZATION CONTROLLABLE UNDULATOR FOR HIGH-GAIN FREE ELECTRON LASERS \*

Ruixuan Huang<sup>†</sup>, Qika Jia<sup>‡</sup>,

University of Science and Technology of China, Hefei, 230026 China

Lijun Chen,

China Academy of Engineering Physics, Mianyang, 621900 China

## Abstract

SASE FEL can generate intense and coherent linearly-polarized X-ray when high energy electron beams travelling through a long planar undulator. It is also of great importance and interest to control the polarization of FEL. One possible solution is utilizing a customized undulator to adjust the magnetic field direction. By tuning the displacement of the magnetic block arrangement, variation of polarization could be achieved. In this paper we study on a polarization controllable undulator to realize the variable polarized magnetic field. Different shapes and design considerations of the magnetic block configuration will be introduced. The value of peak field and the region of good field will be analysed and discussed.

## INTRODUCTION

The X-ray free electron laser (FEL) have the ability to explore the ultra-small and ultra-fast regime. Self-amplified spontaneous emission (SASE) is intense and coherent radiation via an extremely high gain process. SASE FEL usually produces linearly polarized radiation based on planar undulators. The light source polarization is one of the key characteristics of the radiation. Furthermore, arbitrarily polarization control has great application requirement, such as in developing powerful probing spectroscopies [1] and performing circular dichroism experiments [2]. A helical undulator could be used to achieve circular polarization, while challenging to change the polarization between two diametrically opposed helices. Another method to obtain control of polarization is to use a dedicated planar undulator. By tuning the relative displacement between upper and lower magnet array, the phase of the electromagnetic field is shifted and the field strength is adjusted, turning out the polarization change. In this manuscript, we will give the study of different shapes and design considerations of the magnetic block configuration.

## MAGNETIC STRUCTURE

We have studied a novel variable elliptical polarization undulator with different structure arrangement considered. In the original design, the pure permanent magnetic blocks are periodically arranged with four upper and lower blocks. In each period, two opposite horizontal magnetization of

magnets and two opposite longitudinal magnetization of magnets are placed at intervals. The displacement of upper and lower magnet arrays can be mechanically shifted. As a result, a horizontal polarization, a vertical polarization and an elliptical (or circular) polarization can be realized separately. Several magnetic block shapes are considered as shown in Fig. 1.

The magnetic design is performed via the Radia package [3]. In one design specification of the original structure, the simulation results for different polarization modes of the transverse magnetic field distribution on the longitudinal axis are shown in Fig. 2. Undulator parameters of the original block and displacement shift requirement on polarization change are listed in Table 1. The peak field of the periodic distribution can reach above 0.4 T for linear polarizations, and above 0.3 T for circular polarization. Although there is field deformation at ends of the undulator, it can be improved by optimization of the edge blocks. However, the uniform region very small for this original structure. Some techniques have been suggested to improve the transverse field homogeneity [4,5]. We study on three design considerations.

Table 1: Main Parameters of the Original Block Design

Parameter	Specification
Period	100 mm
Number of periods	10
Gap(fixed)	20 mm
Magnet block size(width*height)	60*60 mm
Vertical peak field	0.42 T
Horizontal peak field	0.44 T
Peak field at circular polarization	0.33 T
Shift of vertical polarization	0 mm
Shift of horizontal polarization	50 mm
Shift of circular polarization	35.6 mm

## Side-block Arrangement

In the side-block arrangement, magnet blocks of vertical magnetization are added at both width end of the horizontal magnetization blocks to compensate the region of good field. By proper optimize the geometrical parameters, the uniform field region is increased from less than 0.1 mm to 1.0 mm in horizontal and 1.8 mm in vertical, under field homogeneity  $\Delta B/B \leq 0.5\%$ .

We fix the size of the main magnets and the height of the side blocks, then compare the peak field and the uniform

\* Work supported by the National Natural Science Foundation of China (Grant Number 12175224, 11805200).

<sup>†</sup> rxhuang@ustc.edu.cn

<sup>‡</sup> jiaqk@ustc.edu.cn

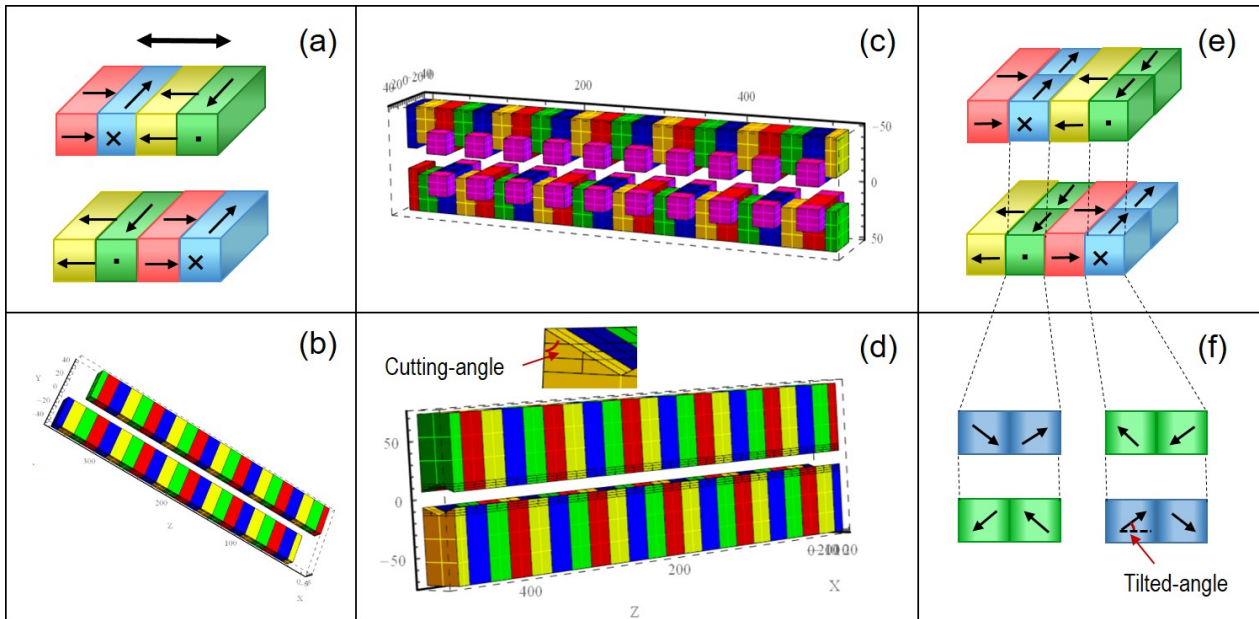


Figure 1: Several magnetic block shapes: the original block with diagrammatic drawing of magnetization directions in (a) and structure arrangement in (b); the side block arrangement in (c); the wedge block arrangement in (d); the tilted magnetization arrangement with diagrammatic drawing of solid figure (e) and with right side views of horizontal magnetized blocks (f)

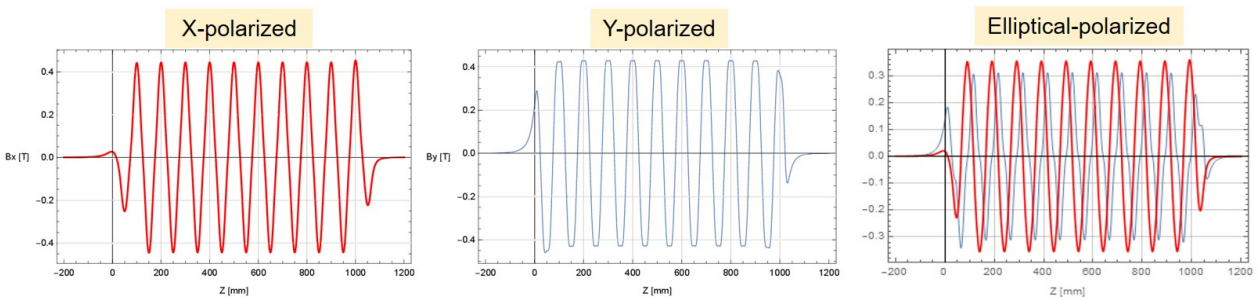


Figure 2: Simulated transverse magnetic field distribution in one original design specification. Left: horizontal polarization mode; Middle: vertical polarization mode; Right: elliptical polarization mode.

field region by varying the size of the side magnets, as shown in Fig. 3. In the vertical polarization mode, the width of side magnets minimally affect both the peak field and the uniform region. In the horizontal polarization mode, when the width decreases the  $B_x$  field is reduced and good region increased. It is notable that the uniform field region in horizontal can be larger than 8 mm.

### Wedge-block Arrangement

In the wedge-block arrangement, the magnet block has a wedge towards the beam axis. In this design, the wedge angle as well as the size of the folded surface's horizontal area should be optimized. Firstly, to balance the uniform field region on both planes, the horizontal length of the folded surface area should be zero or small enough.

We define the cutting-angle as labelled in Fig. 1 (d). If the wedge angle is varied, the magnetic field and its good region will also be changed. As shown in Fig. 4, when the

cutting-angle increases the vertical field is increased and good region increased. While the good region and peak field of the horizontal mode is not optimized.

### Tilted-magnetization Arrangement

In the tilted-magnetization arrangement, the horizontal magnetized block is divided into two with a certain magnetized tilt angle as shown in Fig. 1 (e) and (f). The tilted-angle has a clear impact on the peak field and the homogeneity field region. When the tilted-angle is  $\arctan(0.2)$ , the field distribution for horizontal and vertical polarization modes are shown in Fig. 5. The horizontal peak field is reduced to about 0.08 T, while the vertical peak field can be maintained above 0.34 T. The uniform field region under field homogeneity  $\Delta B/B \leq 0.5\%$  is increased to 1.8 mm in vertical, while reduced to 0.08 mm in horizontal.

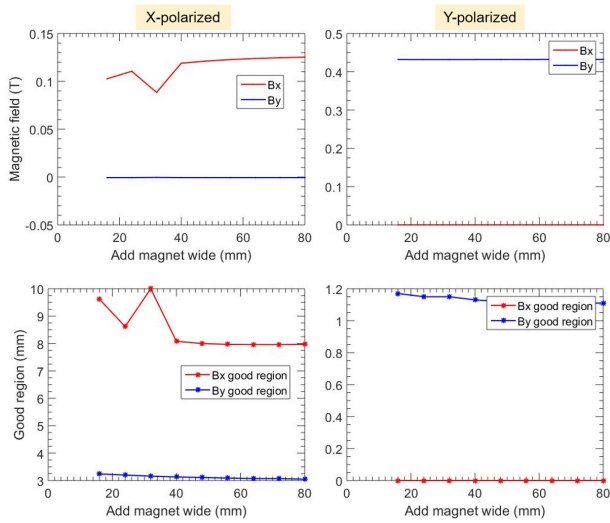


Figure 3: The peak field (upper) and the uniform field region (lower) for side-block arrangement for different sizes of the side magnets. Left: horizontal polarization mode; Right: vertical polarization mode.

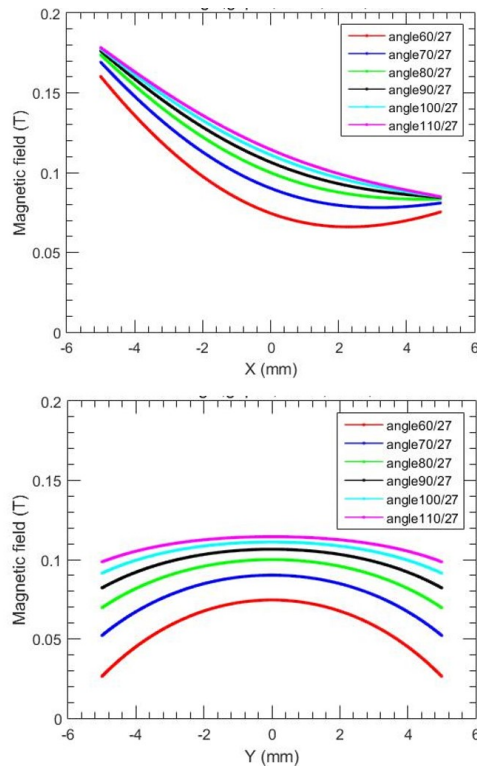


Figure 4: The transverse field distribution of wedge-block arrangement for horizontal polarization mode (upper) and vertical polarization mode (lower).

## CONCLUSION

Various block layouts have been investigated to realize adjusting of the polarization and broadening the homogeneity field region. By tuning the relative displacement between upper and lower magnet array, the phase of the magnetic field

can be changed bringing out polarization control. Among

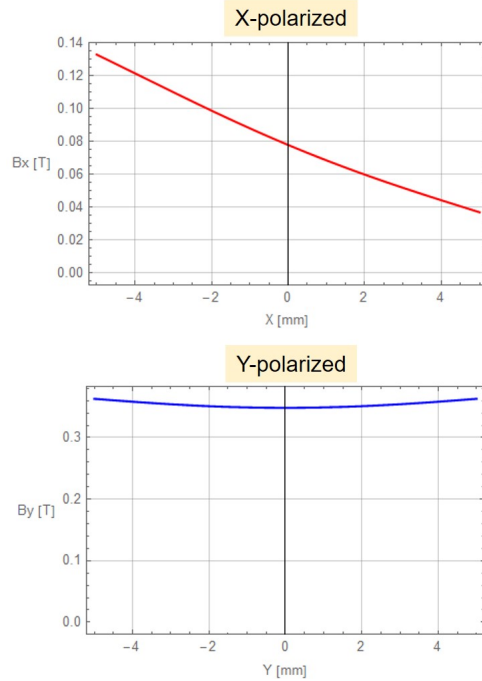


Figure 5: The transverse field distribution of tilted-magnetization arrangement for horizontal polarization mode (upper) and vertical polarization mode (lower).

those block shapes, the side-block arrangement can achieve considerable uniform field region in both polarization modes especially in horizontal plane. While the peak field of horizontal polarization is fairly lowered. The good region under field homogeneity  $\Delta B/B \leq 0.5\%$  can be larger than 8.0 mm in horizontal and 1.1 mm in vertical at the expense of  $B_x$  descent. More magnet structures should be investigated to further improve the undulator field properties.

## REFERENCES

- [1] L. E. MacKenzie *et al.*, “Rapid time-resolved Circular Polarization Luminescence (CPL) emission spectroscopy”, *Nature Communications*, vol. 11, no. 1676, 2020. doi:10.1038/s41467-020-15469-5
- [2] R. Hussain *et al.*, “Circular Dichroism and Synchrotron Radiation Circular Dichroism Applications to Biomaterials”, *Radiation in Bioanalysis*, vol. 8, pp. 147–172, 2019. doi:10.1007/978-3-030-28247-9\_5
- [3] Radia software, [http://www.esrf.fr/machine/groups/insertion\\_devices/Codes/Radia/Radia.html](http://www.esrf.fr/machine/groups/insertion_devices/Codes/Radia/Radia.html).
- [4] C.S. Hwang *et al.*, “Magnet block arrangements for the APPLE-II elliptically polarized undulator”, in *Proc. of PAC07*, pp. 1079–1081, 2007. doi:10.1109/PAC.2007.4440988
- [5] T. Wang and Q. Jia, “Study of Magnetic Block Arrangement of APPLE-II undulator”, in *Proc. of EPAC08*, paper WEPC152, 2362–2364. <https://accelconf.web.cern.ch/e08/papers/wepc152.pdf>

# LOWEST LONGITUDINAL AND TRANSVERSE RESISTIVE-WALL WAKE AND IMPEDANCE FOR NONULTRA-RELATIVISTIC BEAMS\*

J. Tang<sup>†</sup>

Tsinghua University in Beijing (TUB) Accelerator Laboratory Department of Engineering Physics

## Abstract

With the development of the steady state micro bunching (SSMB) storage ring, its parameters reveal that the ultra-relativistic assumption which is widely used is not valid for the electron beam bunch train, which has length in the 100nm range, spacing of 1μm and energy in hundreds MeV range. The strength of the interaction between such bunches and the potential instability may need careful evaluation. At the same time, the effect of the space charge inside a single bunch due to space charge effect also needs to be considered. In this article, we reorganized the lowest-order longitudinal wakefield under non-ultra relativistic conditions, and modified the inconsistent part in the theoretical derivation in some essays of the lowest-order transverse wakefield. We present the modified theoretical results and analysis. The action area are then divided into three parts. It lays foundation in future research.

## INTRODUCTION

Based on published literature, we have reorganized the lowest-order longitudinal wakefield under nonultra-relativistic conditions which is the monopole longitudinal wakefield, and we have modified the inconsistent part in the theoretical derivation of the lowest-order transverse wakefield which is the dipole transverse wakefield in existing literature. We present the modified theoretical results and analysis. The calculation results are evaluated, and the action area of the non-ultra relativistic wakefield is divided into a short-range dominated by the source charge space force, a middle section dominated by the mirror space charge force, and a long-range resistive wall that can be estimated using classical ultra-relativistic assumption. This lays the foundation and clarifies the ideas for subsequent beam dynamics analysis.

## LONGITUDINAL WAKEFIELD

### Previous Result

The classical Longitudinal Wakefield for multipole has an analytical expression [1]

$$W_m(z) = -\frac{c}{\pi b^{2m+1} (1 + \delta_{m0})} \sqrt{\frac{Z_0}{\pi \sigma_c}} \frac{L}{|z|^{\frac{1}{2}}} \quad (1)$$

$$W'_m(z) = -\frac{c}{2\pi b^{2m+1} (1 + \delta_{m0})} \sqrt{\frac{Z_0}{\pi \sigma_c}} \frac{L}{|z|^{\frac{3}{2}}} \quad (2)$$

where  $b$  is the radius of the pipe,  $\sigma_c$  is the conductivity of the surrounding medal. This result is obtained by ultra-relativistic limit  $\gamma \rightarrow +\infty$ , e.g. the speed of the electron is the speed of light  $c$ . Meanwhile, the effective region of the longitudinal coordinate is

$$\chi^{\frac{1}{3}} b \ll |z| \ll \chi^{-\frac{1}{3}} \frac{c}{b}, \quad z < 0 \quad (3)$$

where  $\chi = \frac{1}{\mu \sigma_c b c}$ . For Aluminum pipe whose radius is in several centimeters range, the effective region will be  $1.95 \times 10^{-5} m \ll z \ll 1.54 \times 10^{13} m$ .

In order to calculate short range wakefield, in SLAC-PUV-95-7074 [2] there is a formula for longitudinal Electric Field in the time-space domain

$$E_z^m(z) = -16\gamma \left( \frac{1}{3} e^{-\gamma \frac{z}{s_0}} \cos \frac{\sqrt{3}\gamma^{\frac{2}{3}} z}{s_0} - \frac{\sqrt{2}\gamma}{\pi} \int_0^\infty \frac{x^2 e^{-x^2 \frac{z}{s_0}}}{x^6 + 8\gamma^2} \right) \quad (4)$$

where

$$s_0 = b^{\frac{1}{2}} \left( \frac{c}{2\pi\sigma} \right)^{\frac{1}{3}} \quad (5)$$

this equation is valid for all  $z \leq 0$ .

### SSMB Case Monopole Wake Benchmark

For the SSMB Parameters showed at Table 1 reveal that the space charge effect estimate by  $\frac{2b}{\gamma}$  would be about 30.6 μm. Such an effective length would be much larger than the spacing between bunch to bunch. So, it would be better that we consider if it is appropriate to view space charge electromagnetic field as a round plate.

Table 1: SSMB Bunch Train Parameters

Parameter	Value	Purpose
Length	10 nm	Longitudinal Coherent
Transverse size	10–100 μm	
Spacing	1 μm	High Average Power
Energy	250 MeV	$\gamma \approx 490.2$

There is such a monopole result derived for nonultra-relativistic beam [3, 4] by solving the Maxwell equation by Fourier Transformation, the longitudinal impedance is showed as Eq. (7). And when we get the expression of the impedance, we can obtain the Longitudinal Wake Field through Inverse Fourier Transformation.

$$W'_0(z, r) = \frac{1}{2\pi v} \int_{-\infty}^\infty Z_{\parallel}(\omega, r) e^{\frac{i\omega z}{v}} d\omega \quad (6)$$

\* Work supported by Tsinghua University Accelerator Laboratory

<sup>†</sup> tjz21@mails.tsinghua.edu.cn

It should be noticed that there is a coefficient named  $\nu$  on the denominator before the integration. This is because we should take the correspond Fourier Transformation pair when we do this operation.

Usually we take the numerical integration to get the Inverse Fourier Transformation for the longitudinal Impedance. As a benchmark, this relativistic formula is more general than the ultra case. And when we set the energy of the elec-

$$Z_{\parallel}(\omega, r) = \frac{iZ_0ck_r^2}{2\pi\omega} \left[ K_0(k_r r) + I_0(k_r r) \frac{\omega^2 \lambda K_1(bk_r) K_0(b\lambda) + k_r c^2 (\lambda^2 - k^2) K_0(bk_r) K_1(\lambda b)}{\omega^2 \lambda I_1(bk_r) K_0(b\lambda) - k_r c^2 (\lambda^2 - k^2) I_0(bk_r) K_1(\lambda b)} \right] \quad (7)$$

It should be noticed that in the mean time, at the long range, the wake field we calculate has a good agreement with the classical equation given by A.Chao [1], which is

$$W'_0(z) = -\frac{c}{4\pi b} \sqrt{\frac{Z_0}{\pi \sigma_c}} \frac{L}{|z|^{\frac{3}{2}}} \quad (8)$$

And an example is showed at Table 2 and Fig. 2

Table 2: Consistency Between Classical Equation and General Equation

$z/m$	$\chi$	formula	numerical
-0.01	$5.7 \times 10^{-5}$	$-5.47 \times 10^9$	$-5.35 \times 10^9$

## TRANSVERSE WAKEFIELD

### Misleading Point in Pervious Result

In essays [3, 4] corresponding this question, they did not mention the mathematical expression for such a *dipole current*, the model they are considering about is pretty much vague. If we take the model they consider, which is

$$\begin{aligned} j_{\phi} &= 0, \\ j_r &= 0, \\ \int j_s dr d\phi &= \nu \lambda_b \end{aligned} \quad (9)$$

when we follow the derivation given by pervious result, we will have to determine a coefficient given by the strength of the dipole charge, and the equivalence mathematical problem is that we solve the green function given by

$$\frac{1}{r} \frac{\partial}{\partial r} \left( r \frac{\partial \tilde{A}_s}{\partial r} \right) - \left( \frac{1^2}{r^2} + k_r^2 \right) \tilde{A}_s = -\mu_0 \tilde{j}_s \quad (10)$$

The general solution of the problem is  $CI_1(k_r r) + DK_1(k_r r)$ . We can then expand the strange part of the general solution

MOPB004

tron to infinity, it should approach to the ultra-relativistic limit naturally. Fig. 1 show that when we take the limit we said, the wake field have the feature that when  $z > 0$ , wake field is zero, when  $z < 0$  it is not zero. This is the result of causality, which means that the speed of the electromagnetic field's propagation is not faster than the speed of the electron which is  $c$  when energy is infinity.

as

$$\begin{aligned} K_1(x) &= \frac{1}{x} + \frac{1}{4}x(2\ln x + 2\gamma - 1 - 2\ln 2) + \\ &\frac{1}{64}x^3(4\ln x + 4\gamma - 5 - 4\ln 2) + O(x^4) \quad (11) \\ K_1(k_r r) &\approx \frac{1}{k_r r} \end{aligned}$$

this model will lead to a equation showed below

$$\begin{aligned} \Phi(0, 0) &= \\ \lim_{\varepsilon \rightarrow 0} 2\pi \left( \Phi(x^*, y^*) D \frac{-1}{k_r \varepsilon} - D \frac{1}{k_r} \frac{\partial \Phi}{\partial r}(x^*, y^*) \right) \end{aligned} \quad (12)$$

which can not determine the coefficient D in the general solution. So, the model given by pervious is not self-consistent.

### Dipole Ring Model

We can give a *dipole ring model* and solve the electromagnetic field surround it. We explicitly give the source term of the dipole ring, which is Eq. (13)

$$\begin{aligned} \rho_m &= \frac{q}{\pi a} \delta(s - vt) \delta(r - a) \cos m\theta \\ j_m &= c \rho_m \hat{s} \end{aligned} \quad (13)$$

By solving the Maxwell equation under Lorentz Gauge, we give the general solution of vector potential  $A_r, A_{\phi}, A_s$  and potential  $\phi$ . In different area, we have

$$\begin{aligned} r < a \\ A_r &= \frac{1}{2} (p_+^c I_2(k_r r) + p_-^c I_0(k_r r)) \cos \varphi e^{ikz} \\ A_{\phi} &= \frac{1}{2} (p_+^c I_2(k_r r) - p_-^c I_0(k_r r)) \sin \varphi e^{ikz} \\ A_s &= p_s^c I_1(k_r r) \cos \varphi e^{ikz} \\ \phi &= p_0^c I_1(k_r r) \cos \varphi e^{ikz} \end{aligned} \quad (14)$$

where Lorentz Gauge requires that

$$p_+^c = -p_-^c, \quad p_0^c = \frac{c^2 k}{\omega} p_s^c \quad (15)$$

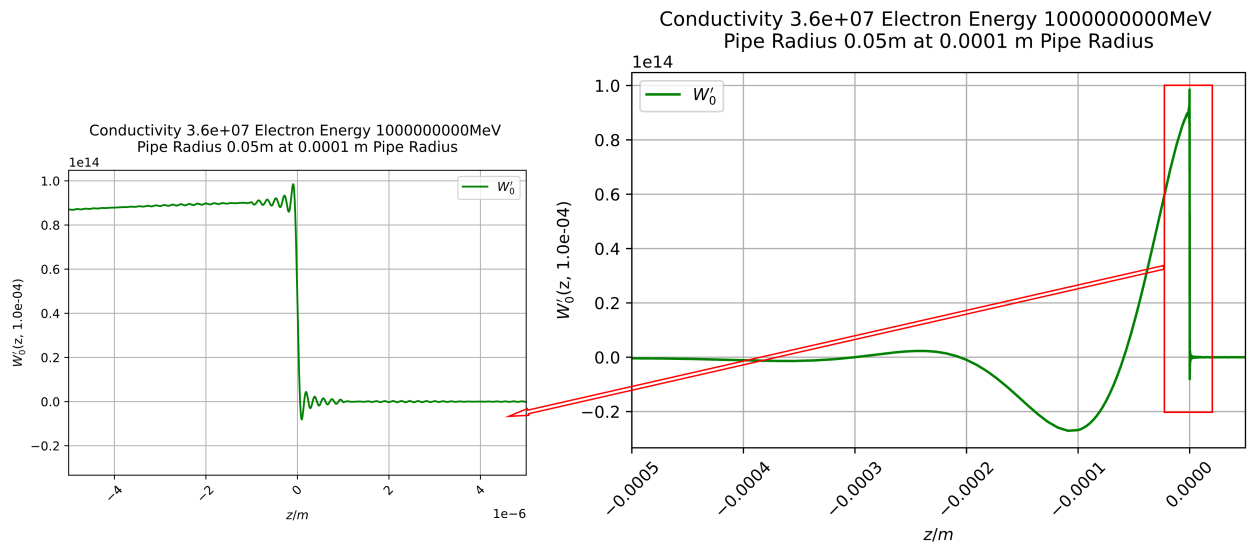


Figure 1: Wake field for ultra-relativistic electron near  $r = 0$  as a benchmark.

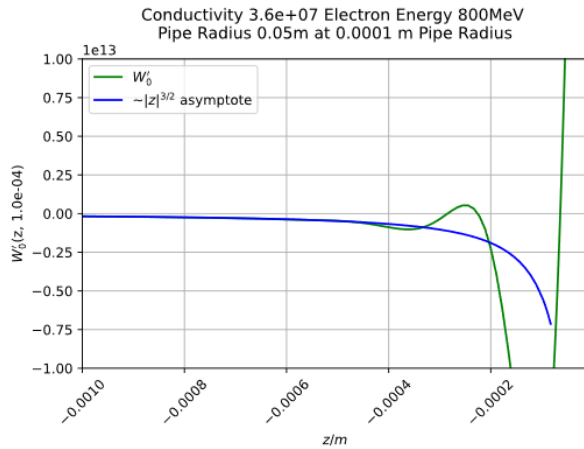


Figure 2: Long range asymptote.

then

$$a < r < b$$

$$\begin{aligned} A_r &= \frac{1}{2} (p_+ I_2(k_r r) + q_+ K_2(k_r r) + p_- I_0(k_r r) \\ &\quad + q_- K_0(k_r r)) \cos \varphi e^{ikz} \\ A_\varphi &= \frac{1}{2} (p_+ I_2(k_r r) + q_+ K_2(k_r r) - p_- I_0(k_r r) \\ &\quad - q_- K_0(k_r r)) \sin \varphi e^{ikz} \\ A_s &= (p_s I_1(k_r r) + q_s K_1(k_r r)) \cos \varphi e^{ikz} \\ \phi &= (p_0 I_1(k_r r) + q_0 K_1(k_r r)) \cos \varphi e^{ikz} \end{aligned} \quad (16)$$

where Lorentz Gauge requires that

$$p_- = -p_+, \quad p_0 = \frac{c^2 k}{\omega} p_s, \quad q_- = -q_+, \quad q_0 = \frac{c^2 k}{\omega} q_s \quad (17)$$

The area  $r > b$  are not listed. At last we can determine totally eight parameters through the continuous of electromagnetic field, which can be calculated by Mathematica. However, it is too long to show in this paper.

## CONCLUSION

We finally get a more self-consistent dipole wake and benchmark the monopole wake. After this work, we can move forward to dynamic analysis.

## ACKNOWLEDGEMENTS

Thanks to the discussion with Cai Chengying, Deng Xiujie, A.Chao, Tang Chuanxiang.

## REFERENCES

- [1] A. W. Chao, *Lectures on Accelerator Physics*, World Scientific, 2020. doi:10.1142/12004
- [2] K. L. F. Bane and M. Sands, "The Short-Range Resistive Wall Wakefields," *AIP Conference Proceedings*, vol. 367, no. 1, pp. 131–149, 04 1996. doi:10.1063/1.50300
- [3] G. Stupakov, "Resistive-wall wake for nonrelativistic beams revisited," *Phys. Rev. Accel. Beams*, vol. 23, p. 094401, Sep 2020. doi:10.1103/PhysRevAccelBeams.23.094401
- [4] F. Zimmermann and K. Oide, "Resistive-wall wake and impedance for nonultrarelativistic beams," *Phys. Rev. ST Accel. Beams*, vol. 7, p. 044201, Apr 2004. doi:10.1103/PhysRevSTAB.7.044201

# DESIGN OF BEAM DYNAMICS FOR A HIGH-POWER DC PROTON ACCELERATOR AT THE MeV LEVEL\*

Zi-Feng He<sup>#</sup>, Minghua Zhao, Shanghai Institute of Applied Physics, Chinese Academy of Sciences,  
Shanghai 201800, China

Weishi Wan, Shanghai University of Science and Technology, Shanghai 201210, China

## Abstract

This paper aims to design the beam dynamics of a MeV-level high-power DC proton accelerator for use in high-voltage accelerators. The high-power proton accelerator has essential applications such as ion implantation equipment, neutron therapy equipment, and accelerator-based neutron source equipment. With the increasing use of high-voltage generators due to their stable and reliable operation, these accelerators have gained significant popularity in the field. The paper discusses the design considerations of the accelerator equipment, including the functions and requirements of the acceleration tube, electric field distribution, and voltage holding issues. Additionally, the paper focuses on the design aspects of beam optics, encompassing topics such as electric field distribution, beam focusing, beam transmission, divergence, and the impact of space charge effects on beam quality. Calculations and optimizations are performed based on the parameters and requirements specific to high-voltage accelerators. Finally, the paper presents and analyzes the results of the accelerator tube and beam optics design.

## INTRODUCTION

MeV-level proton accelerators, as powerful and versatile particle acceleration devices, play a significant role in various industries, scientific research, and medical applications. In the industrial sector, MeV-level proton accelerators are widely utilized in material processing and surface treatment techniques, enabling high-energy material modification and ion implantation processes. In the field of scientific research, MeV-level proton accelerators provide robust tools for nuclear physics and particle physics investigations. In the medical domain, MeV-level high-power DC proton accelerators generate high-power proton beams that produce neutrons through target interactions. These neutrons are utilized in Boron Neutron Capture Therapy (BNCT) for targeted tumor radiation treatment. For MeV-level high-power DC proton accelerators operating with a single-ended electrostatic acceleration scheme, beam optics design becomes particularly crucial.

## DESIGN ISSUES OF ACCELERATOR TUBES

### *Beam Parameters of the Incident Ion Beam in the Accelerator Tube*

Based on the output characteristics of the high-current DC microwave ion source [1-3], the beam parameters of the incident ion beam in the accelerator tube can be set as shown in the Table 1.

Table 1: Parameters of the Incident Beam at the Entrance of the Accelerator Tube

Parameters	Value
Emittance $\epsilon$	$0.5 \pi$ mm mrad
$\alpha$	0.2
$\beta$	0.4 mm/mrad
Spot diameter	4 mm

### *The Space Charge Effect of the Ion Beam*

As the current passing through the accelerator tube increases, the effect of space charge becomes more significant, leading to an increase in the radius of the ion beam and a deterioration in the focusing properties of the accelerator tube system. Consequently, more current is lost on the electrodes, resulting in a sharp increase in the load on the accelerator tube due to secondary electrons. The simulation results for proton beams with beam currents of 0.1 mA, 1 mA, and 15 mA, initial energy of 40 keV, and a 1 cm beam spot radius drifting in an infinite space are shown in Figure 1.

The radial potential distribution of the ion beam is a crucial aspect of the accelerator's beam dynamics, as shown in Figure 2. It describes the variation of electric potential across the radial dimension of the ion beam.

Considering the ion beam to be infinitely long and axially symmetric, the potential distribution function generated by space charge is determined by the following equation.

$$U(r) = \begin{cases} \frac{\rho r_b^2}{4\epsilon_0} \left[ 1 + 2 \ln \left( \frac{R}{r_b} \right) - \left( \frac{r}{r_b} \right)^2 \right], & 0 \leq r \leq r_b \\ \frac{\rho r_b^2}{4\epsilon_0} \ln \left( \frac{R}{r_b} \right), & r_b \leq r \leq R \end{cases} \quad (1)$$

\* Work supported by Major Development Project of the Shanghai Institute of Applied Physics, CAS [Y951011031].  
# hezifeng@sinap.ac.cn

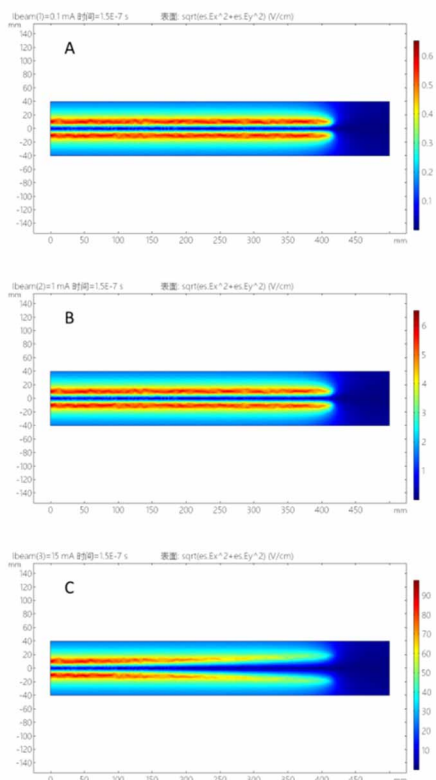


Figure 1: The radial electric field distribution.

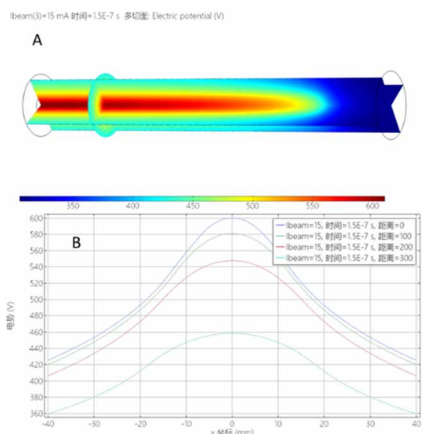


Figure 2: Radial Potential Distribution of the Ion Beam.

The  $r_b$  represents the beam radius,  $\rho$  is the spatial charge density distribution, and  $\rho = I/\pi r_b^2 v$ , where  $v$  is the velocity of particles in the beam.

In practical calculations, the beam divergence needs to be taken into account, and  $r_b$  will gradually increase along the direction of beam propagation. In the simulation process, the beam divergence has already been considered. The electric field generated by the space charge on the beam axis is  $E(0) = 0$ . The radial electric field distribution caused by the space charge is shown in Figure 1.

The charged beam simultaneously generates a spatial distribution of the magnetic field. The magnetic force acting on particles due to this magnetic field is relatively

small compared to the electric force. Therefore, it can be neglected in subsequent calculations.

### Beam Divergence Caused by Space Charge

As mentioned earlier, higher beam currents generate significant electric and magnetic fields. The electric field force due to space charge always leads to beam divergence, while the magnetic field force from space charge has a certain axial converging component. For slow-moving particles at the head of the accelerator, the magnetic field force is relatively weak compared to the dominant electric field force. Consequently, the beam at the head of the accelerator exhibits a stronger tendency to diverge. For smaller parallel beams, such as a 0.1 mA proton beam, the particles only deviate by 0.06 mm from their initial positions after a free-space drift of 400 mm. However, as the current increases to 15 mA, the deviation of particles from their initial positions at the end of the drift will reach 8 mm. Therefore, in the design of the head section of the accelerator, a strong focusing force is required to mitigate the spatial divergence effect for high-current low-energy beams.

## ACCELERATOR TUBE AND BEAM OPTICS DESIGN

### High-current Accelerator Tube System

As the effect of space charge increases, the radius of the ion beam also increases, deteriorating the system's focusing properties. Consequently, the beam collision on the electrodes increases, and the load on the accelerator tube sharply rises due to the secondary electrons generated. The vacuum conditions of the accelerator tube also deteriorate due to the increased flow of neutral gas generated by the ion source. To maintain a stable voltage on the tube section despite the increased leakage current, the current passing through the voltage-divider resistors should be increased. Among the lens electrodes in the uppermost part of the accelerator tube, the double-cylinder lens has the highest voltage ratio, which also has the most significant impact on the overall focusing characteristics.

### The Particle's Motion Equation and Focusing System

In the high-voltage accelerator tube's electric field, the radial motion equation of particles is as follows, where  $r$  represents the radial coordinate of the particle,  $z$  is the axial coordinate, and  $\rho$  is the spatial charge density. In different regions of the accelerator tube, the variation of electric field gradients is not uniform, and the entire optical electric field gradients have different Q-value regions along the axial direction. When  $Q > 0$ , the focusing effect of the externally applied electric field is greater than the divergent effect of the space charge. When  $Q < 0$ , the divergent effect of the space charge field predominantly affects the beam. When  $Q \approx 0$ , the focusing effect of the external electric field is essentially balanced with the divergent effect of the space charge field, and the radial size of the beam remains unchanged.

0.001, Voltage\_Focus=40 时间=2.4E-7 s 点轨迹 lbeam=15, Voltage\_Focus=40 时间=2.4E-7 s 点轨迹 lbeam=20, Voltage\_Focus=40 时间=2.4E-7 s 点轨迹

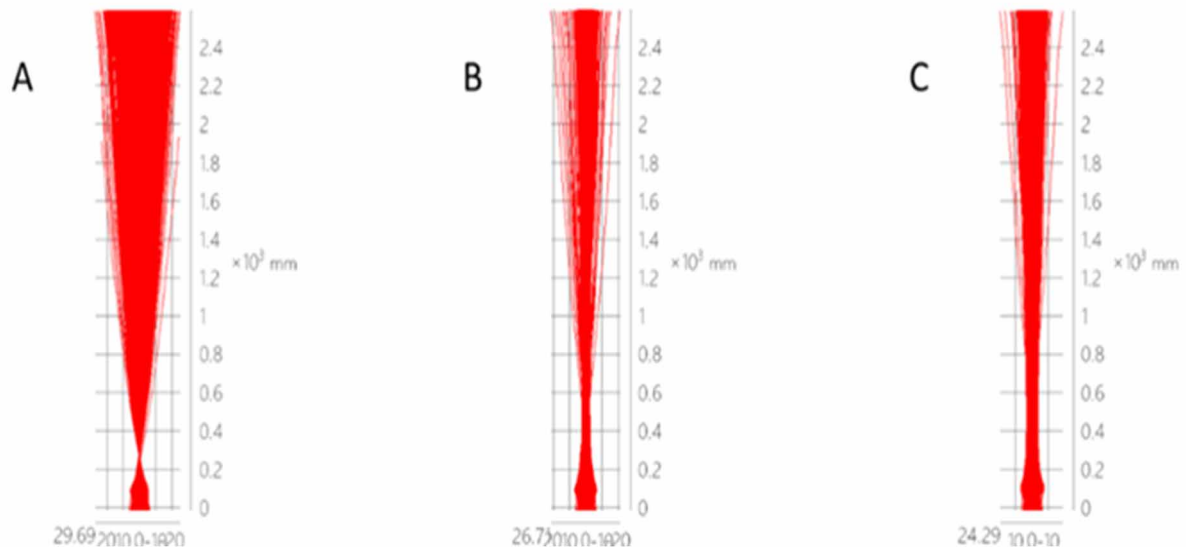


Figure 3: 2.5 MeV Proton Beam, A–0.001mA, B–15mA, C–20mA.

$$r'' + \frac{U'}{2U} r' + \frac{1}{4U} \left( U'' + \frac{\rho}{\epsilon_0} \right) r = r'' + \frac{U'}{2U} r' + \frac{Q}{4U} r = 0 \quad (2)$$

By placing optical elements at different positions in the accelerator tube, it is possible to create an axial electric field gradient distribution that satisfies the beam's passage. This gradient distribution can be obtained by establishing a full-size simulation model. In general, in the forward direction of the beam, in addition to the initial focusing system, compensation for the accelerator system's aberration should also be designed.

The design approach of the initial focusing system is to adjust its parameters, such as the focusing voltage  $V_F$ , when the space charge effect caused by the ion beam's current affects the characteristics of the initial focusing system. By doing so, the image point can be brought back to the desired position, and the focusing system can be in a matched state. This kind of system typically employs a single lens, where the focusing characteristics of the initial focusing system can be adjusted by changing the potential of the middle electrode without affecting the characteristics of other lenses adjacent to it in the front and rear.

The focusing compensation of the acceleration system can be achieved using either magnetic lenses or electrostatic lenses. If electrostatic lenses are used, the potential distribution inside the acceleration tube can be utilized to set potentials on the internal electrodes of the tube, allowing the addition of several individual lenses within the acceleration tube. These individual lenses can provide focusing compensation for the ion beam inside the acceleration tube [4, 5].

## RESULT

The envelope calculations of the beam for different current intensities are shown in the Figure 3. Since the focusing system of the accelerator's electrode is optimized for high beam currents, the focusing effect of the beam is not very good for low beam currents. Therefore, during the accelerator tuning process, it is necessary to quickly raise the beam to the optimized design point.

## REFERENCES

- [1] T. Taylor, "High-current dc microwave ion sources (invited)," *Review of Scientific Instruments*, vol. 63, no. 4, Apr. 1992, pp. 2507-2512. doi: 10.1063/1.1143826
- [2] R. Thomae, R. Gough, R. Keller, K. N. Leung, T. Schenkel, A. Aleksandrov, M. Stoeckli, and R. Welton, "Beam measurements on the H<sup>-</sup> source and low energy beam transport system for the Spallation Neutron Source," vol. 73, no. 5, May 2002, pp. 2016-2019. doi: 10.1063/1.1470238
- [3] PENG Shixiang, ZHANG Meng, ZHAO Jie, XU Rong, REN Haitao, LU Pengnan, SONG Zhizhong, YU Jinxing, YUAN Zhongxi, and GUO Zhiyu, "Progress in developing a high current RFQ injector", *Nuclear Techniques*, vol. 32, no. 3, 2009, pp. 165-168. doi: 10.3321/j.issn:0253-3219.2009.03.002
- [4] M. M. Elkind, "Ion Optics in Long, High Voltage Accelerator Tubes," *Review of Scientific Instruments*, vol. 24, no. 2, 1953, pp. 129-137. doi: 10.1063/1.1770640
- [5] J. D. Larson, "Resolving beam transport problems in electrostatic accelerators," *Revue de Physique Appliquée*, vol. 12, no. 10, 1977, pp. 1551-1561. doi: 10.1051/rphysap:0197700120100155100

# APPROXIMATION OF SPACE CHARGE EFFECT IN THE PRESENCE OF LONGITUDINAL MAGNETIC FIELDS

H. Y. Li<sup>†</sup>, J. R. Shi, H. Zha<sup>\*</sup>, W. H. Gu, Q. Gao, H. B. Chen, Tsinghua University, Beijing, China

## Abstract

The space charge effect plays a significant role in the evolution of phase space during beam transport. Applying an external longitudinal magnetic field has been shown to effectively reduce beam expansion through the mechanism of beam rotation. In this article, we present a fast approximation algorithm for estimating the impact of an external magnetic field on beam expansion. The algorithm enables efficient computations and provides insights into controlling the phase space dynamics of the beam in the presence of longitudinal magnetic fields.

## INTRODUCTION

In particle accelerators, space charge forces have a significant impact on the transmission process, causing the beam to expand in both the transversal and longitudinal dimensions. This expansion leads to an increase in emittance, the formation of beam halo, and even beam loss [1]. Notably, the space charge force is proportional to  $1/\gamma^2$ , where  $\gamma$  represents the Lorentz factor [2]. Therefore, the influence of the space charge force becomes more pronounced for low-energy high-intensity beams. As the transmission distance increases, the impact of the space charge force on high-energy beams gradually becomes significant. In the simplest scenario, using an infinitely long uniform beam model, the expression for the space charge force can be given as follows:

$$F_r = \frac{qI r}{2\pi\epsilon_0\beta c a^2 \gamma^2} \quad (1)$$

As shown in Figure 1,  $a$  is the radius of the beam.

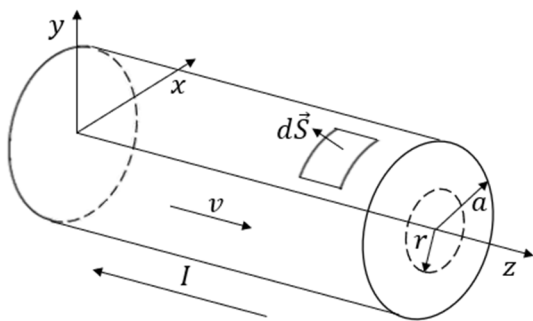


Figure 1: The infinitely long uniform beam model.

When a longitudinal magnetic field  $B$  is applied, it can help alleviate the space charge effect. As macroparticles

experience space charge forces and gain radial velocity, the Lorentz force causes the beam to rotate in the angular direction. This rotation dissipates some of the total energy derived from the electromagnetic potential. Consequently, this process can effectively slow down the radial expansion of the beam.

Furthermore, the angular rotation of particles gives rise to an induced longitudinal magnetic field  $B_1$ , which acts to weaken the original magnetic field  $B$ . However, through simulation, it has been observed that  $B_1$  is significantly smaller than  $B$ . Consequently, in the subsequent discussion, we will neglect the influence of  $B_1$ . Additionally, we assume that the transverse velocity is much smaller than the longitudinal velocity, which is close to the speed of light. In the Cartesian coordinate system, with the longitudinal direction defined as the  $z$ -axis, the equation of motion for the macroparticles can be expressed as follows:

$$\ddot{x} = A_1 x - A_2 \dot{y}; \quad \ddot{y} = A_1 y + A_2 \dot{x} \quad (2)$$

Wherein  $A_1 = qI/\gamma^3 m_0 2\pi\epsilon_0\beta c a^2$ ;  $A_2 = qB/\gamma m_0$ .  $m_0$  is the static mass of an electron. By utilizing the fourth-order Runge-Kutta method, we can update the position of a macroparticle based on an appropriate time step. This numerical technique allows us to accurately calculate the particle's trajectory and track its motion throughout the simulation.

From Eq. (1) and Eq. (2), we observe that in a uniform electron beam, the accelerations and velocities of particles are both proportional to their radial positions. As a result, after expansion, the ratio of radial coordinates for different particles remains constant, indicating that the beam remains uniform. In order to simplify the computation, a fast approximation algorithm can be employed, where only the motion of the outermost particle is calculated. This approximation allows for a more efficient calculation process while still capturing the overall behaviour of the beam.

## PROGRESS

### Verification with Astra

We have developed a fast approximation algorithm utilizing Eq. (1) and Eq. (2). In order to validate the accuracy of this approximation algorithm, we can compare its results with those obtained from Astra, a space charge tracking algorithm developed by DESY [3]. For this comparison, we can utilize the single-bunch model. If the length of the beam remains relatively constant after transport, its equivalent current can be considered constant as well. Under such circumstances, Astra's finite-cylinder model is equivalent to the infinitely long beam model. By comparing the results of our approximation algorithm with Astra's

<sup>†</sup> li-hy22@mails.tsinghua.edu.cn  
<sup>\*</sup> zha\_hao@tsinghua.edu.cn

simulations under these conditions, we can assess the correctness of our approach.

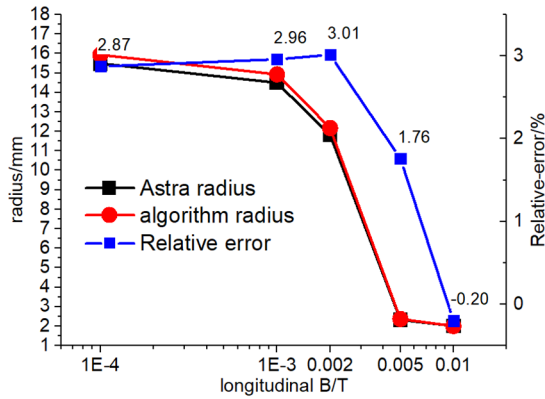


Figure 2: Comparison with Astra.

Based on the results depicted in Fig. 2, it is evident that the fast approximation algorithm accurately approximates the expansion of the beam under various longitudinal magnetic fields. The initial parameters of the electron beam used in the simulations are presented in Table 1. When compared to the results obtained from Astra, the algorithm exhibits a relative error of less than 3%. Moreover, it significantly reduces the computation time from several minutes to less than a second. These findings demonstrate the effectiveness and efficiency of the fast approximation algorithm in accurately modelling the beam's expansion behaviour.

Table 1: Initial Parameters of the Beam

Parameters	Value
Gamma	20.57
Initial radius/mm	2.0
Initial length/mm	50
Transport distance/m	50
Charge/nC	-0.5

### Algorithm Results

Figure 2 clearly illustrates that as the longitudinal magnetic field strength increases, the mitigation of beam expansion becomes more pronounced. However, the presence of a longitudinal magnetic field introduces a non-monotonic behaviour in the beam's radius with respect to the transport distance. Instead of continuously increasing, the beam radius exhibits periodic oscillations, as demonstrated in Fig. 3. The parameters employed in these simulations are the same as those used in Fig. 2.

Indeed, in the scenario where the beam radius exhibits periodic oscillations due to the presence of a longitudinal magnetic field, focusing solely on the final radius at a fixed transport distance may not provide a comprehensive understanding. Instead, it becomes crucial to analyse the oscillation period and amplitude.

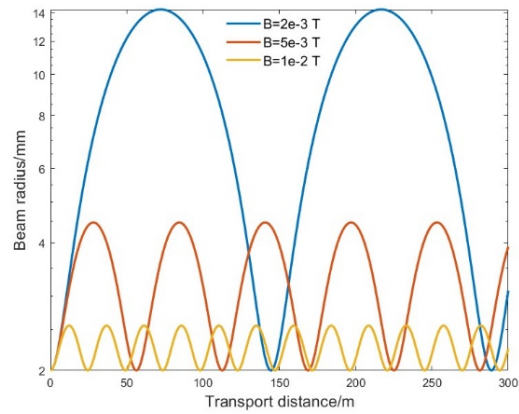


Figure 3: Oscillation of the beam radius.

As depicted in Fig. 3, we observe that with increasing magnetic field strength, the oscillation period becomes shorter, and the maximum radius decreases. This implies that by employing a solenoid to generate an appropriate magnetic field, we can effectively suppress the space charge effect of the beam to the desired extent. Stronger magnetic fields yield better results in terms of beam control. Developing an approximation method for such a process would significantly contribute to the phase space control of the beam, enabling precise manipulation of its behaviour.

### Further Approximation

By simulating the beam described in Table 1 under various longitudinal magnetic fields, we can obtain the maximum radius  $R_m$  during oscillation and the corresponding distance  $D$  required to reach it, which is also half of the oscillation period. To enhance the visual representation, we use the reciprocal of the magnetic field strength ( $1/B$ ) as the x-axis in Figs. 4(a, b). The simulation results are depicted as a blue line. Notably, both curves appear to be smooth and nearly linear. Consequently, we can approximate these curves using polynomials to provide a simplified representation.

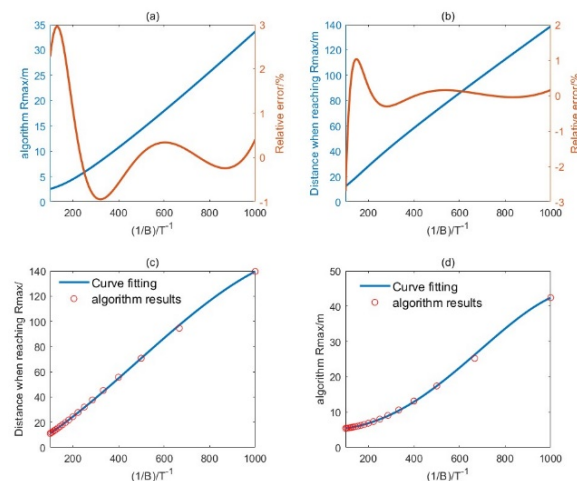


Figure 4: Fitting of the oscillation.

It's obvious that when  $B$  is zero, the  $R_m$  will be  $\infty$ ; when  $B$  is  $+\infty$ , the  $R_m$  will be  $R_0$ , which is the initial radius of the beam. Thus, we can get the fitting curve using the expression below:

$$R_m = \sum_{i=1}^4 m_i B^{i-5} + R_0 \quad (3)$$

Considering that for large values of  $B$ , the corresponding distance  $D$  becomes negligible, we can simplify the approximation of  $D$  using a third-order polynomial, whose expression is:

$$D = \sum_{i=1}^4 n_i B^{i-4} \quad (4)$$

The relative errors of the fitting process are illustrated as orange lines in Figs. 4(a, b), with all relative errors falling below 3%. This suggests that the approximation provided by Eq. (3) and Eq. (4) accurately captures the behaviour of the beam. In order to further validate the effectiveness of these equations, we select another set of initial parameters for a test beam, as presented in Table 2. By analysing the behaviour of the test beam and comparing it with the approximation derived from Eq. (3) and Eq. (4), we can assess the validity and generalizability of the proposed equations.

Table 2: Initial Parameters of the Test Beam

Parameters	Value
Gamma	20
Initial radius/mm	5.0
Initial length/mm	50
Transport distance/m	50
Charge/nC	-1.0

To validate the form of Eqs. (3, 4), we employ the algorithm with four different magnetic field strengths ( $B$ ) to obtain four sets of results for the test beam. Subsequently, we solve for the parameters in Eqs. (3, 4) and compare the newly obtained curve fitting with the simulation results of the test beam. The comparison results are presented in Figs. 4(c, d). Remarkably, despite using only four data points for approximation, the curves fit closely with the algorithm results, thereby confirming the validity of the proposed equations.

## CONCLUSION

In summary, when an external longitudinal magnetic field is introduced, the expansion of the beam under the influence of space charge is mitigated through beam rotation. Additionally, the beam's radius exhibits periodic oscillations as the transport distance increases. By employing a fast approximation algorithm, we are able to accurately fit the oscillation parameters using polynomials of the reciprocal of the magnetic field. These results provide valuable insights for controlling the phase space of the beam, enabling precise manipulation of its behaviour and characteristics.

## REFERENCES

- [1] J. Amundson, P. Spentzouris, and J. Qiang *et al.*, "Synergia: An accelerator modeling tool with 3-D space charge", *J. Comput. Phys.*, vol. 211, pp. 229-248, 2006.  
doi: 10.1016/j.jcp.2005.05.024
- [2] K. Schindl, in *Joint US-CERN-Japan-Russia Particle Accelerator School on Beam Measurement*, Ed. by S.I. Kurokawa, Montreux, Switzerland, 1998, pp. 127-151.  
doi: 10.1142/9789812818003\_0004
- [3] <https://www.desy.de/~mpyf1o/>

# IMPACT OF NEG COATING THICKNESS AND RESISTIVITY ON BEAM COUPLING IMPEDANCE

Tianlong He\*, Weiwei Li, Zhenghe Bai, Hongliang Xu<sup>†</sup>  
National Synchrotron Radiation Laboratory, USTC, Hefei 230029, China

## Abstract

In diffraction-limited storage rings, non-evaporable getter (NEG) coatings are generally used to assure the ultrahigh vacuum, which, however, also increase the beam coupling impedance that can affect beam dynamics. Ignoring the influence of coating roughness, the impact of NEG coatings on the impedance mainly depends on the coating thickness and resistivity. In this paper, we investigate the impedance characteristics of a round CuCrZr vacuum chamber coated by NEG with different thickness and resistivity.

## INTRODUCTION

For diffraction-limited storage rings (DLSRs) designed based on multi-bend achromat lattice, its vacuum chamber size is generally limited by the requirements for high gradient multipole magnets and high performance insertion devices. Small vacuum chamber is not conducive to maintaining the ultra-high vacuum environment for beam circulating in the ring. To assure the ultra-high vacuum, it is necessary to make a layer of NEG coating on the inner surface of vacuum chamber to improve the pumping speed [1]. However, NEG coating will increase significantly the resistive wall (RW) impedance especially in the high frequency region, resulting in a reduction in the threshold of single bunch instabilities, e.g., microwave instability and transverse mode coupling instability [2].

For vacuum chambers with NEG coating, the IW2D (ImpedanceWake2D) code is most widely used to calculate the RW impedance [3, 4]. For ease of impedance calculation in the windows operating system, we referred to the core source code of IW2D and wrote a Mathematica script to substitute for IW2D. After debugging, both results were basically consistent. Therefore, all impedance calculations in this paper were performed using this Mathematica script.

To calculate the RW impedance, in addition to the parameters of vacuum chamber, generally, two key parameters of NEG coating are required to set: thickness and resistivity. For DLSRs, the coating thickness is usually around 1  $\mu\text{m}$  [1], and the coating resistivity, depending on the coating method, often varies in the range of  $1.25 \times 10^{-6} \sim 7.1 \times 10^{-5} \Omega \cdot \text{m}$  [5]. It naturally leads to the question: what is the best choice of the thickness and resistivity of NEG coating for mitigating its influence on the RW impedance? To answer this question, it is better to sweep the two parameters and evaluate the impedance accordingly. Once obtained the impedance data, we can further calculate the longitudinal loss factor

and transverse kick factor to preliminarily assess the impact of NEG coating.

## THEORY AND METHOD

### Impedance Calculation

As mentioned earlier, we used a Mathematica script (equivalent to IW2D) for NEG coating parameter sweeping calculation. The resistivity and thickness of NEG coating are swept in the range of  $1 \times 10^{-7} \sim 1 \times 10^{-4} \Omega \cdot \text{m}$  and  $0.1 \sim 2 \mu\text{m}$ , respectively. The round vacuum chamber is assumed to have a radius of 11 mm and material of CuCrZr with resistivity of  $\rho = 2.18 \times 10^{-8} \Omega \cdot \text{m}$ .

### Loss Factor and Kick Factor

For a Gaussian bunch, the loss factor and the kick factor are respectively given by :

$$K_{loss} = \frac{\omega_0}{2\pi} \sum_{p=-\infty}^{\infty} \text{Re}[Z_{\parallel}(p\omega_0)] \exp[-(p\omega_0\sigma_t)^2], \quad (1)$$

and

$$K_{\perp} = -\frac{\omega_0}{2\pi} \sum_{p=-\infty}^{\infty} \text{Im}[Z_{\perp}(p\omega_0)] \exp[-(p\omega_0\sigma_t)^2], \quad (2)$$

where  $\sigma_t$  is the rms bunch length,  $\omega_0$  is the revolution angular frequency,  $p$  is an integer,  $\text{Re}[Z_{\parallel}]$  is the real part of the longitudinal RW impedance and  $\text{Im}[Z_{\perp}]$  is the imaginary part of the transverse RW impedance.

## IMPACT OF NEG COATING

### Impact of NEG Coating Resistivity on Impedance

Figures 1 and 2 show the longitudinal and transverse RW impedances of per-unit-length vacuum chamber with a 1  $\mu\text{m}$  NEG coating, respectively. It is obvious that the NEG coating mainly affects the impedance behaviour in the frequency region of higher than 10 GHz. It should be noted, in this frequency region, that the impedance behaves like a resonator, and the resonant peak of the real part gets higher and the corresponding bandwidth gets narrower with the increase of resistivity. For the cases of resistivity in  $5 \times 10^{-6} \sim 1 \times 10^{-4} \Omega \cdot \text{m}$ , the difference among them is small. It indicates that, with the resistivity in this range, the impact of NEG coating on the longitudinal and transverse impedance has a weak dependence on resistivity. For the case of resistivity in  $1 \times 10^{-7} \sim 5 \times 10^{-6} \Omega \cdot \text{m}$ , the imaginary part significantly decreases with a decrease in resistivity, while the real part exhibits complexity as shown in Figs. 1 and 2(top) where different curves cross each other in  $10^{10} \sim 10^{13}$  Hz.

\* htlong@ustc.edu.cn

<sup>†</sup> hlxu@ustc.edu.cn

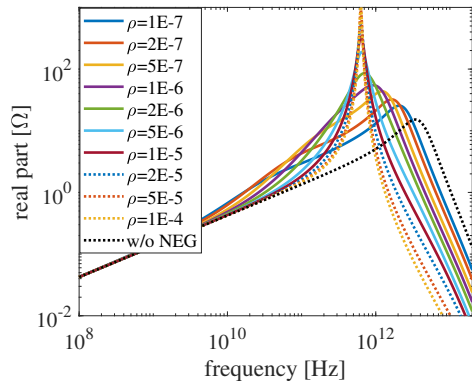


Figure 1: Longitudinal RW impedance of per-unit-length vacuum chamber with different NEG resistivities.

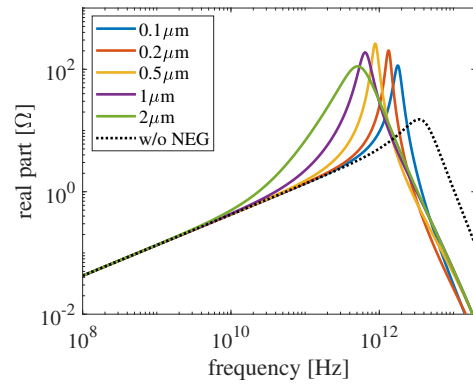


Figure 3: Longitudinal RW impedance of per-unit-length vacuum chamber with different NEG thickness.

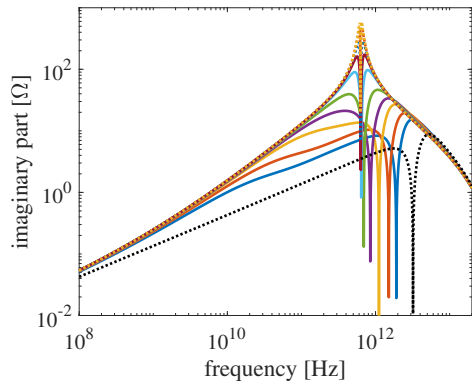


Figure 2: Transverse RW impedance of per-unit-length vacuum chamber with different NEG resistivities.

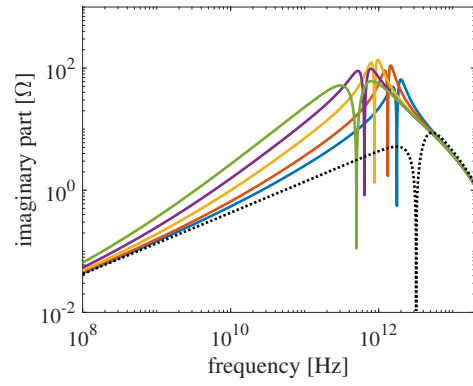
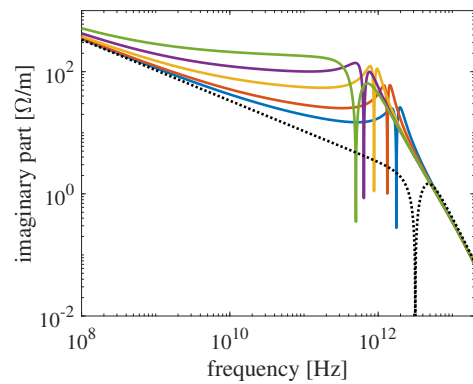
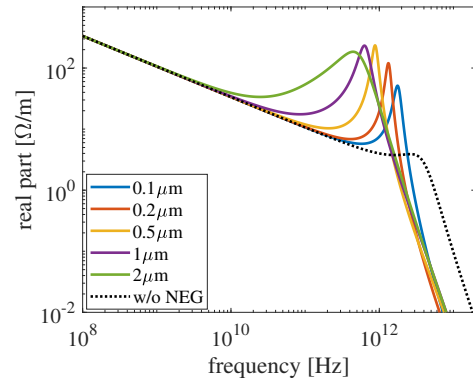
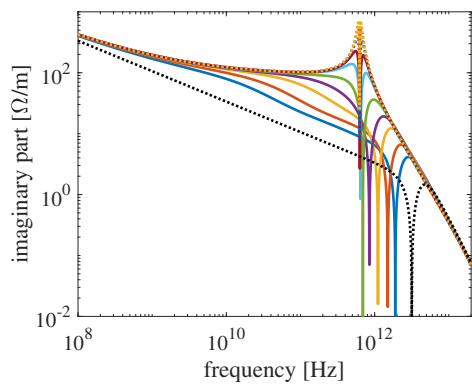
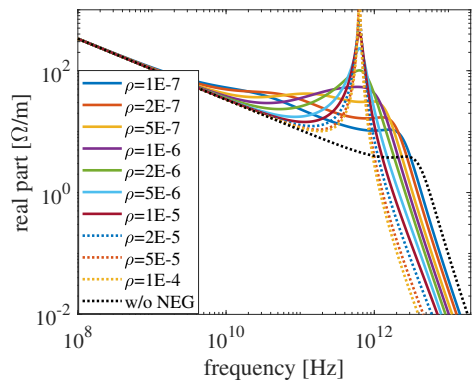


Figure 4: Transverse RW impedance of per-unit-length vacuum chamber with different NEG thickness.



### Impact of NEG Coating Thickness on Impedance

We choose the case of resistivity of  $5 \times 10^{-6} \Omega \cdot \text{m}$  to evaluate the impact of NEG coating thickness. As shown in Figs. 3 and 4, both longitudinal and transverse impedances behave like a resonator in the frequency range of  $10^{10} \sim 10^{13}$  Hz: the resonant peak gets lower as the thickness is raised from 0.5 to 2  $\mu\text{m}$  or descended from 0.5 to 0.1  $\mu\text{m}$ , and the resonant frequency gets smaller with increasing the thickness. It is found that the NEG coating thickness has a larger influence on the imaginary part than the real part, e.g. the observable discrepancy of the real part between the cases of '2  $\mu\text{m}$ ' and 'w/o NEG' starts from about  $10^{10}$  Hz which is two orders of magnitude higher than that of the corresponding imaginary part. It is obvious that the imaginary part is increased significantly with the thickness.

### Impact of NEG Coating on the Loss Factor and Kick Factor

The longitudinal loss factor and transverse kick factor of per-unit-length NEG coated vacuum chamber are shown in Figs. 5 and 6, respectively. As expressed in Eqs. (1) and (2), both factors are a function of the rms bunch length. The case of 2 mm rms bunch length is taken into account here.

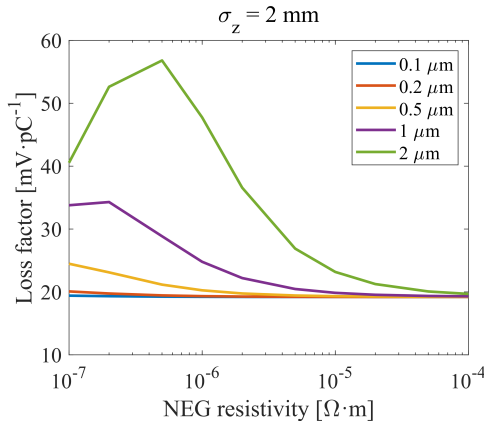


Figure 5: Loss factor for different resistivity and thickness of NEG coating.

We can see that both loss and kick factors can be reduced by reducing NEG coating thickness, and that the reduction level of loss factor increases with reducing the resistivity, while it is contrary for the kick factor. For the case of thickness in the range of 0.1~1  $\mu\text{m}$ , the resistivity variation in the range of  $5 \times 10^{-6} \sim 1 \times 10^{-4} \Omega \cdot \text{m}$  has a slight effect on the loss factor and the kick factor. For the case of thickness in the range of 1~2  $\mu\text{m}$ , the loss factor generally increases obviously and the kick factor decreases significantly with the decrease of resistivity in  $1 \times 10^{-7} \sim 1 \times 10^{-5} \Omega \cdot \text{m}$ .

As for the kick factor shown in Fig. 6, we can see that if the thickness is reduced from 1 to 0.5  $\mu\text{m}$  in the resistivity range of  $1 \times 10^{-6} \sim 1 \times 10^{-4} \Omega \cdot \text{m}$ , the kick factor can be reduced by ~33%; if the thickness is further reduced to 0.2  $\mu\text{m}$ , the kick factor can be reduced by ~54%. This reduction is significant. If the thickness is set to 1~2  $\mu\text{m}$ , the kick factor

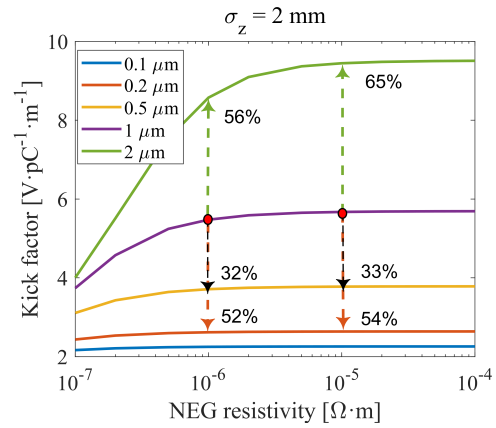


Figure 6: Kick factor for different resistivity and thickness of NEG coating.

can be reduced significantly by reducing the resistivity only less than  $5 \times 10^{-7} \Omega \cdot \text{m}$ . If the thickness is set to 0.5  $\mu\text{m}$ , or even to 0.1~0.2  $\mu\text{m}$ , the kick factor is hardly reduced with the reduction of the resistivity.

## CONCLUSION AND OUTLOOK

In this paper, the RW impedances of the round vacuum chamber with radius of 11 mm and material of CuCrZr were calculated using a Mathematica script, via sweeping the resistivity and thickness of NEG coating in the ranges of  $1 \times 10^{-7} \sim 1 \times 10^{-4} \Omega \cdot \text{m}$  and 0.1~2  $\mu\text{m}$ , respectively. Resonance-like impedance with a high peak was observed for the longitudinal RW impedance in the case of resistivity in the range of  $5 \times 10^{-6} \sim 1 \times 10^{-4} \Omega \cdot \text{m}$ . Reducing the resistivity can decrease the kick factor, but it is likely to increase the loss factor. The impact of NEG coating had only been discussed with the impedance, loss factor and kick factor. In the future, the impact of NEG coating on the single bunch instability for a designed DLSR will be further studied through macro-particle tracking simulations.

## ACKNOWLEDGEMENTS

This work was supported by National Natural Science Foundation of China (No. 12105284 and No. 12075239) and the Fundamental Research Funds for the Central Universities (No. WK2310000090).

## REFERENCES

- [1] E. Al-Dmour, J. Ahlback, D. Einfeld, P. F. Tavares and M. Grabski, "Diffraction-limited storage-ring vacuum technology", *J. Synchrotron Rad.*, vol. 21, p. 878, 2014.
- [2] M. Migliorati, E. Belli, M. Zobov, "Impact of the resistive wall impedance on beam dynamics in the Future Circular  $e^+e^-$  Collider", *Phys. Rev. Accel. Beams*, vol. 10, p. 041001, 2018.
- [3] N. Mounet and E. Metral, "Electromagnetic field created by a macroparticle in an infinitely long and axisymmetric multilayer beam pipe, Report No. CERN-BE-2009-039", 2009.
- [4] <https://github.com/amorimd/CloneIW2D>

- [5] O. B. Malyshev, L. Gurran, P. Goudket, K. Marinov, S. Wilde, R. Valizadeh and G. Burt, “RF surface resistance study of non-evaporable getter coatings”, *Nucl. Instrum. Methods A*, vol. 844, p. 99, 2017 .

# DEVELOPMENT OF A VLASOV SOLVER FOR ARBITRARY SUB-OPTIMAL LENGTHENING CONDITIONS IN DOUBLE-RF SYSTEM

Jingye Xu<sup>1</sup>, Institute of High Energy Physics (IHEP), Chinese Academy of Sciences, Beijing, China\*

Chuntao Lin, Institute of Advanced Science Facilities (IASF), Shenzhen, China

Na Wang<sup>1</sup>, Haisheng Xu<sup>1</sup>, Yuan Zhang<sup>1</sup>, Institute of High Energy Physics (IHEP),  
Chinese Academy of Sciences, Beijing, China

<sup>1</sup> also at University of Chinese Academy of Sciences (UCAS), Beijing, China

## Abstract

Solving Vlasov equation is a classic method for analyzing collective beam instabilities. Considering longitudinal impedance and the nonlinear longitudinal potential well, we developed a new Vlasov solver which can be used to study the transverse mode-coupling instability under the arbitrary sub-optimal lengthening and the optimal lengthening conditions in a double-RF system. Several different techniques to deal with the radial direction of longitudinal phase space have been tested. Numerical discretization method is selected in this paper. The development of the solver is presented in details here. Benchmarks and crosscheck of the solver have been made and presented as well.

## INTRODUCTION

Most (semi-)analytical Vlasov solvers are based on a single RF cavity or do not contain synchrotron tune spread [1,2]. In 2014, A. Burov proposed the NHTVS (Nested Head-Tail Vlasov Solver), which can contain small synchrotron tune spread but it is based on Gaussian bunches [3]. In 2018, Venturini proposed radial discretization which contains large synchrotron tune spread and flat-top distribution, it is only applicable for optimal lengthening. [4]. They may result in significant errors under conditions where the longitudinal distribution is completely different from Gaussian or the synchrotron tune spread cannot be ignored. There is currently no general Vlasov solver for sub-optimal lengthening conditions.

In this paper, we proposed a method to deal with arbitrary sub-optimal lengthening bunch by discretization of Vlasov equation. It is a general method to dominate Gaussian, sub-optimal and optimal lengthening bunches.

At first, we will derivate Vlasov equation similar to Ref. [5]. Then we choosed two typical cases and compared our method with Chuntao Lin's transfer matrix method [6]. The specific sampling process will be described in this section.

\* xujingye@ihep.ac.cn

## FORMULA DERIVATION

The single-particle equations of motion are:

$$\begin{cases} \dot{y}(s) = p_y \\ \dot{p}_y(s) = - \left( \frac{\omega_\beta}{c} \right)^2 y + \frac{1}{E} F_y(z, s) \\ \dot{z}(s) = - \eta_p \delta \\ \dot{\delta}(s) = \frac{eV_1}{EC} \mathcal{V}'(z) \end{cases} \quad (1)$$

Here  $F_y$  is transverse wake force,  $E$  is particle energy,  $\omega_\beta$  is betatron frequency,  $\eta_p$  is slippage factor,  $C$  is circumference of the storage ring, and  $V_1 \mathcal{V}'(z)$  is the voltage of double RF system, where

$$\begin{aligned} \mathcal{V}'(z) = & \sin \left( \phi_s - \frac{2h_1\pi}{C} z \right) - \sin \phi_s \\ & + r \sin \left[ \phi_{2s} - \frac{2h_1h\pi}{C} z \right] - r \sin \phi_{2s}. \end{aligned} \quad (2)$$

We use action-angle variables  $J, \phi$  in the longitudinal phase space and polar coordinates  $q, \theta$  in the transverse. So the perturbation formalism of density distribution  $\psi(J, \phi, q, \theta; s)$  can be written as

$$\psi = f_0(q)g_0(J) + f_1(q, \theta)g_1(J, \phi)e^{-i\Omega s/c}.$$

Substitute  $\psi$ , Eqs. (6.168) and (6.173) in Ref. [5] into the Vlasov equation,

$$\begin{aligned} i(\Omega - \omega_\beta)g_1 = & \frac{ce^2}{2E\omega_\beta T_0^2} g_0 \sum_p \tilde{\rho}_1(\omega') Z_1^\perp(\omega') e^{i\omega'z/c} \\ & + B(J, \phi) \left[ \frac{\partial g_1}{\partial J} - \frac{1}{D} \frac{f_0'}{f_0} \frac{\partial g_0}{\partial J} e^{i\Omega s/c - i\theta} \right] + C(J, \phi) \frac{\partial g_1}{\partial \phi}, \end{aligned} \quad (3)$$

here

$$\begin{aligned} B(J, \phi) = & \dot{\delta}(z) \frac{\partial J}{\partial \delta} \Big|_z + \dot{z}(t) \frac{\partial J}{\partial z} \Big|_s = \frac{d\vec{r}(t)}{dt} \cdot \nabla J = \frac{dJ}{dt} = 0, \\ C(J, \phi) = & \dot{\delta}(z) \frac{\partial \phi}{\partial \delta} \Big|_z + \dot{z}(t) \frac{\partial \phi}{\partial z} \Big|_s = \frac{d\vec{r}(t)}{dt} \cdot \nabla \phi = \omega_s(J). \end{aligned} \quad (4)$$

Here  $\vec{r}$  is the vector from the original point to the particle coordinate  $(z, \delta)$  in the longitudinal phase space. By the same manipulation of Fourier expansion of  $g_1$  in Ref. [5],

we finally get

$$\begin{aligned} & (\Omega^{(l)} - \omega_\beta)R_l(J) \\ &= g_0(J) \sum_{l'} \int_0^\infty dJ' R_{l'}(J') G_{l,l'}(J, J') \\ &+ \sum_{l'} l' R_{l'}(J) \delta_{l,l'} \omega_s(J). \end{aligned} \quad (5)$$

Here  $g_0(J)$  is the normalized radial distribution,  $R_l(J)$  is radial distribution of angular mode  $l$ ,  $\omega_s(J)$  is synchrotron tune,  $G_{l,l'}(J, J')$  defines as

$$G_{l,l'}(J, J') = -\frac{iN\pi c e^2}{E\omega_\beta T_0^2} \int_{-\infty}^\infty d\omega Z_1^\perp(\omega) S_l^*(\omega, J) S_{l'}(\omega, J') \quad (6)$$

which corresponds to Eq. (6.195) in Ref. [5], but considering angular mode coupling. Here  $S_l(\omega, J)$  defines as

$$S_l(\omega, J) = \frac{1}{2\pi} \int_0^{2\pi} d\phi e^{i l \phi - i \frac{z(J, \phi)}{c} \left( \omega - \frac{\xi \omega_\beta}{\eta} \right)}, \quad (7)$$

which degenerates to

$$i^{-l} J_l \left( \frac{r}{c} \left( \omega - \xi \omega_\beta / \eta \right) \right)$$

in Eqs. (6.177-6.178) in Ref. [5]. Eq. (7) is a compromise on asymmetric potential. Almost all existing models, such as water-bag model, hollow bunch, parabolic bunch, small amplitude approximation of Gaussian and ideal-lengthening bunch, are symmetric. Because of asymmetry, function  $S_l(\omega, J)$  will be numerically calculated combined with discretization that not only in radial direction as Venturini did but also angular direction.

By discretization of Eq. (5) in radial direction, it becomes an eigen value problem

$$\begin{aligned} (\Omega^{(l)} - \omega_\beta) \tilde{R}_{lj} &= M_{lj, l'j'} \tilde{R}_{l'j'} \\ M_{lj, l'j'} &= g_0(J_j) G_{l,l'}(J_j, J_{j'}) \Delta J_{j'} + l' \delta_{l,l'} \omega_s(J_j) \end{aligned} \quad (8)$$

Notice that at vanishing beam intensity  $N = 0$ ,  $M_{lj, l'j'}$  will be a diagonal matrix with elements  $\{l\omega_s(J_j) | j = 1, \dots, n_J\}$ . That's the reason of tune spread of each azimuthal mode, except  $l = 0$ .

## COMPARE WITH TRANSFER MATRIX METHOD

### Settings

The toy model of HEPS is shown in Table 1 and settings of two cases are shown in Table 2, Case #1 represents a set of sub-optimal lengthening parameters, while Case #2 represents optimal lengthening parameters.

### Sampling Method

Assuming maximum  $z$  of sampling points reaches  $n\sigma_z$ , the number of radial, angular discretization meshes is  $n_J$ ,  $n_\phi$ , where  $n_\phi$  is an even number. Then we can sample as described below:

Table 1: Toy Model of HEPS

Parameter	Value
Beam energy, $E$ , GeV	9
Circumference, $C$ , m	1360.4
Primary harmonic number, $h_1$	756
Ratio of harmonic number, $h = h_2/h_1$	3
Energy spread, $\sigma_\delta$	$1.06 \times 10^{-3}$
Momentum compaction factor, $\alpha_c$	$1.56 \times 10^{-5}$
Vertical betatron tune, $\nu_y$	106.23
Bunch charge, $N$ , nC	2

Table 2: Settings of Two Cases

Parameter	#1	#2
Primary RF Voltage, $E$ , MV	3.6395	3.6395
Voltage ratio, $r = V_2/V_1$	0.1819	0.1802
Primary RF phase, $\phi_s$ , rad	1.8928	2.0390
Harmonic RF phase, $\phi_{2s}$ , rad	5.2598	5.7005
Bunch length, $\sigma_z$ , cm	2.5763	2.9078
Average synchrotron tune, $\langle \nu_s \rangle$ , $10^{-4}$	1.6145	0.9912
Number of radial samples, $n_J$	60	80
Number of angular samples, $n_\phi$	300	400
Maximum angular mode, $l_m$	3	3
$n = z_{\max}/\sigma_z$	4	4

- Calculate longitudinal density  $\rho(z)$ ;
- Uniformly sample  $n_J$  points within the range of 0 to  $n\sigma_z$ , which is  $n_J z_{\max}$ 's of Hamiltonian tori;
- Calculate  $n_J z_{\min}$ 's, Hamiltonian  $H$ 's, radial unperturbed density  $g_0(J) = \rho(z_{\max})$  of these Hamiltonian tori.
- Calculate action variable  $J$  of each torus according to

$$J = \frac{1}{\pi} \int_{z_{\min}}^{z_{\max}} \delta dz;$$

- Calculate synchrotron tune spread  $\nu_s(J)$  and average synchrotron tune  $\langle \nu_s \rangle$  by:

$$\begin{aligned} \nu_s(J) &= \frac{C}{2\pi} \frac{dH}{dJ}, \\ \langle \nu_s \rangle &= 2\pi \int_0^\infty g_0(J) \nu_s(J) dJ. \end{aligned}$$

- Take angular sample of each torus between  $z_{\min}$  to  $z_{\max}$  by

$$z_i = z_p + r \cdot \cos \frac{i \cdot 2\pi}{n_\phi}, \quad (0 \leq i \leq n_\phi)$$

here  $z_p = 0.5(z_{\min} + z_{\max})$ ,  $r = 0.5(z_{\max} - z_{\min})$ .

- Calculate angle variable  $\phi$  at each point according to

$$\begin{aligned} F_2(z, J) &= \int_z^{z_{\max}} \delta(z, J) dz, \\ \phi &= \frac{\partial F_2}{\partial J}. \end{aligned}$$

## Results

We compared our method with Chuntao Lin's transfer matrix method [6]. We compared two typical settings, sub-optimal and optimal lengthening, and the corresponding longitudinal distribution  $\rho(z)$  and synchrotron tune spread  $\nu_s(z)$  was shown in Fig. 1. As shown in Fig. 1, the synchrotron tune spread cannot be ignored, or the density distribution is asymmetric.

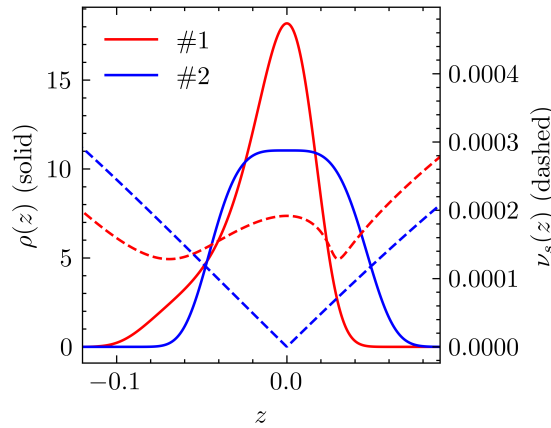


Figure 1: Distribution (solid) and synchrotron tune spread (dashed) of Case #1 (red) and Case #2 (blue) lengthening.

Under sub-optimal and optimal lengthening conditions, our results are consistent. As shown in Fig. 2, we can clearly see when the  $l = 0$  mode and the  $l = -1$  mode are coupled, the instability occurs. In Fig. 3, we cannot find the threshold of instability clearly as Venturini said [4]. In fact, the tune shift points at  $N = 0$  nC are dominated by radial sampling points, and the maximum tune shift of  $l = -1$

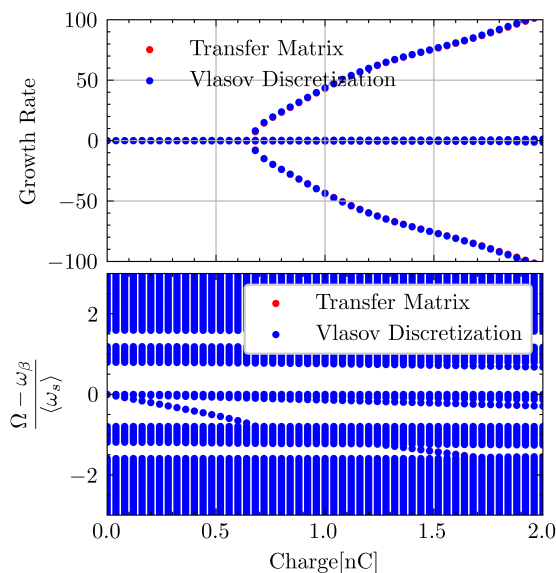


Figure 2: Growth rate per second and tune shift of Case #1 (sub-optimal).

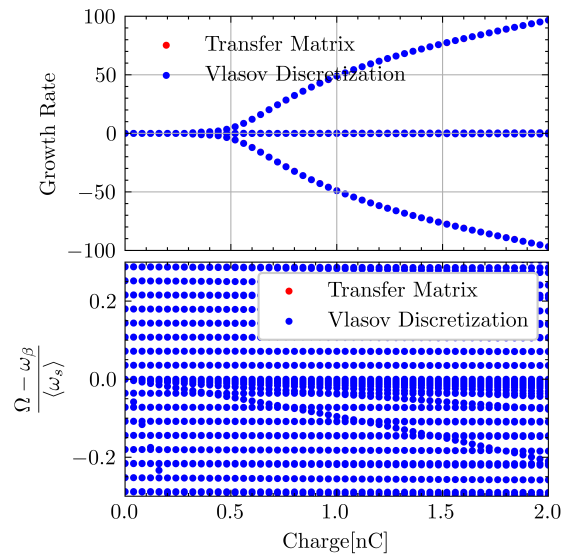


Figure 3: Growth rate per second and tune shift of Case #2 (optimal).

mode is broadened to  $l = 0$  mode under optimal lengthening condition.

## CONCLUSION

In this paper, we proposed a general Vlasov discretization method that can calculate growth rate and mode coupling for arbitrary sub-optimal and optimal lengthening bunches.

## REFERENCES

- [1] Mounet N., "DELPHI: an analytic Vlasov solver for impedance-driven modes", 2014. <https://cds.cern.ch/record/1954277/files/CERN-ACC-SLIDES-2014-0066.pdf>
- [2] Sacherer F., "Methods for computing bunched-beam instabilities", 1972. [https://cds.cern.ch/record/2291670/files/2291670\\_001.pdf](https://cds.cern.ch/record/2291670/files/2291670_001.pdf)
- [3] Burov A., "Nested head-tail Vlasov solver", *Physical Review Special Topics-Accelerators and Beams*, vol. 17, no. 2, p. 021007, 2014. doi:10.1103/PhysRevSTAB.17.021007
- [4] Venturini M., "Harmonic cavities and the transverse mode-coupling instability driven by a resistive wall", *Physical Review Accelerators and Beams* vol. 21, no. 2, p. 024402, 2018. doi:10.1103/PhysRevSTAB.17.021007
- [5] Chao A W., "Physics of collective beam instabilities in high energy accelerators", *Wiley series in beam physics and accelerator technology*, 1993. <https://www.semanticscholar.org/paper/Physics-Of-Collective-Beam-Instabilities-In-High-Chao/2caac8f3ac2d779069631f225da33d0c1008a4c7>
- [6] Lin C, Ohmi K, and Zhang Y., "Coupling effects of beam-beam interaction and longitudinal impedance", *Physical Review Accelerators and Beams*, vol. 25, no. 1, p. 011001, 2022. doi:10.1103/PhysRevAccelBeams.25.011001

# MATCHING SECTION DESIGN AT THE MeV ULTRAFAST ELECTRON BEAM EXPERIMENTAL FACILITY

H. Qi, C.-Y. Tsai, J. Wang, Z. Z. Liu<sup>†</sup>, K. J. Fan<sup>†</sup>  
Huazhong University of Science and Technology, Wuhan, China

## Abstract

This paper introduces the design and optimization of the matching section beamline for the ultrafast electron research platform at Huazhong University of Science and Technology (HUST). The matching section serves as a connection between the main beamline and the beam physics research beamline, aiming to achieve efficient and precise control over the electron beam trajectory and parameters. To evaluate its performance, particle tracking simulations using GPT software were conducted. When the beam is set at 3 MeV and 1 pC charge, the matching section is capable of compressing the bunch length to approximately 50 fs. This level of compression is crucial for ultrafast electron research applications, as it enables the study of phenomena that occur on extremely short time scales, demonstrating its effectiveness in achieving precise beam control and compression.

## INTRODUCTION

The ever increasing demand for high-power and wide-band THz radiation has led to its growth in various research fields such as communication [1], biological imaging [2], and plasma diagnostics [3]. To address this demand, we are currently developing a second beamline at HUST that will focus on beam physics research, specifically investigating terahertz radiation and beam Space-Charge (SC) effects.

Figure 1 illustrates the layout of the MeV ultrafast electron beam experimental facility at Huazhong University of Science and Technology (HUST), featuring two beam lines. The primary beamline is dedicated to achieving sub-100 fs time resolution in a MeV ultrafast electron diffraction (UED) setup [4]. The second beamline is connected to the downstream experimental facility through a matching section [5,6], which serves multiple purposes: bending the electron beam and further compressing the bunch.

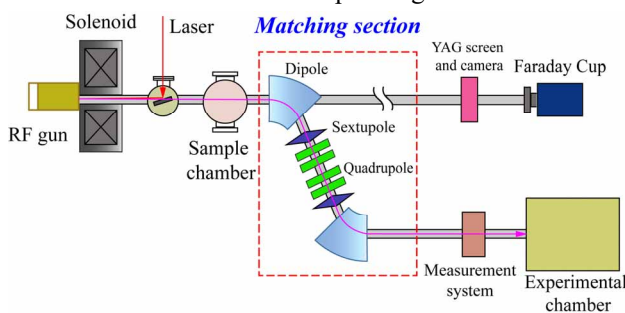


Figure 1: Schematic of the proposed MeV HUST facility.

\* Work supported by the National Natural Science Foundation of China (NSFC 12235005 and 12275094), and National key research and development program of China (2022YFA1602202).

<sup>†</sup> kjfan@hust.edu.cn; <sup>†</sup> zzliu@hust.edu.cn

Typically, a matching section consists of two dipoles along with quadrupoles and sextupoles that help mitigate dispersion. In the matching section, an electron beam with energy chirp undergoes phase rotation. Through careful design, a positive energy chirp is transformed into a negative chirp, leading to beam compression and ultimately reaching a beam waist downstream. This optimization ensures efficient and compact electron beam propagation.

## BEAM OPTICS DESIGN

During the initial design phase of the matching section, it is typically adequate to consider the first-order beam transport matrix. This matrix, denoted as  $R$ , describes the transformation of beam parameters from the entrance to the exit of the matching section.

In the matching section,  $R$  is composed of the transport matrices of the dipole, quadrupole, and drift elements [7-9]. The linearized form of  $R$  can be expressed as follows:

$$R = \begin{bmatrix} R_{11} & R_{12} & 0 & 0 & 0 & R_{16} \\ R_{21} & R_{22} & 0 & 0 & 0 & R_{26} \\ 0 & 0 & R_{33} & R_{34} & 0 & 0 \\ 0 & 0 & R_{43} & R_{44} & 0 & 0 \\ R_{51} & R_{52} & 0 & 0 & 1 & R_{56} \\ 0 & 0 & 0 & 0 & 0 & 1 \end{bmatrix}. \quad (1)$$

The explicit expression of the transport matrix  $R$  for the matching section can be obtained by straightforwardly multiplying the transport matrices of each individual element.

Since the matching section serves as a bunch compressor for the second beamline, it is essential to ensure that the energy chirp becomes negative at the exit in order to generate the longitudinal beam waist downstream. This requirement imposes a condition on the transport matrix  $R$  of the matching section, specifically that the matrix element  $R_{56}$  must be less than zero. Furthermore, the dipole magnets in the matching section introduce a dispersion term that cannot be ignored, which can cause a significant transverse position offset and result in beam loss. To mitigate this issue, dispersion matching becomes necessary, which involves setting the matrix elements  $R_{16}$  and  $R_{26}$  to zero at the exit of the matching section, effectively eliminating the leakage of dispersion.

The matching section implemented at the HUST experimental facility is designed to be symmetric, and its specific layout is illustrated in Fig. 2. The dipole magnet in this section has a bending angle ( $\theta$ ) of 60 degrees and an effective radius ( $\rho$ ) of 0.26 m. Between the two dipole magnets, four

quadrupoles are strategically positioned to adjust the dispersion term  $R_{16}$  and its derivative  $R_{26}$ . This adjustment aims to minimize the maximum beam size. Additionally, two sextupoles are placed adjacent to the quadrupoles. These sextupoles function as second-order magnet elements but can be considered as drift spaces in terms of first-order optics matching. The lengths of the drifts in the matching section are as follows:  $L1=0.4$  m,  $L2=0.15$  m,  $L3=0.075$  m,  $D1=0.2$  m, and  $D2=0.1$  m, respectively.

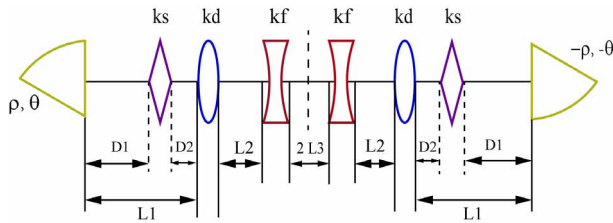


Figure 2: Schematic of the matching section.

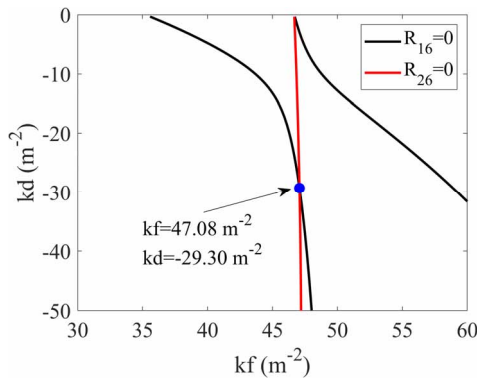


Figure 3: The first-order dispersion ( $R_{16}$  and  $R_{26}$ ) as a function of the quadrupole coefficient.

In the first-order optics design of the matching section, we calculate the total transfer matrix  $R$ . As shown in Fig. 3, by setting the quadrupole coefficients  $kf=47.08$   $m^{-2}$  and  $kd = -29.30$   $m^{-2}$ , we achieve  $R_{16} = R_{26} = 0$ , indicating that the matching section is achromatic at the end of the second dipole. However, this calculation provides a rough approximation as it does not account for the variation of beam parameters (Twiss parameters) within the section. To obtain more accurate results, further analysis is performed using MAD-X software [10]. The matching results are displayed in Fig. 4. In this analysis, the quadrupole coefficients used in the matching section are adjusted to  $kf = 49.64$   $m^{-2}$  and  $kd = -25.80$   $m^{-2}$ . Additionally, the longitudinal dispersion  $R_{56}$  is determined to be  $-0.051$  m. By applying negative longitudinal dispersion to a positive energy chirp at the entrance of the section, it is possible to generate the longitudinal waist downstream in the second beamline. This configuration allows for the achievement of the minimum bunch length.

The compression section is not purely linear but incorporates higher-order (nonlinear) contributions, which might lead to longitudinal phase space distortion and disruption of the bunch profile. To correct these higher-order terms, multi-pole magnets are typically required. However, for single-pass transport, considering the second-order effect is generally sufficient. In the absence of sextupole

magnets, the second-order longitudinal term  $T_{566}$  is calculated to be  $-2.1$  m. Two sextupole magnets are employed to mitigate this effect. The sextupoles have opposite polarities and a gradient value of  $8.69$  T/ $m^2$ , and the value of  $T_{566}$  is reduced to 0, effectively eliminating the second-order term.

By achieving full compression, the downstream beamline can achieve the minimum bunch length. This configuration greatly enhances the quality of the compressed beam.

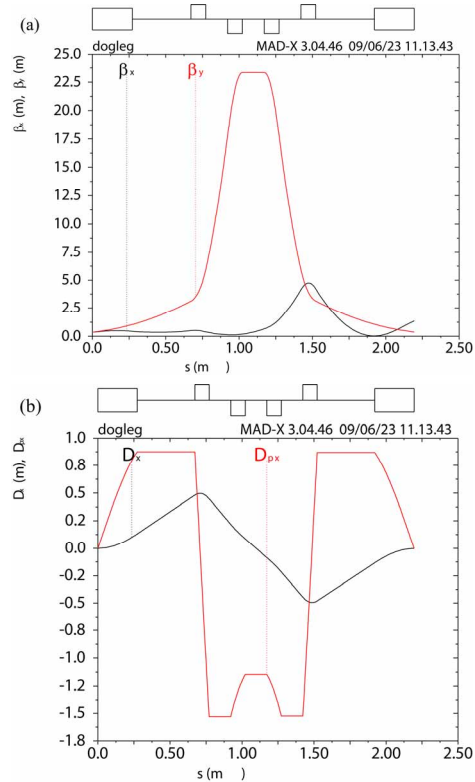


Figure 4: Beam optics in the matching section. The evolution of the (a) betatron function and (b) the first-order dispersion in the section.

## SIMULATION RESULTS

In order to evaluate the efficacy of the lattice design within the matching section, particle tracking simulations that traced the trajectory of particles from the cathode to the downstream region were conducted using the General Particle Tracer (GPT) software [11]. The parameters employed in the simulation are specified in Table 1.

Table 1: Parameters of RF Gun and Solenoid Magnet

Parameters	Value (unit)
Laser spot size	0.05 mm
Laser RMS pulse duration	> 15 fs
Beam energy	3 MeV
Injection phase	65 deg
Beam charge	1 pC
Peak field in Solenoid	0.1445 T

Figure 5 presents the tracking results obtained under different conditions at two locations: the entrance and down-

stream of the matching section. In Fig. 5(a), the longitudinal phase space and charge density profile at the entrance are depicted. It can be observed that the energy chirp appears to be nearly linear, with a measured value of  $h_0=30.09 \text{ m}^{-1}$ . Upon passing through the matching section, the chirp undergoes compression, as depicted in Fig. 5(b). However, the absence of sextupoles leads to the formation of a tail in the compressed beam bunch, resulting in an undesirable increase in the bunch length.

To effectively mitigate the impact of the second-order term  $T_{566}$  in the beam, sextupole correction is incorporated. This correction significantly improves the tailing behavior of the beam, as illustrated in Fig. 5(c). Consequently, the root mean square (RMS) bunch length can approach approximately 50 fs without the SC effect. However, when the SC effect is taken into account, the RMS bunch length increases to approximately 100 fs due to the interactions between electrons, as shown in Fig. 5(d).

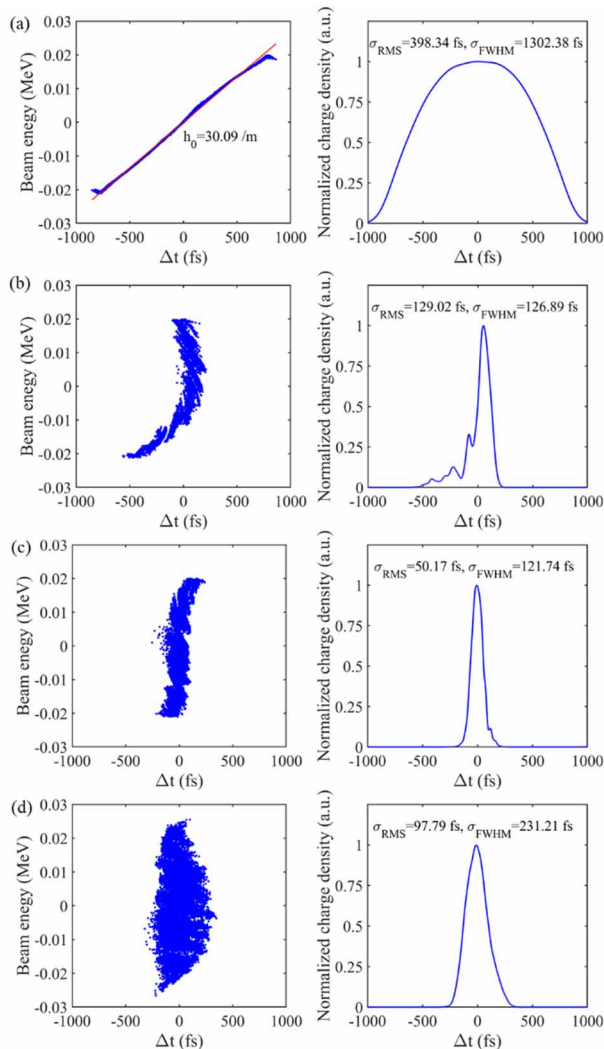


Figure 5: The longitudinal phase space of the beam (left) and its corresponding charge density profile (right), (a) at the entrance of the matching section, and after the matching section tracked (b) without both sextupole correction and SC, (c) with sextupole correction and without SC, and (d) with both sextupole correction and SC incorporated.

Figure 6 illustrates the evolution of beam parameters, specifically the longitudinal bunch length and transverse emittance, as the particles travel from the cathode to the downstream region of the matching section, specifically along the second beamline. Notably, a distinct compression of the bunch length is observed beyond the matching section. However, this compression is accompanied by an increase in the transverse emittance, particularly in the  $x$  direction. On the other hand, minimal changes are observed in the  $y$  direction.

To further preserve the transverse emittance, precise adjustments to the gradient of the sextupole magnets are necessary, requiring additional efforts. It is crucial to focus on these improvements to optimize the overall performance of the system.

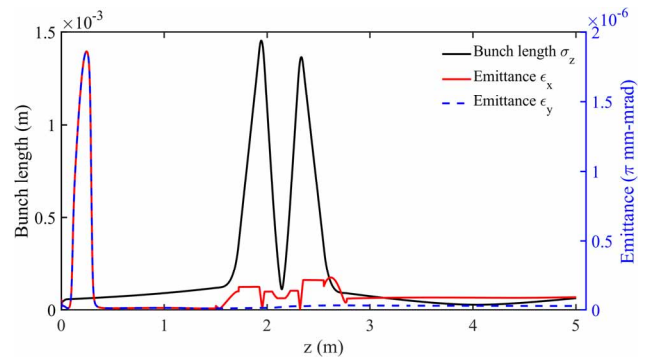


Figure 6: The evolution of beam parameters in the second beamline with SC.

## CONCLUSION

This paper introduces an analytical design of the matching section for a second parallel beamline and subsequently conducts particle tracking simulations to assess its effectiveness and performance. The results demonstrate that the proposed matching section successfully achieves compression of the RMS bunch length, reducing it from 0.4 ps to 50 fs, with an idealistic bunch compression factor of 8. However, when considering the space charge effect, the energy chirp increases, leading to an extension of the RMS bunch length to approximately 100 fs, with a compromised bunch compression factor of 4. Furthermore, the simulations indicate a degradation in the emittance, highlighting the need for further optimization in this aspect. The development of this dual-beam-line configuration, along with the inclusion of the matching section, provides enhanced capabilities for the MeV UED facility at HUST.

## REFERENCES

- [1] K. Ishigaki *et al.*, “Direct intensity modulation and wireless data transmission characteristics of terahertz-oscillating resonant tunnelling diodes”, *Electron. Lett.*, vol. 48, no. 10, pp. 582-583, May 2012. doi:10.1049/el.2012.0849
- [2] Z. Yang *et al.*, “Study on an artificial phenomenon observed in terahertz biological imaging”, *Biomed. Opt. Express*, vol. 12, no. 6, pp. 3133-3141, Jun. 2021. doi:10.1364/BOE.424445

- [3] B. H. Kolner *et al.*, “Plasma characterization with terahertz pulses”, *IEEE J Quantum Electron*, vol. 14, no. 2, pp. 505-512, Apr. 2008. doi:10.1109/JSTQE.2007.913395
- [4] Y. Song *et al.*, “MeV electron bunch compression and timing jitter suppression using a THz-driven resonator”, *Nucl. Instrum. Methods. Phys. Res. A*, vol. 1047, pp. 167774, Feb. 2023. doi:10.1016/j.nima.2022.167774
- [5] A. Weinberg and A. Nause, “Dogleg design for an MeV Ultra-fast electron Diffraction beam line for the hybrid Photo-emitted RF GUN at Ariel University”, *Nucl. Instrum. Methods. Phys. Res. A*, vol. 989, pp. 164952, Feb. 2021. doi:10.1016/j.nima.2020.164952Z
- [6] R. J. England *et al.*, “Beam shaping and compression scheme for the UCLA Neptune Laboratory”, in *Proc. 2003 Particle Accelerator Conf. (PAC2003)*, Portland, OR, May 2003, p. 3258. doi:10.1109/PAC.2003.1289880
- [7] A. Wolski, “Beam dynamics in high energy particle accelerators”, World Scientific, 2014.
- [8] C.-Y. Tsai *et al.*, “Low-energy high-brightness electron beam dynamics based on slice beam matrix method”, *Nucl. Instrum. Methods. Phys. Res. A*, vol 937, pp. 1-20, Sep. 2019. doi:10.1016/j.nima.2019.05.035
- [9] C.-Y. Tsai and K. Fan, “A Semi-Analytical Approach to Six-Dimensional Path-Dependent Transport Matrices With Application to High-Brightness Charged-Particle Beam Transport”, in *Proc. 2019 North American Particle Acc. Conf. (NAPAC2019)*, Lansing, MI, US, Sep. 2019, pp. 792-795. doi:10.18429/JACoW-NAPAC2019-WEPLS12
- [10] H. Grote and F. Christoph Iselin, “User’s Reference Manual for the MAD-X Program”, version 5.08.01, Geneva, Switzerland, Feb. 2022.
- [11] General Particle Tracer, <http://www.pulsar.nl/gpt>.

# ANALYSIS OF THE FLUCTUATION OF RESONANCE DRIVING TERMS FOR NONLINEAR LATTICE OPTIMIZATION

Bingfeng Wei, Jiajie Tan, Zhenghe Bai\*, Guangyao Feng<sup>†</sup>  
National Synchrotron Radiation Laboratory, USTC, Hefei, China

## Abstract

Minimizing resonance driving terms (RDTs) of nonlinear magnets is a traditional approach to enlarge the dynamic aperture (DA) of a storage ring. The local cancellation of nonlinear dynamics, which is adopted by some diffraction-limited storage rings, is more effective than the global cancellation. The former has smaller fluctuation of RDTs along the ring. In this paper, the correlation between two kinds of RDT fluctuations is found. The physical analysis shows that minimizing the RDT fluctuations is beneficial for controlling the crossing terms and thus enlarging the DA. This physical analysis is supported by the statistical analysis of nonlinear solutions of a double-bend achromat lattice.

## INTRODUCTION

The widely-used analytical approach for the nonlinear optimization of storage rings is to minimize resonance driving terms (RDTs) of nonlinear magnets. In this approach, the Hamiltonian for particle motion is split into linear and nonlinear parts, and the nonlinear parts is expanded as the resonance basis, i.e. RDTs [1]. Minimizing the RDTs can control the corresponding resonance and thus enlarge the dynamic aperture (DA). The local nonlinear cancellation, which is used in the lattice design of some diffraction-limited storage rings, is more effective than the global cancellation [2]. And the former has smaller fluctuation of RDTs along the ring. There are two ways to calculate the longitudinal fluctuation of RDTs. One is to calculate the accumulated RDTs with a fixed starting position, and the build-up and cancellation of RDTs are shown in this way. We call it the RDT build-up fluctuation. We have shown that minimizing the RDT build-up fluctuations is more effective than minimizing the commonly used one-turn RDTs in enlarging the DA [3]. The other is to calculate the one-turn map (or one-period map) with varying longitudinal starting position [4]. In this paper, we will study the correlation between these two kinds of RDT fluctuations. And then we will analyze the effects of minimizing the RDT fluctuations.

## RELATION BETWEEN TWO KINDS OF RDT FLUCTUATIONS

For a storage ring lattice with  $N$  sextupoles, the one-period map observed at  $s_0$  is

$$\mathcal{M}(s_0) = \mathcal{A}_{s_0}^{-1} e^{i: h} \mathcal{R} \mathcal{A}_{s_0}, \quad (1)$$

where  $\mathcal{A}_{s_0}$  is a normalizing map,  $\mathcal{R}$  is a rotation, and  $e^{i: h}$  is the nonlinear Lie map. For the on-momentum particles, the  $n$ -th order generator of  $e^{i: h}$  can be expanded as:

$$h_n = \sum_{j+k+l+m=n} h_{jklm} h_x^{+j} h_x^{-k} h_y^{+l} h_y^{-m}, \quad (2)$$

where  $h_x^\pm \equiv \sqrt{2J_x} e^{\pm i \phi_x}$ ,  $h_y^\pm \equiv \sqrt{2J_y} e^{\pm i \phi_y}$ , with  $(J, \phi)$  being action-angle variables, and  $h_{jklm}$  is the driving terms. For any thin sextupole  $a$ , its normalized Hamiltonian  $\hat{V}_a$  can be expanded in the same way:

$$\hat{V}_a = \sum_{j+k+l+m=3} h_{a,jklm} h_x^{+j} h_x^{-k} h_y^{+l} h_y^{-m}. \quad (3)$$

For the third-order RDTs of one-period map, we have  $h_{jklm} = \sum_{a=1}^N h_{a,jklm}$ . The build-up fluctuation  $h_{1 \rightarrow t, jklm} \equiv \sum_{a=1}^t h_{a, jklm}$  shows the accumulated RDTs from  $s_0$  to the  $t$ -th sextupole.

For the case of multiple periods, the accumulated RDTs from  $s_0$  to  $t$ -th sextupole in the  $(u+1)$ -th period is:

$$\begin{aligned} \sum_{a=1}^{uN+t} h_{a, jklm} &= \sum_{a=1}^{uN} h_{a, jklm} + \sum_{a=uN+1}^{uN+t} h_{a, jklm} \\ &= \sum_{a=1}^N h_{a, jklm} \frac{1 - e^{i u m \cdot \mu}}{1 - e^{i m \cdot \mu}} + \sum_{a=1}^t h_{a, jklm} e^{i u m \cdot \mu} \\ &= \frac{\sum_{a=1}^N h_{a, jklm}}{1 - e^{i m \cdot \mu}} - \left( \frac{\sum_{a=1}^N h_{a, jklm}}{1 - e^{i m \cdot \mu}} - \sum_{a=1}^t h_{a, jklm} \right) e^{i u m \cdot \mu}, \end{aligned} \quad (4)$$

where  $\mathbf{m} = (j - k, l - m)$  is the mode of resonance and  $\boldsymbol{\mu} = (\mu_x, \mu_y)$  is the phase advances of one period. The third-order RDT build-up fluctuation can be written in the form of  $C_{0, \mathbf{m}} + C_{t, \mathbf{m}} e^{i u \mathbf{m} \cdot \boldsymbol{\mu}}$ , which is a circle in the complex plane when  $u$  is a variable. And  $C_{t, \mathbf{m}}$  is dependent on the sextupole index  $t$ , so the build-up fluctuation of the RDT  $h_{jklm}$  is a series of concentric circles in the complex plane.

The second kind of RDT fluctuations shows the period map observed at different longitudinal positions. And we can measure it on a real machine. In order to measure the RDTs, we need another transformation to find the nonlinear invariants [4]:

$$e^{i: -F} e^{i: h} R e^{i: F} = e^{i: H} R, \quad (5)$$

where  $H$  is the phase-independent Hamiltonian in normal forms, and  $F$  is such a transformation. When the observation position  $s$  is between  $n$ -th and  $(n+1)$ -th sextupole, the third

\* baizhe@ustc.edu.cn

<sup>†</sup> fenggy@ustc.edu.cn

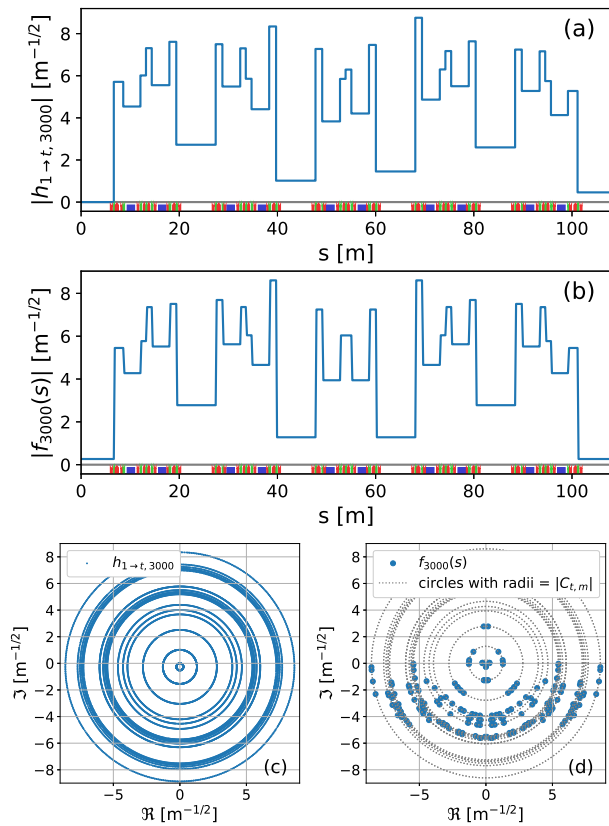


Figure 1: Correlation between two kinds of RDT fluctuations of the SSRF storage ring lattice. (a) The build-up fluctuation of  $h_{3000}$  in one SP. (b) The fluctuation of  $f_{3000}(s)$  in one SP. (c) The build-up fluctuation of  $h_{3000}$  for 100 turns in the complex plane. We calculate multiple turns in order to make concentric circles visible. (d) The RDT  $f_{3000}(s)$  in the complex plane.

order terms in  $F$  are:

$$\begin{aligned}
 f_{jklm}(s) &= \frac{\sum_{a=n+1}^{n+N} h_{a,jklm} e^{-im \cdot \Delta\phi}}{1 - e^{im \cdot \mu}} \\
 &= \frac{\left( \sum_{a=1}^N - \sum_{a=1}^n + \sum_{a=N+1}^{N+n} \right) h_{a,jklm} e^{-im \cdot \Delta\phi}}{1 - e^{im \cdot \mu}} \\
 &= \frac{\sum_{a=1}^N h_{a,jklm} - (1 - e^{im \cdot \mu}) \sum_{a=1}^n h_{a,jklm}}{1 - e^{im \cdot \mu}} e^{-im \cdot \Delta\phi}, \quad (6)
 \end{aligned}$$

where  $\Delta\phi$  is the phase advances between the observation position  $s$  and  $s_0$ . And we can see that  $|f_{jklm}(s)|$  equals to  $|C_{t,m}|$ . So these two kinds of RDT fluctuations are strongly related.

Figure 1(a) and 1(b) show these two kinds of RDT fluctuations for one super-period (SP) of the SSRF storage ring lattice. The SSRF storage ring consists of 4 SPs, each with 5 double-bend achromat (DBA) cells [5]. The term  $h_{3000}$  is almost cancelled after one SP. The term  $C_{0,m}$  in Eq. (4) is small and the two kinds of RDT fluctuations are almost the same. Figure 1(c) shows the build-up fluctuation in the complex plane. We calculate multiple turns in order to make

the concentric circles visible. These circles have the same center  $C_{0,m}$  and different radii  $|C_{t,m}|$ . In Fig. 1(d),  $f_{jklm}(s)$  is also plotted in the complex plane. And we can see that they are on the circles with radii  $= |C_{t,m}|$ . The fourth-order cases are more complex, but the relation still exists. For a fourth-order resonance  $m = m_1 + m_2$ , where  $m_1$  and  $m_2$  are third-order resonances, the RDT build-up fluctuation has the form of  $C_{0,m} + C_{t,m} e^{im \cdot \mu} + C'_{t,m_1} e^{im_1 \cdot \mu} + C'_{t,m_2} e^{im_2 \cdot \mu}$ , and the fourth-order  $|f_{jklm}(s)|$  still equals to  $|C_{t,m}|$ .

## EFFECTS OF MINIMIZING RDT FLUCTUATIONS

### Physical Analysis

Since the RDTs are derived from the one-period map, it seems the build-up and cancellation of RDTs in the period is not important. For an ideal cancellation situation, e.g. two identical thin sextupoles separated by  $-I$  transformation, the nonlinear effects are completely cancelled. And the fluctuation of RDTs, which is determined by the strength of sextupoles, does not affect the cancellation. However, when the thickness of sextupoles is considered, an "error map" containing higher-order nonlinear terms appears. Reducing the strength of sextupoles can control the error map as well as the RDT fluctuations. The calculation of these two examples can be found in Ref. [6] (pages 146-149).

We think the cross-talk effect of sextupoles is the key. The perturbations of sextupoles drives fourth-order resonances by the cross-talk effect:

$$h_4 = \sum_{b>a=1}^N [\hat{V}_a, \hat{V}_b] = \sum_{b=2}^N \left[ \sum_{a=1}^{b-1} \hat{V}_a, \hat{V}_b \right], \quad (7)$$

and  $\sum_{b>a=1}^N [\hat{V}_a, \hat{V}_b]$  shows the build-up fluctuations of fourth-order RDTs. The third-order RDT build-up fluctuations are involved in the calculation of fourth-order RDTs. Minimizing RDT fluctuations is beneficial for controlling the crossing terms and thus controlling the fourth-order resonances. Moreover, the cross-talk effect can also generate the fifth- and higher-order RDTs. So minimizing the RDT fluctuations is beneficial for controlling higher-order resonances. And this is the physics why minimizing the RDT fluctuations is more effective than minimizing the one-turn RDTs in enlarging the DA.

### Statistical Analysis

We will then use numerous nonlinear lattice solutions to demonstrate this physical analysis. Some indicators need to be defined. The RDT  $h_{jklm}$  of the one-turn map is denoted as  $h_{jklm,ring}$ . And when all the  $n$ -th order one-turn RDTs are considered together, we have  $h_{n,ring} = \sqrt{\sum_{j+k+l+m=n} h_{jklm,ring}^2}$ . Since these two kinds of RDT fluctuations are related by  $|C_{t,m}|$ , we can use  $h_{jklm,ave} = \sum_{t=1}^N |C_{t,m}| / N$  to show the RDT fluctuations. And similarly the  $n$ -th order RDT fluctuations is denoted as  $h_{n,ave} =$

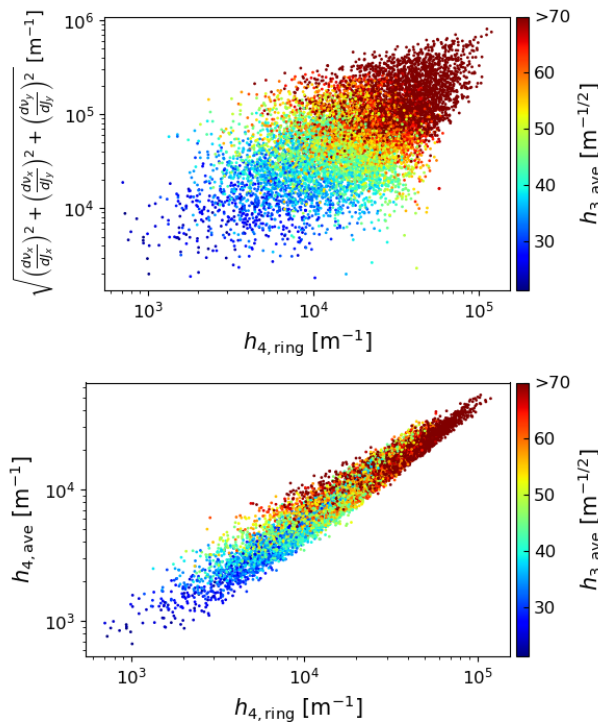


Figure 2: Correlation between the third-order RDT fluctuations  $h_{3,ave}$  and the crossing terms. The ADTS terms, the fourth-order one-turn RDTs  $h_{4,ring}$  and the fourth-order RDT fluctuations  $h_{4,ave}$  are generated by the cross-talk effect of sextupoles.

$\sqrt{\sum_{j+k+l+m=n} h_{jklm,ave}^2}$ . The correlation between these indicators can be measured using the Spearman rank-order correlation coefficient, which is a nonparametric measure of the monotonicity of the relationship between two datasets [7]. Like other correlation coefficients, it varies between -1 and +1 with 0 implying no correlation. Correlations of -1 or +1 imply an exact monotonic relationship.

The SSRF lattice is also taken as the example. The strengths of sextupoles are changed to produce different nonlinear solutions, with the horizontal and vertical chromaticities corrected to (1, 1). A set of nonlinear solutions were generated randomly. Figure 2 shows the correlation between the third-order RDT fluctuations and the crossing terms. Both the fourth-order RDTs and the amplitude-dependent tune shift (ADTS) terms are generated by the sextupole crossing terms. We see that as the third-order RDT fluctuations reduce, the ADTS terms, the fourth-order one-turn RDTs and the fourth-order RDT fluctuations also roughly reduce. The Spearman correlation coefficient between  $h_{3,ave}$  and  $h_{4,ring}$  is 0.75, and it is 0.76 for  $h_{3,ave}$  and  $h_{4,ave}$ , and 0.82 for  $h_{3,ave}$  and ADTS terms. All indicate strong correlations. Therefore, minimizing the RDT fluctuations can effectively control the crossing terms.

Figure 3 shows the correlation between the third-order one-turn RDTs  $h_{3,ring}$ , the third-order RDT fluctuations  $h_{3,ave}$  and the DA area for a set of optimized nonlinear so-

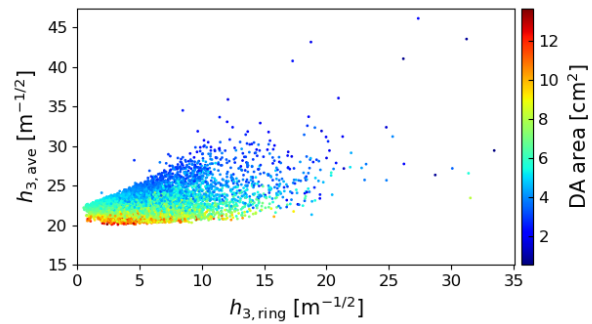


Figure 3: Correlation between the third-order RDT fluctuations  $h_{3,ave}$ , the third-order one-turn RDTs  $h_{3,ring}$  and the DA area.

lutions. We see that the colors, which represent the DA areas, are roughly horizontally layered, and the red dots with large DAs sink to the bottom. This distribution indicates that minimizing  $h_{3,ave}$  is more effective than minimizing  $h_{3,ring}$  in enlarging the DA. The Spearman correlation coefficient between  $h_{3,ave}$  and DA area is -0.87, indicating a very strong correlation.

## CONCLUSION

The local cancellation of nonlinear effects is more effective than the global cancellation. The former has smaller longitudinal RDT fluctuations, which means minimizing RDT fluctuation can be beneficial for enlarging the DA. The relation between two kinds of longitudinal RDT fluctuations was found in this paper. The physical analysis showed that minimizing the RDT fluctuations is beneficial for controlling the crossing terms, which drive the higher-order resonances and ADTS. Therefore, minimizing RDT fluctuations is beneficial for optimizing the nonlinear dynamics and enlarging the DA. This physical analysis was demonstrated by the statistical analysis of nonlinear solutions of a DBA lattice. The code for calculating the RDT fluctuations was shared on a github page [8].

## ACKNOWLEDGEMENTS

This work was supported by the National Natural Science Foundation of China under Grant No. 11875259.

## REFERENCES

- [1] J. Bengtsson, “The Sextupole Scheme for the Swiss Light Source (SLS): An Analytic Approach”, PSI, Villigen, Switzerland, SLS Note 9/97, 1997.
- [2] R. Bartolini, “Storage Ring Design for Synchrotron Radiation Sources”, in *Synchrotron Light Sources and Free-Electron Lasers*, Switzerland: Springer, Cham, 2020, pp. 273–322. doi:10.1007/978-3-319-04507-8
- [3] B. Wei *et al.*, “Analyzing and optimizing dynamic aperture based on minimizing the fluctuation of resonance driving terms”, in *Proc. IPAC’23 Venezia*, 05 2023, pp. 3241–3244. doi:10.18429/jacow-ipac2023-wep1078

- [4] A. Franchi, L. Farvacque, F. Ewald, G. Le Bec, and K. B. Scheidt, “First simultaneous measurement of sextupolar and octupolar resonance driving terms in a circular accelerator from turn-by-turn beam position monitor data”, *Phys. Rev. Spec. Top. Accel Beams*, vol. 17, p. 074001, 2014. doi:10.1103/PhysRevSTAB.17.074001
- [5] G. Liu *et al.*, “Lattice design for SRF storage ring”, *High Energy Phys. and Nucl. Phys.*, vol. 30, pp. 144–146, 2006.
- [6] A. Chao, “Lie Algebra Techniques for Nonlinear Dynamics”, in *Lecture Notes on Special Topics in Accelerator Physics*. <https://www.slac.stanford.edu/~achao/LieAlgebra.pdf>
- [7] S. W. Looney and J. L. Hagan, “2 - statistical methods for assessing biomarkers and analyzing biomarker data”, in *Essential Statistical Methods for Medical Statistics*, NorthHolland, Boston, 2011 pp. 27–65.
- [8] Simple storage ring, <https://github.com/wei0852/simplestoragering>

Content from this work may be used under the terms of the CC BY 4.0 licence (© 2023). Any distribution of this work must maintain attribution to the author(s), title of the work, publisher, and DOI

# LONGITUDINAL BEAM DYNAMICS DESIGN FOR SUPER TAU-CHARM FACILITY

Linhao Zhang<sup>\*</sup>, Tao Liu, Sangya Li, Jingyu Tang<sup>†</sup>, and Qing Luo<sup>‡</sup>  
University of Science and Technology of China, 230026, Hefei, Anhui, China

## Abstract

The project of Super Tau-Charm Facility (STCF) proposed in China, as a new-generation high-luminosity e<sup>+</sup>/e<sup>-</sup> collider in the low-energy region with the center-of-mass energy of 2–7 GeV, is well underway. The luminosity is targeted at  $1.0 \times 10^{35} \text{ cm}^{-2}\text{s}^{-1}$  at the optimized beam energy of 2 GeV. Longitudinal beam dynamics becomes of great importance for the STCF due to the constraints from the novel beam-beam effect called coherent X-Z instability and severe beam collective effects. In this paper, we will develop an iterative optimization model for the STCF longitudinal beam dynamics design, which takes into account the influence of transverse dynamics, coherent X-Z instability, and collective effects.

## INTRODUCTION

The STCF proposed in China is a new-generation super high luminosity e<sup>+</sup>/e<sup>-</sup> collider in the low-energy region spanning the center-of-mass energy of 2–7 GeV. It aims to explore the rich physics in the tau-charm energy range and even search for new physics beyond the standard model [1]. The goal luminosity of STCF reaches  $1.0 \times 10^{35} \text{ cm}^{-2}\text{s}^{-1}$  at the optimized beam energy of 2 GeV, which is two orders of magnitude higher than that of the existing e<sup>+</sup>/e<sup>-</sup> collider in the tau-charm field in China, BEPCII.

To achieve such high luminosity, a large Piwinski angle combined with the crab-waist collision scheme has been widely recognized as an effective approach [2], and adopted in the new-generation e<sup>+</sup>/e<sup>-</sup> colliders such as SuperKEKB [3], BINP-SCTF [4], FCC-ee [5], and CEPC [6], etc. On one hand, through introducing a large Piwinski angle  $\phi$ , the vertical beta function at the interaction point (IP)  $\beta_y^*$  can be squeezed into the level of effective bunch length  $\sigma_z/\phi$ , to significantly raise the luminosity; On the other hand, the synchro-betatron coupling resonance introduced by the large Piwinski angle can be suppressed by the crab-waist correction scheme using crab sextupoles properly positioned on both sides of the IP. However, this scheme will introduce a novel beam-beam effect called coherent X-Z instability [7], which imposes stringent constraints on the longitudinal beam dynamics by requiring the horizontal beam-beam parameter  $\xi_x$  to be much less than the synchrotron tune  $\nu_z$ .

Furthermore, the STCF is characterized by the beam properties of low energy, small emittance, high bunch intensity and large bunch numbers, which means that the

STCF faces significant beam collective effects. This also places strict limitations on the longitudinal parameters such as bunch length and energy spread.

Therefore, special attention is paid to the longitudinal beam dynamics design for STCF in this paper, which requires iterative optimization with transverse dynamics, beam-beam effects, and collective effects, etc., in order to search for possible optimal solutions.

## DESIGN CONSIDERATIONS

The following are the specific considerations and requirements.

### Luminosity

For fully symmetric flat electron-positron beam collisions, the relationship between luminosity and the associated parameters is illustrated in Fig. 1. One can see that the luminosity  $L$  is closely related to total beam current  $I$ , vertical beta function at IP  $\beta_y^*$ , vertical beam-beam parameter  $\xi_y$ , and hourglass factor  $F_h$  that is always less than 1. To achieve the goal luminosity of  $1.0 \times 10^{35} \text{ cm}^{-2}\text{s}^{-1}$  at the optimized beam energy of 2 GeV, the beam current of 2 A and submillimeter  $\beta_y^*$  of 0.6 mm are first identified, which suggests that  $\xi_y$  is at least larger than 0.07 assuming  $F_h$  to be 1. This also implies a limitation on the bunch length  $\sigma_z$  since  $\xi_y$  is inversely proportional to  $\sigma_z$  under a large Piwinski angle  $\phi$  with the total crossing angle of  $2\theta = 60 \text{ mrad}$ . Additionally, it is noted that the time resolution at the detector requires  $\sigma_z$  not larger than 12 mm.

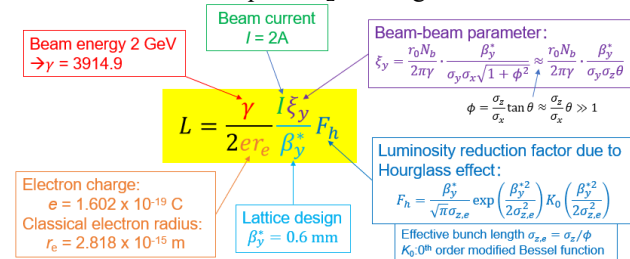


Figure 1: Luminosity and the correlated parameters.

### Coherent X-Z Instability

Coherent X-Z instability, as a newly discovered coherent beam-beam interaction under a large Piwinski angle, primarily leads to an increase in the horizontal emittance  $\epsilon_x$  [8]. Considering the coupling between horizontal and vertical emittances, it eventually results in an increase in the vertical emittance  $\epsilon_y$  and thus a collapse of the luminosity. This instability cannot be suppressed through beam feedback systems but can only be avoided through appropriate parameter optimization. Typically, a stringent

<sup>\*</sup> zhanglinhao@ustc.edu.cn

<sup>†</sup> jytang@ustc.edu.cn

<sup>‡</sup> luoqing@ustc.edu.cn

requirement of  $\xi_x \ll v_z$  is imposed to prevent its occurrence. In the case of STCF,  $v_z$  is at least 3 times larger than  $\xi_x$ .

### Lattice Design and Damping Wigglers

Lattice design is crucial for achieving high luminosity by ensuring the required optical parameters at IP and by optimizing nonlinear dynamics aperture. Additionally, it defines the momentum compaction factor  $\alpha_p$  and natural energy spread  $\sigma_\delta$  in the electron storage ring through five synchrotron radiation integrals. These parameters ( $\alpha_p$  and  $\sigma_\delta$ ) are of utmost importance in the longitudinal dynamics.

Particularly, the STCF needs to introduce damping wigglers to control the damping time and maintain beam emittance almost constant throughout the entire energy range. This inevitably increases the synchrotron radiation energy loss per turn, raising the demand for RF power, and also increases the natural energy spread, resulting in a proportional growth in bunch length. The lattice including damping wigglers has been designed for STCF [9].

### Non-impedance-induced Collective Effects

Non-impedance-induced collective effects mainly include the intrabeam scattering (IBS) and Touschek effect. IBS typically refers to multiple small-angle Coulomb scattering processes that do not immediately cause particle loss in the bunch but increase the equilibrium bunch length, energy spread and transverse emittances. On the other hand, the Touschek effect refers to single large-angle scattering processes that limit the lifetime of the stored beam (i.e., the Touschek lifetime). These two effects are directly related to the 6D phase-space size and thus associated with longitudinal parameters such as the bunch length. Bunch lengthening caused by a higher harmonic RF system and longitudinal impedance can help mitigate the IBS effect and improve the Touschek lifetime to some extent. In our case, the ELEGANT code [10] is used to calculate IBS and the Touschek lifetime.

### Impedance-induced Collective Effects

Impedance-induced collective effects on a single bunch are also crucial for determining the equilibrium bunch parameters. These effects include bunch lengthening due to potential well distortion (PWD), longitudinal microwave instability (LMWI), and transverse mode coupling instability (TMCI), as expressed below respectively:

$$\left(\frac{\sigma_z}{\sigma_{z0}}\right)^3 - \frac{\sigma_z}{\sigma_{z0}} = \frac{I_b \alpha_p}{\sqrt{2\pi} v_z^2 E / e} \left(\frac{R}{\sigma_{z0}}\right)^3 \text{Im}\left(\frac{Z_{||}}{n}\right)_{\text{eff}}, \quad (1)$$

$$I_b^{\text{LMWI}} = \frac{\sigma_z \sqrt{2\pi} \alpha_p E / e}{R |Z_{||}/n|_{\text{eff}}} \sigma_\delta^2, \quad (2)$$

$$I_b^{\text{TMCI}} = \frac{\sigma_z 4\sqrt{\pi} v_z E / e}{R \langle \beta \rangle \text{Im} Z_\perp^{\text{eff}}}, \quad (3)$$

where  $\sigma_{z0}$ ,  $R$ ,  $I_b$ ,  $\langle \beta \rangle$ ,  $\text{Im}(Z_{||}/n)_{\text{eff}}$ ,  $\text{Im} Z_\perp^{\text{eff}}$  are the natural bunch length at zero beam current, the average radius of ring, single-bunch current, the average beta function of

ring, the longitudinal normalized effective impedance and transverse effective impedance, respectively.

These three collective effects are all related to longitudinal parameters like the synchrotron tune and bunch length. Therefore, it is necessary to design the longitudinal parameters for STCF appropriately in order to control the bunch lengthening caused by PWD within 12 mm and to prevent the occurrence of LMWI and TMCI.

## LONGITUDINAL PARAMETER DESIGN

The above considerations can be divided into two categories: one is the input factors, including the transverse lattice design parameters (considering damping wigglers), requirements for coherent X-Z instability, and IBS; the other is the design optimization objectives, including the satisfaction of bunch length for luminosity and detector requirements (Goal 1), no occurrence of impedance-induced single-bunch collective instabilities (Goal 2), and a minimum Touschek lifetime of 300 s (Goal 3). Figure 2 illustrates the impact of these factors on longitudinal dynamics parameters and their interrelationships.

The design process is as follows: 1) Given the five synchrotron radiation integrals obtained from lattice design that includes damping wigglers, calculate the beam energy spread under the balance of radiation damping and quantum excitation; 2) Taking into account the requirements for coherent X-Z instability, compute the bunch length and synchrotron tune without considering IBS effects; 3) Incorporate radiation damping, quantum excitation, and IBS to obtain the new equilibrium energy spread and bunch length, and check if they meet Goal 1 and Goal 2; 4) Calculate the required RF voltage for achieving the new equilibrium bunch length and its corresponding RF energy acceptance (which should be greater than the momentum aperture from transverse dynamics tracking), and then evaluate the Touschek lifetime to check if Goal 3 is fulfilled.

To achieve the optimization objectives, adjustments may be required in the input constraint parameters. This can involve modifying the synchrotron tune, bunch length, and potentially lattice and damping wiggler parameters, to continue iterative optimization. It is important to prioritize beam stability (Goal 2) and achieving the luminosity target (Goal 1) when the three objectives cannot be simultaneously satisfied. Notably, the Touschek lifetime relies heavily on the optimization of transverse nonlinear dynamics, which is considered highly challenging for STCF[9].

After preliminary optimization, the longitudinal dynamics parameters for STCF have been initially determined. The bunch length is 8.04/8.94 mm (without/with IBS), the energy spread is 7.88/8.77 $\times 10^{-4}$  (without/with IBS), and the synchrotron tune is 0.0099. Correspondingly, the required RF voltage is 1.2 MV, providing the RF energy acceptance of 1.56%. Considering IBS, the luminosity can reach 1.45 $\times 10^{35}$  cm<sup>-2</sup>s<sup>-1</sup> with  $\xi_y = 0.111$ . Table 1 shows the main parameters of STCF at 2 GeV, along with a comparison to the main parameters of SuperKEKB LER.

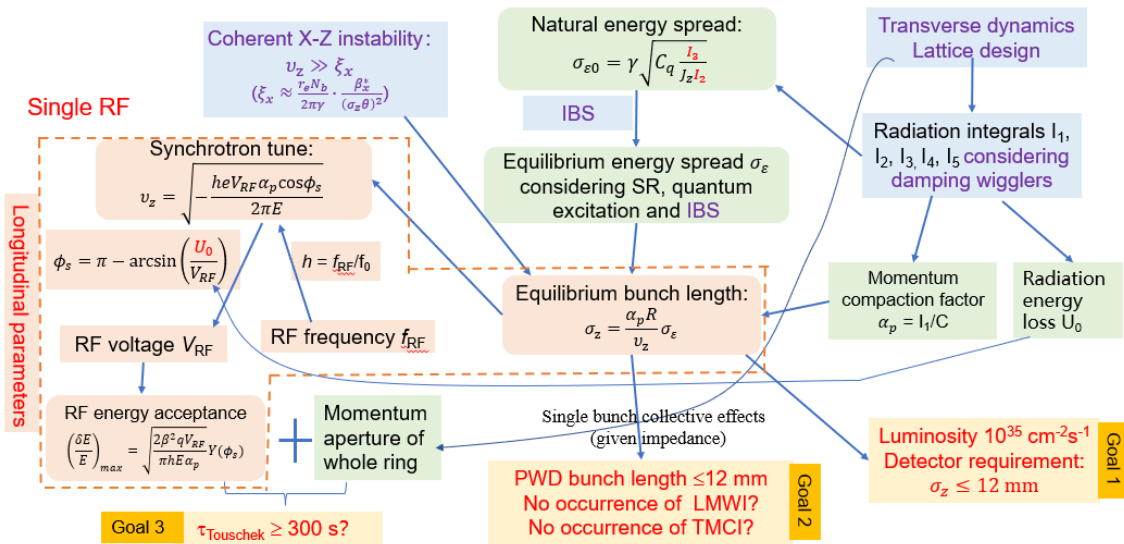


Figure 2: The interrelationships between different limiting factors and longitudinal dynamics parameters.

Table 1: Main Parameters of STCF in Comparison with SuperKEKB LER. Values in Parentheses Denote Parameters without IBS

Parameters	STCF	SuperKEKB LER
$E$ [GeV]	2	4
$C$ [m]	616.76	3016.315
$2\theta$ [mrad]	60	83
$\epsilon_x$ [nm]	4.47 (3.12)	3.2 (1.9)
$\beta_x^*/\beta_y^*$ [mm]	40/0.6	32/0.27
$\nu_x/\nu_y$	31.552/24.572	44.530/46.570
$\alpha_p$ [ $10^{-4}$ ]	10.27	3.25
$\sigma_\delta$ [ $10^{-4}$ ]	8.77 (7.88)	8.14 (7.96)
$I$ [A]	2	3.6
$n_b$	512	2500
$I_b$ [mA]	3.91	1.44
$U_0$ [keV]	273	1870
$\tau_x/\tau_z$ [ms]	30.1/15.0	43.2/21.6
$f_{RF}$ [MHz]	497.5	508.9
$h$	1024	5120
$V_{RF}$ [MV]	1.2	9.4
$\nu_z$	0.0099	0.0247
$\sigma_z$ [mm]	8.94 (8.04)	6.0 (5.0)
$\delta_{RF}$ [%]	1.56	2.52
$\xi_x/\xi_y$	0.0032/0.111	0.0028/0.083
$L$ [ $\text{cm}^{-2}\text{s}^{-1}$ ]	$1.45 \times 10^{35}$	$8 \times 10^{35}$

## EVALUATIONS AND DISCUSSIONS

### Impact on Lattice Design

To meet  $\xi_x \ll \nu_z$  required by coherent X-Z instability, simply optimizing the longitudinal dynamics is not sufficient. Therefore,  $\beta_x^*$  is reduced from the initial 90 mm to 40 mm to decrease  $\xi_x$ , which significantly reduces the

dynamic aperture and limits the lifetime. Thus, further iterative optimization will be necessary in the future.

### Beam-beam Effects

Beam-beam simulations indicate that by carefully selecting a suitable working point, the present parameter design can effectively mitigate coherent X-Z instability. Additionally, the simulated steady-state luminosity essentially meets the design objective.

### Collective Effects

PWD-induced bunch lengthening and LWMI are estimated under the assumption of  $\text{Im}(Z_{\parallel}/n)_{\text{eff}} = 0.1 \Omega$  that is a typical value for modern storage rings. The results indicate that the stretched bunch length is 12 mm, and the threshold bunch current for LWMI is about 4.8 mA, higher than the design bunch current of 3.9 mA.

The transverse effective impedance, approximately calculated as  $\text{Im}Z_{\perp}^{\text{eff}} = 2R/b^2 \cdot \text{Im}(Z_{\parallel}/n)_{\text{eff}}$  (the Panofsky-Wenzel theorem), is estimated to be 14 k $\Omega$ /m with the vacuum chamber half-aperture of  $b = 37.5$  mm. Accordingly, the threshold bunch current for TMCI is about 28.9 mA. Therefore, ordinary vacuum chamber impedance will not cause TMCI. However, further study is needed to determine if the addition of special components, especially collimators, will induce TMCI.

The assessment of coupled bunch instabilities driven by higher-order modes of the accelerating cavities and resistive-wall impedance is ongoing.

## SUMMARY

This paper introduces an optimization model of longitudinal dynamics design, which comprehensively considers the coherent X-Z instability, transverse dynamics, and collective effects. It provides crucial support for the physical design of STCF. Further iterative optimization is still needed, particularly in evaluating collective instabilities, including fast ion instabilities and electron cloud effects.

## REFERENCES

- [1] H.P. Peng, Y.H. Zheng, X.R. Zhou, “Super Tau-Charm Facility of China”, *PHYSICS*, vol. 49, no. 8, pp. 513-524, 2020. doi: 10.7693/wl20200803
- [2] M. Zobov, *et al.*, “Test of crab-waist collisions at DAΦNE  $\Phi$  factory”, *Phys. Rev. Lett.*, vol. 104, p. 174801, 2010.
- [3] K. Akai, *et al.*, “SuperKEKB collider”, *Nuclear Inst. and Methods in Physics Research, A*, vol. 907, pp. 188–199, 2018.
- [4] V. V. Anashin, A. V. Anisenkov, *et al.*, “Super Charm-Tau Factory Conceptual Design Report Part Two”, 2018.
- [5] A. Abada *et al.*, “FCC-ee: the Lepton Collider: Future Circular Collider Conceptual Design Report”, *Eur. Phys. J. Spec. Top.*, vol. 228, no. 2, pp. 261–623, 2019.
- [6] CEPC Study Group, “CEPC Conceptual Design Report. Volume I. Accelerator”, IHEP-CEPC-DR-2018-01, 2018.
- [7] K. Ohmi, *et al.*, “Coherent beam–beam instability in collisions with a large crossing angle”, *Phys. Rev. Lett.*, vol. 119, p. 134801, 2017.
- [8] Y. Zhang *et al.*, “Self-consistent simulations of beam-beam interaction in future  $e^+e^-$  circular colliders including beamstrahlung and longitudinal coupling impedance”, *Phys. Rev. Accel. Beams*, vol. 23, p. 104402, 2020.
- [9] T. Liu, C. Zhang, L. Wang, and Q. Luo, “Design of a hybrid seven-bend-achromat-based lattice for a super tau charm facility”, presented at the IPAC'23, Venice, Italy, May 2023, paper MOPL091, unpublished.
- [10] M. Borland, “elegant: a flexible sdds-compliant code for accelerator simulation”, Advanced Photon Source LS-287, September 2000.

# DEVELOPMENT STATUS OF BEAM DYNAMICS SOFTWARE APES FOR CEPC\*

Weibin Liu<sup>†1</sup>, Yuan Zhang<sup>1</sup>, Tianmu Xin, Zhe Duan, Zhiyuan Li<sup>1</sup>,  
Yaliang Zhao, Huiping Geng, Mengyu Su<sup>1</sup>, Yixian Dai<sup>1</sup>, Xiaohan Lu, IHEP, Beijing, China  
<sup>1</sup>also at UCAS, Beijing, China

## Abstract

The physical design and beam dynamics study of the Circular Electron Positron Collider (CEPC) is an unprecedented challenge. In the simulation studies to evaluate its performance limitations and mitigation, the cross-talk between many physical phenomena must be properly modelled, including the crab-waist collision scheme with a large Piwinski angle, strong nonlinear effects, the energy sawtooth, beam-beam interactions, machine impedances, etc. To address this challenge, a software project APES was proposed in 2021 and received support from the IHEP Innovative Fund in 2022. The progress of the APES project are described in this paper.

## INTRODUCTION

The CEPC was first proposed as a circular Higgs factory in 2012 and the conceptual design report was published in 2018 [1]. FCC-ee is a similar project proposed in CERN. During the design of these future colliders, the beam lifetime limitation due to the beamstrahlung effect, the synchrotron radiation induced by collision leading to a bunch lengthening and an increase in the beam energy spread, has been found and studied [2]. Different from conventional colliders, not only the transverse beam size, but also the longitudinal dynamics would be clearly influenced by the collision. That is why the 3D flip-flop instability may appear in CEPC or FCC-ee [3].

There would also be strong synchrotron radiation in the arc bending magnets of the machines, leading to a substantial “sawtooth”-shape variation of the central beam energy along the ring, which is the so-called sawtooth effect. The magnet tapering method has been proposed to mitigate this effect [4]. This requires new optics calculation method to consider the energy change along the ring.

After the crab-waist scheme was proposed around 2006 [5], the new collision scheme has become the baseline design for the following high performance circular e+e- colliders. However sub-millimeter scale  $\beta_y^*$  in future machines would induce strong lattice non-linearity and a very small dynamic aperture. During the lattice design and optimization, it has been found that the short-term dynamic aperture tracking could not predict the long-term beam lifetime [6].

In recent years, a new horizontal coherent beam-beam instability (X-Z instability) has been found [7]. The following simulation and analysis also show that the potential-well distortion effect would impact the behaviour of X-Z instability

clearly [8,9]. This tells us the cross-talk between beam-beam and longitudinal impedance could not be ignored.

Apart from these novel effects uncovered in the design study of CEPC and FCCee, the commissioning of SuperKEKB also reveal that there is still a gap in the modelings and simulations to explain and mitigate the difficulties in the practical machine tunings [10]. These have told us that the beam dynamics of future e+e- colliders would be very challenging.

A beam dynamics software project “APES” (Accelerator Physics Emulation System) has been proposed, with an objective to address the beam physics issues in CEPC in a unified, extendable manner:

- The modeling of the collider, especially the complicated interaction region and the cross-talk of common hardware shared by the two rings.
- Lattice design and performance evaluation, including symplectic tracking, optics calculation/matching, emittance calculation, modeling of the sawtooth and tapering effect, analysis of nonlinear optics performance, spin dynamics evaluation, machine error effects and correction algorithms, multi-objective optimization etc.
- Performance evaluation/prediction of the collider, the cross-talk between realistic lattice, beam-beam interaction, spin, collective effects and necessary hardware modeling.
- Interface with detector (MDI) and machine protection (particle-matter interaction), easy access and interaction with software dedicated for these purposes.

These functionalities and features will empower users to design, analyze, and optimize accelerator systems with greater accuracy and efficiency. Additionally, we can foresee several potential applications when these capabilities have been fully developed:

- Tracking simulations to evaluate the luminosity and beam lifetime with the realistic lattice and the strong-strong beam-beam interaction, as well as impedance effects.
- Simulations of the injection process, to evaluate the injection efficiency in the presence of machine imperfections, beam-beam interaction and impedance effects, and to prepare beam loss information for the design of collimators and evaluation of the influence to the detectors.

\* Work supported by IHEP Innovative Fund

<sup>†</sup> liuw@ihep.ac.cn

## SOFTWARE PROGRESS

As mentioned earlier, APES is a comprehensive accelerator simulation software that will entail intricate accelerator modeling, intensive computation, and extensive data processing. Additionally, we will face challenges such as integrating various software, facilitating cross-platform usage, and enabling collaborative development among multiple individuals. Python, being a rapidly growing programming language in recent years, offers numerous advantages for coding and future development. It is known for its ease of learning, versatility, powerful standard library, rich ecosystem of third-party libraries and frameworks, and cross-platform compatibility. Moreover, there has been a significant trend of using Python in both domestic and international accelerator software development this year. Therefore, we have chosen Python as the foundation for our software development.

### Framework of APES

In the APES package, a foundational set of classes has been constructed to form the core of the entire framework. The hierarchical structure of APES is depicted in Figure 1. This section primarily focuses on elucidating the fundamental logical pathway that underpins the design of this framework. For further details regarding the technological implementation and hierarchical relationships among classes please refer to related chapters in the code manual.

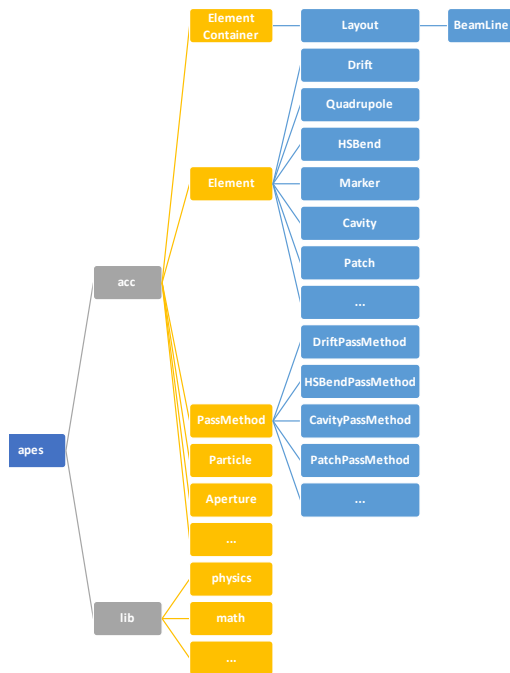


Figure 1: APES Hierarchical Structure Diagram.

**Local Frame** Within an accelerator, as a particle traverses through various components, it encounters fields in the local frame of each element. Consequently, the dynamics of the particle are articulated within these local frames.

Presently, in APES, each element is associated with two reference frames - the entrance frame and the exit frame (Figure 2).

**Global Frame** As the name suggests, the Global Frame serves as a reference for delineating the relative positions of various entities, such as elements and particles, within the overarching framework of the accelerator (Figure 2).

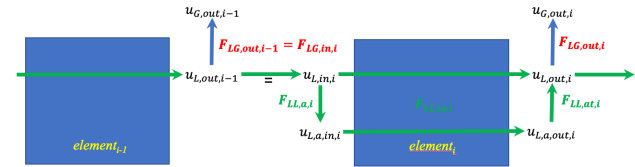


Figure 2: Element Coordinate Transformation Diagram.

- u: coordinates
- F: coordinate transformation
- i: element index
- L: Local frame
- G: Global frame
- in: at the entrance of the element
- out: at the exit of the element
- LG: from local frame to global frame
- io: from the entrance to the exit of the element
- ta: from ideal frame to actual frame
- at: from actual frame to ideal frame

**Patch** To facilitate tracking of a particle as it navigates through individual elements of the accelerator, geometric transformations between different frames are imperative. In APES, these transformations are termed as “Patches”. A Patch is essentially an affine transformation applied to the particle’s coordinates, comprising translation and rotation components. Typically, each element is equipped with at least two Patches – one that addresses the transformation from the exit frame of the preceding element to its own entrance frame, and another to handle the transformation between its exit frame and the next element entrance frame. To enhance practicality, distinct Patches are employed to describe transformations between frames arising from different sources, such as frame shifts due to specialized installations or misalignments due to installation errors.

**Element** The concept of the Element has been mentioned but yet to be defined. In the code of APES, an element is a base class that contains some universally useful attributes and methods when deriving specific type of element from it. At this stage, the element class contain its own set of patch generator. Namely it can handle the transformation between the ideal and real entrance local frame, the one between the entrance and exit frame, and the one between the real and ideal exit frame. Together with the transfer map of each subclasses derived from the element class, the chain of patches and maps will form the main stream of operations the particles need to go trough during the tracking process.

**Element Container** For the construction of the accelerator within the Global Frame, an additional class termed “Element Container” is employed to augment the capabilities of the basic Element class. This grants users greater control and flexibility in manipulating elements (e.g., modifying surveys, scaling strengths, or altering species and directionality). The Element Container class exhibits three distinct functionalities. First, it maintains a table of “Instances” and acts as a “Container”. Instances can be a composite of elements, element containers, or patches that represent groups of entities assembled for various purposes. Secondly, it employs Patches to establish bidirectional connections between the Global Frame and the Element’s Local Frame. Lastly, the Element Container provides users with the ability to manipulate various parameters of the elements encompassed within its scope. Figure 3 portrays a conceptual illustration of the Element Container using a simplified cell to depict how a dipole element is encapsulated within its container. In basic applications, the containerization is largely automated, minimizing the necessity for user intervention

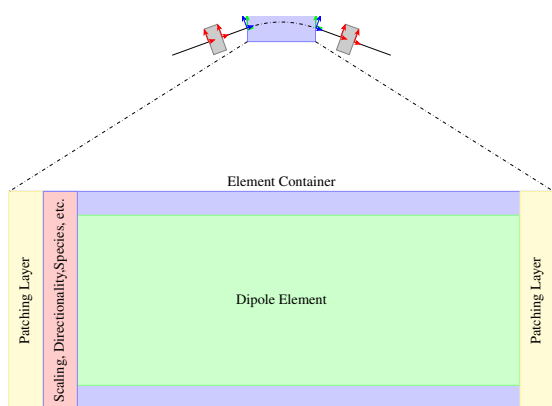


Figure 3: Cartoon illustration to the concept of element and element container.

**Layout** As a subclass derived from the ElementContainer class, an additional class called “Layout” has been established. The Layout class is designed with two primary objectives in mind. The first objective is to compute the survey information of the elements within the Global Frame. The second objective involves generating an “element table” which will be indispensable for future particle tracking.

To construct the accelerator, the current methodology involves adding entities to the “table” attribute of a Layout object. These entities can be elements, element containers, or patches, which can be added using the “append” or “insert” methods. Python’s reference passing strategy proves to be particularly advantageous in this context, as it enables the seamless addition of the same instance to different sections of the layout, while managing their relative positions through patches.

**BeamLine** The “BeamLine” class plays a critical role in encapsulating the information extracted from Layout.table. Through the BeamLine class, a streamlined and concise table is produced, from which a sequence of maps is generated. These maps are integral to the process as they guide the path that particles will follow during the tracking phase.

In essence, the BeamLine class acts as a repository for the refined information drawn from the Layout class, ensuring that only the pertinent data required for particle tracking is retained in an organized manner. This, in turn, facilitates a more efficient and streamlined tracking process.

Some commonly used calculations are encapsulated in the BeamLine class, such as Jacobian Matrix calculation, closed orbit calculation, Twiss calculation, etc. And more functionalities will be added soon.

### PassMethod

The “PassMethod” class serves as the fundamental class for calculations, with specific subclasses created for each component type, including DriftPassMethod, QuadrupolePassMethod, HBendPassMethod, PatchPassMethod and others. These subclasses assign tracking maps for each element type. During optics calculations or particle tracking, a list of PassMethod instances is automatically generated. In principle, the pass method for any element can be freely configured.

### Tracking Map of APES

The design of colliders requires accurate symplectic map of magnets to ensure right beam dynamics result. Due to very small  $\beta_y^*$ , the non-linearity of drift must be considered in modern/future high-performance e+ e- colliders. Non-linear Maxwellian fringe field of magnets should also be considered. Currently, the program has implemented maps of drifts, dipoles, quadrupoles, sextupoles, octupoles, RF-cavities, solenoids, multipoles and more referring to the method of SAD [11]. It supports the modeling of hard and soft edge fringe fields of magnetic elements, tilted strong solenoids for particle detection in interaction regions (IRs), and the handling of combined solenoid/multipole elements. What’s more, there is an optional map for the patch according to Etienne Forest. [12]. Initial benchmark tests comparing with SAD have proved the high accuracy of particle tracking using SuperKEKB lattice. The synchrotron radiation effect has not been included so far.

Currently the tracking map section is implemented in C language for optimized computational speed, building upon previous work. It is utilized through efficient function calls.

### Beam Optics Calculation

The APES package has recently been enhanced with several important functionalities. These additions encompass various capabilities, including closed orbit calculation for a ring, Jacobian Matrix calculation, Twiss parameters calculation, and emittance calculation, among others. Additionally, there are ongoing developments for some important features.

For instance, there are two method for emittance calculation. One is the SLIM method published by Alexander W. Chao [13] and another one is the envelope matrix method published by K. Ohmi [14]. Specially for SLIM, we found that the dependence on transverse coordinates of radiation emitted in dipole was not mentioned in the paper, and this effect would be significant when some parameters are unusual. After modification, the emittance and the damping rate given by SLIM and by the envelope matrix method are reasonable compared with the exiting code, such as SAD.

## APPLICATION EXAMPLES

We have completed the main components of the APES Framework and have added several beam physics calculation functionalities. Below are some examples of using APES.

### Layout Modeling

Creating a layout is the initial step in simulating an accelerator. The following code demonstrates the process of defining elements and creating the layout for BEPCII BPR. The Affine transformation startAT establishes the initial coordinate system direction for the BPRLayout. This transformation is utilized to calculate the BPR survey. Subsequently, some elements are defined. BPRList stores all the elements in a specific order and is employed to define the BPRLayout. Figure 4 displays a portion of the element information and survey data for BPR, while Figure 5 shows the layout plotted using APES based on the survey data.

```

1 from apes.acc.Layout import *
2 from apes.acc.Element import *
3 from apes.acc.Particle import *
4 from apes.lib.math.AffineTransformation import *
5 ...
6 ...
7 initRotate = -0.011
8 startAT = AT.createAT(azimuth=initRotate)
9
10 IP = Marker('IP')
11 R4CBPM00 = Marker('R4CBPM00')
12
13 D4I01 = Drift('D4I01', length=0.539)
14 D4I01P = Drift('D4I01P', length=0.370)
15 ...
16 PSCQ4I=Patch.createPatch('PSCQ4I', azimuth=
17     initRotate, dx=0.0099988)
18 ...
19 SSCQI = Quadrupole('SSCQI', length=0.59989336,
20     k1=-1.073308053)
21 SSCQ0 = Quadrupole('SSCQ0', length=0.59989335,
22     k1=-1.073308053)
23 ...
24 R4ISPB = HSBend('R4ISPB', length=0.600669, angle=
25     -0.03951362, anglein=-0.01975681, angleout
26     =-0.01975681)
27 R4IMB = HSBend('R4IMB', length=1.034466, angle=
28     -0.113089342, anglein=-0.056544671, angleout
29     =-0.056544671)
30 ...
31 BPRList = [IP, D4I01, R4CBPM00, D4I01P, PSCQ4I,
32     SCQI, ...]

```

```

BPRLayout = Layout('BPR', entryLGCT=startAT,
    elementList=BPRList)
surveytable = BPRLayout.getSurveyTable(level=1)
print(surveytable)

```

Name	Type	Length	Xout	Yout	Zout	Pitchout	Yawout	Rollout	Element	
0	__BPR_Start__	Marker	0.000	0.000	0.000	0.000	-0.000	-0.011	-0.000	<apes.acc.Element.Marker object at 0x787283ad...>
1	IP	Marker	0.000	0.000	0.000	0.000	-0.000	-0.011	-0.000	<apes.acc.Element.Marker object at 0x78725a50...>
2	D4I01	Drift	0.539	0.006	0.000	0.539	-0.000	-0.011	-0.000	<apes.acc.Element.Drift object at 0x7872594c668>
3	R4CBPM00	Marker	0.000	0.006	0.000	0.539	-0.000	-0.011	-0.000	<apes.acc.Element.Marker object at 0x78725a50...>
4	D4I01P	Drift	0.370	0.010	0.000	0.909	-0.000	-0.011	-0.000	<apes.acc.Element.Drift object at 0x78724341908>
5	P_SCQ_4I	Patch	0.000	-0.000	0.000	0.909	-0.000	0.000	-0.000	<apes.acc.Element.Patch object at 0x787256c6da0>
6	SSCQI	Quadrupole	0.600	-0.000	0.000	1.509	-0.000	0.000	-0.000	<apes.acc.Element.Quadrupole object at 0x7872...>
7	P_SCQ_4O	Patch	0.000	0.021	0.000	1.509	-0.000	-0.026	-0.000	<apes.acc.Element.Patch object at 0x7872170a160>
8	D4I02	Drift	0.641	0.038	0.000	2.150	-0.000	-0.026	-0.000	<apes.acc.Element.Drift object at 0x7872594c828>
9	R4IBPM00	Marker	0.000	0.038	0.000	2.150	-0.000	-0.026	-0.000	<apes.acc.Element.Marker object at 0x78725a60...>
10	D4I02P	Drift	0.150	0.042	0.000	2.300	-0.000	-0.026	-0.000	<apes.acc.Element.Drift object at 0x7872594c978>
11	R4ISPB	HSBend	0.601	0.070	0.000	2.900	-0.000	-0.066	-0.000	<apes.acc.Element.HSBend object at 0x78720e77...>
12	D4I03	Drift	0.624	0.111	0.000	3.523	-0.000	-0.066	-0.000	<apes.acc.Element.Drift object at 0x7872594ca8c>
13	R4IQ1A	Quadrupole	0.254	0.127	0.000	3.776	-0.000	-0.066	-0.000	<apes.acc.Element.Quadrupole object at 0x7872...>
14	D4I04	Drift	0.174	0.139	0.000	3.950	-0.000	-0.066	-0.000	<apes.acc.Element.Drift object at 0x7872594cc18>
15	R4IBPM01	Marker	0.000	0.139	0.000	3.950	-0.000	-0.066	-0.000	<apes.acc.Element.Marker object at 0x78725a60...>
16	D4I05	Drift	0.068	0.143	0.000	4.018	-0.000	-0.066	-0.000	<apes.acc.Element.Drift object at 0x7872594cd58>
17	R4IQ1B	Quadrupole	0.464	0.174	0.000	4.481	-0.000	-0.066	-0.000	<apes.acc.Element.Quadrupole object at 0x7872...>
18	D4I06	Drift	1.221	0.254	0.000	5.700	-0.000	-0.066	-0.000	<apes.acc.Element.Drift object at 0x7872594ceb8>
19	R4IBV02	Drift	0.000	0.254	0.000	5.700	-0.000	-0.066	-0.000	<apes.acc.Element.Drift object at 0x78725992ac8>

Figure 4: Layout Table of BEPCII BPR.

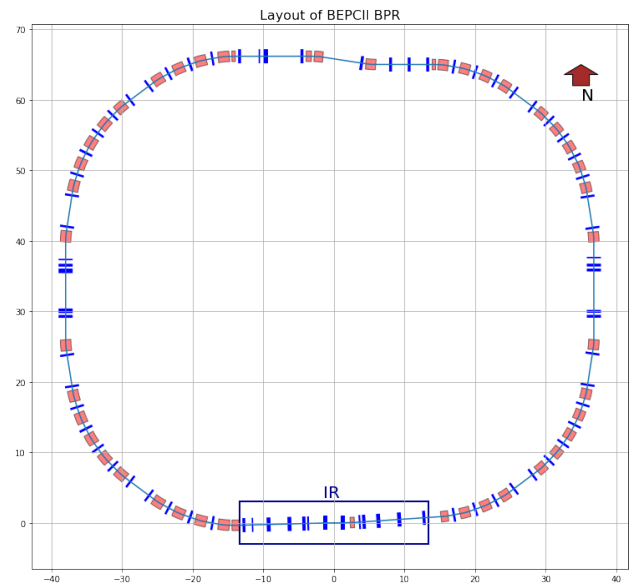


Figure 5: Layout of BEPCII BPR.

### Modeling for Special Cases

With the assistance of Patch, modeling certain special cases becomes much simpler. Here is an example of modeling interaction region of Beijing Electron Positron Collider (BEPCII). BEPCII is an asymmetric double-ring collider. The layout of positron ring (BPR) is shown in Figure 5. The electron and positron beams have a cross angle at the interaction region. There are superconducting quadrupoles (SCQs) on each side of the interaction point. Electron and positron beams pass SCQ off centre. The traditional method for dealing with this situation involves treating SCQ as a combined magnet of bend and quadrupole, which can be inconvenient for creating a lattice. However, with the introduction of APES, a new approach has been implemented

Content from this work may be used under the terms of the CC BY 4.0 licence (© 2023). Any distribution of this work must maintain attribution to the author(s), title of the work, publisher, and DOI

(Figure 6). We added one patch element before the SCQ and another after the SCQ to realize the the layout and lattice. When positron beam leaving the interaction point, the beam has a 11 mrad horizontal angle before entering the SCQ. The first patch element rotates the beam coordinate system by -11 mrad and then shifts it horizontally towards the center line of SCQ. This converts the coordinates of the positron particles to the SCQ coordinate system. The beam then passed through SCQ quadrupole. At the exit of SCQ, the second patch element shifts the coordinate system origin to the beam exit position on the exit plane of the SCQ. Then the coordinate system is rotated horizontally to align the longitudinal axis with the center line of the next element. By implementing these patch elements, the inconvenience of creating a lattice with the SCQs can be overcome.

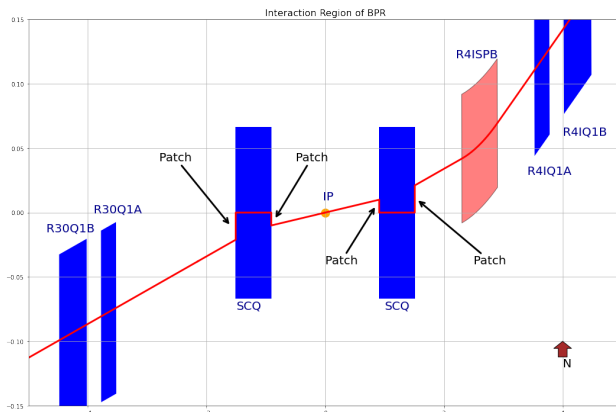


Figure 6: Interaction Region of BEPCII BPR.

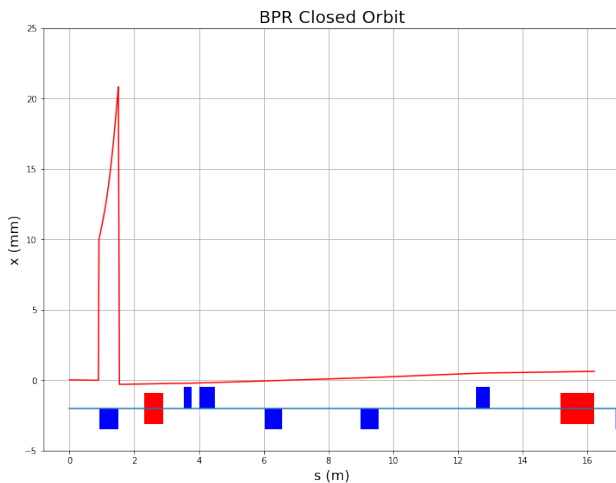


Figure 7: BEPCII BPR Horizontal Closed Orbit in IR.

### Beam Line

When a layout of a lattice is created, the BeamLine can be get easily. The following code defines a reference particle of Positron and generates a BeamLine using the previously defined BPRLayout. Certain parameters are specified: *isRing=True* indicates that the BeamLine is a ring, and a

dictionary is assigned to *paraDict*, with some elements in the dictionary being divided into 10 slices for calculation. With this BeamLine, further beam optics calculations can be performed. Figure 7 depicts the closed orbit of the BEPCII BPR in the interaction region, computed using APES. The left side of the figure provides a clear representation of the orbit in the SCQ.

```
1 refParticle = Positron(P=1.89E9)
2 beamline = BPRLayout.getBeamLine('BPR',
   refParticle=refParticle, isRing=True,
   checkRing=True, paraDict={'D4I02': {'Slice':
   10}, 'D3002': {'Slice': 10}})
```

### Alignment Error

With the introduction of the Patch class and its pass method, handling element misalignment becomes significantly simpler. The alignment error can be assigned during the element definition or specified at a later stage. During survey or optics calculations, the alignment error is treated as two patches, as mentioned above. The following code snippet demonstrates how the BEPCII positron transfer line is managed in the presence of misalignment. First, an affine transformation that includes rotation and translation is defined to represent the misalignment of the TCQ1. Then, the alignment error of TCQ1 is updated. The same treatment is applied to the other elements as well. By activating the alignment error switch, a BeamLine that includes alignment errors is obtained. Finally, the optics calculation is performed. Figure 8 illustrates the horizontal orbit of the BEPCII e+ transport line affected by the misalignment without orbit correction.

```
1 ...
2 tcq1AT = AT.createAT(elevation=ax, azimuth=ay,
   tilt=az, dx=dx, dy=dy, dz=dz)
3 TCQ1.update({'inAlignmentLLCT': tcq1AT})
4 ...
5 beamline = TPLayout.getBeamLine('TP',
   refParticle=refParticle, isRing=False,
   alignmentError=True)
6 result = beamline.calBeamLineTwiss(X0=np.zeros
   (6), betax=12.5, alphax=0, betay=12.5,
   alphas=0)
7 ...
```

## SUMMARY

APES has made significant progress by completing the initial framework, which includes preliminary accelerator design and computational capabilities. Furthermore, there are plans to gradually incorporate more accelerator physics calculation features.

## ACKNOWLEDGEMENTS

The authors would like to thank K. Ohmi, D. Zhou, K. Oide and E. Forest for their support and fruitful discussions. This project is supported by IHEP Innvation Study.

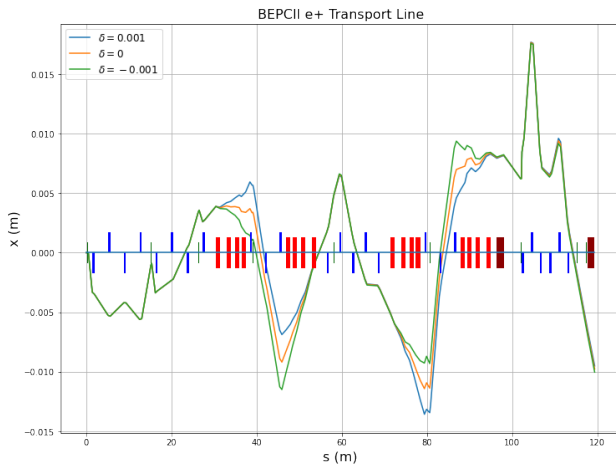


Figure 8: BEPCII e+ Transport Line Horizontal Orbit with Alignment Errors measured in the summer of 2022.

## REFERENCES

- [1] CEPC Study Group, “CEPC Conceptual Design Report: Volume 1 - Accelerator”.  
doi:10.48500/arXiv.1809.00285
- [2] V.I. Telnov, “Restriction on the energy and luminosity of  $e^+e^-$  storage rings due to beamstrahlung”, *Phys. Rev. Lett.*, vol. 110, p. 114801, 2013.  
doi:10.1103/PhysRevLett.110.114801
- [3] D. Shatilov, “FCC-ee Parameter Optimization”, *ICFA Beam Dyn. Newsl.*, vol. 72, p. 30, 2017.
- [4] K. Oide *et al.*, “Design of Beam Optics for the Future Circular Collider e+e- Collider Rings”, *Phys. Rev. Accel. Beams*, vol. 19, p. 111005, 2016.  
doi:10.1103/PhysRevAccelBeams.19.111005
- [5] P. Raimondi, “Introduction to Super B-Accelerators”, presented at the 2nd Workshop on Super B-Factory, Frascati, Italy, Mar. 2006.
- [6] J. Wu *et al.*, “Dynamic aperture optimization with diffusion map analysis at CEPC using differential evolution algorithm”, *Nucl. Instr. and Meth. A*, vol. 959, p. 163517, 2020.  
doi:10.1016/j.nima.2020.163517
- [7] N. Kuroo *et al.*, “Cross-wake force and correlated head-tail instability in beam-beam collisions with a large crossing angle” *Phys. Rev. Accel. Beams*, vol. 21, p. 031002, 2018.  
doi:10.1103/PhysRevAccelBeams.21.031002
- [8] Y. Zhang *et al.*, “Self-consistent simulations of beam-beam interaction in future  $e^+e^-$  circular colliders including beamstrahlung and longitudinal coupling impedance”, *Phys. Rev. Accel. Beams*, vol. 23, p. 104402, 2020.  
doi:10.1103/PhysRevAccelBeams.23.104402
- [9] C. Lin, K. Ohmi, and Y. Zhang, “Coupling effects of beam-beam interaction and longitudinal impedance”, *Phys. Rev. Accel. Beams*, vol. 25, p. 011001, 2022.  
doi:10.1103/PhysRevAccelBeams.25.011001
- [10] D. Zhou *et al.*, “Simulations and experimental results of beam-beam effects in SuperKEKB”, Accepted by *Phys. Rev. Accel. Beams*.
- [11] <https://acc-physics.kek.jp/SAD/>
- [12] E. Forest *et al.*, “The correct local description for tracking in rings”, Accepted by *Gordon and Breach Science Publishers, S.A.*
- [13] Chao A. W. , “Evaluation of beam distribution parameters in an electron storage ring”, *Journal of Applied Physics*, vol. 50, no. 2, pp. 595–598, 1979.
- [14] K. Ohmi *et al.*, “From the beam-envelope matrix to synchrotron-radiation integrals”, *Physical Review E*, vol. 49, pp. 751–765, 1994.

# PHYSICAL DESIGN FOR EEHG BEAMLINES AT S<sup>3</sup>FEL

Li Zeng, Xiaofan Wang\*, Yifan Liang, Huaiqian Yi, Weiqing Zhang<sup>1†</sup>, Xueming Yang<sup>2</sup>

Institute of Advanced Science Facilities, Shenzhen, China

<sup>1</sup>also at Dalian Institute of Chemical Physics, CAS, Dalian, China

<sup>2</sup>also at Southern University of Science and Technology, Shenzhen, China

Chao Feng, Zhen Wang

Shanghai Advanced Research Institute, CAS, Shanghai, China

Yong Yu, Jitao Sun, Xinmeng Li

Dalian Institute of Chemical Physics, CAS, Dalian, China

## Abstract

The proposed Shenzhen Superconducting Soft X-Ray Free-electron Laser (S<sup>3</sup>FEL) aims at generating FEL pulses from 1nm to 30nm. At phase-I, two undulator beamlines work at echo-enable harmonic generation (EEHG) principle. The two undulators will cover the spectral ranges 2.3-15 nm (~ 83-539 eV) and 5-30 nm (~ 41-248 eV), respectively, when receiving electrons from 2.5 GeV superconducting linac. However, the generated FEL radiation is sensitive to various electron beam properties, e.g., its energy profile influenced by collective effects such as Coherent Synchrotron Radiation (CSR), especially at high harmonics. To generate intense full coherent FEL radiation at ultra-short wavelength, a novel technique of EEHG cascaded harmonic lasing method is also considered. Physical design and FEL performance are described in this paper.

## INTRODUCTION

The proposed Shenzhen Superconduction Soft X-Ray Free-electron Laser (S<sup>3</sup>FEL) [1] is a high repetition rate FEL facility that consist of a 2.5 GeV CW superconducting linac and four initial undulator lines, which aims at generating X-rays between 40 eV and 1 keV at rates up to 1 MHz.

Two undulator beamlines (FEL-3 and FEL-4) work at echo-enable harmonic generation (EEHG) [2] principle which has the major advantage of full coherence, precisely arrival time control, uniform longitudinal profile and so on. The shortest wavelength is about 2.3 nm at a harmonic over one hundred. Since the various collective effects, the degrading of FEL performance becomes severer at such high harmonic number. One possible solution is adapting a novel technique called EEHG cascaded harmonic lasing method. This paper presents the detailed FEL simulation results for start-to-end electron beam coming from the superconducting linac.

## FEL PERFORMANCE

The basic electron beam parameters after linac are listed in Tabel 1. The slice parameters of the start-to-end electron beam are shown in Fig. 1. The core of the bunch has rela-

tively flat energy and current with normalized emittance of about 0.5 mm-mrad.

Table 1: Electron Beam Parameters

Parameter	Value	Unit
Beam energy	2.5	GeV
Slice energy spread	200	keV
Peak current	800	A
Charge	100	pC
Normalized emittance	0.5/0.5	mm·mrad

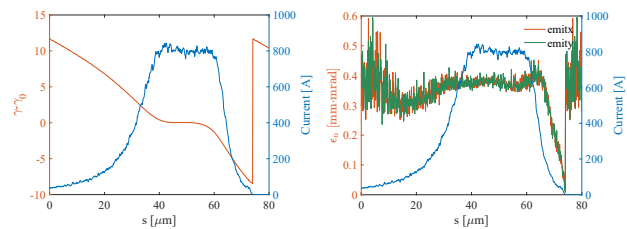


Figure 1: Beam energy (left), normalized emittance (right) and current (blue) of the electron beam.

The parameters of undulator beamlines and seed lasers are listed in Table 2. The FEL simulations are performed with electron beam after corresponding beam transport line and carried out by the time-dependent mode of GENESIS [3].

Table 2: Undulator Beamlines, Seed Lasers (SL) Parameters

Parameter	FEL-3	FEL-4
FEL wavelength [nm]	2.3-15	5-30
Undulator type	PMU	PMU+EPU
Undulator period [mm]	43	50
SL wavelength [nm]	266.7/240-267	266.7/240-267
SL pulse length [fs]	100	100
SL peak power [MW]	>200	>200
SL Rayleigh length [m]	1.0	1.0

### FEL-3 (EEHG, 2.3–15 nm)

FEL-3 generates FEL radiation from 2.3 nm to 15 nm, covering the entire water window (2.3-4.4 nm).

\* wangxf@mail.iasf.ac.cn

† weiqingzhang@dicp.ac.cn

The layout and  $\beta$ -function of 2.3nm@FEL-3 is shown in Fig. 2. Using the optimized EEHG parameters [4], the bunching at radiator entrance is nearly 6%. This is sufficient to achieve saturation of the FEL power at 2.3 GW already after 6 undulators, as show in Fig. 3. Figure. 3 also shows the FEL spot after radiator as well as the power profile and spectrum at saturation. The pulse duration is about 47 fs while the bandwidth of spectrum is close to 0.012 %. The transverse spot size is about 500  $\mu\text{m}$  and the transverse divergence is 6.7  $\mu\text{rad}$  at the end of the radiator.

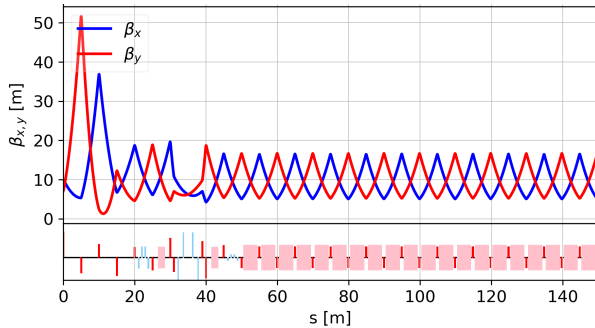


Figure 2: The layout of 2.3nm@FEL-3.

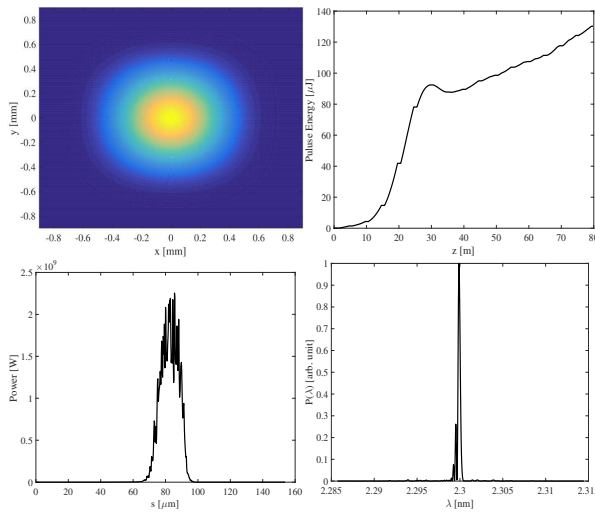


Figure 3: Simulation results of 2.3nm@FEL-3.

As for the 15 nm case at FEL-3, the saturation power is about 5.7 GW after 10 m of amplification. The pulse energy is around 360  $\mu\text{J}$  with a pulse duration of 60 fs. The bandwidth of spectrum is 0.057 %, indicating a nearly transform-limited pulse. The transverse spot size and divergence are about 1 mm and 45  $\mu\text{rad}$  after the radiator.

### FEL-4 (EEHG, 5–30 nm)

FEL-4 also operates in EEHG mode and generates FEL radiation between 5 nm and 30 nm, corresponding to a photon energy of 41-248 eV. It can provided fully coherent extreme ultraviolet (EUV) and X-ray beams with full wavelength and polarization tunability.

Figure 4 shows the layout and  $\beta$ -function of 5 nm@FEL-4. The maximum bunching factor is 10% at the entrance of undulator after optimization. The FEL pulse reaches saturation after 20 m of amplification, while pulse energy is nearly 226  $\mu\text{J}$ . The power profile and spectrum at saturation are also shown in Fig. 5. The pulse duration is about 55 fs with a spectrum bandwidth around 0.023 %. At the exit of the radiator, the transverse spot size and divergence are 760  $\mu\text{m}$  and 12.4  $\mu\text{rad}$ , respectively.

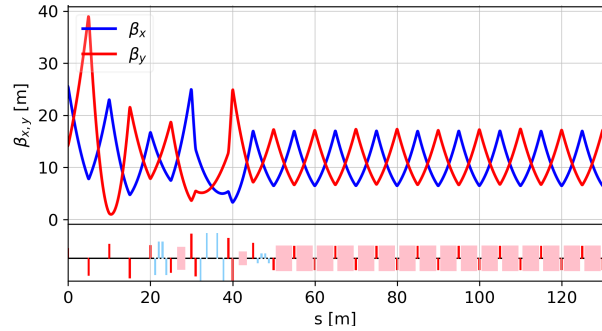


Figure 4: The layout of 5nm@FEL-4.

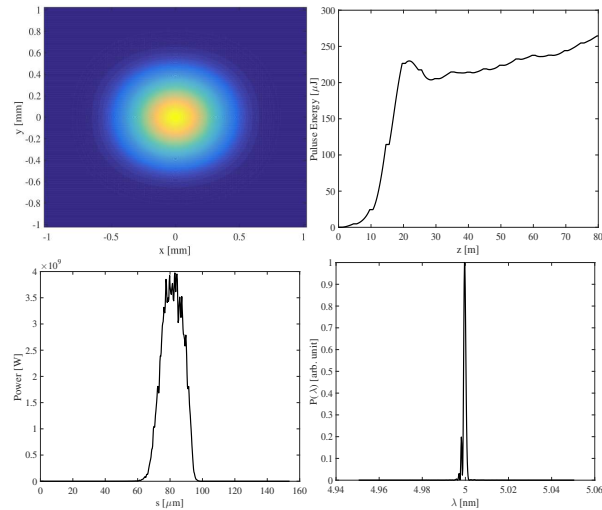


Figure 5: Simulation results of 5nm@FEL-4.

In the case of 30nm@FEL-4, the saturation peak power is about 6.0 GW after 2 undulators. The pulse energy at saturation is 348  $\mu\text{J}$  with a pulse duration of 57 fs. The FEL spectrum has a bandwidth of 0.112 % and the TBP is about 0.64. The transverse spot size and divergence are 1.3 mm and 70  $\mu\text{rad}$  at the exit of radiator.

## COLLECTIVE EFFECTS

### Coherent Synchrotron Radiation (CSR)

The strong chicane needed in the first dispersion section makes the system vulnerable to the CSR effect. Besides increasing emittance and energy spread, CSR also imprints a long-wavelength energy modulation on the electron bunch. Such energy modulation will interfere with bunching pro-

cess, which eventually leads to a loss of longitudinal coherence [5]. Taking 2.3nm@FEL-3 as an example, the simulation results have been illustrated in Fig. 6. The bunching factor decrease to 2.5% and the saturation length is slightly increased.

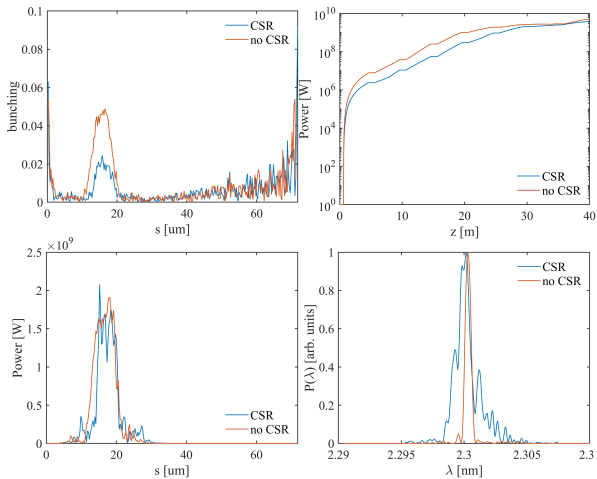


Figure 6: The influence of CSR on EEHG.

### Incoherent Synchrotron Radiation (ISR)

Despite of the CSR, the ISR effect induced by the strong chicane will also smear the fine structure of the longitudinal phase space. The ISR quantum diffusion induced energy spread growth can be written as [6]

$$(\sigma_{\Delta E})_{ISR} = \left[ \frac{7\hbar}{15mc} L r_c \gamma^4 k_\omega^3 K_\mu^2 F(K_\mu) \right]^{-1/2}, \quad (1)$$

where  $r_c$  is the classical radius of electron,  $k_\omega$  and  $K_\mu$  denote the undulator wave-number and the strength of undulator, respectively.  $F(K_\mu) = 1.2K_\mu + 1/(1 + 1.33K_\mu + 0.4K_\mu^2)$ . According to the parameters at S<sup>3</sup>FEL, the ISR-induced quantum diffusion effect is calculated about 12.7 eV, which is much smaller than the spacing of adjacent energy bands (~70 keV) and therefore negligible.

### Intra-Beam Scattering (IBS)

IBS describes multiple Coulomb scattering in the electron beam, which leads to an increasing in electron beams size and energy spread. The IBS-induced energy spread growth can be expressed as [7]

$$(\sigma_{\Delta E})_{IBS} \approx \left( 2\pi^{3/2} \ln \Lambda r_c \frac{I}{I_A} \frac{1}{4\pi\sigma_x^3} \frac{\beta_x}{\gamma} s \right)^{1/2} E_0, \quad (2)$$

where  $I$  denotes the beam current,  $I_A \approx 17kA$  is the Alfvén current,  $\sigma_x$  and  $\beta_x$  denote transverse beams size and transverse  $\beta$ -function,  $s$  is the distance along the beamline and  $E_0 \approx 511$  keV is the static electron energy.  $\ln \Lambda$  denotes Coulomb logarithm which calculated as

$$\ln \Lambda = \ln \left( \frac{\sqrt{2}}{6} \frac{\epsilon_N^3}{r_c \sigma_x^2} \left( \frac{I}{I_A} \right)^{-1/2} \gamma^{1/2} \right) - \ln \left( \frac{2\epsilon_N}{\eta \sigma_x} \right), \quad (3)$$

where  $\epsilon_N$  denotes the electron beam normalized emittance.

The decreasing bunching factor can be estimated by  $b_h = b_h^{(0)} e^{-l/L}$  [8], where  $l$  is the distance between the exit of the first dispersion section and the radiator entrance,  $L = 2\sigma_E^2/Dm^2B_2^2$ . According to the parameters at S<sup>3</sup>FEL, the IBS-induced energy spread growth is about 9.8 keV. The bunching factor decrease to about 1.7% which is still sufficient to suppress the electron beam shot noise and improving the temporal coherence of final FEL pulses.

## EEHG CASCADED HARMONIC LASING

Although EEHG has the highest harmonic up-conversion efficiency, it's difficult to achieve lasing with a harmonic number up to 100 experimentally. Recently, a novel technique called EEHG cascaded harmonic lasing has been proposed [9]. With the parameters of S<sup>3</sup>FEL, a start-to-end simulation result has been shown in Fig. 8. An intense, almost Fourier transform-limited pulse can be generated.

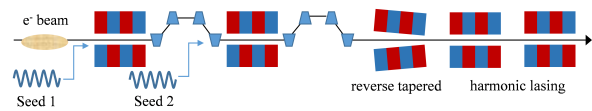


Figure 7: The layout of EEHG cascaded harmonic lasing.

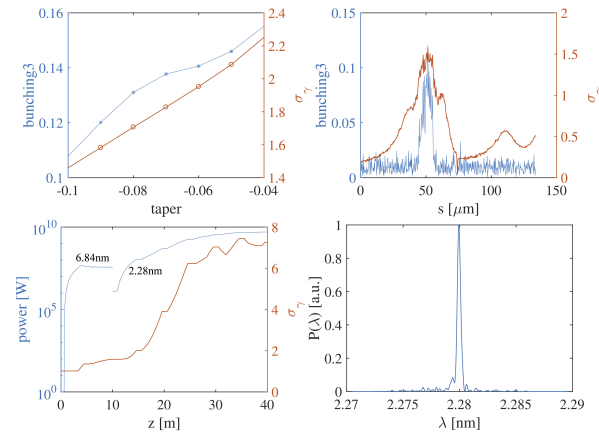


Figure 8: Simulation results of proposed scheme.

## CONCLUSION

In this paper, the physical design and FEL performance of EEHG beamlines at a newly proposed FEL facility, S<sup>3</sup>FEL, have been described. We also investigated the influence of various collective effects on the radiation at EEHG using theoretical analysis and numerical simulations. The design and optimization of EEHG cascaded harmonic lasing in the case of 2.3 nm@FEL-3 is preliminary studied.

## ACKNOWLEDGEMENTS

This work is supported by the National Key R&D Program of China (Grant No.2018YFE0203000) and the National Natural Science Foundation of China (Grant No.22288201).

## REFERENCES

- [1] X. Wang, *et al.*, “Physical Design for Shenzhen Superconducting Soft X-Ray Free-electron Laser (S3FEL)”, in *Proc. IPAC’23*, Venice, Italy, TUPL043.
- [2] G. Stupakov, “Using the Beam-Echo Effect for Generation of Short-Wavelength Radiation”, *Phys. Rev. Lett.*, vol. 102, p. 074801, 2009.  
doi:10.1103/PhysRevLett.102.074801
- [3] S. Reiche, “GENESIS 1.3: a Fully 3D Time-dependent FEL Simulation Code”, *Nucl. Instr. Meth. A*, vol. 429, pp. 243–248, 1999. doi:10.1016/S0168-9002(99)00114-X
- [4] D. Xiang, *et al.*, “Echo-enabled Harmonic Generation Free Electron Laser”, *Phys. Rev. ST Accel. Beams*, vol. 12, p. 030702, 2009. doi:10.1103/PhysRevSTAB.12.030702
- [5] M. Pop, *et al.*, “Mitigation of CSR Induced Spectral Broadening in EEHG FEL”, *Nucl. Instr. Meth. A*, vol. 1048, p. 167926, 2023. doi:10.1016/j.nima.2022.167926
- [6] C. Feng, *et al.*, “Hard X-ray Free-electron Laser Based on Echo-enabled Staged Harmonic Generation scheme”, *Chinese Science Bulletin*, vol. 55, pp. 221–227, 2010.  
doi:10.1007/s11434-010-0002-0
- [7] K. Zhou, *et al.*, “Feasibility Study of Generating Ultra-high Harmonic Radiation with a Single Stage Echo-enabled Harmonic Generation Scheme”, *Nucl. Instr. Meth. A*, vol. 834, pp. 30–35, 2016. doi:10.1016/j.nima.2016.07.021
- [8] W. Fan, *et al.*, “Hybrid Echo-enabled Harmonic Generation scheme for Seeding Coherent Soft X-ray Free-electron Lasers”, *Nucl. Instr. Meth. A*, vol. 1027, p. 166241, 2022.  
doi:10.1016/j.nima.2021.166241
- [9] K. Zhang, *et al.*, “Extending the Photon Energy Coverage of a Seeded Free-Electron Laser via Reverse Taper Enhanced Harmonic Cascade”, *Photonics*, vol. 8, p. 44, 2021.  
doi:10.3390/photonics8020044

# A SCHEME OF FULLY COHERENT X-RAY FREE ELECTRON LASER FOR THE SHINE BASED ON FRESH-SLICE

Y. X. Liu<sup>†</sup>, T. Liu

Shanghai Institute of Applied Physics, Chinese Academy of Sciences Shanghai, China  
 University of Chinese Academy of Sciences, Beijing 100049, China  
 Shanghai Advanced Research Institute Chinese Academy of Sciences, Shanghai, China

## Abstract

In this paper, the fresh-slice self-seeding free electron laser scheme is studied, and the feasibility of its application in the SHINE project is analyzed. The scheme used the fresh-slice method to generate the beam with adjustable spatial distribution, which can effectively improve the longitudinal coherence and stability of the self-seeding output radiation. Through the FEL simulation, we demonstrated that this scheme can produce a highly stable, narrow bandwidth pulse output under the SHINE's parametric conditions, which will be beneficial to further improve the performance of this device in the future.

## INTRODUCTION

Conventional SASE pulses originate from stochastic noise and are essentially random [1], which significantly affects the stability and output power of the self-seeding FEL. However, when a self-seeding scheme generates FEL using an ultra-short, high-current electron beam with a specific duration [2], the level of fluctuations can be reduced to a few percent while also maintaining a temporally coherent FEL output, resembling an ideal laser or an external-seeded FEL.

The fresh-slice method, also paving the way to very high peak power and high brightness XFEL pulses [3], uses either two different electron bunches or two single bunch slices, one to generate the seed signal and the other to amplify it in a tapered undulator to very high peak power. The method effectively eliminates the compromise between the seed power at the monochromator exit and the energy spread of electron slices within the seeded undulator section [4], thereby enhancing electron capture and reducing susceptibility to sideband instability [5].

Using the fresh-slice method to enhance the stability and power of self-seeding is an extremely appealing choice, while the SHINE project focuses on studying self-seeding FEL schemes covering the 5-15 keV hard X-ray range [6]. The changes to the self-seeding approach would contribute to improve the future performance of the SHINE. In this manuscript, we will demonstrate the simulation results of a bunch with high-current head using the fresh-slice method, which will provide some insights for the design of SHINE in the future.

\* Work supported by the CAS Project for Young Scientists in Basic Research (YSBR060), the Shanghai Natural Science Foundation (23ZR1471300), and the CAS-Helmholtz International Laboratory on Free Electron Laser Science and Technology (HZXM2022500500).

<sup>†</sup> email address: liuyixuan@sinap.ac.cn.

## FRESH-SLICE SELF-SEEDING

A schematic of the fresh-slice self-seeding used in the simulation is shown in Fig. 1. Selectively lasing with different slices of the electron beam is achieved with the fresh slice method. The electron bunch experiences a head-tail transverse kick by the wakefield generated in the D1 dechirper, set to an offset from the machine axis. Before the initial undulator phase, orbit correctors are utilized to direct the bunch into a head-lasing orbit. A saturated photon pulse is produced in the first section of the high-current bunch head. Then the photon pulse transmits from the diamond monochromator and generates a narrow bandwidth portion of it that is diffracted. The transmitted X-ray pulse presents a short, wide-bandwidth pulse followed by a stable, long, narrow-bandwidth tail. The chicane is used to delay the electron bunch tail such that it is overlapped with the narrow-bandwidth tail of the photon pulse. The bunch orbit is switched to a tail-lasing one around the chicane, and the monochromatic seed is amplified by the fresh electrons on the bunch tail in the second undulator section.

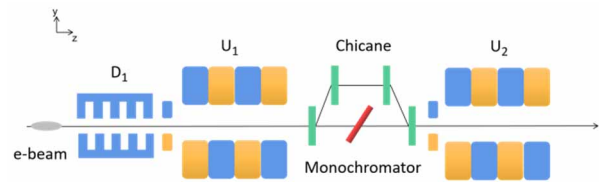


Figure 1: Schematic layout of the proposed scheme based on fresh slices.

## Beam Parameters

Based on the proposed scheme, FEL simulations were performed using the code Elegant [7] and Genesis 1.3 [8]. The overall electron beam parameters and radiation parameters used in the simulations are presented in Table 1.

Table 1: Electron Beam and Radiation Parameters

Parameter	Value	Unit
Beam energy	8	GeV
Energy spread	0.01	%
Normalized emittance	0.5	mm • mrad
Undulator period	2.6	cm
Undulator strength K	1.3415	-
FEL wavelength	0.1	nm

Content from this work may be used under the terms of the CC BY 4.0 licence (© 2023). Any distribution of this work must maintain attribution to the author(s), title of the work, publisher, and DOI

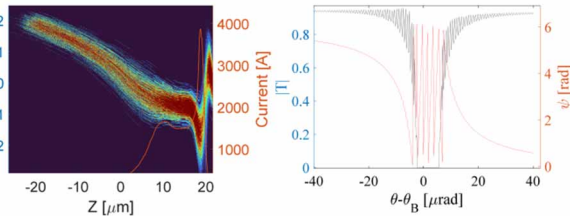


Figure 2: The beam profile and the modulus and phase of the transmissivity function (sigma polarization) from a diamond crystal in the Bragg (400) diffraction with a thickness of 0.1 mm. The relevant data was obtained by using the open X-ray software XOP [9].

In the first stage of the scheme, the on-axis high-current head of the bunch generates saturated single-spike-like SASE pulses which will effectively modulate the bunch tail in the second stage, so as to maintain the energy spread and improve output stability.

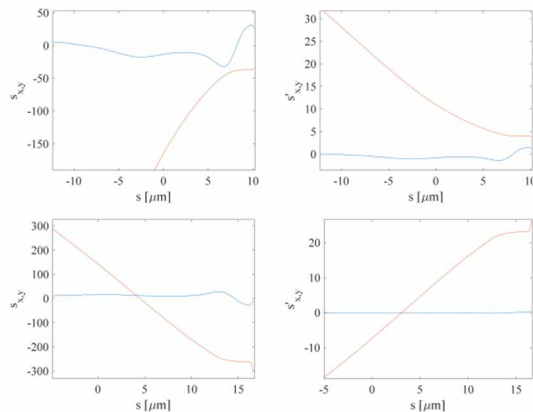


Figure 3: The sliced transverse offsets (top-left) and the angular deviation (top-right) of x (blue) and y (red) after the dechirper. Before the seeded stage (bottom). Bunch tail is at the left side of s coordinate axis.

The beam envelope of  $s = 0$  position is matched for FEL radiation. The matched results are shown in Fig. 3. It is noted that the mismatch and offset of the beam exist, that will impact on the radiation pulse performance.

## SIMULATIONS

Each undulator module in the beamline is a 4-m-long planar structure with 152 periods of  $\lambda_u = 26$  mm and an adjustable magnetic gap. The simulation of enhanced self-seeding and fresh-slice self-seeding schemes was performed under the undulator condition, and the beam parameters were the same.

### SASE Stage

A series of 50 separate GENESIS runs have been performed to analyze the statistical fluctuation of the radiation pulse. Figure 4 presents the 12.4 keV SASE FEL performance. For the enhanced self-seeding scheme, the output radiation in both the time domain and frequency domain is similar to the SASE radiation because of the low current contrast and the lack of taper in the SASE stage to maintain the energy spread of the beam portion with flat current. For

the fresh-slice scheme, the output has a relatively low power but a "pure" spectrum.

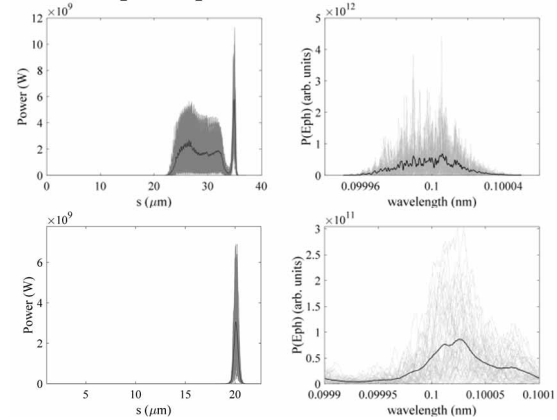


Figure 4: The saturation power distribution (left) and the spectrum (right) of 50 SASE pulses. (Top) Enhanced self-seeding. (Bottom) With fresh-slice method.

### Seeded Stage

Figure 5 shows the seed power profile from the enhanced self-seeding and the fresh-slice self-seeding. Obviously, the high current spike reaches saturation at the mono, which significantly reduces intensity fluctuations of the seed compared to enhanced self-seeding, where the signal is interfered with by the wide-bandwidth regime. Comparing wake monochromator power, the seed with a fresh-slice SASE pulse has a more stable mode than a normal SASE pulse with the same beam parameters.

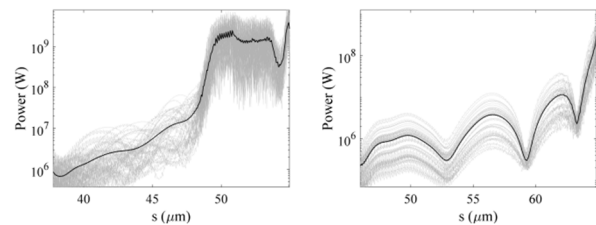


Figure 5: The seed power after the mono filter of the enhanced self-seeding scheme (left). With the fresh-slice method (right).

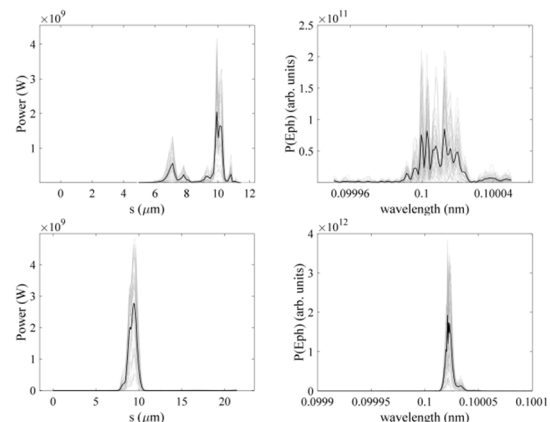


Figure 6: Results of power profile (top-left) and spectrum (top-right) of the self-seeding. (Bottom) With fresh-slice method.

As shown in Fig. 6, the output radiation with the fresh-slice method at the exit of the radiation undulator is about 3 GW, with a normalized spectral width (FWHM) of  $8 \times 10^{-5}$  reduced about 4 times compared with the enhanced self-seeding scheme under the same beam parameters. The gain curve of average power is shown in Fig. 7. The average seed power is over 1MW, and the result of exponential gain is about 10 $\mu$ J (saturation).

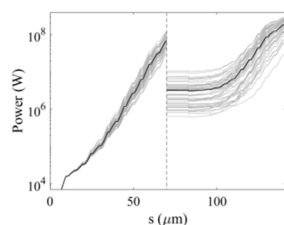


Figure 7: FEL power along the undulator beamline for the fresh-slice scheme.

The final result shows a considerable margin for improvement. The high-current still produces spikes within the wide-bandwidth pulse, leading to inadequate control over the power fluctuations of the seed. To enhance the stability of the system, one possible approach is to compress the beam, which would allow for better control over the number of spikes. Furthermore, this scheme exhibits notable benefits in terms of harmonic lasing self-seeding. It effectively overcomes the trade-off between seed power and electron slice energy spread, which is a crucial factor influencing the performance of the harmonic. This aspect warrants further investigation and exploration.

## CONCLUSION

Through the beam parameters of the SHINE, the enhanced self-seeding results combined with fresh-slice are simulated. Shot-to-shot results prove the reliability of the scheme. To improve the stability of the output and generate high-quality harmonics through this scheme, the related work is ongoing.

## REFERENCES

- [1] Saldin, Evgenij L., Evgeny A. Schneidmiller, and M. V. Yurkov, "Statistical properties of radiation from VUV and X-ray free electron laser", *Optics communications*, vol. 148.4-6, pp. 383-403, 1998.
- [2] Hemsing, Erik, Aliaksei Halavanau, and Zhen Zhang. "Enhanced self-seeding with ultrashort electron beams", *Physical Review Letters*, vol. 125.4, p. 044801, 2020.
- [3] Emma, C. *et al.*, "Experimental demonstration of fresh bunch self-seeding in an X-ray free electron laser", *Applied Physics Letters*, vol. 110.15, 2017.
- [4] Ben-Zvi, Ilan, K. M. Yang, and L. H. Yu, "The "fresh-bunch" technique in FELs", *Nuclear Instruments and Methods in Physics Research Section A: Accelerators, Spectrometers, Detectors and Associated Equipment*, vol. 318.1-3, pp. 726-729, 1992.
- [5] Emma, C., *et al.*, "High efficiency, multiterawatt x-ray free electron lasers", *Physical Review Accelerators and Beams*, vol. 19.2, p. 020705, 2016.

- [6] Liu, Tao, X. Dong, and C. Feng, "Start-to-end simulations of the reflection hard X-ray self-seeding at the SHINE project", *Proceedings of the 39th international free electron laser conference—FEL*, vol. 19, 2019.
- [7] M. Borland, *User's Manual for Elegant*, APS-ANL, Chicago, IL, 2017.
- [8] S. Reiche, "GENESIS 1.3: a fully 3D time-dependent FEL-simulation code", *Nucl. Instrum. Methods Phys. Res. A*, vol. 429, no. 1-3, p. 243, 1999. doi:10.1016/S0168-9002(99)00114-X.
- [9] ESRF, X-ray Oriented Programs Software Package, <https://www.aps.anl.gov/Science/Scientific-Software/XOP>.

# INVESTIGATION ON THE TRAPPED MODES OF CPMU AT HEPS

Sen Yue <sup>\*</sup>, Na Wang <sup>†</sup>, Saike Tian, Jintao Li  
Institute of High Energy Physics, [100049] Beijing, China

## Abstract

The Cryogenic Permanent Magnet Undulator (CPMU) is a crucial component in synchrotron radiation sources. Due to the small magnet gap of CPMU, the interaction between the beam and its surroundings is strong, which can result in a significant contribution to coupling impedance. In this work, the influence of CPMU on coupling impedance was investigated using wakefield and eigenmode solvers. The results indicate that some of the transverse impedance resonances in CPMU were much stronger than the impedance threshold determined by synchrotron radiation damping, which could cause vertical beam instability. To address this issue, different types of damping materials were investigated through simulations to suppress the resonances.

## INTRODUCTION

The in vacuum undulator (IVU) is a device, whose magnet is put inside in the vacuum box, and thus the magnet gap can be designed as much small as possible [1]. CPMU is a kind of undulator, whose magnet is working at cryogenic. Compared with IVU, it can provided a stronger magnetic at the same magnet gap, which can help to increase the frequency of synchrotron radiation generated by electron beams.

Due the small gap, the interaction between beam and its surroundings can be strong. Recently, multiple light sources, such as the Canadian Light Source [2], the Australian Light Source [3], and SLAC's SPEAR3 [4], have all discovered beam instability phenomena caused by the trapped mode inside the IVU.

In the first phase of the High Energy Photon Source (HEPS) project, 6 CPMUs will be installed in the storage ring. The CPMU have a longitudinal length of approximately 2.6 m, with a standard magnet gap of 5 mm. Therefore, the evaluation of its influence on beam is crucial to ensure the stable operation of the beam within the storage ring.

## VERTICAL IMPEDANCE

Due to limited computational resource, the three-dimensional model of CPMU need to be simplified. Its unnecessary detailed structures were removed, and the length of mangnet was reduce to 1 m, to reduce the mesh number for a short simulation time. Figure 1 shows the simplified model, and the right figure depicts the transverse cross section of CPMU, which similar to a circular ridge waveguide.

Compared to circular waveguide, the ridge waveguide has a lower cutoff frequency. As the size of beam pipe is large compared to the magnet gap, the cutoff frequency formed

by the magnet and vacuum cavity is lower than that of the beam pipe. As a result, some modes with low-frequency can be trapped in CPMU, and it is also called as trapped modes.

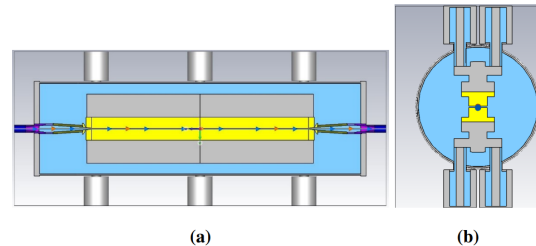


Figure 1: The simplified model of CPMU. (a): vertical cross section; (b): transverse cross section.

Through the CST wakefield solver, the vertical coupling impedance of the simplified model is shown in Fig. 2. In the simulation, the RMS length of the beam bunch was set to 100 mm, and the calculation length of the wakefield is 20 m.

Figure 2 shows that there are mainly two obvious impedance peaks at 96 MHz and 189 MHz. The real part impedance of these two peak are 2.1 and 0.6 M $\Omega$ /m, respectively. Due to these two peaks have a high  $Q$  factor, the wakefield is hard to convergence. Thus, the magnitude of the vertical impedance is smaller than expected value.

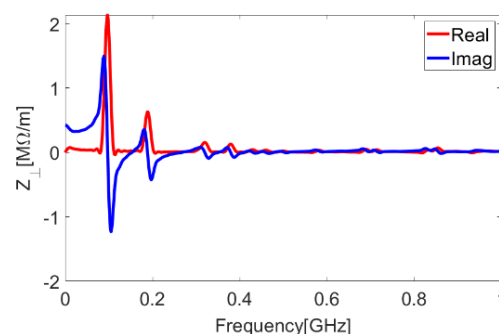


Figure 2: The vertical coupling impedance.

## TRAPPED MODES

Although the CPMU model has been simplified, the simulation still takes nearly one month to obtain the impedance results in Fig. 2. As the simulation time is proportional to the wakefield length, it will require a large amount of time and computational resources, to obtain a converged result. Therefore, the eigenmode solver is adopted to analyze these two impedance peaks, which requires little computational resources and time.

<sup>\*</sup> yuesen@ihep.ac.cn

<sup>†</sup> wangn@ihep.ac.cn

The relationship of five eigenmodes, between the  $R/Q$  and the vertical displacement, is shown in Fig. 3. The eigenmode frequency of Mode 1 and Mode 3 are 96 MHz and 189 MHz, respectively, which is consistent with the frequency of impedance peak in Fig. 2. The relationship curves for Mode 1 and Mode 3 resemble parabolic shape, which is agree with the relationship between the transverse impedance's  $R/Q$  and its transverse displacement. Therefore, Mode 1 and Mode 3 can be thought as the vertical impedance mode, and it is also called as trapped modes.

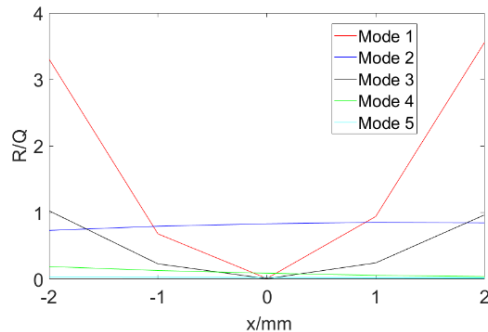


Figure 3: The  $R/Q$  of five eigenmodes at different vertical displacement.

According to the eigenmode results, the coupling impedance for these two modes were calculated and presented in Table 1. The transverse shunt impedance for Mode 1 and Mode 3 can reach 150 and 32.6 M $\Omega$ /m, respectively. However, the vertical impedance threshold in HEPS, determined by synchrotron radiation (SR) damping, is approximately 4.7 M $\Omega$ /m. When the frequency of trapped modes is overlap with the beam spectrum, the impedance of trapped modes can be a huge value, and thus some measures need to be adopted to inhibit it.

Table 1: Eigenmode Results of Trapped Modes

	$f$ [MHz]	$\frac{R}{Q_{\perp}}$ [M $\Omega$ /m <sup>2</sup> ]	$Q$	$R_s$ [M $\Omega$ /m]
Mode1	96	0.78	773	150
Mode3	189	0.22	1154.8	32.6

The  $Q$  factor of trapped mode can be damped by placing damping materials at specific locations inside the model, which would result in a decrease in the magnitude of its coupling impedance. Therefore, in this section, two approaches are proposed to suppress these trapped modes: electric damping and magnetic damping.

### Electric Damping

To achieve a good mode damping effects, it is usually necessary to place the damping materials in the region with strong field distribution. Taking the mode of 96 MHz as an example, its electric field distribution is shown in Fig. 4, and the field distribution at 189 MHz is similar to that at 96 MHz.

The electric field at 96 MHz is strong in the magnet gap and near the girder. Considering the influence of damping materials on the magnetic field at the magnet pole, we only consider placing it on the girder and study its damping effects on the trapped modes.

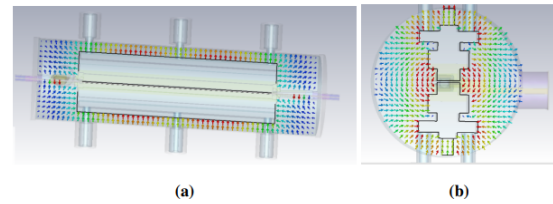


Figure 4: The electric field distribution of the eigenmode at 96 MHz. (a): vertical cross-sectional view at its center; (b): transverse cross-sectional view.

The size of the electric damping material, placed at the girder, is 60\*30\*20 mm, and a total of 4 pieces are used, as shown in Fig. 5. In order to study the influence of its electromagnetic properties on the  $Q$  factor, a parameter sweep is conducted on the dielectric constant and magnetic permeability:  $\epsilon'$ ,  $\epsilon''$ ,  $\mu'$ ,  $\mu''$ .

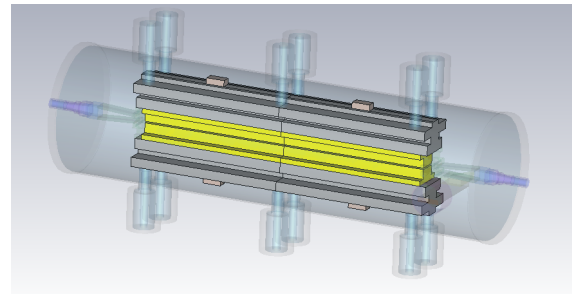


Figure 5: The location of electrical damping material, and it is the earthy yellow elements on the girder.

The default electromagnetic parameters for the electric damping material at 100 MHz are set as  $\epsilon' = 5$ ,  $\epsilon'' = 2.5$ ,  $\mu' = 5$ ,  $\mu'' = 2.5$ . When scanning one variable, the other parameters remain unchanged. The scanning range for variable  $\epsilon'$  and  $\epsilon''$  is 5, 10, and 20, and that for  $\mu'$  and  $\mu''$  is 2.5, 5, 7.5, and 10. Figure 6 shows the sweep results of  $Q$  factor at 96 MHz. To facilitate comparison, four air blocks were placed at the location of the damping material, whose electromagnetic properties is  $\epsilon = \mu = 1$ .

In Fig. 6, the electric damping material can effectively reduce the  $Q$  factor of trapped mode, compared to the case without damping material. Increasing the value of  $\mu''$ , especially for  $\epsilon''$ , can significantly enhance its damping effect on  $Q$  factor. That suggests that, the damping material with a large value of  $\epsilon''$ , can help to suppress the trapped modes in the model.

### Magnetic Damping

Figure 7 illustrates the magnetic field distribution at 96 MHz. In addition to the strong field distribution at the magnet gap, there is also a significant field distribution near

Content from this work may be used under the terms of the CC BY 4.0 licence (© 2023). Any distribution of this work must maintain attribution to the author(s), title of the work, publisher, and DOI

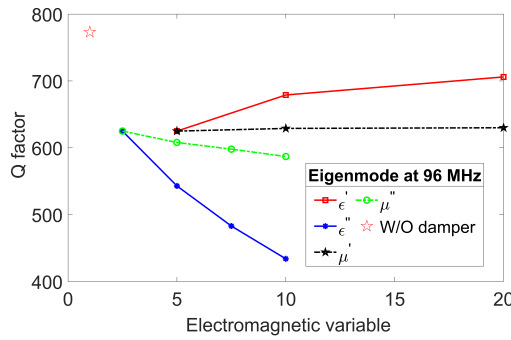


Figure 6: The damping effect of electric damping material with different electromagnetic variables on the  $Q$  factor.

the linked rods. To avoid interference with the magnetic field at the magnet gap, the magnetic damping material is selected to be placed around the linked rods.

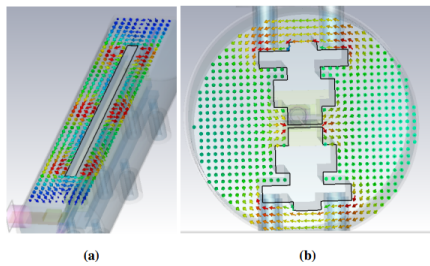


Figure 7: The magnetic field distribution of the eigenmode at 96 MHz. (a): horizontal cross-section at the girder; (b): transverse cross-section.

The location of the magnetic material in the model is shown in Fig. 8, with dimensions of 50\*50\*5 mm for each of the 12 pieces.

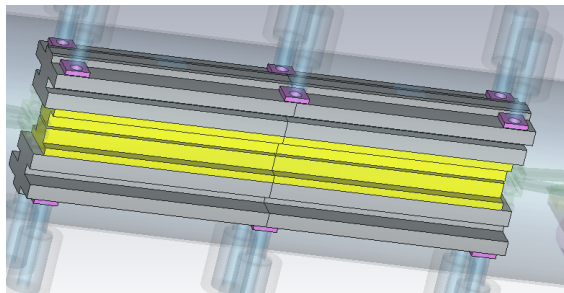


Figure 8: The location of magnetic damping material, and it is the magenta components around linked rods.

The influence of four electromagnetic parameters on the damping effect of  $Q$  factor was also investigated, using the same parameter sweep settings as mentioned in the section of *Electric Damping*. Figure 9 displays the  $Q$  factor results under different electromagnetic variables.

According to Fig. 9, the variable  $\mu''$  has the most significant suppression effect, and it can decrease the  $Q$  factor from 773 to 10. This indicates that the damping effect of magnetic material is significantly better than that of electric material.

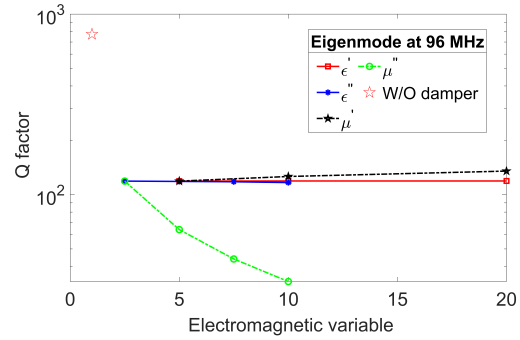


Figure 9: The damping effect of magnetic damping material with different electromagnetic variables on the  $Q$  factor.

Therefore, the magnetic damping material is finally selected to suppress the trapped modes in CPMU.

Considering the practical conditions, the ferrite material of HOM absorber in RF cavity is selected as the magnetic damping material to suppress the trapped mode. The eigenmode results with ferrite material are shown in Table 2.

Table 2: Eigenmode Results with Ferrite Material

	$f$ [MHz]	$\frac{R}{Q_{\perp}}$ [ $M\Omega/m^2$ ]	$Q$	$R_s$ [ $M\Omega/m$ ]
Mode1	96	0.94	17.7	4.5
Mode3	189	0.24	52.6	1.6

Compared with Table 1, the ferrite material significantly reduces the  $Q$  factor of these two trapped modes, whose value is decreased from 773 and 1154.8 to 17.7 and 52.6, respectively. The transverse impedance finally decreases to 4.5 and 1.6  $M\Omega/m$ , which is less than the impedance threshold determined by SR damping. Considering the bunch by bunch feedback system, the influence of trapped modes on beam is acceptable.

## CONCLUSION

In our study, we observed that the trapped mode in CPMU can lead to large vertical impedance. When the frequency coincides with beam spectrum, it will significantly exceed the impedance threshold. To address this issue, two types of material: electric material and magnetic material, are proposed to suppress it, and the magnetic material has an excellent performance.

After implementing ferrite material, the  $Q$  factor as well as the transverse impedance are significantly reduced. That indicates ferrite materials can effectively suppress the influence of trapped modes on beam.

## REFERENCES

- [1] S. Yamamoto, "Construction of an in-vacuum type undulator for production of undulator x rays in the 5–25 keV region", *Rev. Sci. Instrum.*, vol. 63, no. 1, pp. 400-403, 1992.
- [2] E. Ericson, "Simulation and analysis of wake fields and trapped RF modes in insertion device vacuum chambers at the Cana-

dian Light Source”, in *Proc. IPAC 2019*, Melbourne, Australia, 2019.

- [3] R. Dowd, “Investigation of trapped resonant modes in insertion devices at the Australian Synchrotron”, in *Proc. IPAC 2016*, Busan, Korea, 2016.
- [4] K. Tian, “Damping trapped modes in an in-vacuum undulator at a synchrotron radiation light source”, *PRAB*, vol. 22, p. 050702, 2019.  
doi:10.1103/PhysRevAccelBeams.22.050702

# MULTI-BUNCH OPERATION MODE FOR SIMULTANEOUSLY SERVING SASE AND SEEDING FEL BEAMLINES

Yifan Liang, Xiaofan Wang\*, Li Zeng, Huaiqian Yi, Weiqing Zhang<sup>1†</sup>, Xueming Yang<sup>1,2</sup>

Institute of Advanced Science Facilities, Shenzhen, China

<sup>1</sup>also at Dalian Institute of Chemical Physics, CAS, Dalian, China

<sup>2</sup>also at Southern University of Science and Technology, Shenzhen, China

Yong Yu, Jitao Sun, Xinmeng Li

Dalian Institute of Chemical Physics, CAS, Dalian, China

## Abstract

Modern free-electron laser (FEL) facilities are designed to simultaneously serve multiple undulator lines to provide x-ray pulses with high peak power and tunable wavelengths. To satisfy different scientific demands, it is preferred to make the separate undulator lines work under different FEL schemes, such as the self-amplified spontaneous emission (SASE) scheme and the echo-enabled harmonic generation (EEHG) scheme. However, different FEL schemes have different requirements on the beam longitudinal distribution. Here, we propose to use multiple bunches to simultaneously serve the undulator lines and put the bunches at different acceleration phase to change the bunch length with two compressor chicanes. The acceleration phase for each bunch is varied by adjusting the time delays of the photocathode drive laser pulses with the accelerator settings unchanged. The start-to-end simulation demonstrates that a fs bunch with high peak current can be produced to serve the SASE line while a bunch with hundred-of-fs length and uniform current distribution can be produced to serve the EEHG line. The FEL performances are simulated and discussed.

## INTRODUCTION

Modern FEL facilities are designed to operate two or more undulator lines simultaneously with a single-pass linac-based machine and exploit beam distribution systems to send electron bunches to their respective beamlines. In normal conducting linacs, limited by the low repetition rate, only a modest average brightness can be provided. It is necessary to accelerate two electron bunches in the same radiofrequency (RF) macropulse to increase the repetition rate, as in SwissFEL [1]. In superconducting RF linacs, megahertz (MHz) electron bunches can be provided and the photon average brightness is greatly enhanced. The MHz electron bunches are then sent to different undulator lines in a group mode as in European XFEL [2] and FLASH [3] or one by one as in LCLS-II [4] and SHINE [5].

To extend the application range of FEL generated light, it is preferred to operate different undulator lines under different schemes to provide either sub-fs or fully longitudinally coherent pulses. However, different FEL schemes have different requirements on the beam longitudinal

distribution. The SASE scheme requires fs electron bunch with high peak current to shorten the saturation length and increase the peak power, while seeding schemes require bunches with hundred-of-fs length and uniform current distribution to improve the modulation stability. To satisfy the requirements of different FEL schemes, one solution is to accelerate the bunches at different accelerating phases and change the bunch lengths with compressor chicanes. The acceleration phase for each bunch can be varied by changing the microwave amplitude and phase as has been done in SwissFEL [1] and FLASH [6]. However, in superconducting RF linacs with MHz repetition rate of macropulses, changing the amplitude and phase of different macropulses is a challenge and might affect the machine stability.

In this paper, we study the multi-bunch scheme and change the acceleration phase of each bunch by adjusting the time delays of the photocathode drive laser. A bunch with hundred-of-fs length and uniform current distribution is produced for EEHG lasing while a sub-fs bunch with high peak current can be produced for SASE lasing under the same machine parameters.

## MULTI-BUNCH SCHEME

The multi-bunch scheme has been studied both theoretically and experimentally [7-10]. Here, we concentrate on modulating the longitudinal distribution of the bunches into different shapes to simultaneously maximize the radiation performance of different FEL schemes in different undulator lines. We take the typical two-stage compression beamline at S3FEL as an example, as shown in Fig. 1. Laser pulses with a repetition rate of 1 MHz illuminate the photocathode to produce electron bunches. Two chicanes are used to compress the bunch length from several picoseconds to tens of femtoseconds. After acceleration to 2.5 GeV, the bunches are distributed to separate undulator lines respectively. Two of the undulator lines exploit the SASE scheme to lase and the other two exploit the EEHG scheme. To simultaneously maximize the radiation performance of all the undulator lines, the bunches directed into different undulator lines are put on different acceleration phase and thus different compression just by changing the time delay of the photocathode laser pulses.

## Injector

The injector includes a normal-conducting continuous-wave (CW) RF gun operating at 217 MHz (6th sub-

Email address: \*wangxf@mail.iasf.ac.cn

†weiqingzhang@dicp.ac.cn

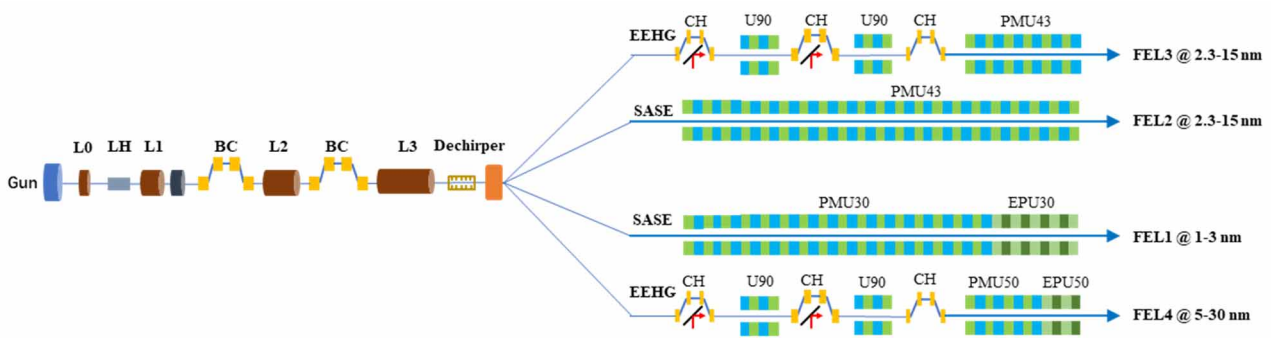


Figure 1: Schematic layout of S3FEL. Electron bunches are extracted from a VHF gun and subsequently accelerated in super-conducting Linac sections and compressed in the two magnetic chicanes. The beam is accelerated to 2.5 GeV before directed to different undulator lines.

harmonic of 1.3 GHz), a 1.3 GHz buncher and a superconducting acceleration module. The beam dynamics in the injector for a 100 pC bunch charge is simulated by ASTRA (Floettmann, 2017). The detailed parameters of the injector are shown in Table 1.

Table 1: Parameters of the Injector

Parameter	Value	Unit
<b>Drive laser</b>		
Beam charge	100	pC
Laser temporal profile	Flat-top	
Laser FWHM $L_t$	29	ps
Flat-top edge width $r_t$	1	ps
Transverse RMS size	0.19	mm
Thermal emittance	0.19	$\mu\text{m}$
<b>VHF gun</b>		
RF frequency of gun	217	MHz
Acceleration gradient	26	MV/m
Injection phase	-5	degree
<b>Buncher</b>		
RF frequency of buncher	1.3	GHz
Acceleration gradient	1.8	MV/m
Acceleration phase	-90	degree
Cavity position	0.86	m
<b>Eight-cavity cryomodule</b>		
RF frequency of cavities	1.3	GHz
1st cavity position	2.76	m
1st cavity gradient	15	MV/m
1st cavity phase	-5	degree
2nd cavity gradient	0	MV/m
3rd-8th cavities gradient	26	MV/m
3rd-8th cavities phase	0	degree

The bunch arrival time at the exit of the injector, which may change the downstream compression, depends on the injection time of the photocathode drive laser. Figure 2 gives the arrival time of the bunches with different injection time in the gun, relative to the arrival time of the nominal bunch. An evident negative correlation between the beam arrival time and the injection time offset results from

the  $-90^\circ$  acceleration phase of the velocity buncher. Figure 2b gives the relative arrival time along the beamline of the bunches with injection time offsets 5 ps and -5 ps. The bunch that arrives earlier will obtain a lower velocity in the buncher. After passing through the drift space between the buncher and the first acceleration section, the bunch will be delayed relative to the nominal bunch.

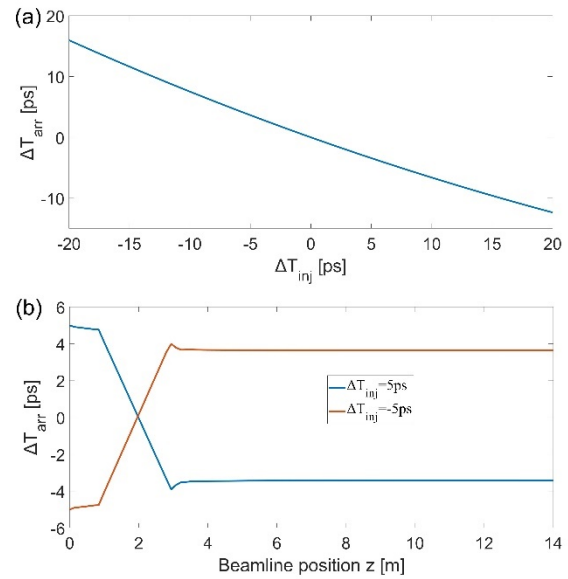


Figure 2: (a) Relative beam arrival time for different injection time offset. (b) Relative beam arrival time along the beamline for injection time offset 5 ps and -5 ps.

### Main Linac

Negative energy chirp is imposed on the beam in the acceleration module L1 and L2. After the two-stage compression, the beam is then accelerated to 2.5 GeV in the acceleration module L3. First of all, 1D simulation code LiTrack (Bane & Emma, 2005) is used to optimize the acceleration and compression parameters to obtain a bunch with hundred-of-fs length and uniform current distribution for EEHG lasing. The code Elegant (Borland, 2000) is then used to simulate the complete beam dynamics. The detailed parameters of the main linac are given in Table 2. Figure 3a shows the longitudinal phase space and current distribution of the nominal EEHG bunch. The electron

bunches with different injection time will experience different compression due to the change of the acceleration phase. Figure 3b shows the longitudinal phase space and the current distribution of the bunch at the end of the main linac with 20 ps gun injection time offset, which we call the SASE bunch here. The change of the harmonic cavity phase makes the compression nonlinear and a high peak current appears after the second compression chicane (BC2). After the electron beam exits the BC2, longitudinal space charge force within the high current spike induces a strong energy chirp [11], which can be utilized to further compress the spike with a positive R56 in a dogleg, reaching a peak current of above 8 kA. To avoid too large energy chirp inside the current spike, here, the charge of the SASE bunch is reduced to 60 pC.

Table 2: Parameters of the Main Linac

Parameter	Value	Unit
L1 voltage	246.3	MV
L1 phase	-18.4	degree
Lc voltage	60.2	MV
Lc phase	-159.7	degree
BC1 R56	-82.4	mm
BC1 beam energy	269.5	MeV
L2 voltage	931.3	MV
L2 phase	-13.2	degree
BC2 R56	-14	mm
BC2 beam energy	1175.8	MeV
L3 voltage	1335	MV
L3 phase	0	degree
L3 exit beam energy	2500	MeV

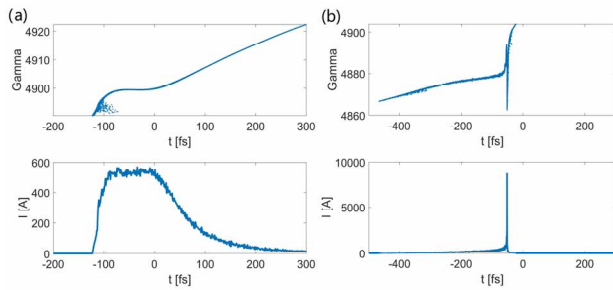


Figure 3: Longitudinal phase space and current distribution of the (a) EEHG bunch (100 pC) and (b) SASE bunch (60 pC) at the end of the main linac.

To avoid the emittance dilution due to the CSR effect, the strengths of the quadrupoles are optimized. The normalized emittance of the EEHG bunch and the SASE bunch can be both maintained smaller than 0.4  $\mu\text{m}$ .

## FEL PERFORMANCE

The EEHG bunch and SASE bunch are directed to the EEHG undulator line and SASE undulator line respectively. Figure 4 shows the FEL power and the spectrum of the two kinds of bunches. The EEHG spectrum is typically clean and the linewidth is  $\sim 1.8 \times 10^{-4}$ . The SASE pulse width is

$\sim 380$  as and the peak power is  $\sim 29$  GW, which offers an opportunity for studying the ultrafast processes.

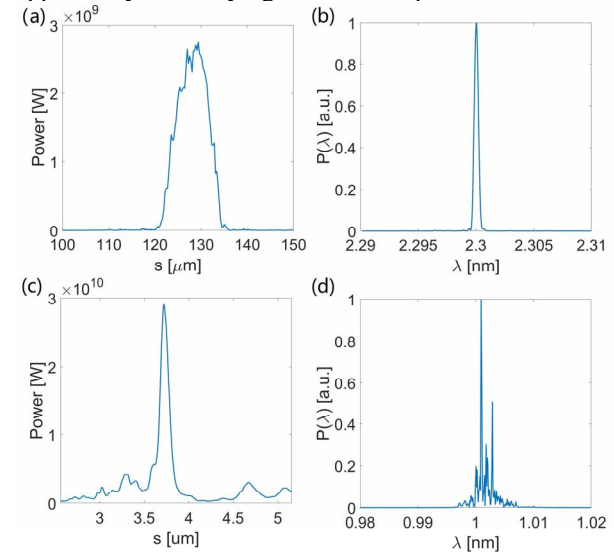


Figure 4: FEL power and spectrum. (a) EEHG power and (b) EEHG spectrum from the EEHG bunch. (c) SASE power and (d) SASE spectrum from the SASE bunch. The full width of half maximum (FWHM) of the SASE pulse is  $\sim 380$  as.

## CONCLUSION

The start-to-end simulation shows that the EEHG scheme and the SASE scheme can be operated simultaneously in different undulator lines, served by different electron bunches with different longitudinal length and shape. Taking advantage of the space charge force, a 380 as FEL pulse at 1 nm with peak power of 29 GW can be generated.

## ACKNOWLEDGEMENTS

We wish to thank Chao Feng and Zhen Wang for their many interesting discussions. This work was supported by the National Key R&D Program of China (Grant No. 2018YFE0203000) and the National Natural Science Foundation of China (22288201).

## REFERENCES

- [1] M. Paraliiev *et al.*, "SwissFEL double bunch operation", *Phys. Rev. Accel. Beams*, vol. 25, no. 12, 2022. doi:10.1103/PhysRevAccelBeams.25.120701
- [2] L. Fröhlich *et al.*, "Multi-Beamline Operation at the European XFEL", in *Proc. FEL'19*, Hamburg, Germany, Aug. 2019, pp. 335-338. doi:10.18429/JACoW-FEL2019-WEP008
- [3] B. Faatz *et al.*, "Simultaneous operation of two soft x-ray free-electron lasers driven by one linear accelerator", *New Journal of Physics*, vol. 18, no. 6, 2016. doi:10.1088/1367-2630/18/6/062002
- [4] Z. Zhang, Y. Ding, C. Adolphsen, and T. Raubenheimer, "Multienergy operation analysis in a superconducting linac based on off-frequency detune method", *Phys. Rev. Accel. Beams*, vol. 22, no. 11, 2019. doi:10.1103/PhysRevAccelBeams.22.110702

- [5] J. Yan and H. Deng, "Multi-beam-energy operation for the continuous-wave x-ray free electron laser", *Phys. Rev. Accel. Beams*, vol. 22, no. 9, 2019. doi:10.1103/PhysRevAccelBeams.22.090701
- [6] V. Ayvazyan *et al.*, "Low Level RF Control Implementation and Simultaneous Operation of Two FEL Undulator Beamlines at FLASH", in *Proc. of ICALEPCS2015*, Melbourne, Australia, 2015, vol. MOC3O07, pp. 42–5.
- [7] F. J. Decker *et al.*, "Tunable x-ray free electron laser multi-pulses with nanosecond separation", *Sci Rep*, vol. 12, no. 1, p. 3253, Feb 28 2022. doi:10.1038/s41598-022-06754-y
- [8] A. Marinelli *et al.*, "High-intensity double-pulse X-ray free-electron laser", *Nat Commun*, vol. 6, p. 6369, Mar 6 2015. doi:10.1038/ncomms7369
- [9] G. Penco *et al.*, "Two-bunch operation with ns temporal separation at the FERMI FEL facility", *New Journal of Physics*, vol. 20, no. 5, 2018. doi:10.1088/1367-2630/aac059
- [10] Z. Zhang *et al.*, "A high-power, high-repetition-rate THz source for pump-probe experiments at Linac Coherent Light Source II", *J Synchrotron Radiat*, vol. 27, pp. 890-901, Jul 1 2020. doi:10.1107/S1600577520005147
- [11] S. Huang *et al.*, "Generating Single-Spike Hard X-Ray Pulses with Nonlinear Bunch Compression in Free-Electron Lasers", *Phys. Rev. Lett.*, vol. 119, no. 15, p. 154801, Oct 13 2017. doi:10.1103/PhysRevLett.119.154801

# PHYSICAL DESIGN OF AN S-BAND COLD CATHODE RF GUN\*

Tian Hui He<sup>†</sup>, Hanxun Xu, Kui Zhou, Zheng Zhou

Institute of Applied Electronics, Chinese Academy of Engineering Physics, Mian Yang, China

## Abstract

In recent years, the properties of new field emission materials have been gradually improved with the advancement of materials research fields, which have provided the possibility for the research and realization of cold cathode microwave electron guns. A 0.32+1 cell S-band microwave electron gun was designed based on the emission properties of carbon nanotube films and ultra nano diamond films. This article mainly introduces the selection of electron gun cavity, RF design and corresponding thermal analysis. The physical design results basically meet the design requirements.

## INTRODUCTION

With the continuous advancement of accelerator technology, radio frequency guns are also iteratively developed from generation to generation, from the original hot cathode RF gun to the now widely used photocathode RF gun. The hot cathode RF gun has a large beam intensity and serious electronic backlash; Although the photocathode RF gun has good beam quality, the current intensity is not large, and additional costs are required for the laser. At present, with the advancement of material technology, the use of cold cathode is gradually increasing, cold cathode RF gun because of its beam quality is relatively good, the current intensity is large, and does not require additional filament heating power supply and laser, low cost, compact structure, so as to be expected by more and more institutes. Based on the emission characteristics of diamond film cathode [1] and carbon nanotube cathode [2] described in the existing literature, a 0.32+1 cell S-band cold cathode RF gun is designed.

The cold cathode is based on the principle of field-induced emission, and the distribution of field-induced emission current density in the microwave field is similar to the Gaussian distribution on time scales [3].

$$J(t) = J_0 e^{-C \frac{\phi^{3/2}}{\beta E_0} \frac{(\omega t - \pi/2)^2}{2}} \quad (1)$$

Its rms width is:

$$\sigma = \sqrt{\beta E_0 / (C \phi^{3/2})} \quad (2)$$

In the microwave field, the maximum value of the field-induced emission current distribution is exactly in the middle of the positive half-period of the microwave field, and since the area occupied by  $\pm 2\sigma$  accounts for 95% of the total area of the Gaussian distribution, it can be considered that the width of the field-induced emission is  $\pm 2\sigma$ .

\* Work supported by Infrared terahertz free electron laser device project  
<sup>†</sup> htth111@163.com

## CAVITY TYPE SELECTION

The general cold cathode RMS width  $\sigma$  is about  $15^\circ$ , and its emission width in the microwave field is about  $\pm 2\sigma$ , that is,  $-30^\circ \sim 30^\circ$ . An emission phase width of  $60^\circ$  will inevitably lead to electron back burst when the field strength of the cathode plane is not large enough. In order to avoid back bombardment, there are two solutions to the design of the first cavity, one is to reduce the length of the first cavity, and the other is to increase the cathode surface field strength. The problem with reducing the length of the first cavity is that the maximum field strength in the first cavity is offset and concentrated on the platter, and the length of the first cavity is too short, which increases the difficulty of processing and commissioning. Increasing the field strength of the cathode surface leads to a sharp increase in the emission phase width for the field-induced emission cathode, making the field-induced emission similar to the hot cathode emission. At present, the opening electric field of nitrogen-doped diamond film cathode is generally about 10 MV/m, and the opening electric field of carbon nanotube cathode is lower, generally 48 MV/m, and its maximum emission electric field is about 20 MV/m, which will inevitably lead to back bombing. Therefore, the only alternative method at present is to reduce the length of the first cavity.

Assuming that the field-induced emission RMS width  $\sigma$  is  $15^\circ$ , the relationship between the minimum field strength required for the last emitted electron at  $30^\circ$  overflows the first cavity and the length of the first cavity, as shown in Fig. 1. As can be seen from the figure, the shorter the first cavity, the smaller the minimum field strength required for the end electrons to overflow the first cavity. Under the cathode

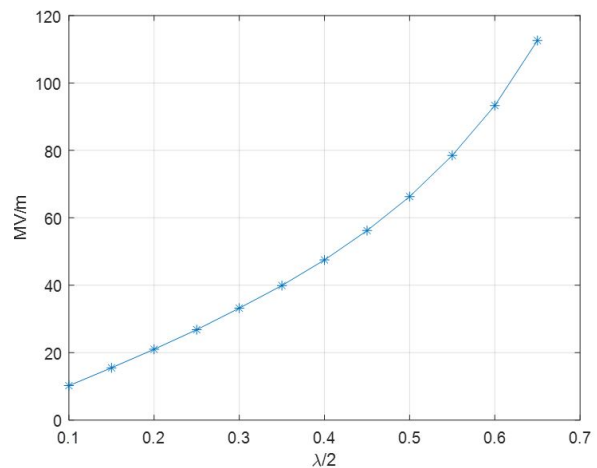


Figure 1: The relationship between the minimum field strength of the cathode plane required for the end electron overflow the first cavity and the length of the first cavity.

surface field strength of 40 MV/m, the cavity length is less than 0.35 cell, and the design of the first cavity length of 0.32 cell and the secondary cavity of 1.0 cell is adopted.

### RF DESIGN

When the length of the first and the secondary cavity were determined, the design of the RF gun entered the RF design part. The RF design process of RF gun is to first determine the basic structure of the cavity, and then enter the eigenmode solution optimization process, and add input waveguide, probe, cathode and other components after the cavity model optimization to complete the design of the whole gun structure. After that, iterative optimization is continued under the driving mode or eigenmode, and a better result of the whole gun is obtained. Here, CST and HFSS are used to optimize the design of the RF gun, and the two results are compared to prevent large error results.

#### Cavity Structure

The RF gun design requires an operating frequency of 2856 MHz and a  $\pi$  mode of operation, a mode interval greater than 10 MHz, and a field strength ratio of the secondary cavity to the first cavity is greater than 1. The basic structure of the electron gun is shown in Fig. 2.

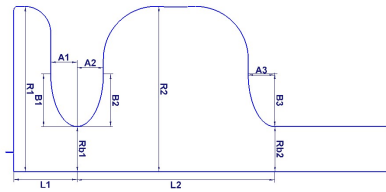


Figure 2: Basic structure of electron gun.

#### Eigenmode Design and Optimization

After completing the eigenmode optimization of the cavity, on this basis, adding coupling holes, transmission waveguides, vacuum pipes and probes, a complete vacuum model of RF gun is formed, and the RF design of RF gun can be basically completed through iterative optimization of the whole gun model. The results after the optimization are shown in Table 1 below.

Table 1: Optimization Results

Parameter	Value	Unit
$f_0$	2840.0139	MHz
$f_\pi$	2856.0492	MHz
$E_2/E_1$	1.0624	
$\beta$	1.0353	
$R/Q$	111.6220	MΩ/m
$Q_0$	11867.32	
$Q_e$	11462.89	

The mode interval between zero mode and  $\pi$  mode is about 16 MHz, and the probe coupling degree is calculated

to be about 53 dB. The axial electric field distribution is shown in Fig. 3. The electromagnetic field distribution and surface current are shown in Fig. 4.

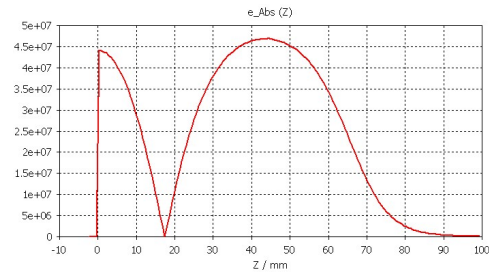


Figure 3: Axial electric field distribution of RF gun.

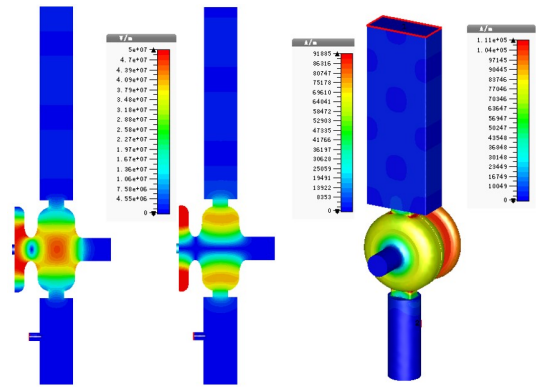


Figure 4: On the left is the electric field distribution, in the middle is the magnetic field distribution, and on the right is the surface current distribution.

#### Drive Mode Verification

After completing the eigenmode optimization design of the RF gun, the parameters are imported into HFSS and the driving mode calculation is performed on the same model.

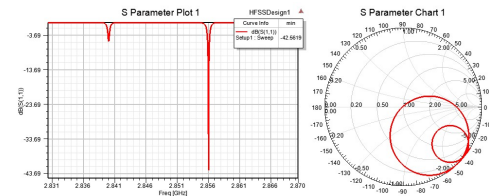


Figure 5: S11 parameter plot and SMITH chart.

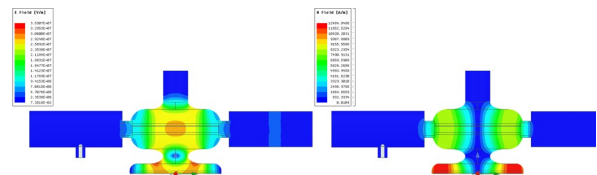


Figure 6: On the left is the electric field distribution, on the right is the magnetic field distribution.

When the input microwave power is 1 MW, the cathode surface field strength reaches 34 MV/m. Considering the beam load, the microwave coupling must be over coupling state, and the degree of coupling can be seen from the Smith chart. The S11 parameters and the Smith chart are shown in Fig. 5. And the electromagnetic field distribution is shown in Fig. 6.

## THERMAL ANALYSIS

### Mechanical Design

Using the final optimization results, the mechanical design of the RF gun was completed, and the finished RF gun is shown in Fig. 7.

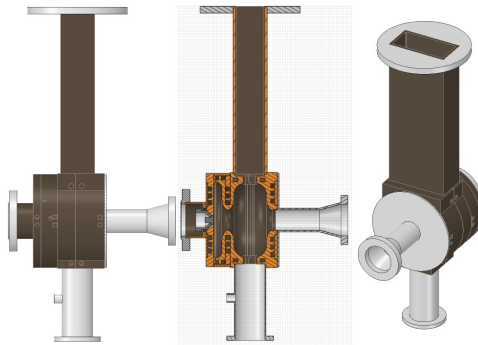


Figure 7: Mechanical design drawing (left is the whole, the middle is the section, the right is the positive triaxial measurement).

### Thermal Analysis

After completing the mechanical design of the RF gun, a thermal analysis was performed on the RF gun. The RF gun cavity shape, electric field distribution and surface heat loss distribution are shown in Fig. 8. And it can be seen that the heat loss is mainly concentrated on the side of the coupling hole near the cavity except for the first cavity wall. This indicates that the temperature rise of the coupling hole is relatively high.

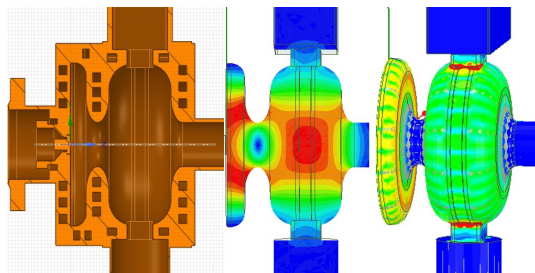


Figure 8: Cavity shape, electric field distribution and surface heat loss.

Using ANSYS' HFSS module, the cathode surface field strength is calculated to be 30 MV/m, and the heat loss of the electron gun cavity wall is 0.73 MW, and the duty cycle of this electron gun is set to be 0.8 %.

Since the HFSS simulation is set to a continuous wave condition, the average heat loss in pulse mode can be obtained by using the duty cycle. By adjusting the value of the excitation signal under eigenmode, set the initial setting of the electron gun that can output an average heat loss of 5.82 kW. Enter this setting into the FLUENT module and calculate the temperature distribution of the cavity. By adjusting the flow rate of the cooling water, the heat of the surface heat loss is taken away, so that the electron gun works at the desired temperature state.

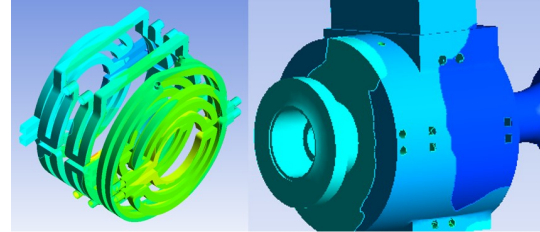


Figure 9: Temperature distribution of cooling water channel and chamber temperature distribution.

The temperature rises more at the cavity wall of the first cavity and at the coupling hole, the first cavity wall is about 25 degrees, and the temperature of the coupling hole below is about 40 degrees. The temperature distribution is shown in Fig. 9. Since the repetition frequency of the cold cathode microwave electron gun is actually very low, below 10 Hz, at this time, the heat loss of the cavity wall is below 0.15 kW, which will be quickly taken away by the cooling water, and the actual temperature rise will be very low. Therefore, the waterway design fully meets the requirements.

## CONCLUSION

According to the characteristics of the RF gun and the emission characteristics of the field emission cathode, the appropriate cavity shape of the RF gun was selected, and the optimized design of the electron gun was made by CST and HFSS, and the mechanical design and thermal analysis were carried out according to the optimization design results. Through several iterations of optimization, the design of the S-band cold cathode microwave electron gun was finally completed.

## REFERENCES

- [1] K. Nichols *et al.*, "Diamond field emitter array cathode experimental tests in RF gun," in *North American Particle Accelerator Conference (NAPAC'19)*, Lansing, MI, USA, 01-06 September 2019, JACoW Publishing, Geneva, Switzerland, 2019, pp. 618-621.
- [2] Y. Taira, H. Kato, R. Kuroda, H. Toyokawa, *et al.*, "Development of a C-band RF gun with a coniferous-tree-type carbon nanostructure field emission cathode," 2015.
- [3] X. Li, M. Li, L. Dan, Y. Liu, and C. Tang, "Cold cathode RF guns based study on field emission," *Physical Review Special Topics-Accelerators and Beams*, vol. 16, no. 12, p. 123401, 2013.

# STUDIES ON BEAM INJECTION SYSTEM FOR WUHAN ADVANCED LIGHT SOURCE STORAGE RING

Y. Zou<sup>†</sup>, H. H. Li, Y. Chen, J. H. He, IAS, Wuhan University, Wuhan, China

## Abstract

Wuhan Advanced Light Source is the low-energy 4th generation advanced light source, which is proposed by Wuhan University, China. It includes a 1.5 GeV full-energy LINAC injector, a 180 m circumference, 1.5 GeV low-emittance storage ring, and a series of state-of-the-art beam lines. The standard 7BA magnetic focusing structure is adopted for the storage ring to lower the beam natural emittance and the lattice has been well-designed and optimized by multiple-objective genetic algorithm to maximize the dynamic aperture and energy acceptance. The dynamic aperture of the storage ring at injection can reach up to 8 mm in the horizontal plane, which makes the off-axis beam injection method possible. An off-axis beam injection scheme based on the pulsed nonlinear magnet is to be employed for the storage ring. Detailed studies about the beam injection scheme, including the beam optical design, nonlinear magnet design and optimization, have been performed and multi-particle simulations have also been carried out to study the beam injection procedure.

## INTRODUCTION

Wuhan Advanced Light Source (WALS) project was proposed by Wuhan University in 2016 [1], of which the accelerator includes a 1.5 GeV full-energy LINAC injector, and a 180 m circumference of low-emittance storage ring. The ring lattice is 8-fold symmetrical structure, of which each cell includes a hybrid 7BA structure and a 6.8 m of long straight section. The horizontal nature emittance is around 214 pm rad. Several measures have been taking into account to reach this target, e.g., employing bending magnets with both transverse and longitudinal gradients; employing two groups of the reverse dipoles, etc. A superbend magnet, of which the peak field strength reaches as high as 3.57 T, is adopted in the center of each cell to expand the application boundaries of the synchrotron radiation light source to the field of hard X-ray. Both permanent and electro-magnets are used in the storage ring. A series of sextupoles are employed at high dispersion zone to correct the chromaticity with moderate strength. Nonlinear effects would be introduced in the ring by sextupoles, which would reduce the dynamic aperture and momentum acceptance that need to be addressed. The multiple-objective genetic algorithm (MOGA) is introduced to optimise the lattice design in order to obtain the maximum dynamic aperture and energy acceptance. Two of the eight straight sections are reserved for beam injection system and RF system, respectively. Beam injection system is to bend the electron beam into the storage ring while RF system is to supplement the electron energy loss and stretch the bunches in the ring to increase the beam lifetime. The other straight

<sup>†</sup> Email address: ye.zou@whu.edu.cn

sections are reserved for insertion devices. Figure 1 shows one eighth of the lattice and Twiss parameters for the WALS storage ring while Table 1 shows the main parameters.

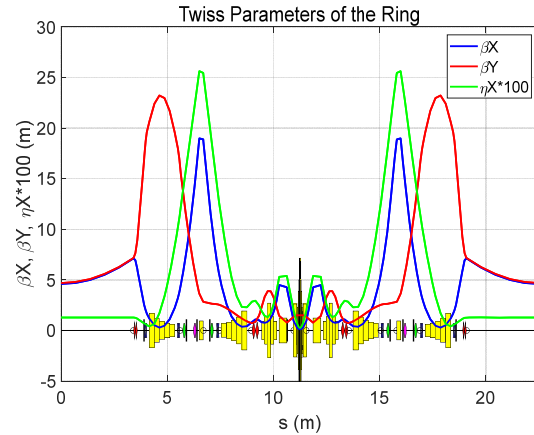


Figure 1: One eighth of the lattice and Twiss parameters for the WALS storage ring.

Table 1: the Main Parameters of the Storage Ring

Parameter	Value
Energy (GeV)	1.5
Beam current (mA)	500
Circumference (m)	180
Revolution period (ns)	600
Harmonic number	300
Horizontal emittance (pm rad)	214.8
Damping time H/V/S (ms)	7.08/17.02 /28.52
Betatron tunes Hor./Ver.	20.279/10.190
Energy acceptance (%)	4.2
Momentum compact factor	0.00036
Radiative loss per turn (keV)	105.9
Synchrotron phase (deg)	169.8
Bunch length (ps)	16.37

## BEAM INJECTION SCHEME

The beam injection system is employed to bend the electron beam into the storage ring. Since the beam dynamics aperture is relatively large, the off-axis accumulate injection scheme is available. The philosophy of injection system design is to seek high injection efficiency while being transparent to the storage beam. The traditional off-axis injection is normally implemented by a local bump formed by two groups of bump magnets. This method needs a relatively long injection straight section and the local bump is difficult to be fully closed mainly due to the fields error of the bump magnets. An alternative off-axis injection method based on pulsed nonlinear magnet (PNM) was firstly introduced at KEK [2, 3], and has been well studied and implemented at several facilities, e.g., BESSY [4],

MAXIV [5], ALS-U [6]. The key of this method is the design of the PNM, which is used to “kick” the injection beam into the ring acceptance while not affect the storage beam.

### Beam Injection Scheme for WALS Storage Ring

The off-axis accumulative injection scheme based on the PNM is proposed for the WALS storage ring. Figure 2 shows the layout of the injection scheme. A thick septum is used to bend the injected beam with 120 mrad, followed by a thin septum with the septum thickness of less than 1.5 mm to bend the injected beam with 45 mrad, while not affect the storage beam. Half sine-wave is adopted for both thin and thick septa with the wave width of 60  $\mu$ s and 120  $\mu$ s, respectively. The repetition rate is 10 Hz with the stability of 0.1% for both septa.

The PNM is employed after the septa to kick the injection beam into the ring acceptance, while ideally being transparent to the storage beam in the ring. The injection process is as follows: the beam from the exit of the thin septum (-11 mm, 2.5 mrad) drifts about 2.4 m to the entrance of the PNM (-5 mm, 2.5 mrad). The injection beam is then kicked by the PNM to the ring acceptance. To maximize the injection efficiency, the injection beam is being kicked to the center of the ring acceptance, as illustrated in Fig. 3. From Fig. 3, we can see that the injected beam will be kicked around 3 mrad and the maximum injection acceptance is about 1.6  $\mu$ m rad. Table 2 summarizes the main parameters for the injection procedure. Since the normalised emittance of the injection beam is at the level of nm rad, which is smaller than the injection acceptance with around 3 orders of magnitude, so there is no need to match the Twiss function of the injection beam. Nevertheless, on-axis injection is essential for the first few turns of injection since there is no aperture at first. So, a normal kicker (KIK1) is set after the PNM for first step of commissioning. When the dynamic aperture comes to above 5 mm, the PNM starts to work and the KIK1 will be shut down, the on-axis injection will be changed to off-axis injection.

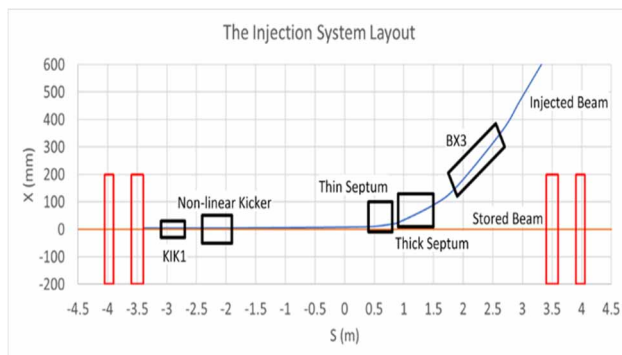


Figure 2: Layout of the injection system for the WALS storage ring.

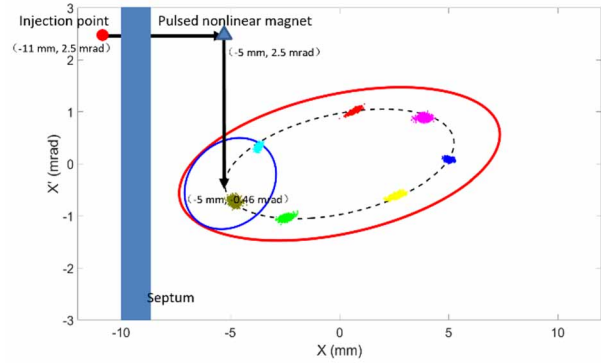


Figure 3: The beam injection procedure (Red ellipse: ring acceptance; blue ellipse: injection beam acceptance; black ellipse: C-S invariant of the injection beam).

Table 2: Main Parameters for Beam Injection Procedure

Parameter	Value
Beta function at the PNM H/V (m)	5.61/5.67
Injected beam position at thin septum exit H/V (mm)	11.0/0
Injected beam position at PNM entrance H/V (mm)	5.0/0
Injected beam angle at PNM entrance H/V (mrad)	2.5
Distance between thin septum and PNM (m)	2.4
PNM length (m)	0.5
PNM deflect angle (mrad)	3
Beam injection acceptance ( $\mu$ m rad)	1.6

### Pulsed Nonlinear Magnet Design

The idea of using a customized spatial magnet field distribution for beam injection was first introduced and implemented at KEK, where a pulsed sextupole injection kicker was proposed and implemented. Then, an alternative configuration was proposed at BESSY and successfully implemented at MAXIV based on an iron-free pulsed nonlinear kicker that uses eight current-carrying wires, which were fixed to a precisely machined ceramic chamber that can produce multipole fields to bend the injected to the ring acceptance while with zero field at the stored beam position. Experience at MAXIV indicates that heating of the PNM ceramic chamber due to the image currents circulating in a thin titanium coating, which is required for electrical continuity would be a big issue. A thicker titanium coating can effectively address this issue.

Figure 4 shows an upper half geometry and the resulting field distribution with different coating thicknesses of the pulsed nonlinear magnet for the WALS storage ring. From Fig. 4, we can see that the magnetic field can reach around 300 Gauss at 5 mm and has slightly difference with 1  $\mu$ m and 5  $\mu$ m of coating thicknesses. In this case, 5  $\mu$ m of coating thickness will be chosen for PNM to mitigate the heating issue. Table 3 shows the main parameters of the PNM.

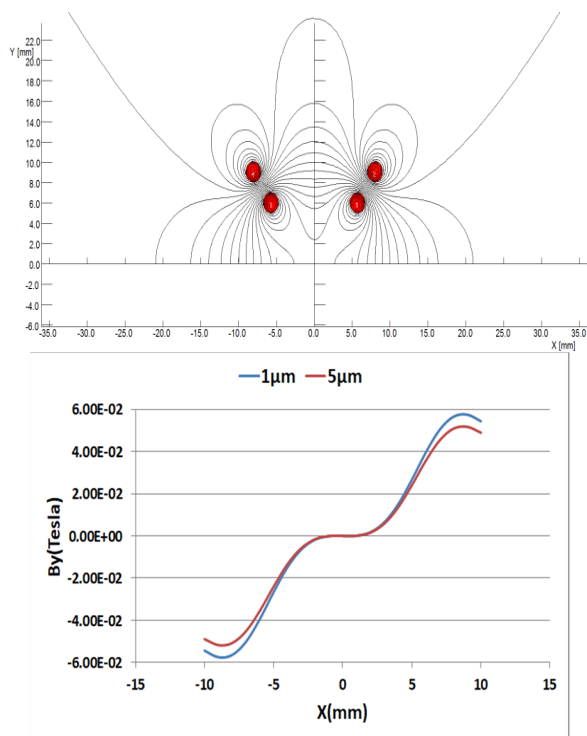


Figure 4: Upper half geometry (Upper) and the resulting field distribution with different coating thicknesses (Lower) of the pulsed nonlinear magnet for the WALS storage ring.

Table 3: the Main Parameters of the PNM

Parameter	Value
Length (m)	0.5
Bending angle (mrad)	3
Beam stay clear Hor./Ver. (mm)	20/14
Field strength (Gauss)	300 @5 mm
Pulse duration half sine-wave (μs)	1.2
Repetition rate (Hz)	10
Amplitude variations (%)	<1
Pulse timing variations (ns)	±5
Field flatness (Gauss)	<5 @±5 mm

### Multi-Particle Simulations

Multi-particle simulations have been performed with the AT code [7] to evaluate the beam injection scheme with PNM. Misalignment and field errors have been taken into account to calculate the horizontal acceptance for injection system. The PNM strength is chosen as  $48000 \text{ T/m}^3$  with 0.1% error and the misalignment errors are chosen as 0.15 mm and 0.25 mrad. Figure 5 shows the injection acceptance in horizontal phase space with errors. From Fig. 5, we can see that the injection point at -5 mm is a good position for injection which has a quite large error tolerance. Nevertheless, if the dynamic aperture is large enough, the injection point can be moved to -5.3 mm, which has a larger error tolerance.

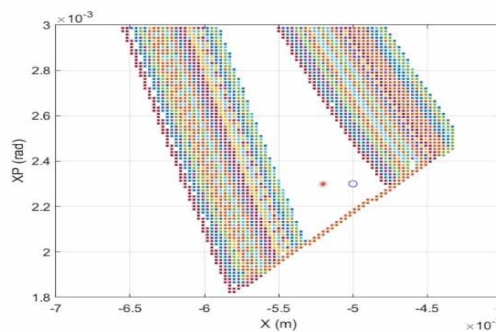


Figure 5: The injection acceptance in horizontal phase space with errors (black circle: current injection point; red star: optimal injection point).

## CONCLUSION

The off-axis injection scheme based on PNM has been introduced for the WALS storage ring due to the quite large dynamic aperture. The injection acceptance is much larger than normalised emittance of the injected beam. The iron-free type of PNM that uses eight current-carrying wires can provide enough magnetic field at injection point to bend the injected beam into the ring acceptance while keep quasi-transparent to the stored beam. Multi-particle simulations show the choice of the injection point is quite reasonable.

## ACKNOWLEDGMENTS

This project is supported by Science and Technology Major Project of Hubei Province (2021AFB001).

## REFERENCES

- [1] H. H. Li, Y. Deng, J. H. He, Y. Nie, L. Tang, J. Wang, Y. X. Zhu, "Project of Wuhan Photon Source", in *Proc. IPAC'21*, Campinas, SP, Brazil, 2021, pp. 346-349. doi:10.18429/JACoW-IPAC2021-MOPAB092
- [2] K. Harada, Y. Kobayashi, T. Miyajima, and S. Nagahashi, New injection scheme using a pulsed quadrupole magnet in electron storage rings, *Phys. Rev. Accel. Beams*, vol. 10, p. 123501, 2007.
- [3] H. Takaki, N. Nakamura, Y. Kobayashi, K. Harada, T. Miyajima, A. Ueda, S. Nagahashi, M. Shimada, T. Obina, and T. Honda, "Beam injection with a pulsed sextupole magnet in an electron storage ring", *Phys. Rev. Accel. Beams*, vol. 13, p. 020705, 2010.
- [4] O. Dressler, T. Atkinson, M. Dirsat, P. Kuske, and H. Rast, "Development of a Non-Linear Kicker System to Facilitate a New Injection Scheme for the BESSY II Storage Ring", in *Proc. IPAC'11*, San Sebastian, Spain, Sep. 2011, paper THPO024, pp. 3394-3396.
- [5] S. C. Leemann, "Pulsed sextupole injection for Sweden's new light source MAX IV," *Phys. Rev. Spec. Top. Accel. Beams*, vol. 15, no. 5, May 2012. doi: 10.1103/physrevstab.15.050705
- [6] C. Sun *et al.*, "Optimizations of nonlinear kicker injection for synchrotron light sources," *Phys. Rev. Accel. Beams*, vol. 23, no. 1, Jan. 2020. doi:10.1103/physrevaccelbeams.23.010702
- [7] A. Terebilo, "Accelerator Toolbox for MATLAB", SLAC-PUB-8732, 2001. doi: 10.2172/784910

# START TO END SIMULATION FOR A COMPACT THz-FEL \*

Ruiying Luo, Qushan Chen<sup>†</sup>

State Key Laboratory of Advanced Electromagnetic Engineering and Technology,  
 Huazhong University of Science and Technology, Wuhan, China

## Abstract

An oscillator type terahertz free electron laser (THz-FEL) is under construction at Huazhong University of Science and Technology (HUST). The designed electron beam energy ranges from 8 MeV to 14 MeV, and the radiation frequency ranges from 3 THz to 10 THz. FEL requires high quality electron beams of emittance, energy spread, bunch charge etc. To know the overall facility performance, a start-to-end simulation (from electron gun to the end of the oscillator) of the THz-FEL is performed. The simulation of the electron gun to the exit of the linac is performed using PARMELA, where the effect of space charge effects is considered. In addition, the effect of beam loading effect is considered for the linac. The transport line is matched and simulated using ELEGANT. GENESIS 1.3 and OPC is used for the lasing process. Results of the simulation are presented and discussed in this paper.

## INTRODUCTION

Terahertz (THz) radiation has attracted more and more attention because it holds the promise of enabling various new scientific and industrial applications. Due to the advantages of high output power, continuously adjustable wavelength, etc, terahertz free electron laser (THz-FEL) has received wide attention and research [1–3]. Huazhong University of Science and Technology (HUST) has constructed a compact oscillator type THz-FEL facility. It mainly consists of an injector and laser. The injector provides the required electron beam, which mainly includes EC-ITC (external cathode and independently tunable cavities) RF (radio frequency) gun, an S-band traveling wave (TW) linac and a double bend achromatic transport line. The laser consists of a pure permanent magnet type undulator and an optical resonant cavity [4]. The layout of HUST THz-FEL is depicted in Fig. 1.

Start-to-end simulation is an important method to understand the performance of FEL. It can take nonlinear effects into account and provide guidance for FEL design and optimization. To know the overall facility performance, a start-to-end simulation is performed. PARMELA is used to simulate the electron gun and linac, where the space charge effect is considered. ELEGANT is used to match and simulate the transport line. GENESIS 1.3 is used to simulate the interaction of the electron bunch with the radiation field in the undulator. And OPC is used to simulate the propagation of the radiation field in the optical cavity. In the paper, taking the beam energy of 14 MeV as an example, the parameters

of bunch at the entrance of the undulator is obtained and the performance of the radiation field is analyzed.

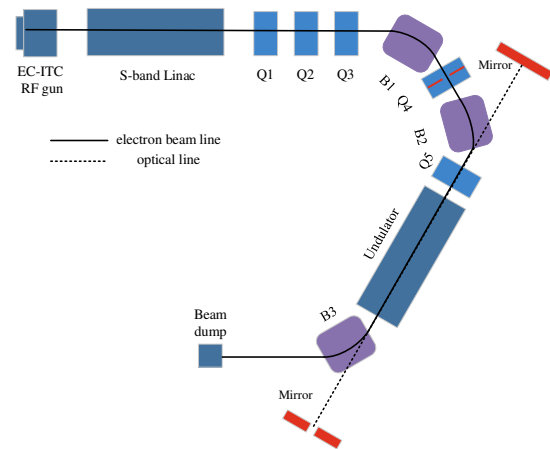


Figure 1: The layout of HUST THz-FEL.

## MACHINE LAYOUT AND SET UP

The EC-ITC gun is composed of a thermionic cathode and two independently tunable cavities. The electrons are extracted from the thermionic cathode by using a high voltage of 15 kV and then injected into two cascaded, but independent tuning standing wave cells [5]. The two standing wave cells (C1 and C2) bunch the electron pulses into multiple electron bunches with an interval of 350 ps and accelerate the bunches to 2.6 MeV. The maximum gradients of C1 and C2 are 40 MV/m and 89 MV/m, respectively. The bunch at the exit of the electron gun has a long tail, which results in beam loss during acceleration and transport processes.

The TW linac operates at 2856 MHz and can accelerates the bunch from 2.6 MeV to 8-14 MeV to meet the requirements of the lasing frequency varying from 3 to 10 THz. Instead of using the typical coupling output structure at the end, it employs coaxial load absorbing cells [6]. The total length of the linac is 875 mm, and there are 24 cells in all, of which the last 4 cells are coaxial load absorbing cells. Since the electron bunch has a long tail, the tail particles will absorb microwave power when they enter the linac. Therefore, careful analysis of the beam loading effect is required to obtain the acceleratng gradient of each cell.

The transport line transports the bunch from the exit of the linac to the entrance of the undulator and makes the bunch with suitable Twiss parameters at the entrance of the undulator. The bunch has a long tail, and the tail particles belongs to useless particles. Therefore, an x-directional slit

\* Work supported by National Natural Science Foundation of China (No.12175077)

<sup>†</sup> chenqushan@hust.edu.cn

with an aperture of 3 mm is placed in the middle of Q4 to remove the trail particles.

An undulator and optical cavity make up the laser. The radiation field is coupled to the output through a hole with a radius of 1 mm in downstream mirror. HUST THz-FEL is a low gain FEL with 30 undulator periods and a total optical cavity length of 2.887 m. Table 1 presents the parameters of the laser.

Table 1: Laser Parameters

Parameter	value
Undulator parameter $K$	1
Undulator period $\lambda_u$	32 mm
Number of Undulator periods $N$	30
Optical cavity length $L$	2.887 m
Radius of curvature of mirror $r$	1.473 m
Reflectivity of output cavity mirror $R$	0.95
Radius of Coupling hole	1 mm

## START TO END SIMULATION

### Injector

For the simulation of the injector, the longitudinal distribution of the bunch at the entrance of the linac needs to be obtained first for the analysis of the beam loading effect. We have proposed an algorithm called macro-particle tracking (MPT) to analyze beam loading effects with long tail bunch [7]. When the linac input power is 14 MW, the bunch can be accelerated to 14 MeV. The accelerating gradient of each cell is obtained by analysis of beam loading effect, and the maximum accelerating gradient is 19.4 MV/m. ELEGANT is used to match the dispersion and Twiss parameters of the transport line. The Twiss parameters at the entrance of the undulator are determined according to the requirement that the beam waist is located at the center of the undulator [8], which is  $\alpha_x = 1.0$ ,  $\beta_x = 1.2$ ,  $\alpha_y = 0.55$ ,  $\beta_y = 0.26$ .

The variation of bunch charge and energy spread from the electron gun to the entrance of the undulator is shown in Fig. 2. It can be seen that there is a beam loss throughout the injection process, which is caused by the long tail of the bunch. The initial thermionic cathode emits electrons with a charge of 875 pC, leaving only 174 pC at the entrance of the undulator. Since the bunch has a long tail, only the head particles are considered for the statistical parameters. Particles with a longitudinal position less than 15 ps are defined as the head of the bunch, which is mainly determined by the bunch length at the entrance of the undulator. There are two more obvious changes in energy spread curve. The first one appears at the linac, mainly due to the effect of the longitudinal electric field. The second one appears in the dispersion region. The sudden increase in energy spread is due to the increase in the number of head particles caused by the compression of the bunch length. The reduction of energy spread is mainly because particles with large transverse

positions are lost. Table 2 presents the bunch parameters at the entrance of the undulator.

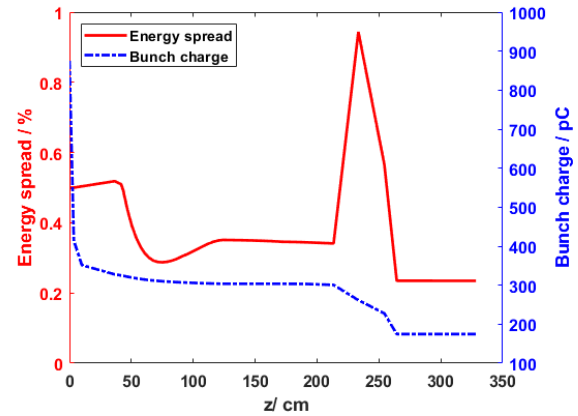


Figure 2: The variation of bunch charge and energy spread from the electron gun to the entrance of undulator

Table 2: Bunch Parameters at the Entrance of Undulator

Parameter	value
Beam energy $E$	14 MeV
peak current $I_p$	11.8 A
Energy spread $\delta_E$	0.24 %
Bunch charge $Q$	174 pC
Bunch length $\sigma_t$	4 ps
Normalized emittance in $x$ $\varepsilon_{xn}$	11.05 mm mrad
Normalized emittance in $y$ $\varepsilon_{yn}$	10.51 mm mrad

### Laser

GENESIS 1.3 combined with OPC allows the simulation of a three-dimensional free electron laser oscillator. We have performed time-dependent simulation of the FEL oscillator using these two software. For oscillator type FEL, cavity length detuning is an important parameter. Since GENESIS 1.3 can only set the cavity length detuning to an integer multiple of half wavelength, we use OPC to vary the relative position of the radiation field and the electron bunch to obtain an arbitrary cavity length detuning.

The frequency of radiation field is 10 THz when the beam energy is 14 MeV. Taking the cavity length detuning of 20  $\mu\text{m}$  as an example, the variation of peak power in the optical cavity and output peak power with the number of cavity passes are shown in Fig. 3. When saturation is reached, the peak power in the cavity is 12.8 MW, but the output power through the hole is only 0.28 MW. Only 2.2% of power in the optical cavity is coupled to output through the hole. When saturation is reached, the micro-pulse energy of radiation field is 2.2  $\mu\text{J}$ . The electron macro-pulse width is 4  $\mu\text{s}$ , and the electron micro-pulse repetition frequency is 2856 MHz. The macro-pulse energy of radiation field is 3 mJ. Fig. 4 demonstrates the power distribution and spectrum of the radiation field at the 20th and 200th cavity passes. In the

initial few passes, there are many frequencies of radiation field in the optical cavity, and as the radiation field gradually increases, there is finally only one major frequency in the optical cavity. At saturation, the longitudinal phase space at the exit of undulator is shown in Fig. 5. Electrons exhibit significant rotation in longitudinal phase space.

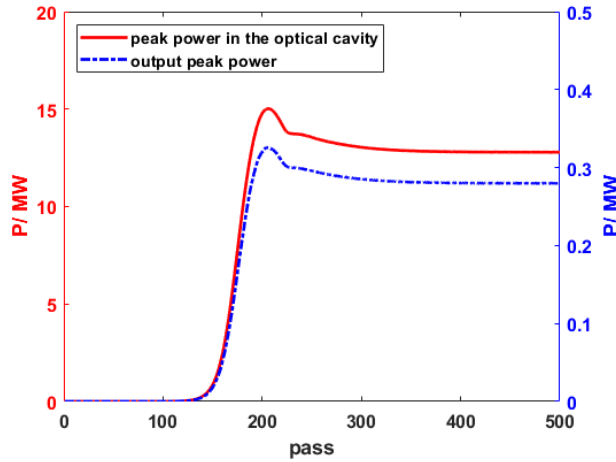


Figure 3: The variation of peak power with number of cavity passes.

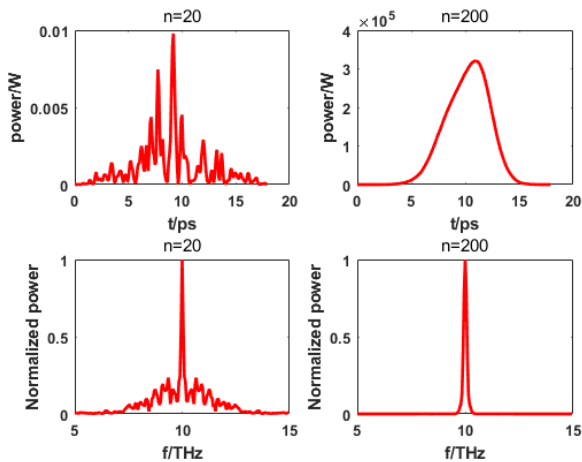


Figure 4: Time and frequency diagram at different cavity passes.

## DISCUSSION AND CONCLUSION

In this paper, a start-to-end simulation of the HUST THz-FEL facility is performed using a 14 MeV electron beam energy and a 10 THz radiation frequency as an example. For the injector, PARMELA and ELEGANT are used for simulation, where space charge effects and beam loading effects are considered. The parameters of the electron bunch at the entrance of the undulator are obtained. For the laser, a 3D time-dependent simulation of the FEL oscillator is accomplished by using GENESIS 1.3 and OPC. The results show that when the radiation frequency is 10 THz and the

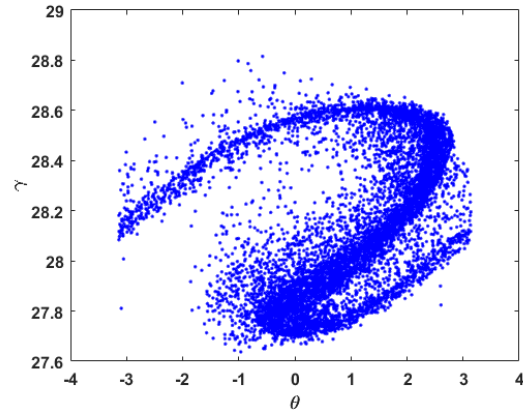


Figure 5: Electron longitudinal phase space at the exit of undulator.

cavity length detuning is 20  $\mu\text{m}$ , the macro-pulse energy of the radiation field is 3 mJ.

In this paper, the radiation performance at 10 THz frequency is preliminary simulated. The optimization of cavity length detuning and the verification of results will be reported in the future paper. In addition, the designed values of HUST THz-FEL radiation frequency are from 3 to 10 THz, but here we only report the case of 10 THz. Different radiation frequency will present different radiation performance, and the simulation results of S2E at different frequency will also be reported in future papers.

## REFERENCES

- [1] A. Nause *et al.*, “6 MeV novel hybrid (standing wave - traveling wave) photo-cathode electron gun for a THz superradiant FEL”, *Nucl. Instrum. Methods Phys.Res., Sect.A*, vol. 1010, p. 165547, 2021.
- [2] X.SU *et al.*, “Widely tunable narrow-band coherent Terahertz radiation from an undulator at THU”, *J. Instrum*, vol. 13, p. C01020, 2018.
- [3] Zhang Kaiqing *et al.*, “A Compact Accelerator-Based Light Source for High-Power, Full-Bandwidth Tunable Coherent THz Generation”, *Appl. Sci.*, vol. 11, p. 11850, 2021.
- [4] B. Qin, P. Tan, L. Yang, and X.L. Liu, “Design considerations of a planar undulator applied in a terahertz FEL oscillator”, *Nucl. Instrum. Methods Phys.Res., Sect.A*, vol. 727, pp. 90-96, 2013.
- [5] T.N. Hu *et al.*, “Development of a novel thermionic RF electron gun applied on a compact THz-FEL facility”, *Nucl. Instrum. Methods Phys.Res., Sect.A*, vol. 887, pp. 1-6, 2018.
- [6] Qushan Chen *et al.*, “RF conditioning and breakdown analysis of a traveling wave linac with collinear load cells”, *Phys. Rev. Accel. Beams*, vol. 21, p. 042003, 2018.
- [7] Ruiying Luo and Qushan Chen, “Analysis of the beam loading effect in a compact linac with long bunch tails”, *Nucl. Instrum. Methods Phys.Res., Sect.A*, vol. 1051, p. 168241, 2023.
- [8] Lei Yang *et al.*, “Optimization of the lattice function in the planar undulator applied for terahertz FEL oscillators”, *Chin. Phys. C*, vol. 38, p. 037004, 2014.

# BEAM DYNAMICS STUDY OF A PHOTO-INJECTOR AT WUHAN LIGHT SOURCE

Ze-Yi Dai, Yuan-Cun Nie<sup>†</sup>, Zi Hui, Jian-Hua Zhong, Lan-Xin Liu, Zi-Shuo Liu, Jia-Bao Guan, Wei-Wei Zhou, Kai-Shang Zhou, Ji-Ke Wang, Yuan Chen, Ye Zou, Hao-Hu Li, Jian-Hua He<sup>††</sup>  
The Institute for Advanced Studies, Wuhan University, Wuhan 430072, China

## Abstract

A photo-injector is under development at Wuhan Light Source (WMLS) to provide beams for the 1.5 GeV storage ring proposed as a fourth-generation synchrotron radiation light source and a future free electron laser (FEL) facility. The photo-injector and the following LINAC will be able to produce electron beams with low emittance ( $<2$  mm·mrad), high bunch charge ( $\sim 1$  nC), small energy spread ( $<0.5\%$ ), and short bunch length, which meet the requirements of the ring injection and the FEL operation simultaneously. The injector boosts the bunch energy to 100 MeV, which is mainly composed of a photocathode RF gun working at 2998 MHz, two solenoid coils for emittance compensation, and two 3-meter-long 2998 MHz traveling-wave (TW) accelerator units. Beam dynamics optimization of the photo-injector is presented in detail, which has been performed with multi-objective genetic algorithm (MOGA) combining theoretical analysis and ASTRA code. After optimization, the 95% projected transverse emittance has reached as low as 0.45 mm·mrad with an RMS bunch length of about 1.0 mm at a bunch charge of 1 nC. Such emittance is close to the intrinsic thermal emittance at the photocathode, implying that there is almost no emittance growth during beam transmission.

## INTRODUCTION

Including the 4th generation diffraction-limited storage rings (DLSR) and FEL, WMLS is proposed to be built in Wuhan, Hubei Province of China. It is planned to construct a 1.5 GeV low-energy storage ring with emittance less than 230 pm·rad in stage I. A photo-injector is an ideal candidate to guarantee performance of the accelerator, which can provide high brightness electron beams at the source.

The photo-injector system at WMLS boosts the bunch energy to 100 MeV with high bunch charge and low emittance, which consists of a 1.6-cell normal conducting RF (NCRF) gun followed by two 3 m-long S-band accelerator units, and two solenoids placed at the exit of the gun and around the first accelerator unit, respectively. Such a design can produce electron beams with high bunch charge and low emittance, which is widely adopted in the similar facilities, such as MAX IV, HALF, LCLS, Pal-FEL, Swiss-FEL, etc. [1-5].

\* Work supported by the Science and Technology Major Project of Hubei Province, China (2021AFB001).

<sup>†</sup> email address: nieyuncun@whu.edu.cn

<sup>††</sup> email address: hejianhua@whu.edu.cn

## BEAM DYNAMICS OPTIMIZATION WITH ASTRA CODE

Layout of the injector system is shown in Fig.1. The projected transverse emittance is determined by a large number of parameters, including transverse and longitudinal distribution of the driving laser pulse, field gradient and phase of the RF gun, magnetic field strength and profile excited by the solenoid coils, field gradient and phase of the S-band TW accelerator units, and locations of these hardwares. To find the global optimal solution, the multi-objective genetic algorithm (MOGA) combined with ASTRA code can be used [6,7]. However, before combination of the two tools, it is necessary to narrow down the scanning range of each parameter to accelerate convergence.

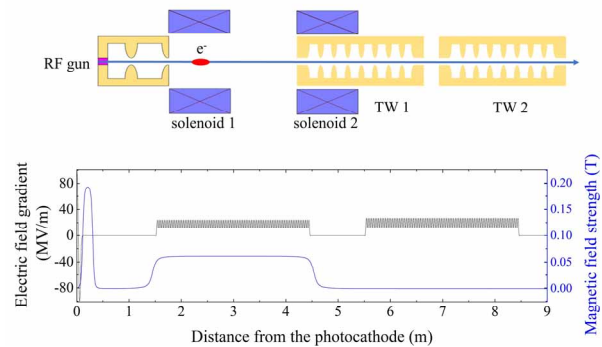


Figure 1: Layout of the photo-injector at WMLS.

The driving laser with temporal flat-top distribution and transversely truncated Gaussian distribution can linearize the space-charge effect [8]. According to experience, flat-top temporal distribution with a full-width-at-half-magnitude (FWHM) pulse length of around 10 ps and transversely about 1 sigma truncation of Gaussian distribution are selected in our simulation. The RMS transverse beam size can be calculated by  $Q = \pi r^2 \epsilon E$ , where  $E$  is the electric field during photoemission,  $r$  is the beam radius,  $\epsilon$  is permittivity of vacuum, and  $Q$  is initial bunch charge. To obtain a bunch charge of 1 nC or even higher, Cs<sub>2</sub>Te semiconductor photocathodes are preferred, which are widely used in photo-injectors with the advantage of high quantum efficiency (QE) and moderate lifetime. Operating RF field gradient in the gun should be as low as possible to prolong the photocathode lifetime. On the other hand, higher field gradient in the gun is profit for improving beam emittance. To make a compromise, the gradient was set to 100 MV/m. The intrinsic thermal emittance at the photocathode was set to 0.9 mm·mrad/mm.

To determine the range of the RF gun phase during optimization process of MOGA, the phase from  $-180^\circ$  to  $180^\circ$  has been scanned with a step of  $1^\circ$  in ASTRA. As implied in Fig.2, to have the output beam energy higher than 4 MeV and bunch charge of 1 nC at the same time, the corresponding phase range should be from  $-20^\circ$  to  $30^\circ$ .

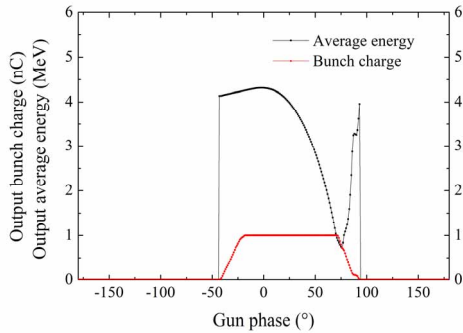


Figure 2: Output bunch charge and beam energy varying with the RF gun phase.

Solenoid 1 focuses the beam transversely and aligns the slice distribution of the bunch in the transverse phase space to compensate for the emittance growth owing to linear space charge forces. As shown in Fig. 3, effects of the magnetic field strength on the transverse emittance and beam envelope have been simulated. It can be seen that the beam envelope keeps increasing along the beamline without a beam waist when the magnetic field strength is 0.17 T. To match the beam to the first accelerator unit, the emittance compensation is needed and the beam envelope should be at a waist when injecting into the LINAC [9]. As the magnetic field strength increases, the beam waist moves closer to the gun with a smaller beam size. To make enough space for installation of beam diagnostics and vacuum systems, the distance between the entrance of TW1 and the photocathode surface need to be more than 1.2 m. As a result, magnetic field strength of solenoid 1 ranges from 0.17 T to 0.2 T in the following simulation of MOGA.

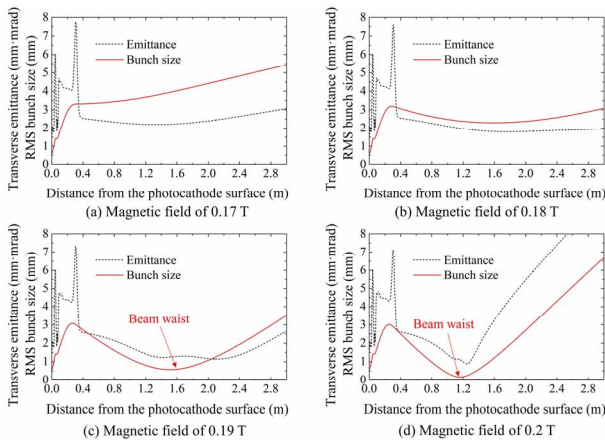


Figure 3: Transverse emittances and bunch sizes at various magnetic fields of Solenoid 1.

The matching waist size is determined by balancing the RF transverse force in the LINAC and the space charge force, which meets the relation of:

$$\sigma_{linac} = \frac{mc^2}{eE_{linac}} \sqrt{\frac{I}{2I_A\gamma}} \quad (1)$$

where  $\sigma_{linac}$  is the RMS transverse beam size at the entrance of the LINAC,  $E_{linac}$  is the peak accelerating field in the LINAC,  $\gamma$  is the relativity factor,  $mc^2$  is the rest energy of electron, and  $I_A=17$  kA. The average beam energy is about 4.3 MeV. To control the RMS beam size within 1 mm, the peak accelerating field larger than 9 MV/m will be required. Thus, the minimum peak accelerating field of TW1 is set to 9 MV/m, while the maximum value is limited to be 25 MV/m according to experience.

## BEAM DYNAMICS OPTIMIZATION BASED ON MOGA

Based on above discussions, the variables in the beam dynamics optimization based on MOGA are listed in Table 1. The population size was set to 100, and the number of generations for each optimization was set to 500. Progression of the Pareto front was monitored every 10 generations after initially 100. When there was no significant improvement of the Pareto front found, the optimization was stopped automatically. To compromise between running time and accuracy, 10k macro particles were used in beam dynamics simulations.

Table 1: Main Parameters for Beam Dynamics Optimization

Decision variables	Ranges
Laser transverse size <sup>a</sup> : $\sigma_{imp}$	0.5~2.0mm
Laser transverse cut <sup>a</sup> : $C_{Cut}$	0.5~2.0
Laser temporal FWHM	5 ~ 20 ps
Gun phase	$-20^\circ \sim 30^\circ$
TW1 start position <sup>b</sup>	1.2~2 m
TW1 field gradient	9~25 MV/m
Solenoid1 field	0.17~0.2 T
Solenoid2 field	0.01~0.2 T
Objectives	Goals
100% projected emittance	Minimize
RMS bunch length	Minimize
Constraints	Ranges
Bunch charge	1 nC
Output energy spread	< 0.5%

<sup>a</sup> Laser transverse truncated 2D-Gaussian distribution:

$$f(x) = \frac{1}{\sqrt{2\pi}\sigma_{imp}} \exp\left(-\frac{x^2}{2\sigma_{imp}^2}\right) \text{ for } |x| \leq C_{cut}\sigma_{imp}$$

<sup>b</sup> Distance from the surface of the photocathode

The obtained Pareto front composed of non-dominant solutions is shown in Fig. 4, which demonstrates the relationship between the 100% projected emittance and RMS bunch length. It indicates that selecting a lower

emittance is usually at the cost of allowing a longer bunch length.

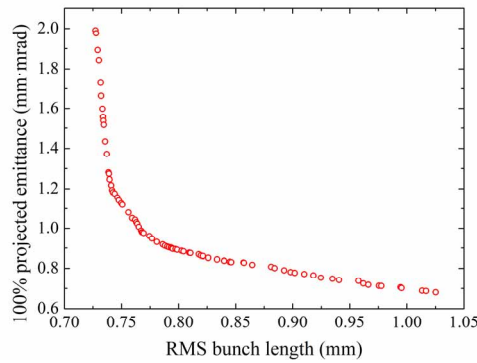


Figure 4: Multi-objective optimization results.

In our design, the minimum 100% projected emittance was set as the working points, and 100k macro particles were simulated to improve accuracy. In Fig. 5, the 100% projected emittance is 0.61 mm·mrad with an RMS bunch length of 1.03 mm. As shown in Fig. 6, the 95% normalized transverse emittance is 0.45 mm·mrad, which is equal to the intrinsic thermal emittance, with a peak current of about 100 A. The corresponding optimization results are shown in Table 2.

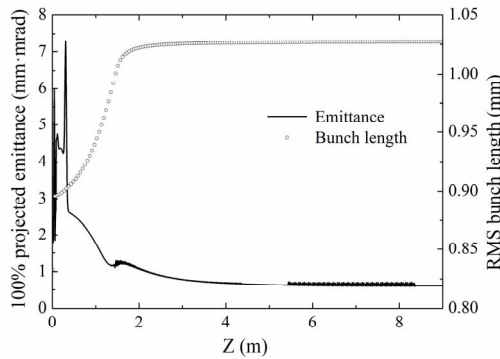


Figure 5: Evolution of 100% projected emittance and RMS bunch length along the photoinjector.

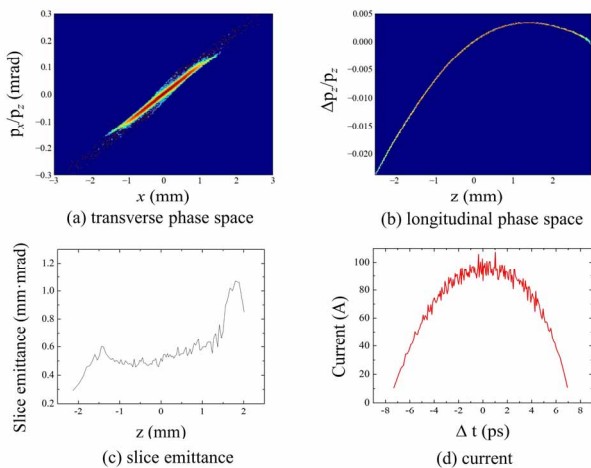


Figure 6: Beam dynamics optimization results at 1 nC.

Table 2: Output Bunch Parameters

Parameters	Values
Energy	100.8 MeV
Energy spread	414 keV
RMS bunch length	1.027 mm
100% projected emittance	0.61 mm·mrad
95% projected emittance	0.45 mm·mrad

## CONCLUSION

In this paper, physics design of the photo-injector at WHLS has been presented in detail. By combining MOGA and ASTRA, the accelerating and focusing components have been optimized globally. A 95% normalized projected transverse emittance as low as 0.45 mm·mrad has been obtained at a bunch charge of 1 nC, which is equal to the intrinsic thermal emittance at the photocathode, indicating that there is almost no emittance growth in the process of beam acceleration and transport.

## REFERENCES

- [1] J. Andersson, F. Curbis, L. Isaksson et al., The Pre-Injector and Photocathode Gun Design for the MAX IV SXL. in Proceedings of IPAC2019, Melbourne, Australia, 2064–2066 (2019).
- [2] W.X. Wang, C. Li, Z.G. He, et al., Commissioning the photocathode radio frequency gun: a candidate electron source for Hefei Advanced Light Facility. Nucl. Sci. Tech. 33, 1–9 (2022).
- [3] P. Emma, R. Akre, J. Arthur et al., First lasing and operation of an ångstrom-wavelength free-electron laser. Nat. Photonics 4,641–647 (2010).
- [4] J. Lee, I.S. Ko, J.H. Han et al., Parameter optimization of PALXFEL injector. J. Korean Phys. Soc. 72, 1158–1165 (2018).
- [5] T. Schietinger, M. Pedrozzi, M. Aiba et al., Commissioning experience and beam physics measurements at the SwissFEL injector test facility. Phys. Rev. Accel. Beams 19, 100702 (2016).
- [6] K. Deb, A fast and elitist multiobjective genetic algorithm: NSGAII. IEEE Trans. Evol. Comput. 6, 182–197 (2002).
- [7] K. Flöttmann: ASTRA: A space charge tracking algorithm, <http://www.desy.de/~mpyflo/>
- [8] F. Zhou, A. Brachmann, P. Emma et al., Impact of the spatial laser distribution on photocathode gun operation. Phys. Rev. ST Accel. Beams 15, 090701 (2012).
- [9] Serafini L, Rosenzweig J B. Envelope analysis of intense relativistic quasilaminar beams in rf photoinjectors: mA theory of emittance compensation. Phys. Rev. E, 1997, 55(6): 7565.

# COMPACT ACCELERATOR LIGHT SOURCE FOR INDUSTRIAL APPLICATIONS \*

Q.L. Zhang <sup>†1,2,3</sup>, C.L. Li<sup>1</sup>, K. Wang<sup>1,2,3</sup>, Y.X. Wang<sup>1,2,3</sup>, Y.J. Lu<sup>4</sup>

<sup>1</sup>Shanghai Advanced Research Institute, CAS, Shanghai, China

<sup>2</sup> Shanghai Institute of Applied Physics, CAS, Shanghai, China

<sup>3</sup> University of Chinese Academy of Sciences, CAS, Beijing, China

<sup>4</sup> Zhangjiang Laboratory, Shanghai, China

## Abstract

Synchrotron radiation has great application potential in industry. However, the large scale of modern light source has limited it from popular use. Compact accelerator light source has many virtues such as small scale, cost effectiveness, maintenance convenience, etc., which make it a main solution of light source application in industry. The idea has attracted great interests from many institutes, and much effort has been put into its research and development. In this paper we present a design of compact accelerator light source with very small scale. The lattice is very simple to ensure its compactness, while the beam parameters remain flexible to industry needs.

## INTRODUCTION

Synchrotron radiation was considered as byproduct of colliders in the past and turned to be a powerful tool in scientific research after the discovery of its merits in light spectrum, brightness, polarization, collimation, etc. Light sources have been widely used as a large research platform for scientists, and numerous achievements have been made with the help of synchrotron radiation.

A light source typically consists of an injector, a storage ring, some beamlines and experiment stations. To satisfy the needs of users, light sources are usually built in a large scale to accommodate various types of beamlines for research in different scientific fields. Such a large facility costs rather great, and funding from government is a routine approach.

Industrial applications of synchrotron radiations attract great interests as well. And some compact light sources were built in a research institute for industrial users or in an industrial enterprise. Most industrial applications are in medicine, pharmacy, chemistry, mechanics, and food industry. Some new applications such as EUV lithography are under exploration.

## INDUSTRIAL APPLICATIONS

Industrial application is a direct way for synchrotron radiation to benefit the society and improve people's life quality. With rapid growth of industrial demand, various applications of synchrotron radiation have been developed.

## Medical Applications

High energy photos can be used in the medical industry in many aspects including physical examination, cancer treatment, pharmacy and so on. X-ray is one of the most common ways for health checkup, and it is also a main part in the spectrum of synchrotron radiation. Gamma ray, which can be radiated from a compact accelerator using techniques such as Compton backscattering, has been used to break the DNA inside cancer cells, stop cancer from growing and cause its death eventually.

In hospitals synchrotron radiations from compact accelerators can be used for medical treatment, while pharmacy industry can use high intensity synchrotron radiations to improve efficiency of medicine research and development. X-ray has been used for protein structure analysis, and new medicine can be developed more efficiently. Another application of X-ray in medicine industry is to reform the drug particles and to conduct a proper distribution of different components.

## Chemical and Mechanical Industry

Catalyst plays an essential role in chemical industry, and synchrotron radiations can help to develop and manufacture high-efficiency kind. Other important applications of synchrotron radiation in chemical industry include material characteristics improvement etc. Using X-ray to detect flaws in solid object is a common approach for its merits such as flexibility, damage-free, and so on.

## Radiation Sterilization

Sterilization can help to preserve food for a long time. Radiation can be used to sterilize the products of food industry in a rather quick and easy-to-tune manner. Compact accelerator is a good option to provide radiations the food industry needs.

## EUV Lithography

Synchrotron radiation as a solution of light source for EUV lithography has been under exploration for years. Comparing to LPP (Laser-Produced Plasma) and DPP (Discharge Produced Plasma) light sources, compact accelerators can provide EUV light with high density and high collimation without pollution from metal particles or plasma ions.

\* Work supported by the Youth Innovation Promotion Association of Chinese Academy of Sciences (No.2020287)

† Email address: zhangql@sari.ac.cn

## TYPICAL FACILITIES

The scale of light sources for industrial applications varies from tens to hundreds of meters. And here we focus on the compact accelerators below 50 meters.

A typical compact accelerator light source is the Metrology Light Source (MLS) [1], open to users since 2008, mainly for applications of radiometry and technological development. The 48-m storage ring consists of 4 DBA cells. The injection is accomplished with an orbit bump covering half of the storage ring.

COSAMI [2] was proposed in 2017 as an EUV metrology source. The storage ring has a circumference of 25.8 meters and consists of two 5BA cells. High flux EUV light is radiated from an undulator with 16-mm period and 0.42-T magnetic field.

Here we present a compact accelerator light source with tow DBA cells (Fig. 1). The circumference of the ring is less than 30 meters, and two 5-m straights can be used to accommodate undulator, RF cavity and injection complex. The general design principles of compact accelerator and specific choice of our design is discussed in the following sections.

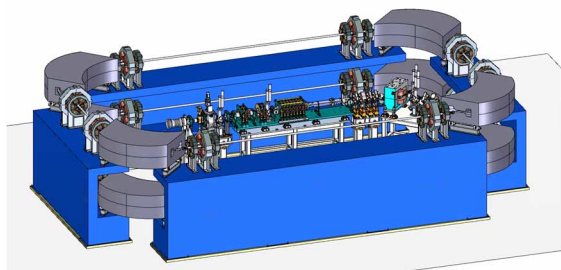


Figure 1: A design of compact accelerator light source.

## COMPACT RING LATTICE

The double bend achromat (DBA) has been the most successful and widespread lattice used for third generation synchrotron-based light sources. Using a DBA structure in a compact storage ring light source will result in significant horizontal dispersion due to the large bending angle of each dipole. Large horizontal dispersion generally leads to smaller energy acceptance, resulting in lower Touschek lifetime. However, a larger dispersion is beneficial for reducing the strength of sextupoles used for chromaticity correction, thereby weakening the nonlinearity introduced by sextupoles.

The emittance of the electron beam is proportional to the cube of the bending angle of the dipoles. Therefore, the triple bend achromat (TBA) lattice has the potential for lower natural emittance than the DBA lattice. Under the same conditions, TBA produces smaller dispersion than DBA, which will result in a greater intensity of the sextupoles used to correct chromaticity.

Small emittance demands strong focusing quadrupoles for stable beam dynamics and strong quadrupoles provoke large natural chromaticity in both transverse planes. Correcting large chromaticity demands strong sextupoles which produce strong nonlinear effects leading to issue such as shrunken dynamic aperture (DA) and reduced

beam lifetime. To mitigate the strong nonlinear effects, two classic lattice types have emerged, a hybrid MBA (HMBA) and a higher-order achromat (HOA). In the HMBA cell, the sextupoles are located in the two dispersion bumps at both sides of the cell, with sextupoles of each family separated by a  $-I$  transformation to cancel part of their nonlinear effects. While, in the HOA cell chromaticity-correcting sextupole magnets are distributed in each unit cell with strict phase advances over the cell such as to cancel basic geometric and chromatic resonance driving terms.

In ref.[3], a torus knot type storage ring that the beam orbit is not closed with one turn but return to the starting point after multiple turns around the ring has been proposed. If this type of lattice is adopted for a light source ring, many insertion devices can be installed for the use of synchrotron radiation and some new experimental techniques become available which could not be used in a small storage ring.

In our design, we used the simplest DBA structure, with only four focusing quadrupoles (two families) in a cell, and the defocusing force was provided by the edge field of the dipoles. Thanks to the low energy of the electron beam and large bending angle of the dipoles, the edge field of the dipoles is sufficient to provide the defocusing force required for stable beam motion. Due to the use of weaker focusing in DBA resulting in small phase advance, the correction of chromaticity between sextupoles does not meet the  $-I$  transformation. Therefore, we used two additional sets of harmonic sextupoles to optimize nonlinearity effects. Finally, the optimized dynamic aperture and beam life meet the design requirements.

## INJECTION

For compact storage rings, injection must be accomplished in a small space under a simple scheme with cost-effective considerations. Available methods involve pulse quadrupole/sextupole magnet (PQM/PSM) [4,5], non-linear kicker (NLK), strip line kicker, deflecting cavity, etc. Here we give a possible approach using NLK.

The NLK injection scheme (Fig. 2) is somewhat like traditional orbit bump injection except there is no orbit bump. The NLK injection scheme typically consists of one NLK instead of four kickers in traditional orbit bump injection scheme, hence the NLK injection requires less space for the kicker and removes the complication of synchronizing four pulsed kicker magnets.

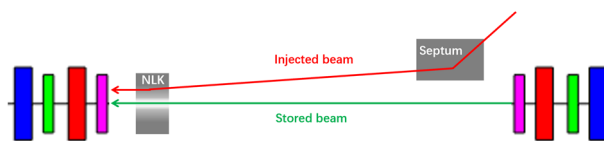


Figure 2: NLK injection scheme for compact test ring.

The NLK provides a nonlinear distribution of magnetic fields which has a maximum value off axis where the injected beam arrives and a zero or near-zero value at the centre where the stored beam passes by. Therefore, the injected beam will receive a kick from NLK and lose its transverse momentum and will be eventually captured by

the storage ring. In the meantime, the stored beam at the centre will receive no kick or slight kick, which significantly reduces the injection perturbations on the stored beam.

## TRANSPORT LINE

The transport line of the compact light source is used to transfer the beam from the injector or pre-accelerator to the storage ring or the next accelerator with more similar design comparing to general light source transport lines. The design goal is to minimize the loss of the beam on the transport line. Unlike general light source, the compact light source has greater restrictions on space layout. It is necessary to have high transport efficiency and high matching flexibility in a limited space, which is the main challenge of compact light source transport line design. When designing a compact light source transport line, the requirements must be put forward according to the actual situation and the beam conditions. The optimization calculation method is then used by appropriately adjusting the geometric and/or electromagnetic parameters of the transport line element. In order to reduce the difficulty of engineering implementation, the transport line design needs to control the magnet strength within a certain range. According to fit the requirements, the long transport line can be divided into multiple segments by different functions. The common magnetic focusing structure of the transport line is usually FODO or FODO-like, containing horizontal or vertical dipoles, several focused and defocused quadrupoles, which matches the beam twiss parameters. To achieve compact layout, high magnetic field strength and tight dividing space is a common choice.

## COLLECTIVE EFFECTS

High beam current improves efficiency for industrial applications. However, collective effects will be a challenge, especially for a low-energy compact accelerator.

Touschek effects dominate the beam lifetime. As the beam current increases, the Touschek scattering gets stronger and reduces beam lifetime significantly. Compromise between high beam current and sufficient beam lifetime must be considered. A common way to increase the beam lifetime is to increase the beam size. High harmonic cavity can be used to lengthen the beam in longitudinal plane. Coupling between horizontal and vertical plane can also significantly affect the beam lifetime. Figure 3 illustrates the calculation of Touschek lifetime under different coupling.

The intra-beam scattering (IBS) effect can cause growth in emittance and energy spread, which decreases the performance of a light source. A proper design should involve comprehensive considerations including IBS effect. For the 30-m test ring, the growth rate due to IBS effect is shown in Fig. 4.

Other effects should also be examined carefully. For example, coherent synchrotron radiation (CSR) effect can cause micro-bunch instability (MBI). Various measures

such as Landau damping are used to handle these collective effects.

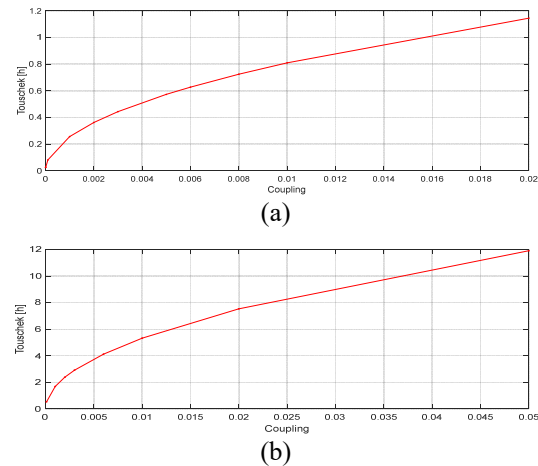


Figure 3: Touschek lifetime under different coupling (a) 30-m test ring with 100mA beam current (b) 100-m test ring with 1000mA beam current.

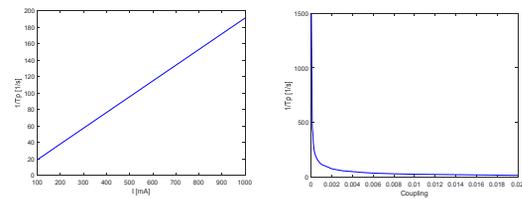


Figure 4: Growth rate of IBS effect (a) coupling 0.6% (b) beam current 200mA.

## CONCLUSION

We give a brief review of the industrial needs and applications of synchrotron light sources based on compact accelerators. Typical facilities and a design with simple DBA lattice is presented. The general design principles and specific design choice of the simple-DBA one are discussed, including storage ring lattice, injection scheme, transport line design and collective effects.

## REFERENCES

- [1] G. Brandt *et al.*, “The Metrology Light Source – The new dedicated electron storage ring of PTB”, *Nucl. Instr. And Meth. In Phys. Res. B* vol. 258, pp. 445-452, 2007.
- [2] T. Garvey *et al.*, “A compact storage ring for the production of EUV radiation,” in *Proc. ANS AccApp’17: 13<sup>th</sup> Int. topical meeting on the applications of accelerators*, Quebec City, Quebec, Canada, July 31 - August 4, 2017.
- [3] S. Sasaki *et al.*, “An innovative lattice design for a compact storage ring”, in *Proc. 2nd Int. Particle Accelerator Conf. (IPAC’11)*, San Sebastián, Spain, September 4-9, 2011, TUPO010.
- [4] K. Harada *et al.*, “New injection scheme using a pulsed quadrupole magnet in electron storage rings”, *Phys. Rev. ST Accel. Beams*, vol. 10, p. 123501, 2007.
- [5] H. Takaki *et al.*, “Beam injection with a pulsed sextupole magnet in an electron storage ring”, *Phys. Rev. ST Accel. Beams*, vol. 13, p. 020705, 2010.

# GENERALIZED LONGITUDINAL STRONG FOCUSING: A RING-BASED BEAM MANIPULATION TECHNIQUE

Zizheng Li, Xiujie Deng, Zhilong Pan, Chuanxiang Tang\*,

Tsinghua University in Beijing (TUB) Accelerator Laboratory Department of Engineering Physics

Alex Chao<sup>†</sup>, SLAC National Accelerator Laboratory (SLAC)

## Abstract

Generalized longitudinal strong focusing (GLSF), a ring-based beam manipulation technique, has been proposed to generate steady-state, nanometer-long electron bunches in laser-driven storage rings. Coherent EUV radiation can thus be produced with greatly enhanced power and photon flux, benefiting a wide range of scientific and industrial communities. The GLSF mechanism invokes precise transverse-longitudinal coupling dynamics and exploits the ultralow vertical beam emittance. In a GLSF ring, kW-level coherent EUV radiation is attainable.

## INTRODUCTION

Storage rings have driven great progress in science and technology for being stable, reproducible, and clean photon sources. Alongside the pursuit of low transverse emittance in recent decades, beam manipulation methods in storage rings flourish as well in longitudinal dimension. Bunches as short as picoseconds can be produced when rings operate in the low- $\alpha$  mode [1, 2].

Ambition to further shorten ring-stored bunches continues. Laser-driven storage rings have been proposed where laser modulators are used for bunching instead of RF cavities [3–6]. With a modulation wavelength reduction of roughly six orders of magnitude, the equilibrium bunch length can be notably decreased to tens of nanometers or even less. The longitudinal weak focusing (LWF) scheme employs low- $\alpha$  and low-partial- $\alpha$  optics to control bunch lengthening from stochastic photon emission [7, 8]. In a longitudinal strong focusing (LSF) ring, multiple laser modulators are included as longitudinal focusing elements, or ‘longitudinal quadrupoles’ [9, 10]. Bunches are strongly manipulated in longitudinal dimension and tailored to be short at specific locations of the ring.

It is challenging, yet rewarding, to manipulate steady-state bunches of nanoscale length in storage rings. These bunches are ideal producers of coherent extreme ultraviolet (EUV) radiation with greatly enhanced average power and photon flux desired by a wide range of applications. The boosted EUV photon flux within a narrow bandwidth has been craved by high-energy-resolution angle-resolved photoemission spectroscopy [11, 12]. In sub-meV bandwidth, key electronic structures may be probed, and findings in condensed matter physics could be made. The high average power of coherent EUV radiation suggests that a storage ring-based light source is a promising option for EUV lithography [13, 14]. Output

power may be tripled from existing facilities, leading to a huge promotion in microchip production. In addition, the produced photon pulse trains with pulse duration of tens of attoseconds is longed for by attosecond physics studies [15]. Besides, once ignored features of beam dynamics may now come to light, opening up a thrilling new frontier for accelerator physics.

Obstacles, however, prevent existing methods from being fully competent when attempting to obtain steady-state nanometer-long bunches on a turn-by-turn basis. Reducing the bunch length in the LWF scheme to nanometers calls for momentum compaction that is presently too low to be technically feasible, while the power of the modulation laser required by the LSF scheme exceeds the capacity of current optical cavities in continuous-wave mode.

A ring-based beam manipulation technique is then desired where coherent EUV radiation could be generated turn by turn. The power of the modulation laser should be controlled below 1 MW, which optical cavities could bear for continuous-wave mode operation. Besides, the status of electron bunches should be recovered after compression. This is pivotal in storage rings, unlike in single-pass devices.

## GENERALIZED LONGITUDINAL STRONG FOCUSING (GLSF)

In this paper, a ring-based beam manipulation technique, generalized longitudinal strong focusing (GLSF), is proposed to produce coherent EUV radiation turn by turn in laser-driven storage rings.

Strong manipulation is imposed and significant variation in bunch length is present in both LSF and GLSF schemes. The way electrons are handled, however, is different. Instead of manipulation in the longitudinal dimension alone, GLSF rings deliberately invoke transverse-longitudinal coupling beam dynamics. The GLSF scheme takes advantage of the extremely low vertical beam emittance in a horizontal-vertical-uncoupled planar ring, by projecting which a short bunch length can be attained with significantly reduced power of modulation lasers. Cancellation of the introduced coupling and modulation after the beam radiates is required to retain an uncoupled bunch and maintain the low vertical beam eigen-emittance, which is intended to be used again in following turns.

Calculation with practical beam parameters shows that kW-level quasi-continuous-wave coherent EUV radiation can be achieved turn by turn in a GLSF ring with a modulation laser power as low as 1 MW, allowing for continuous-wave operation of state-of-the-art optical cavities.

\* tang.xuh@tsinghua.edu.cn

<sup>†</sup> achao@slac.stanford.edu

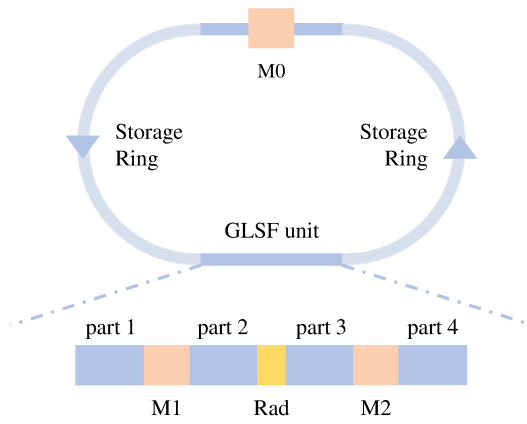


Figure 1: Sketch showing the general layout of a GLSF storage ring. GLSF unit includes four lattices (parts 1-4), two modulators (M1, M2), and a radiator (Rad).

The general composition of a GLSF storage ring is shown in Fig. 1. The GLSF unit consists of four dispersive lattices, two modulators, and one radiator. An additional modulator is placed in the storage ring for pre-bunching. In principle, however, this GLSF approach also works for RF-bunched or coasting beams.

The first half of the GLSF unit, or part 1, M1, and part 2, compresses the beam so that bunch length at RAD reaches the lowest possible degree and depends solely on beam vertical eigen-emittance. The de-compression is accomplished by the second half of the GLSF unit. The introduced modulation from M1 is canceled by M2 with the help of parts 2 and 3. And part 4 decouples the transverse and longitudinal dimensions, allowing an uncoupled bunch at the exit of the unit just as it is at the entrance. The low beam vertical eigen-emittance is then maintained.

It should be underlined that while the creation of EUV radiation is a typical application of GLSF, it is not the only one. The wavelength of coherent radiation could be further decreased, thus X-ray sciences may benefit. It might also be employed in traditional rings to produce coherent THz radiation and ultrashort pulses.

## LINEAR BEAM DYNAMICS

For demonstration, the vertical dimension is taken to be the transverse dimension involved in coupling. Therefore, the particle coordinates of interest are  $(y, y', z, \delta)$ . The linear beam dynamics of the GLSF unit, including bunch compression, modulation cancellation, vertical-longitudinal decoupling, and bunching factor, are covered in this section.

The first step is bunch compression, realized from the unit entrance to the radiator. The idea is to project the vertical emittance  $\epsilon_y$  to bunch length at the radiator  $\sigma_z(\text{Rad})$  and eliminate the contribution from the longitudinal emittance  $\epsilon_z$ . The modulator M1 is sandwiched by parts 1 and 2. By carefully choosing the dispersive terms of lattices and the modulation strength, the dependence of  $\sigma_z(\text{Rad})$  on initial particle coordinates  $(z, \delta)$  can be removed. And there is:

$$\sigma_z(\text{Rad}) = \sqrt{\epsilon_y \mathcal{H}_y(\text{Rad})}. \quad (1)$$

Here,  $\mathcal{H}_y(\text{Rad})$  is a lattice-dependent function.  $\sigma_z(\text{Rad})$  relies solely on vertical parameters.  $\sigma_z(\text{Rad}) = 3 \text{ nm}$  can be expected with  $\epsilon_y = 1 \text{ pm-rad}$  and  $\mathcal{H}_y(\text{Rad}) = 9 \mu\text{m}$ .

The next to do is modulation cancellation, accomplished in between the two modulators. To reverse the modulation M1 has made to the beam, a new laser modulator, M2, is expected. Their modulations have the same waveform and amplitude but the opposite sign. The lattice between them, parts 2 and 3 as a whole, is made longitudinally 'transparent' to particles. In other words, it is both achromatic and isochronous. Coordinates in the  $z$  dimension at M1 and M2 are thus identical. Modulations, as a result, precisely add up and cancel each other out. The cancellation works for arbitrary modulation waveforms.

The following move is vertical-longitudinal decoupling, handled by the lattice at the end of the unit. The intention to decouple is to keep the vertical emittance low and retain beam status for manipulation turn after turn. With modulation canceled, the remaining coupling terms are dispersion-related. A final lattice, part 4, is employed at the end to ensure that the entire GLSF unit is an achromat.

And last, the bunching factor at the radiator  $b_n$ , to whose square the power of coherent radiation is proportional, is investigated.  $b_n$  in a GLSF storage ring is given by [16]:

$$b_n = e^{-\frac{1}{2}k_r^2 \sigma_z^2(\text{Rad})} \left| \sum_{p=-\infty}^{\infty} J_p(n) e^{-\frac{1}{2}(n-p)^2 k_m^2 \sigma_z^2(\text{Mod})} \right|. \quad (2)$$

Here,  $k_r = \frac{2\pi}{\lambda_r}$  ( $k_m = \frac{2\pi}{\lambda_m}$ ) is the radiation (modulation) wave number, with  $\lambda_r$  ( $\lambda_m$ ) the radiation (modulation) wavelength.  $n = \frac{k_r}{k_m} = \frac{\lambda_m}{\lambda_r}$  is the harmonic number, and  $J_p$  is the  $p$ -th order Bessel function of the first kind.  $\sigma_z(\text{Mod})$  is the bunch length measured at M1. The presence of  $\sigma_z(\text{Mod})$  in  $b_n$  indicates that bunching factor can be degraded as the beam distribution is distorted by the nonlinear nature of the *sine-wave* modulation at M1.

The improvement of  $b_n$  is limited by [16]:

$$\sigma_{z-y}(\text{Mod}) \sigma_z(\text{Rad}) \geq \frac{\epsilon_y}{|h|}. \quad (3)$$

Here  $|h|$  is the effective modulation strength.  $\sigma_{z-y}(\text{Mod})$  is the coupling part of  $\sigma_z(\text{Mod})$ . For a given radiation power, the product of bunch lengths is roughly decided. The demand for laser power can then be lowered by exploiting the ultralow  $\epsilon_y$ . This is the exact gist of the GLSF scheme.

## AN ILLUSTRATIVE CASE

An illustrative case with magnet arrangement of a GLSF unit has been produced. It is tested for 'tracking', in which the particle coordinates of a launched Gaussian-distributed beam have been iterated turn-by-turn. Lattice components are linear transfer matrices. The modulation of M0 is sinusoidal ( $\Delta\delta = V_0 \sin(k_m z)$ ), while that of M1 and M2 is either linear ( $\Delta\delta = hz$ ) or sinusoidal ( $\lambda_m = 1 \mu\text{m}$ ).

When a linear modulation is applied at M1 and M2, a steady-state bunch length of 3 nm is attained at the radiator, and the bunching factor at 13.5 nm is 0.372. With sinusoidal modulation at M1 and M2, the bunching factor at 13.5 nm is still as large as 0.153. The produced radiation power can be calculated given the particle coordinates [17]. Assuming beam energy to be  $E_s = 400$  MeV, average beam current  $I = 1$  A, period number  $N_u$  and period length  $\lambda_u$  of the radiator undulator 160 and 1.25 cm, at 13.5 nm and within a  $\pm 2\%$  bandwidth, the average EUV radiation power is 1.2 kW. The modulation laser power is 1 MW, which is tolerable for up-to-date optical cavities in continuous-wave mode.

## CONCLUSION

A ring-based beam manipulation technique, generalized longitudinal strong focusing, is proposed to produce steady-state nanometer-long bunches. Coherent EUV radiation of 1.2 kW can be obtained with 1 MW modulation laser.

## ACKNOWLEDGEMENTS

This work is supported by National Key R&D Program of China (Grant No. 2022YFA1603400), National Natural Science Foundation of China (NSFC Grant No. 12035010), and Tsinghua University Initiative Scientific Research Program.

## REFERENCES

- [1] J. Feikes, *et al.*, “Metrology Light Source: The first electron storage ring optimized for generating coherent THz radiation”, *Phys. Rev. ST Accel. Beams*, vol. 14, no. 3, p. 030705, 2011. doi:10.1103/PhysRevSTAB.14.030705
- [2] I. Martin, G. Rehm, C. Thomas, and R. Bartolini, “Experience with low-alpha lattices at the Diamond Light Source”, *Phys. Rev. ST Accel. Beams*, vol. 14, no. 4, p. 040705, 2011. doi:10.1103/PhysRevSTAB.14.040705
- [3] D. Ratner and A. Chao, “Steady-state microbunching in a storage ring for generating coherent radiation”, *Phys. Rev. Lett.*, vol. 105, no. 15, p. 154801, 2010. doi:10.1103/PhysRevLett.105.154801
- [4] A. Chao, E. Granados, X. Huang, H. Luo, and D. Ratner, “High Power Radiation Sources using the Steady-state Microbunching Mechanism”, in *Proc. IPAC’16*, Busan, Korea, June 2016, pp. 1048-1053. doi:10.18429/JACoW-IPAC2016-TUXB01
- [5] C. Tang *et al.*, “An Overview of the Progress on SSMB”, in *Proc. FLS’18*, Shanghai, China, June 2018, pp. 166-170. doi:10.18429/JACoW-FLS2018-THP2WB02
- [6] X. Deng *et al.*, “Experimental demonstration of the mechanism of steady-state microbunching”, *Nature*, vol. 590, no. 7847, pp. 576-579, 2021. doi:10.1038/s41586-021-03203-0
- [7] Z. Pan *et al.*, “A Storage Ring Design for Steady-State Microbunching to Generate Coherent EUV Light Source”, in *Proc. FEL’19*, Hamburg, Germany, Nov. 2019, pp. 700-703. doi:10.18429/JACoW-FEL2019-THP055
- [8] X. Deng *et al.*, “Breakdown of classical bunch length and energy spread formula in a quasi-isochronous electron storage ring”, *Phys. Rev. Accel. Beams*, vol. 26, no. 5, p. 054001, 2023. doi:10.1103/PhysRevAccelBeams.26.054001
- [9] Y. Zhang *et al.*, “Ultralow longitudinal emittance storage rings”, *Phys. Rev. Accel. Beams*, vol. 24, no. 9, p. 090701, 2021. doi:10.1103/PhysRevAccelBeams.24.090701
- [10] X. Deng, A. Chao, W. Huang, and C. Tang, “Courant-Snyder formalism of longitudinal dynamics”, *Phys. Rev. Accel. Beams*, vol. 24, no. 9, p. 094001, 2021. doi:10.1103/PhysRevAccelBeams.24.094001
- [11] A. Damascelli, Z. Hussain, and Z. Shen, “Angle-resolved photoemission studies of the cuprate superconductors”, *Rev. Mod. Phys.*, vol. 75, no. 2, pp. 473-541, 2003. doi:10.1103/RevModPhys.75.473
- [12] B. Lv, T. Qian, and H. Ding, “Angle-resolved photoemission spectroscopy and its application to topological materials”, *Nat. Rev. Phys.*, vol. 1, no. 10, pp. 609-626, 2019. doi:10.1038/s42254-019-0088-5
- [13] V. Bakshi, *EUV lithography*, 2nd ed. Bellingham, USA: SPIE press, 2018.
- [14] J. Miyazaki, and A. Yen, “EUV Lithography Technology for High-volume Production of Semiconductor Devices”, *J. Photopolym. Sci. Technol.*, vol. 32, no. 2, pp. 195-201, 2019. doi:10.2494/photopolymer.32.195
- [15] F. Krausz, and M. Ivanov, “Attosecond physics”, *Rev. Mod. Phys.*, vol. 81, no. 1, pp. 163-234, 2009. doi:10.1103/RevModPhys.81.163
- [16] X. Deng, W. Huang, Z. Li, and C. Tang, “Harmonic generation and bunch compression based on transverse-longitudinal coupling”, *Nucl. Instrum. Methods. Phys. Res., Sect. A*, vol. 1019, p. 165859, 2021. doi:10.1016/j.nima.2021.165859
- [17] X. Deng *et al.*, “Average and statistical properties of coherent radiation from steady-state microbunching”, *J. Synchrotron Rad.*, vol. 30, no. 1, pp. 35-50, 2023. doi:10.1107/S1600577522009973

# LOW-ALPHA STORAGE RING DESIGN FOR STEADY-STATE MICROBUNCHING TO GENERATE EUV RADIATION

Zhilong Pan\*, Chuanxiang Tang, Xiujie Deng, Wenhui Huang, Alex Chao, Zizheng Li  
Tsinghua University, Beijing, China

## Abstract

A new concept is proposed to minimize the longitudinal emittance of a low momentum compaction factor (low-alpha) storage ring which has the capability to stably store sub-femtosecond electron bunches for the first time. This storage ring is designed for steady-state microbunching (SSMB) to generate kW EUV radiation with level average power, combined with a carefully designed insertion device in which the electron bunches are compressed to nm-long at radiator [1]. The proposed design approach can be applied to any quasi-isochronous storage rings to yield very high power radiation due to longitudinal coherence of the radiation. We obtain an optimal lattice design by minimizing global and local momentum compaction factors simultaneously. Nonlinear dynamics and IBS effect are discussed in this lattice, as there are many differences for them in traditional rings and SSMB ring.

## INTRODUCTION

SSMB, is a new concept, by subtly manipulating the longitudinal phase space of electron bunches in storage rings, to maintain micro-bunches stably [2]. while bunches with nm-level length are maintained and radiate in super high repetition frequency, the EUV radiation with ~ kW average power could be produced, with a wide variety of applications in high-volume chip manufacturing [3] and many advanced science researches, such as high energy resolution in angle-resolved photon-emission spectroscopy [4]. There are many progresses in SSMB research recent years, such as the successful proof of principle experiment [5], several proposed schemes to generate kW average power EUV radiation based on SSMB [6, 7]. Among the proposed schemes, a SSMB storage ring in which electron bunches with a bunch length of less than 100 nm should be stored is essential. In normal storage rings, the achieved bunch length of stored electron bunches is on the magnitude of mm or larger. One important reason is that radio-frequency (RF) cavity whose wavelength is on the magnitude of meter is used to focus the bunch in longitudinal phase space. In SSMB rings, RF will be replaced by laser modulator (LM), with a modulation wavelength of micron-meter. Another issue is low-alpha mode operation of storage rings, M. Sands's formula breaks down as the global alpha of storage ring reaches the minimum limit as many literature pointed out [8, 9]. The underlying physics behind the breakdown is statistical property of radiation excitation, and it can also be defined as partial alpha effects. That is to say, the local alpha all along the ring should be minimized

in lattice design. We introduce the method to minimize local alpha in SSMB storage ring lattice design and give the ring design results first. Based on the ring, we discuss the difference of nonlinear dynamics and IBS between SSMB ring and normal ring. Conclusion is given at the end.

## SSMB RING LATTICE DESIGN

### Design Concept

The SSMB ring, as we mentioned above, should be a low-alpha ring, but also be a low local alpha ring. If we define a point for bunch length observation, then the bunch length contribution from local alpha ( $\widetilde{\alpha}_c$ ) should be the variation of all the alpha (defined as  $I_{\widetilde{\alpha}_c}$ ) from any radiation point to observation point, written as

$$\widetilde{\alpha}_{c,s_r} = \frac{1}{C} \int_{s_r}^{s_0} \frac{\eta(s)}{\rho} ds. \quad (1)$$

Where  $s_r$  is radiation point,  $s_0$  is observation point,  $\eta$  is dispersion function,  $\rho$  is bending radius,  $C$  is the total length from  $s_r$  to  $s_0$ . To minimize  $I_{\widetilde{\alpha}_{c,s_r}}$ , each local  $\widetilde{\alpha}_{c,s_r}$  should be minimized. A straightforward idea is to make the momentum compaction in each dipole be zero and decrease the bending angle of each dipole simultaneously.

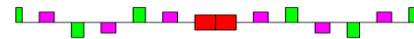


Figure 1: Layout of main cell. The red rectangle represents dipole, green rectangles represent quadrupoles, rose red rectangles represent sextupoles.

Here, we give an instance of lattice design to illustrate the idea above. The basic structure used to achieve the idea is shown in Fig. 1, called main cell. The whole ring will be mainly constructed by main cell. To explain more detailed, we can assume the ring consists of several super periods, for example, two. And each super period will be constructed by several main cells and match cells as shown in Fig. 2.



Figure 2: Sketch of super period constitution.

Looking back on the main cell, one objective is making the integration  $\int_0^{C_1} \frac{\eta(s)}{\rho} ds$  be zero, while  $C_1$  is the total length of main cell. As Fig. 2 shows, the main cell is periodically arranged. If there is, for example, 7 main cells in a super cell, then the tunes of main cell should better be set as  $\nu_x = \frac{i}{7}$  and  $\nu_y = \frac{j}{7}$  which is beneficial for nonlinear dynamics, while  $i$  and  $j$  are integers less than 7.

\* panzl@mail.tsinghua.edu.cn

## Ring Lattice Layout and Parameters

Here, the ring lattice layout is shown in Fig. 3. It is consisted of two super periods, and 12 main cell in each super period.

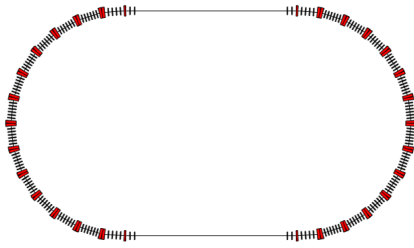


Figure 3: The layout of ring lattice.

And the twiss functions of the ring is shown in Fig. 4.

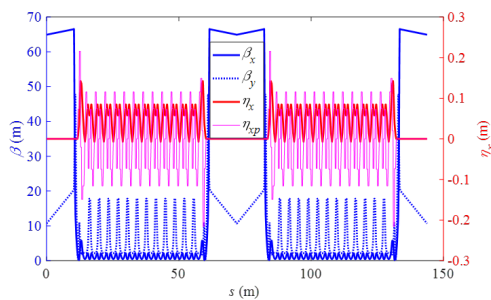


Figure 4: The twiss functions of the ring.

The lattice arrangement and twiss functions of main cell is shown in Fig. 5.

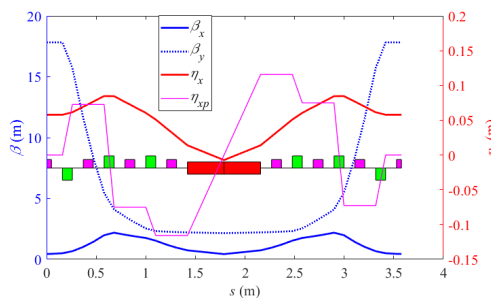


Figure 5: Lattice arrangement and twiss functions of main cell. The red represents dipoles, the green represents quadrupole, the rose red represent sextupole.

The main parameters of the ring are listed in Table 1. The bunch length is calculated by SLIM formula [10], while local momentum compaction is self-consistently considered. The damping time of the ring is a little bit large, more optimization is needed by decreasing bending radius or adding damping wigglers.

Longitudinal dynamics in SSMB ring should be carefully studied, as LM is used as the longitudinal focusing element. The bucket height is only  $6.4 \times 10^{-4}$  with the parameters of Table 1, the quantum lifetime then will be very small if no

Table 1: Ring Parameters

Parameters	Value	Units
Circumference	143.78	m
Beam energy	400	MeV
Tunes x/y	18.58/7.11	/
Phase slippage factor	2.69e-6	/
2nd order phase slippage factor	1.23e-4	/
Natural emittance	281.7	pm
LM wavelength	1	μm
LM voltage	100	kV
Energy spread	$2.23 \times 10^{-4}$	/
Bunch length at straight	91.4	nm
Damping times (x/y/z)	542.2/542.4/271.1	ms
Energy loss per turn	0.71	keV

additional trapping element is used. A barrier bucket or an additional RF could be the potential choice. The detailed study is on-going.

## NONLINEAR DYNAMICS

As the LM bucket width is on the magnitude of micrometer, extra attention is needed in transverse-longitudinal (T-L) coupling non-linearity in SSMB rings. The particles with a transverse size will move in different path with reference particle and result in the path length deviation. In normal storage rings, this path length deviation is typically less small than the RF wavelength and can be easily hold by the phase stability principle. While in SSMB ring, the path length deviation from T-L coupling is very likely larger than the laser wavelength (μm) without careful optimization, so the particle will jump between different LM buckets making the phase stability break down.

Here, we briefly discuss T-L coupling to make it more clear for SSMB ring optimization. The particle motion in storage ring can be described by Hamiltonian. We define the hamiltonian by  $H$ , given as (under 3rd order, longitudinal Hamiltonian is not included)

$$H(J_x, J_y, \delta) = \mu_x J_x + \mu_y J_y + h_{11001} J_x \delta + h_{00111} J_y \delta + |h_{20001}| J_x \delta e^{-2\phi_x j} + |h_{00201}| J_y \delta e^{-2\phi_y j}, \quad (2)$$

where  $J_x$  and  $J_y$  represent the action of the particle in  $x$  and  $y$  direction respectively.  $\mu_x$  and  $\mu_y$  are betatron phase advance in  $x$  and  $y$  direction respectively.  $\delta$  is relative energy deviation,  $\phi_x$  and  $\phi_y$  are betatron phase. The last four terms describe the T-L coupling at dispersion free location, and  $h_{11001}$ ,  $h_{00111}$ ,  $h_{20001}$ ,  $h_{00201}$  determine the strength of T-L coupling.

In Hamiltonian system, the path length deviation per turn for a particle can be expressed as (we only talk the contribution from low order T-L coupling here)

$$\Delta z = \frac{\partial H}{\partial \delta} = h_{11001} J_x + h_{00111} J_y + |h_{20001}| J_x e^{-2\phi_x j} + |h_{00201}| J_y e^{-2\phi_y j}, \quad (3)$$

Eq. (3) says the path length deviation per turn is related to transverse action and some coefficients. The first two terms  $h_{11001}$  and  $h_{00111}$  are independent with betatron phase, which means it will not vary turn by turn. The last two terms consist betatron phase, which means the path length deviation per turn will oscillate with betatron phase. Let  $h_{20001} = |h_{20001}|e^{-2\phi_x j}$  and  $h_{00201} = |h_{00201}|e^{-2\phi_y j}$ .

Comparing the definition of chromaticity, we can get

$$\begin{aligned} h_{11001} &= 2\pi\xi_x \\ h_{00111} &= 2\pi\xi_y. \end{aligned} \quad (4)$$

Without special design, the magnitude of  $|h_{20001}|$  and  $|h_{00201}|$  will be 10 or larger. When injection, the action of injected particle could be  $1 \times 10^{-7}$  m (with 1 mm size and  $\sim 10$  m beta function), then the path length deviation will oscillate with a amplitude of  $A_x = |h_{20001}|J_x \sim 10 * 10^{-7} \sim 1 \mu\text{m}$ . As we mentioned above, the LM bucket width is  $1 \mu\text{m}$ , the T-L coupling will result in that a particle with large transverse action is very likely to jump to adjacent LM bucket and make the longitudinal motion unstable.

We have done preliminary optimization for those T-L coupling terms, and the dynamic aperture (DA) of the ring is shown in Fig. 6.

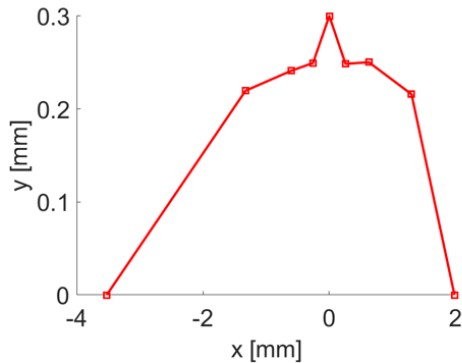


Figure 6: DA of ring, after 20000 turns tracking.

## INTRA-BEAM SCATTERING

Intra-beam scattering (IBS) is coulomb scattering effect due to space charge inside the beam of charged particles. IBS will induce increase of beam emittance in low energy electron storage rings. In normal rings, the bunch length of electron bunch can be regarded as constant around the ring. But it varies dramatically in SSMB ring, as shown in Fig. 7. So the widely used formulas for IBS growth rate calculation is not suitable anymore in SSMB ring.

The IBS growth rate derived by Bjorken and Mtingwa [11] is

$$\frac{1}{T_i} = 4\pi A(\log) \left\langle \int_0^\infty \frac{d\lambda \lambda^{1/2}}{[\det(L + \lambda I)]^{1/2}} \left\{ \text{Tr}L^{(i)} \text{Tr}\left(\frac{1}{L + \lambda I}\right) - 3\text{Tr}L^{(i)}\left(\frac{1}{L + \lambda I}\right) \right\} \right\rangle. \quad (5)$$

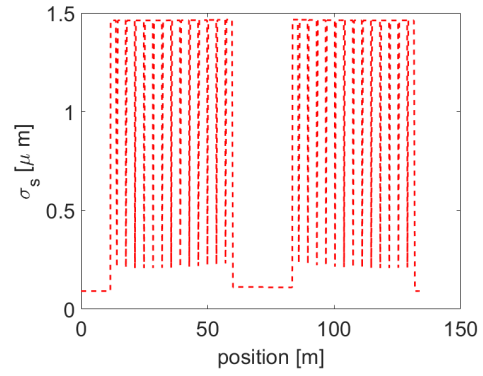


Figure 7: Bunch length of electron bunch vs observation point in SSMB ring.

The  $i$  represent three different directions,  $x$ ,  $y$ ,  $s$ , and  $L = L^{(x)} + L^{(y)} + L^{(s)}$ . In SSMB ring, the  $L^{(s)}$  should be replaced as

$$\begin{aligned} L^{(s)} &= \frac{\gamma^2}{\sigma_p^2} \begin{bmatrix} 0 & 0 & 0 \\ 0 & 0 & 0 \\ 0 & 0 & 1 \end{bmatrix} \\ \Rightarrow L^{(s)} &= \begin{bmatrix} \frac{\gamma_s \eta^2}{\epsilon_s} & 0 & -\gamma \frac{\alpha_s \eta}{\epsilon_s} \\ 0 & 0 & 0 \\ -\gamma \frac{\alpha_s \eta}{\epsilon_s} & 0 & \frac{\gamma^2 \beta_s}{\epsilon_s} \end{bmatrix} \end{aligned} \quad (6)$$

We adopt the correction and calculate the equilibrium beam emittance considering the IBS effect at selected beam current, and the results fit well with SAD in which any coupling situation can be handled for IBS calculation.

## CONCLUSION

In this paper, a SSMB ring who can store the electron bunches with very short bunch length under 100 nm has been designed. A method to minimize the local momentum compaction effect is proposed. We also talk about the non-linear dynamics in this ring, and give a preliminary thoughts to enlarge the DA. The IBS calculation could be a little bit different with in the normal ring. We clarify where the difference comes from and make some correction on widely used IBS growth rate formulas.

## REFERENCES

- [1] Z. Li, X. Deng, Z. Pan, C. Tang, and A. Chao, "Generalized longitudinal strong focusing: A ring-based beam manipulation technique," SAP, Sichuan, China, 2023, paper MOPB037, this conference.
- [2] D. F. Ratner and A. W. Chao, "Steady-state microbunching in a storage ring for generating coherent radiation," *Physical review letters*, vol. 105, no. 15, p. 154 801, 2010.
- [3] V. Bakshi, "Euv lithography," 2009.
- [4] A. Damascelli, Z. Hussain, and Z.-X. Shen, "Angle-resolved photoemission studies of the cuprate superconductors," *Reviews of modern physics*, vol. 75, no. 2, p. 473, 2003.

- [5] X. Deng *et al.*, “Experimental demonstration of the mechanism of steady-state microbunching,” *Nature*, vol. 590, no. 7847, pp. 576–579, 2021.
- [6] Y. Zhang *et al.*, “Ultralow longitudinal emittance storage rings,” *Physical Review Accelerators and Beams*, vol. 24, no. 9, p. 090 701, 2021.
- [7] B. Jiang *et al.*, “A synchrotron-based kilowatt-level radiation source for euv lithography,” *Scientific Reports*, vol. 12, no. 1, p. 3325, 2022.
- [8] Y. Shoji, H. Tanaka, M. Takao, and K. Soutome, “Longitudinal radiation excitation in an electron storage ring,” *Physical Review E*, vol. 54, no. 5, R4556, 1996.
- [9] X. Deng *et al.*, “Breakdown of classical bunch length and energy spread formula in a quasi-isochronous electron storage ring,” *Physical Review Accelerators and Beams*, vol. 26, no. 5, p. 054 001, 2023.
- [10] A. Chao, “Slim—a formalism for linear coupled systems,” *Chinese Physics C*, vol. 33, no. S2, pp. 115–120, 2009.
- [11] J. D. Bjorken and S. K. Mtingwa, “Intrabeam scattering,” *Part. Accel.*, vol. 13, no. FERMILAB-PUB-82-47-THY, pp. 115–143, 1982.

# STUDY ON XiPAF SYNCHROTRON NONLINEAR DYNAMICS\*

X. Y. Liu<sup>1,2,3</sup>, H. J. Yao<sup>1,2,3†</sup>, Y. Li<sup>1,2,3</sup>, Z. J. Wang<sup>1,2,3</sup>, Y. Xiong<sup>1,2,3</sup>, P. Z. Fang<sup>1,2,3</sup>  
S. X. Zheng<sup>1,2,3</sup>, X. W. Wang<sup>1,2,3</sup>, Z. M. Wang<sup>4</sup>

<sup>1</sup>Key Laboratory of Particle & Radiation Imaging, Tsinghua University, Beijing, China

<sup>2</sup>Laboratory for Advanced Radiation Sources and Application, Tsinghua University, Beijing, China

<sup>3</sup>Department of Engineering Physics, Tsinghua University, Beijing, China

<sup>4</sup>State Key Laboratory of Intense Pulsed Radiation Simulation and Effect  
(Northwest Institute of Nuclear Technology), Xi'an, China

## Abstract

Xi'an Proton Application Facility (XiPAF) has been operational since 2020, which can accumulate  $2 \times 10^{11}$  protons after injection and  $1 \times 10^{11}$  protons after acceleration. In this paper, we have investigated the XiPAF synchrotron nonlinearity by simulation and experiments. The beam loss occurs with the resonance  $\nu_x + 2\nu_y = 5$  in the absence of space charge, and the resonance  $2\nu_x - 2\nu_y = 0$  in the presence of space charge. The stripping foil also plays an important role due to its multiple scattering effect and ionization energy loss effect.

## INTRODUCTION

The Xi'an Proton Application Facility (XiPAF) is the first facility that is dedicated to simulations of the space radiation environment in China [1], which consists of a 7 MeV linac injector and a compact 200 MeV synchrotron. After several rounds of machine studies and experiments from 2020, the XiPAF synchrotron can accumulate  $2 \times 10^{11}$  protons after injection and  $1 \times 10^{11}$  protons after acceleration [2, 3].

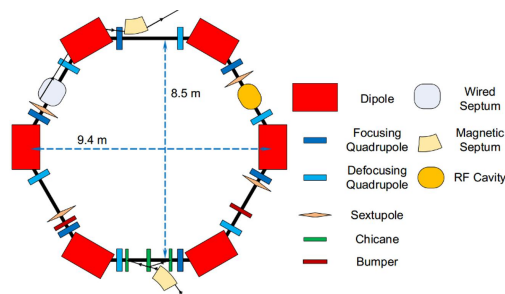


Figure 1: XiPAF synchrotron lattice layout.

The XiPAF synchrotron has 6 periods, with a “missing dipole” lattice structure, shown as Fig. 1. The circumference is 30.9 m, stripping injection turns negative hydrogen beam to proton beam, then the RF cavity voltage ramps from 60 V to 600 V within 10 ms adiabatically, and accelerates particles to 200 MeV. The main parameters are shown in Table 1, and the lattice beta functions are shown as Fig. 2.

During beam commissioning, we found that nonlinear resonance is the main limitation during injection, capture and acceleration. In this paper, the nonlinear dynamics of

Table 1: XiPAF Synchrotron Main Parameters

Parameters	Values	Units
Periodicity	6	
Circumference	30.9	m
Injection Energy	7	MeV
Injection Tune $\nu_x/\nu_y$	1.74 / 1.70	
Extraction Energy	10~200	MeV
Extraction Tune $\nu_x/\nu_y$	1.68 / 1.72	
Natural Chromaticity	-0.32 / -2.39	
Momentum Compaction	0.34	

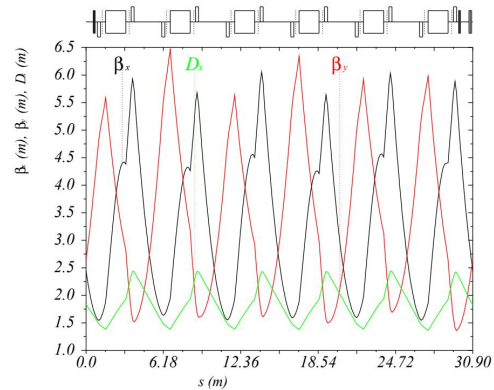


Figure 2: XiPAF synchrotron lattice optics.

the XiPAF synchrotron have been studied, with and without space charge. Possible resonance has been analysed in tune diagram, resonance stopband scan has been used to identify the nonlinearity of the XiPAF synchrotron by simulation and experiment, and the space charge effect has also been discussed.

## RESONANCE LINE AND HARMONIC ANALYSIS

The XiPAF synchrotron has 6 periods. Lattice optics functions are shown as Fig. 2, beta function is not fully symmetric according to the 3 chicane magnets located in the injection long drift section, which are used for stripping injection. Harmonic analysis of beta function shows that the strongest harmonic number is 6 (as shown in Fig. 3), which is the same with the lattice period. Because of the symmetry distortion of chicane magnets, the strength of all harmonic

\* Work supported by National Natural Science Foundation of China (No. 12075131)

† yaohongjuan@tsinghua.edu.cn

numbers is non-zero, this means that the resonance could be induced by any harmonic number.

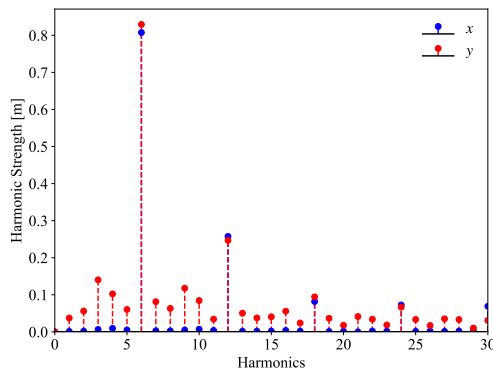


Figure 3: XiPAF synchrotron beta function harmonic analysis.

Based on the lattice harmonic analysis results, we can understand that those resonances with the harmonic number of multiples of 6 are the most dangerous, which are the structure resonances. Resonance lines near the injection and extraction tune are shown in Fig. 4, red lines are structure resonance and blue lines are non-structure resonance but excited by normal high order fields. Critical structure resonance may be  $\nu_x - \nu_y = 0$ , and non-structure resonance may be  $\nu_x + 2\nu_y = 5$ ,  $3\nu_x = 5$  in our interested tune region.

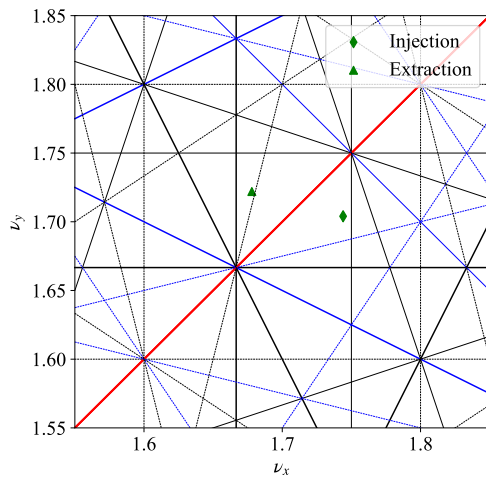


Figure 4: XiPAF synchrotron tune diagram.

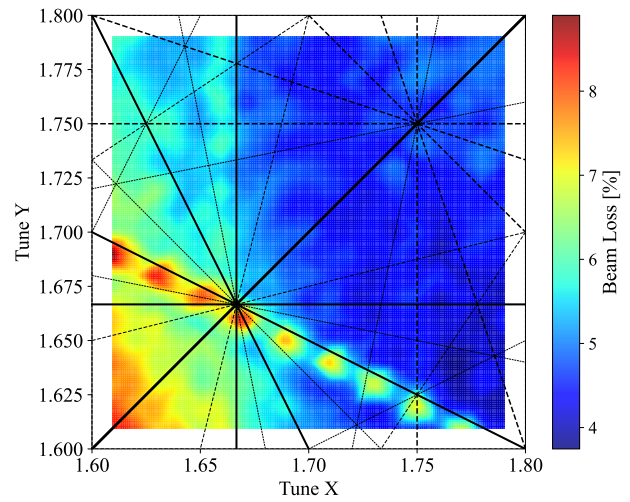
## RESONANCE STOPBAND SCAN

Static resonance stopband scan has been used to study the nonlinear beam loss and space charge effect [4].

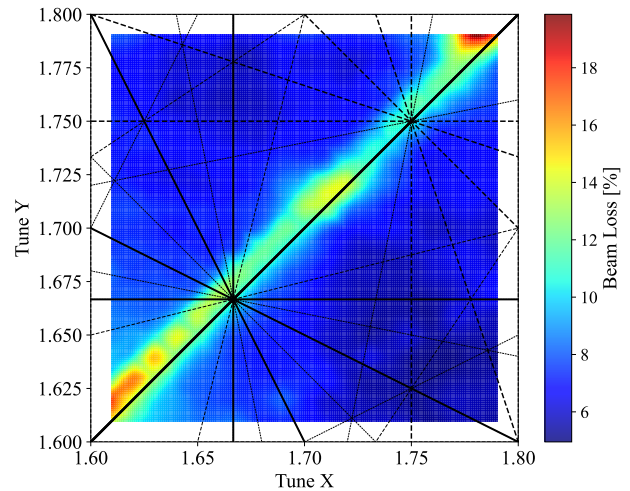
### Simulation

The simulation has been performed using the PyORBIT Code. In the simulation, we added no field errors or alignment errors, the nonlinearity only comes from PyORBIT tracking algorithm.

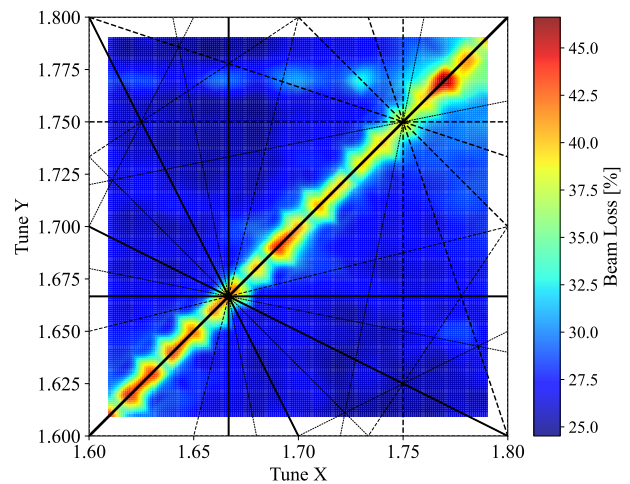
First, we perform the simulation for coast beam. After injection,  $2 \times 10^{11}$  particles are stored in the synchrotron,



(a) Coast beam, without space charge, foil thickness  $5 \mu\text{g}/\text{cm}^2$



(b) Coast beam, with space charge, foil thickness  $5 \mu\text{g}/\text{cm}^2$

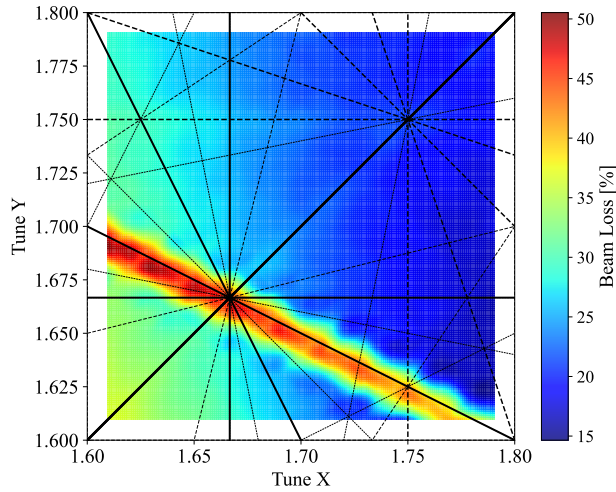


(c) Coast beam, with space charge, foil thickness  $20 \mu\text{g}/\text{cm}^2$

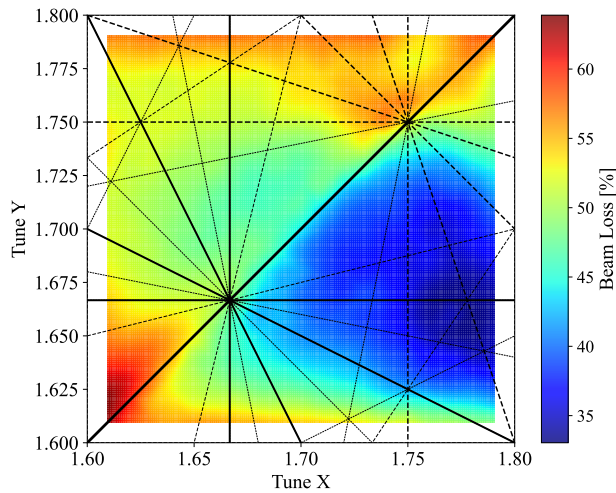
Figure 5: Beam loss for coast beam.

nonlinear resonance and space charge increase the beam emittance and cause beam loss. Without space charge, the main beam loss is caused by the resonance line  $\nu_x + 2\nu_y = 5$ , with the maximum beam loss of about 9%, as shown in Fig. 5.

For the space charge case, the main resonance line changes to  $2\nu_x - 2\nu_y = 0$ , and the maximum beam loss is about 19%, as shown in Fig. 6. If we choose the foil thickness as  $20\ \mu\text{g}/\text{cm}^2$ , the maximum beam loss is about 46%, which means the multiple scattering effect and ionization energy loss effect have a great influence on beam loss.



(a) Bunch beam, without space charge, foil thickness  $5\ \mu\text{g}/\text{cm}^2$



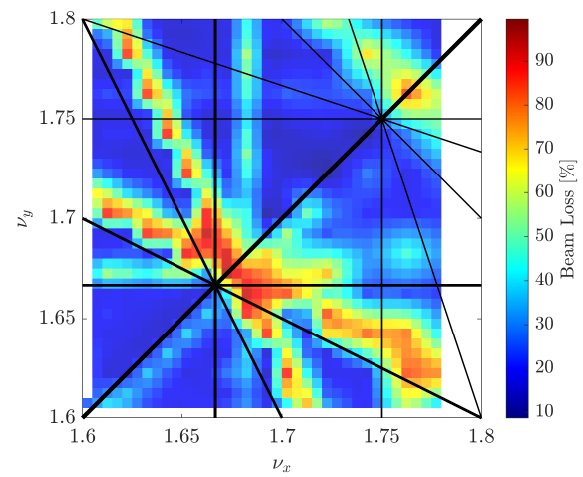
(b) Bunch Beam, without space charge, foil thickness  $5\ \mu\text{g}/\text{cm}^2$

Figure 6: Beam loss for bunch beam.

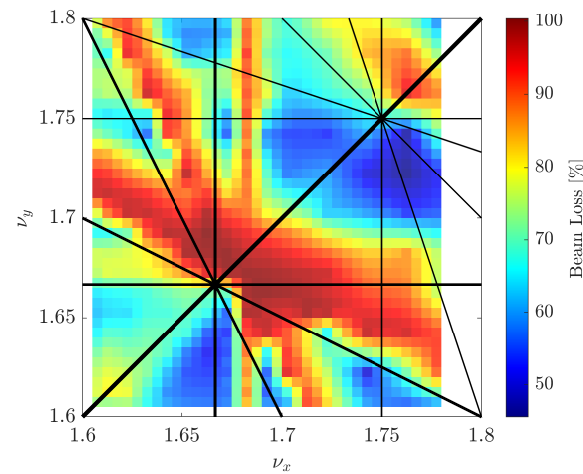
For a bunch beam, without space charge, we get a similar beam loss pattern as for coast beam, but the pattern is quite different for space charge case, the main resonance line is still  $2\nu_x - 2\nu_y = 0$ , and the space charge tune shift makes beam easier to lose above the resonance line, which makes the beam loss at the different sides of the resonance line  $2\nu_x - 2\nu_y = 0$  different.

### Measurement

Figure 7 shows the measured beam loss on XiPAF synchrotron, we can see a similar beam loss at the resonance line  $\nu_x + 2\nu_y = 5$ , as well as other resonances such as  $2\nu_x + \nu_y = 5$ ,  $3\nu_x = 5$ ,  $3\nu_y = 5$  and  $2\nu_x + 2\nu_y = 7$ , which may be due to alignment errors and field errors. The beam



(a) Coast Beam



(b) Bunch Beam

Figure 7: Measured beam loss for coast beam and bunch beam.

loss at  $2\nu_x - 2\nu_y = 0$  is not so serious, that because the particle number in synchrotron is about  $6.4 \times 10^{10}$  when the measurement was taken, the space charge effect is not so strong.

Additionally, we can see that the synchrotron motion in the bunch beam case enlarges the stopband width, the beam loss is more serious, as we expected.

## CONCLUSION

The nonlinear dynamics of the XiPAF synchrotron have been studied through analysis, simulation and experiment. The main resonance is  $\nu_x + 2\nu_y = 5$  for the no space charge case and  $2\nu_x - 2\nu_y = 0$  for the space charge case. The stripping foil plays an important role in beam loss by increasing the emittance. The synchrotron motion enlarges the stopband width, making the beam loss more serious.

## REFERENCES

- [1] Z. M. Wang *et al.*, “Construction and beam commissioning of a compact proton synchrotron for space radiation environment

- simulation”, *Nuclear Instruments and Methods in Physics Research Section A*, 2022.  
<https://doi.org/10.1016/j.nima.2021.166283>
- [2] X. Y. Liu *et al.*, “Injection optimization and study of XiPAF synchrotron”, *12th Int. Particle Accelerator Conf.(IPAC’21)*, Campinas, Brazil, 2021.  
doi:10.18429/JACoW-IPAC2021-TUPAB326
- [3] H. J. Yao *et al.*, “Beam commissioning of XiPAF synchrotron”, *12th Int. Particle Accelerator Conf.(IPAC’21)*, Campinas, Brazil, 2021.  
doi:10.18429/JACoW-IPAC2021-MOPAB189
- [4] Oeftiger, Adrian *et al.*, “Simulation study of the space charge limit in heavy-ion synchrotrons”, *Phys. Rev. Accel. Beams*, 2022. doi:10.1103/PhysRevAccelBeams.25.054402

# EVALUATION OF FIELD QUALITY FOR ELLIPTICAL AND CURVED MAGNETS

Jie Li, Kedong Wang\*, Xueqing Yan, Kun Zhu†,

State Key Laboratory of Nuclear Physics and Technology, and Key Laboratory of HEDP of the Ministry of Education, CAPT, Peking University, Beijing, 100871, China

## Abstract

The elliptical magnetic field zone is a useful tool for beam distribution homogenization and FFAG accelerators. Additionally, strongly curved magnets are studied for their application in beam transmission and nuclear fusion. However, traditional magnetic measurements, known as field harmonics, for straight magnets are not suitable for these two kinds of special magnets. In this article, advanced multipoles are used to characterize the fields of straight magnets with elliptical apertures and 2D axisymmetric enclosed curved magnets. The article provides a detailed analysis of magnetic fields using data from FEA or Biot-Savart law. Furthermore, the article discusses methods for characterizing the field quality of unclosed curved magnets used for gantry.

## INTRODUCTION

Magnets are crucial components for beam transport, and their configuration depends on the specific usage scenario. In this article, we will focus on the evaluation of field quality in strongly curved and elliptical magnets. By utilizing advanced multipoles, we can determine the field in the central part based on the field data from reference curves [1].

## CURVED MAGNETS

When evaluating the central magnetic field of an accelerator magnet, it is common to expand it in terms of circular multipoles, such as dipole, quadrupole and sextupole flux density distributions. The multipole coefficients, also known as field harmonics, are obtained using the Fourier series expansion of the magnetic field component along a circle. These coefficients can also represent the Taylor coefficients of a series expansion of the flux density at the horizontal or vertical axis. They are the transverse coordinates in the co-moving beam coordinate system. However, this approach is not suitable for strongly curved magnets. When particles traverse a curved orbit, they experience a magnetic field up to second order as follows.

$$\begin{aligned} \frac{ec}{\beta E} B_x &= -\kappa_y - kx + ky - \frac{1}{2}m(x^2 - y^2) \\ &+ mxy + \frac{1}{2}(-\kappa_y k + \kappa_x k + \kappa_y'')x^2 \\ \frac{ec}{\beta E} B_y &= +\kappa_x + ky + kx + \frac{1}{2}m(x^2 - y^2) \\ &+ mxy - \frac{1}{2}(\kappa_x k + \kappa_y k + \kappa_x'')y^2 \end{aligned}$$

\* wangkd@pku.edu.cn

† zhukun@pku.edu.cn

It is clear that different orders are mixed in the magnetic field if curvature is not zero. The Fourier coefficients from the reference circle deviate from the Taylor coefficients at the transverse coordinate axis. In beam dynamics, we are interested in the latter one. Assuming axial symmetry for a curved magnet, solutions of the vector Laplace equation can be found using bipolar coordinates in Fig. 1, where  $k = \cosh \eta - \cos \xi$ . Here are the expressions for the azimuthal magnetic vector potential inside and outside the current shell.

$$A_\phi^{in} = k^{1/2} [-b_n \cos(n\xi) + a_n \sin(n\xi)] Q_{n-1/2}^1(\cosh \eta) \quad (1)$$

$$A_\phi^{out} = k^{1/2} [-d_n \cos(n\xi) + c_n \sin(n\xi)] P_{n-1/2}^1(\cosh \eta) \quad (2)$$

One advantage of using bipolar coordinates is that the iso- $\eta$  lines are circular, although their centres may differ slightly from the focuses. Typically, we require the good field region to be circular. Our goal is to reconstruct the magnetic field based on point data acquired along a reference circle.

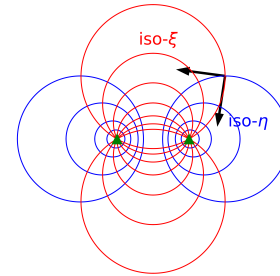


Figure 1: Bipolar coordinates.

The corresponding patterns of magnetic field, including normal and skew patterns, are shown in Fig. 2. It should be noted that the normal  $n = 0$  pattern does exist. Associated Legendre functions with half-integer indexes are used, we can calculate the value from this paper [2]. With the increase of the value that bend radius divided by the bore radius, the focus approaches the bore centre, and traditional multipoles recover. Here are the expression of the magnetic field inside the current shell.

$$\begin{cases} B_\xi^{in} = \frac{-b_n k^{3/2}}{a} \left[ \frac{n+\frac{1}{2}}{\tanh \eta} Q_{n-1/2}^1 - \frac{1}{2} \sinh \eta k^{-1} Q_{n-1/2}^1 \right. \\ \quad \left. - \frac{n+\frac{1}{2}}{\sinh \eta} Q_{n-3/2}^1 \right] (-\cos n\xi) \\ B_\xi^{in} = \frac{-a_n k^{3/2}}{a} \left[ \frac{n+\frac{1}{2}}{\tanh \eta} Q_{n-1/2}^1 - \frac{1}{2} \sinh \eta k^{-1} Q_{n-1/2}^1 \right. \\ \quad \left. - \frac{n+\frac{1}{2}}{\sinh \eta} Q_{n-3/2}^1 \right] \sin n\xi \end{cases}$$

$$\begin{cases} B_\eta^{in} = \frac{-b_n k^{3/2}}{a} \left[ -n \sin n\xi - \frac{1}{2} k^{-1} \sin \xi \cos n\xi \right] Q_{n-1/2}^1(\cosh \eta) \\ B_\eta^{in} = \frac{-a_n k^{3/2}}{a} \left[ -n \cos n\xi + \frac{1}{2} k^{-1} \sin \xi \sin n\xi \right] Q_{n-1/2}^1(\cosh \eta) \end{cases}$$

If we obtain magnetic field data at several points sampled along a reference circle, the Fourier coefficients of the radial field  $B_\rho$  directly represent the multipole strength for straight

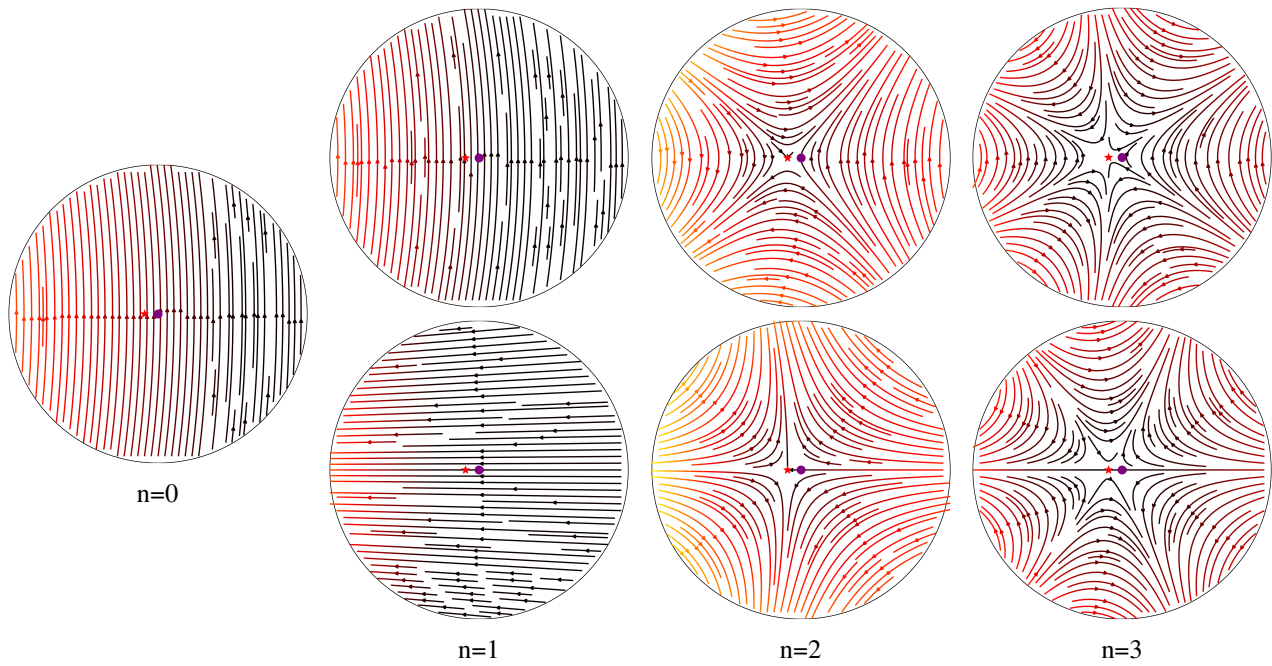


Figure 2: Toroidal harmonics.

magnets. The discrete Fourier series can also be used as a fitting function for the magnetic field along the reference circle. The toroidal harmonics are suitable for field description in a curved system. Decomposing the real data into toroidal harmonics is challenging due to the complex nature of the function  $f(\xi)$  in the toroidal harmonics. However, if we calculate the Fourier series for the first several toroidal harmonics and combine them with the real discrete Fourier series, we can determine the strengths of the toroidal harmonics by using linear algebra. High-order pattern accounts little for the real field. This algorithm may not be precise, but it can work well.

Specifically, we can use the following equations to calculate the toroidal strengths  $a_n$  &  $b_n$ :  $\langle a_n | A_m \rangle = \frac{1}{2\pi} \int_0^{2\pi} B_\eta^{in}(n, skew) \cdot \cos(m\theta) d\theta$  (where if  $m = 0$ , and the result is divided by 2), and  $\langle b_n | B_m \rangle = \frac{1}{2\pi} \int_0^{2\pi} B_\eta^{in}(n, normal) \cdot \sin(m\theta) d\theta$ . We used COMSOL to construct a closed curved magnet with  $R = 1$  m,  $r = 0.3$  m,  $r_{ref} = 0.18$  m, and a current density proportional to  $J_\phi \sim 2 \cos 2\theta + \sin 2\theta$ . We sampled 20 points uniformly along the reference circle, and then calculated Fourier series  $A_n(n = 0, \dots, 10)$ ,  $B_n(n = 1, \dots, 9)$  of  $B_\rho$ , as shown in Fig. 3. If 21 points, then  $A_n(n = 0, \dots, 10)$  and  $B_n(n = 1, \dots, 10)$ . The number of data is conserved anyway. Regarding the toroidal harmonics,  $b_n(n = 0, 1, \dots)$  only contributes to  $B_n(n = 1, 2, \dots)$  items, while  $a_n(n = 1, 2, \dots)$  only contributes to  $A_n(n = 0, 1, \dots)$  items. We used singular value decomposition (SVD) to obtain  $a_n(n = 1, 2, \dots, 10)$  even if we lost one data point. We made the assumption that  $B_{10} = 0$ , and then used linear algebra to obtain  $b_n(0, \dots, 9)$ .

The magnetic field along the local horizontal axis can be represented by its derivatives, which approximate the coeffi-

cients of traditional Fourier series along the reference circle. In toroidal harmonics, we can fit the magnetic field of the analytical solution to get derivatives along horizontal axis. Finally, we compare the derivatives of the magnetic field along the local horizontal axis obtained from the traditional Fourier series and toroidal harmonics. The results show that toroidal harmonics provide a more precise characterization of the field as shown in Fig. 4. We also constructed an enclosed CCT coil to evaluate its feasibility, as shown in Fig. 5. We found that the relative error increases as the order of the derivative increases. However, even though the high order derivatives have a larger relative error, values are small enough to make little difference to the total magnetic field.

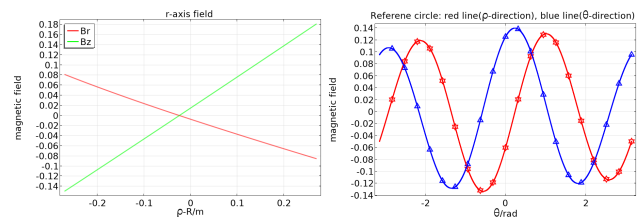


Figure 3: Field data at the horizontal axis and along a circle.

Unclosed curved magnets are often used for beam transmission to make it more compact, as shown in Fig. 6. But it is important to note that when magnets curve, the inner part of the magnet will be compressed while the outer part will be stretched. As a result, particles in the outer part will travel a longer distance, which is equivalent to passing through an enhanced magnetic field. To compensate for this effect, we can use  $\frac{r}{R}\vec{B}$  as the new magnetic field. Here,  $r$  represents the local bend radius, and  $R$  represents the average bend radius. In Maxwell's equation,  $\frac{r}{R}\vec{B}$  will violate

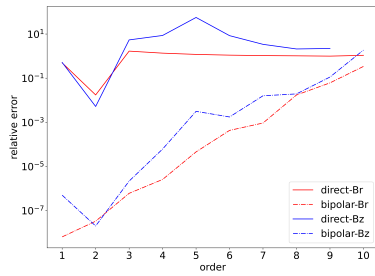


Figure 4: Field error from COMSOL FEA.

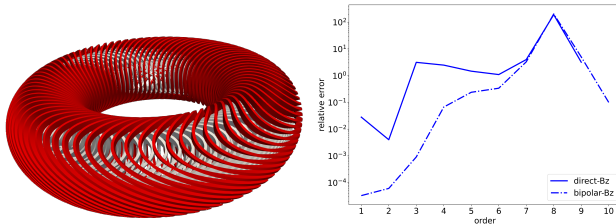


Figure 5: Field error in enclosed CCT coils.

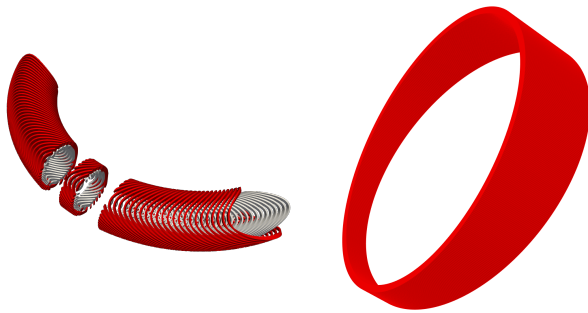


Figure 6: Unclosed curved magnets.

$\nabla \times \vec{B} = 0$  formally, but they satisfy  $\nabla \cdot \vec{B} = 0$ , which is different from traditional harmonics. Following equations are in cylindrical coordinates.

$$\nabla \cdot \vec{B} = \frac{1}{r} \frac{\partial (rB_r)}{\partial r} + \frac{\partial B_z}{\partial z} = 0 \Rightarrow \frac{\partial (rB_r)}{\partial r} + \frac{\partial (rB_z)}{\partial z} = 0$$

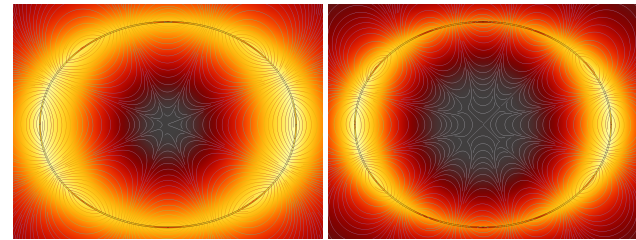
$$\nabla \times \vec{B} = \vec{e}_\phi \left[ \frac{\partial B_r}{\partial z} - \frac{\partial B_z}{\partial r} \right] = 0 \Rightarrow \frac{\partial (rB_r)}{\partial z} - \frac{\partial (rB_z)}{\partial r} = -B_z$$

The field of beam physics places more importance on low-order harmonics. Due to the relatively weak curvature of the magnets used in beam physics, the difference in magnitude between harmonics and the field Taylor series is slight. In terms of integrated harmonics, the traditional harmonics correspond to integration over angle, while the compensation case is over distance. The integration path is a series of concentric circles. As for magnet engineers, real particle tracking is more reliable for field quality control. Particles have the same bending radius and the integration path is a series of eccentric circles with the same radii, and then integration over distance. We can not guarantee which measurement method is better.

## ELLIPTICAL MAGNETS

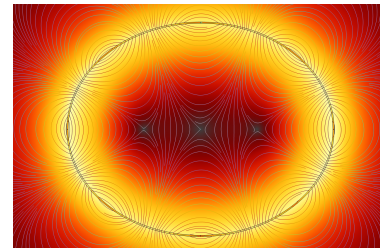
In the context of beam distribution homogenization and FFAG accelerators, a magnetic field requires a narrow and

elongated area [3]. A narrow beam profile can effectively decouple the two transverse spaces in beam distribution homogenization. Elliptical magnets are a proper choice, octupole and dodecapole magnetic fields are shown in Fig. 7. By measuring the magnetic fields along the elliptical boundary, we can employ cylindrical elliptical multipoles to reconstruct the magnetic field inside. Notably, there exists a linear transformation between cylindrical elliptical multipoles and cylindrical circular multipoles. This process is similar to that used for enclosed curved magnets.



Octupole

Dodecapole



Cylindrical elliptical multipoles, n=4

Figure 7: Elliptical field zone.

## CONCLUSION

This article focuses on the evaluation of field quality in curved and elliptical magnets. We introduce toroidal harmonics as a means to reconstruct the magnetic field in 2D axisymmetric enclosed curved magnets. Additionally, we provide suggestions for characterizing field quality in unclosed curved magnets. In an elliptical magnet, we can utilize cylindrical elliptical multipoles to reconstruct the magnetic field within the elliptical good field zone. All of the demonstrations are carried out in the two-dimensional case, either with rotational axis symmetry or in the two-dimensional plane. We hope this work can enlighten the use of curved and elliptical magnets.

## REFERENCES

- [1] P. Schnizer, *Advanced multipoles for accelerator magnets*, Springer Tracts Modern Physics 277, 2017.
- [2] D. Veres *et al.*, "A new algorithm for optimizing the field quality of curved CCT magnets," *IEEE TASC*. doi:10.1109/TASC.2022.3162389.
- [3] K. Wang *et al.*, "Beam distribution homogenization design for laser-driven proton therapy accelerator," *NIMA*. doi:10.1016/j.nima.2022.167196

# GENERAL DESIGN OF 180 MHz RFQ FOR BNCT

Zhi-Qiang Ren, Xin-Miao Wan, Yu-Fei Yang, Peng-Tai Lin, Wen-Long Liao, Xiao-Bao Luo, Xue-Jiang Pu, Zhi-Hui Li†

The Key Laboratory of Radiation Physics and Technology of Ministry of Education, Institute of Nuclear Science and Technology, Sichuan University, Chengdu 610065, China

## Abstract

Accelerator based boron neutron capture therapy (AB-BNCT) is a promising cancer treatment technology. A general design has been proposed of a 180 MHz radio frequency quadrupole (RFQ) accelerator for BNCT. The particularity of dynamic design of the RFQ is that the average aperture radius changes along the accelerator. Beam dynamics design results show that the length of accelerator which accelerates protons from 35 keV to 2.81 MeV is 5.07 m, and the transmission up to 99.65%. Meanwhile, 20 pairs of Pi-mode stabilizer rods are considered to keep the frequency of dipole mode away from the working quadrupole mode. The simulation results show that a large mode separation of more than 20 MHz between the operating quadrupole mode and nearest dipole mode can be obtained, this is sufficient to deal with the errors caused by machining and misalignment. The initial insertion depth

## BEAM DYNAMICS DESIGN

BNCT requires sufficient flux ( $10^9$  n/cm<sup>2</sup>/s) of epithermal neutrons (0.5 eV ~ 10 keV), because of this, an RFQ accelerator has been proposed: accelerating 25 mA proton beam (continuous wave mode) to 2.8 MeV to meet the requirements of BNCT. Based on the requirement of high beam transmission efficiency (greater than 99%), the beam dynamic design adopts the idea of making the average aperture variable along the accelerator 0. The beam dynamic parameters are shown in Figure 1.

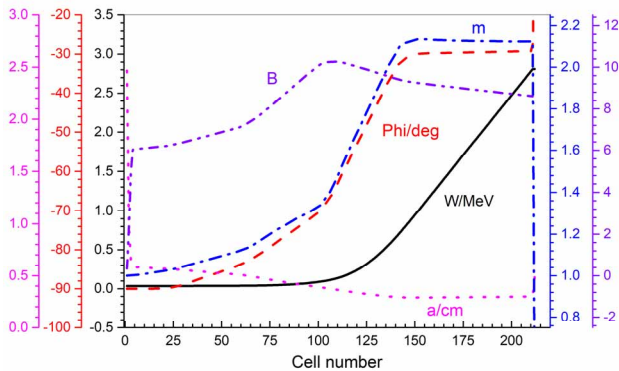


Figure 1: RFQ Accelerator beam dynamic parameters.

As for beam dynamic simulations,  $10^5$  macro particles with an initial 4D water-bag distribution are simulated with PARMTEQM 0, as shown in Figure 2 and Figure 3.

\* Work supported by the National Natural Science Foundation of China (Grant Nos. 11375122 and 11875197)  
† lizhahui@scu.edu.cn

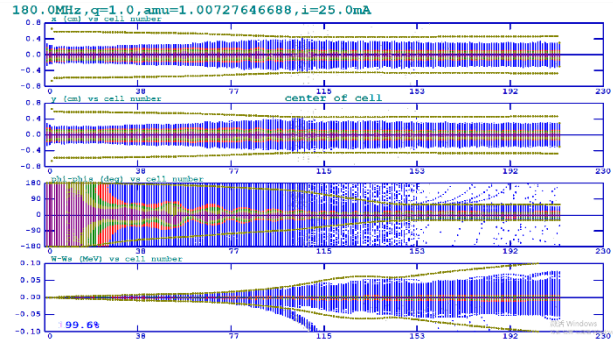


Figure 2: RFQ beam transmission process of the RFQ.

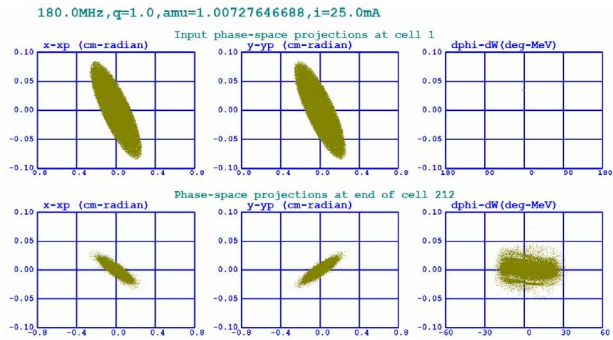


Figure 3: Beam profiles at the entrance and exit of the RFQ.

After simulation, the parameter results are shown in Table 1.

Table 1: Simulation Results

Parameter	Value
Frequency	180 MHz
Input energy	35 keV
Output energy	2.81 MeV
Voltage	72 kV
Current	25 mA
$\epsilon_t$ (norm. rms, entrance)	$0.20 \pi$ .mm.mrad
$\epsilon_t$ (norm. rms, exit)	$0.22 \pi$ .mm.mrad
$\epsilon_l$ (norm. rms, exit)	$0.62 \pi$ .mm.mrad
Vane length	507.73 cm
Transmission	99.65 %

## CROSS SECTION DESIGN

The design and simulation of a full length 3D model of whole cavity is usually based on slice cavity. By simulation with slice cavity, some high frequency parameters of the cavity can be obtained easily and the approximate range of cavity size L (shown in Figure 4) can be quickly

determined when restoring the quadrupole mode frequency to the operating frequency. The 2D cross-sectional structure adopts a quadrilateral structure 0, which has the advantages of easy water cooling and lower cost compared with octagonal cavity. The schematic diagram of the structure and the specific structural parameter values are shown in Figure 4 and listed in Table 2.

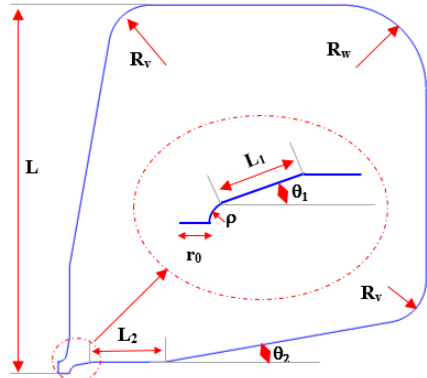


Figure 4: 2D cross-sectional structure schematic.

Table 2: Cross-sectional Parameters of RFQ

Parameter	Value
$r_0$	Decided by beam dynamics
$\rho/r_0$	0.75
$\theta_1$	10 degree
$\theta_2$	10 degree
$R_v$	20 mm
$R_w$	40 mm
$L_1$	20 mm
$L_2$	20 mm
$L$	Decided by $r_0$

$L$  is the only tuning parameter to change the operating frequency to 180 MHz, so it is depend on the variable average aperture  $r_0$ . Based on the beam dynamics design, The simulation results of high frequency parameters of a slice cavity with a thickness of 50mm with respect to  $r_0$  are shown in the Figure 5. With the increase of the  $r_0$ , the quality factor  $Q$  and  $L$  increase linearly, while the power loss per unit length  $P$  and the maximum surface electric field  $KP$  decrease. On average,  $L$  is about 160mm and  $Q$  is 16150 with respect to variable  $r_0$ .

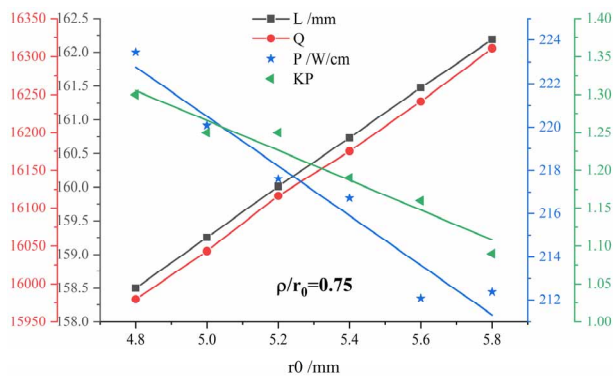


Figure 5: High frequency parameters with respect to  $r_0$ .

## PI-MODE STABILIZER LOOPS (PISL) AND TUNER DESIGN

From a beam dynamics point of view, the RFQ accelerator is about 5m long, so it is divided into 5 modules. In order to save computer resources and reduce computation time, it is decided to perform the 3D simulation of full length RFQ model without modulation. With this condition, it was found that the frequency difference between adjacent dipole mode and working mode was less than 1MHz after whole cavity simulation with CST MICROWAVE STUDIO 0. Therefore, special structure must be considered to keep the frequency of dipole mode away from working quadrupole mode. Dipole stabilizing rods have been considered firstly. It is shown from the simulation result that a frequency interval about 12 MHz can be reached, this requires extremely high accuracy for the accelerator manufacturing. So it was decided finally to add 20 pairs of Pi-mode rods to separate the dipole mode and operating mode. The key factor determining the frequency interval is the distance between a pair of Pi-mode rods. In order to ensure sufficient redundancy, the distance was finally determined to be 55 mm, resulting in a frequency interval more than 20 MHz. Afterwards, 100 tuners are also accepted to deal with field errors caused by accelerator assembly. Meanwhile, it is also used to change the distribution of voltage in this design.

The initial insertion depth is set to 20mm according to common accelerator devices.

The detailed PISL and tuner parameters are shown in Figure 6.

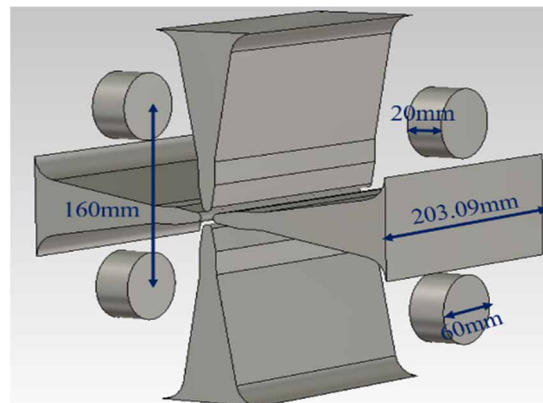
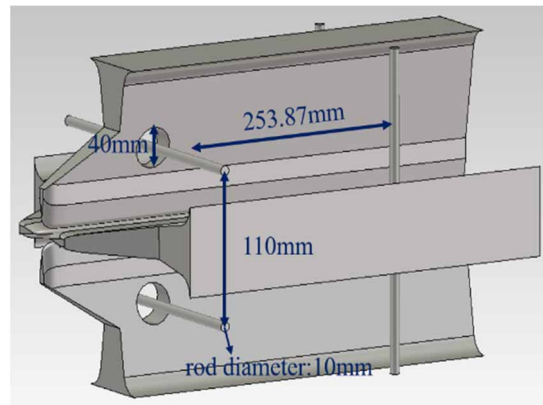


Figure 6: Detailed PISL and tuner parameters.

Results of whole cavity simulation are listed in Table 3. The presence of the other quadrupole mode can deteriorate the longitudinal beam dynamics, so they must also be carefully considered. But the frequency separation between nearest quadrupole mode and operating mode in this design is greater than 2 MHz, no additional consideration such as coupling structure is required.

Table 3: Whole Cavity Simulation Results

Parameter	Value
Working mode frequency $f_q$	180.00 MHz
Nearest quadrupole frequency $f$	182.26 MHz
Nearest dipole frequency $f_d$	200.95 MHz
$ f_q - f $	2.26 MHz
$ f_q - f_d $	20.95 MHz
L	155.70 mm
Q factor	13766.20

## ADJUSTMENT OF FIELD FLATNESS

After the entire cavity structure is established, the adjustment of the field flatness is crucial in the design of RFQ accelerator. For conventional RFQ accelerator with constant average aperture, field flatness is typically characterized by measuring the longitudinal distribution of the transverse electric field. In this particular design, however, the average aperture is not constant, the measurement of electric field are no longer applicable. Fortunately the inter-vane voltage remains constant. Therefore, the field flatness is evaluated by measuring the longitudinal distribution of the transverse inter-vane voltage. Due to the quadrupole symmetry of the cavity model, four tuners in different quadrants at the same position always have the same depth in the tuning process. By adjusting the undercut and the tuners and evaluate the transverse voltage by utilizing the macro in CST, the fluctuation of the field is less than  $\pm 2.5\%$  finally. The dimension of undercut is shown as Figure 7 and the voltage distribution before and after tuning are shown as Figure 8.

## CONCLUSION

The final beam dynamic design results of the 180 MHz RFQ accelerator is that the accelerator length is 5.07 m and the beam transmission efficiency is 99.65%. In terms of cavity structure, cross-sectional structure adopts a quadrilateral structure and the 3D cavity model adopts 20 pairs of Pi-mode rods to achieve a frequency separation of 20 MHz between dipole mode and the quadrupole mode, this prevents the beam dynamics from deteriorating transversely and is beneficial for the construction work of the RFQ accelerator. At the same time, by changing the depth of tuner, the unflatness of voltage distribution is less than  $\pm 2.5\%$ , which basically meets the project requirements and further adjustment and optimization of voltage flatness are still ongoing.

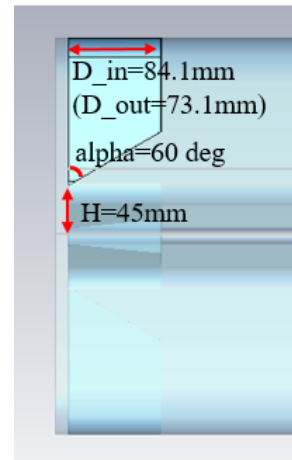


Figure 7: Final Dimension of undercut.

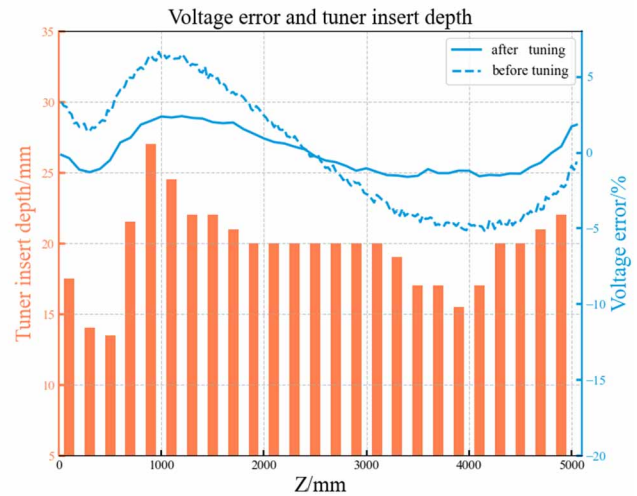


Figure 8: Transverse inter-vane voltage distribution before and after tuning.

## ACKNOWLEDGMENTS

This work was supported by the National Natural Science Foundation of China (Grant Nos. 11375122 and 11875197).

## REFERENCES

- [1] C. Zhang *et al.*, “Beam dynamics studies on a 200mA proton radio frequency quadrupole accelerator,” *Nucl. Instr. Meth.*, vol. 582, pp. 153-159, 2008.  
doi: 10.1016/j.nima.2007.12.001.
- [2] K.R. Crandall, LANL Internal Report, Nr. LA-UR-96-1836, Revised December 7, 2005.
- [3] G. Romanov *et al.*, “Project X RFQ EM Design”, in *Proc. 9th Int. Particle Accelerator Conf. (IPAC’12)*, New Orleans, USA, 2012, pp. 3883-3885.
- [4] CST Studio Suite, <http://www.cst.com>.

## DYNAMICS DESIGN ON 70-250MeV PROTON LINAC\*

Yu-Fei Yang, Xin-Miao Wan, Zhi-Qiang Ren, Peng-Tai Lin, Zhi-Hui Li†

The Key Laboratory of Radiation Physics and Technology of Ministry of Education, Institute of Nuclear Science and Technology, Sichuan University, Chengdu 610065, China.

### Abstract

Charged proton beams have broad application prospects, and research on compact S-band proton linear accelerators is increasingly heating up in recent years. For radiation therapy, to achieve the conventional penetration range of water-equivalent tissues, protons with energy of 70 to 230 MeV are required. The design of electromagnetic structure is closely related to particle dynamics design. A flexible and controllable particle dynamic tracking code (PDT) through both traveling wave and standing wave acceleration has been compiled to simulate particle trajectory and satisfy automatic tuning of the various components in the entire acceleration chain. The linac with a total length of approximately 7.89 m composed of 16 tanks of backward traveling wave structures and permanent magnet quadrupole lenses was designed, operating at an RF frequency of 2.856 GHz with a target acceleration gradient of 30 MV/m, and accelerating proton beam from 70 MeV to 250 MeV while maintaining low emittance and high transmission efficiency.

### INTRODUCTION

Proton linear accelerator is widely used in basic research, medical treatment, and industrial manufacturing, among other fields. It can be used in the manufacture of microelectronic devices, surface modification of materials. Currently, it's mainly concentrated in the field of radiation therapy. Compared with advanced photon therapy technologies such as intensity-modulated radiation therapy and volumetric arc therapy, proton therapy can significantly reduce the dose of radiation to normal tissue surrounding the tumor, reducing the possibility of inducing second primary tumors [1]. Traditional proton therapy equipment is bulky, difficult to install and manufacture, and expensive, making it difficult to be widely promoted. Currently, research into miniaturization and compactness of proton linear accelerator is underway worldwide.

Currently, the main high-gradient RF acceleration structures include the TeV Energy Superconducting Linear Accelerator (TESLA) structure [2], Coupled Cavity Linac (CCL) [3], and Backward Traveling Waveguide (BTW) structure [4] is used in the TULIP project, which is dedicated to developing a compact proton linac capable of achieving an accelerating gradient of 50 MV/m, and peak surface electric field and shunt impedance within acceptable ranges even in low- $\beta$  configurations. Due to the scarcity of simulation software for proton acceleration using traveling wave architecture, we utilized our own

compiled open-source particle dynamic tracking code (PDT) based on traveling wave acceleration to conduct preliminary dynamic design of a 70-250 MeV BTW proton linac.

### PDT CODE

Compared with the abundant available design tools for standing wave proton linac, the design tool for tracking protons through traveling wave structures is relatively hard to find. Most particle tracking programs are designed to handle standing waves or use the superposition of two standing waves to approximate traveling waves, making them unsuitable for BTW structures. Additionally, these programs often function as closed systems, limiting customize and expand the solver capabilities according to our specific requirements.

Due to the unique demands of proton therapy, it is necessary to adjust the kinetic energy of the output particles within a certain range while maximizing the transmission efficiency. This implies that the PDT code not only needs to simulate the particles trajectories through acceleration channel but also incorporate the beam matching functionality [5]. *TraceWin* is capable of calculating the transfer matrix of a given structure and handling standing wave electromagnetic field map represented by real numbers, whereas PDT code accepts not only real numbers but also traveling wave with complex numbers. Since the electromagnetic structure design and particle dynamics design are closely related, it is important to find a starting point.

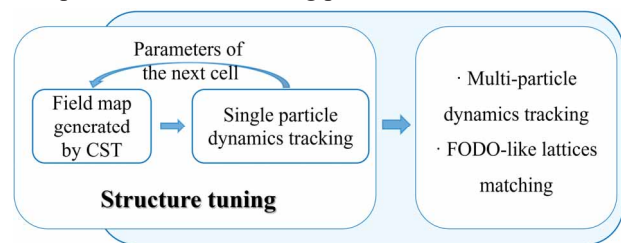


Figure 1: The Simplified scheme of PDT code architecture.

The commonly used simulation software CST studio suite [6] makes it feasible to extend the use of the program to traveling wave structures. CST is used to model and tune the single cell for calculating the electromagnetic field map, while MATLAB serves as the core of the code. The whole solving process is mainly divided into two modules. Since the RF structure design and particle dynamics design are closely related, it is important to find a starting point. In the first part, it makes full use of automated MATLAB and CST co-simulation to track the dynamics of a single particle in the longitudinal direction and tune waveguide structure as an interactive multi-run simulation. has added

\* Work supported by the National Natural Science Foundation of China (Grant Nos. 11375122 and 11875197)

† lizhahui@scu.edu.cn

this module to create appropriate wires to enable communication between MATLAB and CST, for speeding up the design process. Another module incorporates longitudinal and transverse multi-particle tracking, as well as transverse focusing of FODO-like lattices approximate matching for bunched beams to maximize the transmission. Its modular design permits adjustment and extend of functions for different design requirements, including seeking the optimal starting point for energy modulation, and optimization of elements parameters.

Finally, the benchmark with the *TraceWin* shows its accuracy both in energy gain and envelopes are good. The simulation model integrative framework is proposed as in Fig. 1.

## LINAC DESIGN

Protons with the kinetic energy of 70 MeV are decided inject into a compact BTW linac with an accelerating gradient of 30 MV/m, operating at frequency of 2.856 GHz. The linac is composed of several different tanks, and each tank consists of multiple same BTW cells, as the particle reference velocity  $\beta$  in each tank does not change significantly, which refers to a small unit cell length change. Nevertheless,  $\beta$  between tanks changes greatly which cannot be ignored, the length of the BTW cells in the adjacent tank needs to be adjusted with it.

### Structure Tuning

After completing the modeling of the low  $\beta$  BTW single cell structure in CST, the geometry of the regular BTW structure is showed in Fig. 2. Then optimize the geometric parameters, such as the nose cone and coupling holes, to better the characteristics including the shunt impedance, transit time factor and filling time. Based on this prototype and some input data, such as particle species, initial kinetic energy, synchronous phase, operating mode, acceleration gradient, and target output energy, PDT calculates the cell length, optimal number of cells and particle energy in each tank, and obtains the corresponding electromagnetic field maps of every unit cell generated by CST.

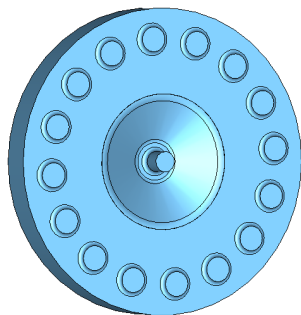


Figure 2: Model diagram of BTW accelerating structure.

A compact 16 accelerating tanks linac is chosen, with a constant number of 19 cells per tank operating at  $5/6\pi$  mode. The optimal incident phase is obtained through the optimization algorithm in PDT code and the synchronous phase is chosen to 10 degrees. The TTF of particles in each tank is above 0.905, which achieves the desired

acceleration efficiency. The total length of waveguide is 7.17 m, which is designed for the main acceleration cavity.

### Lattice Design

The transmission efficiency is directly related to the transverse emittance of the beam. Meanwhile, the cavity has the impact of defocusing for particles along transverse direction when linac boost the particles longitudinally. For a constant aperture of the RF structure, the excessive particle radial distance in general can lead to particle loss. In the following, we derive the condition to maximize the transmission of a beam line composed of permanent magnetic quadrupole structures (PMQs), for a given lattice geometry.

Traditionally, in a FODO lattice structure, the tanks have a fixed length, and the magnetic elements are designed accordingly for beam focusing and defocusing. This allows for a relatively straightforward matching of the transverse ellipses. When the lengths of the tanks increase with acceleration and the relativistic  $\beta$  increases, the matching process becomes more complicated, requiring a more comprehensive analysis and optimization approach to ensure proper beam dynamics and stability. Optimize the magnetic field gradients of the quadrupole lens and calculate the transfer matrix by PDT code to find the optimal matching point between the magnetic field gradient and the Twiss parameters. This process involves iteration and numerical techniques to converge on the optimal matching value.

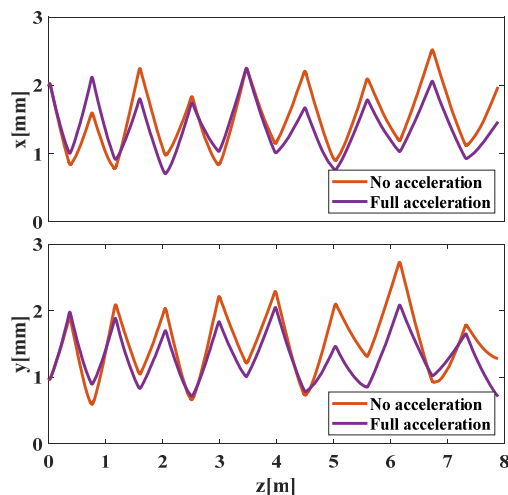


Figure 3: Transverse beam envelop with full acceleration and no acceleration.

To achieve the maximum acceleration efficiency, each tank requires the particle to enter with an individually calculated optimal incident phase. Consequently, drifts must be incorporated between the tanks to ensure alignment between the exit phase of the preceding tank and the incident phase of the subsequent tank. If the length of the quadrupole lens, which is 0.03 m, exceeds the required ideal drift length, an extension of one wavelength of the period should be considered. This adjustment is necessary to ensure that the drifts is appropriately sized to achieve the desired matching between the tanks.

Content from this work may be used under the terms of the CC BY 4.0 licence (© 2023). Any distribution of this work must maintain attribution to the author(s), title of the work, publisher, and DOI

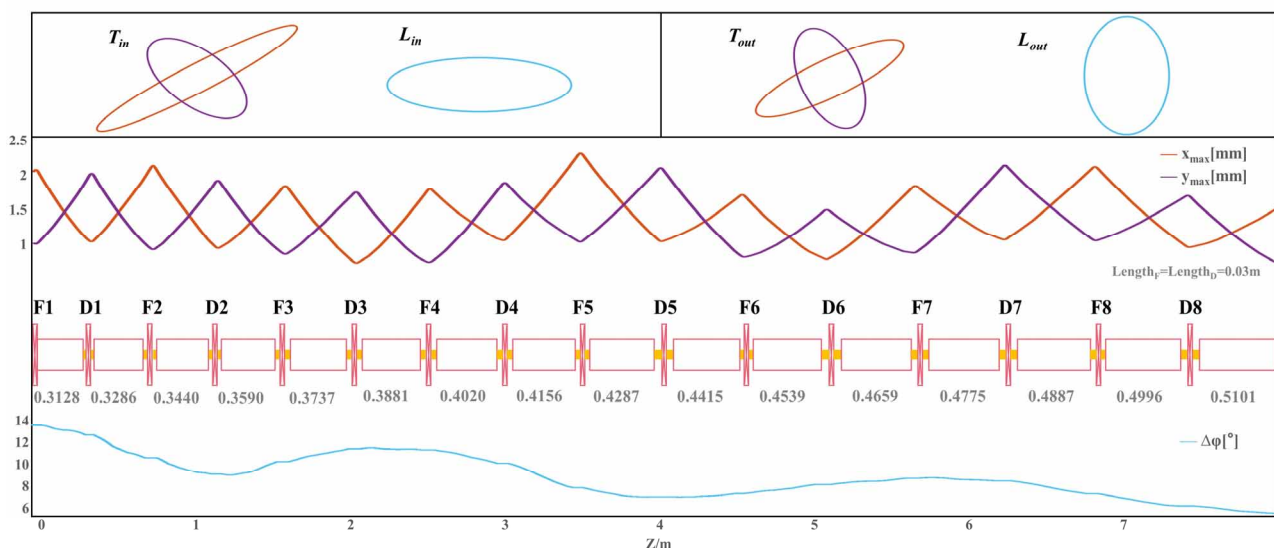


Figure 4: Configuration of the overall structure of linac (F and D are PMQs), with the envelope throughout the acceleration ( $x_{\max}$ ,  $y_{\max}$ ,  $\Delta\phi$ ), the phase-space ellipses at the beginning and the end of the acceleration ( $T$  is transverse while  $L$  is longitude).

The transverse beam envelopes of two extreme cases with on acceleration and full acceleration are successfully limited to an acceptable range and are shown in Fig. 3. The overall length of the acceleration channel is 7.89 m.

## PARTICLE TRACKING RESULTS

The distribution modes of the beam particles in phase space include Gaussian and Kapchinskij-Vladimirskij (K-V) distribution for typical numerical simulating. K-V distribution is chosen that provides clearer boundaries in an intuitive way, which is good for studying particle focusing phenomena and envelope matching in the phase space ellipsoid. Fig. 4 shows the normalized phase-space ellipses of the multiple particles with scale [mm·mrad] at the beginning and the end of the linac. The results show that transverse ellipses can almost be matched after eight complete lattice structures. This suggests that the beam's transverse characteristics, such as the beam size and shape, are close to being properly aligned and matched to the lattice structure.

The small amplitude oscillation of the longitudinal envelope in Fig. 4 is related to the oscillation of the optimal incident phase synchronous phases. In addition, the overall amplitude of the longitudinal envelope follows Adiabatic Phase Damping, which means that the phase spread decreases as the energy increases. This is due to the effect of energy dispersion.

## CONCLUSION

A flexible tool *PDT* code that works for a variety type of particles and electromagnetic field maps is certainly free to include any element as we desired to. It's used for a S-band compact proton linac dynamic design. The result achieves a close match of the transverse ellipses after lattice structures, it indicates that the accelerating and focusing channel is properly designed and configured to preserve the beam quality and optimize its performance.

## REFERENCES

- [1] PAGANETTI H *et al.*, "The risk for developing a secondary cancer after breast radiation therapy: comparison of photon and proton techniques", *Radiother Oncol*, vol. 149, pp. 212-218, 2020. doi: 10.1016/j.radonc.2020.05.035
- [2] Vogel E, "High gain proportional rf control stability at TESLA cavities", *Phys.Rev.ST Accel. Beams*, vol. 10, p. 052001, 2007. doi:10.1103/physrevstab.1-0.052001
- [3] C. Ronsivalle *et al.*, "The TOP IMPLART LINAC: Machine status and experimental activity", in *Proc. 8th Int. Particle Accelerator Conf. (IPAC'17)*, Copenhagen, Denmark, 14-19 May 2017. doi:10.18429/JACoW-IPAC2017-THPVA090
- [4] S. Benedetti *et al.*, "RF Design of a Novel S-Band Backward Traveling Wave Linac for Proton Therapy", in *Proc. 27th Linear Accelerator Conf. (LINAC'14)*, Switzerland, September 2014.
- [5] TraceWin, <http://irfu.cea.fr/dacm/en/logiciels>
- [6] CST STUDIO SUITE, <https://www.cst.com>

# CONTROL OF CAFe BEAM ENERGY USING LINEAR ACCELERATOR SIMULATION SOFTWARE AVAS AND BEAM LINE CALIBRATION TECHNOLOGY\*

Chao Jin, Chi Feng, Xin Qi<sup>†</sup>, Zhijun Wang, Yuan He<sup>†</sup>, Institute of Modern Physics, Lanzhou, China  
also at Advanced Energy Science and Technology Guangdong Laboratory, Huizhou, China

## Abstract

A new accelerator simulation code named Advanced Virtual Accelerator Software (AVAS) was developed by the Institute of Modern Physics, Chinese Academy of Science. Although the code is proposed to simulate the particle transport in the linac of the China Initiative Accelerator Driven System (CiADS), it can be also used for common linacs. We have constructed a framework for the accelerator simulation program AVAS based on the structure, function, parameters, errors, and operational logic of real accelerators. The mapping relationship between the operating parameters and simulation parameters of the Chinese ADS Front-end Demo Linac (CAFe) superconducting section was successfully established through AVAS. In the testing experiment, AVAS successfully set the operating parameters of the CAFe superconducting section, and the deviation between the energy setting value and the actual measurement value was about 0.5%.

## INTRODUCTION

AVAS [1] is a linear accelerator simulation code developed for the requirements of the CiADS [2]. The code is based on particle-in-cell (PIC) algorithm [3] and implemented in the C++ language. All accelerator elements as well as algorithms are packaged into an executable program, which can be run after installation on the windows operating system. On the one hand, AVAS has developed the S-PICNIC [4] algorithm by improving the standard PICNIC [5] algorithm, which significantly reduces the computational effort to solve for space charge effects. On the other hand, AVAS achieves efficient parallelism. The above work has resulted in a significant reduction in the AVAS multi-particle simulation time, which is a significant advantage in large-scale multi-particle simulations.

The operating parameters of the accelerator are different from those used in the accelerator simulation program. In order to obtain the operating parameters of the accelerator directly from the numerical simulations, it is necessary to establish a correspondence between the operating parameters of the accelerator and the numerical simulation parameters. In this paper, AVAS program is introduced first, and then how to establish the corresponding relationship between accelerator operating parameters and AVAS simulation parameters is explained. Finally, it is tested on CAFe [6] superconducting section.

\* Work supported by National Natural Science Foundation of China (Grant No. 11775282)

<sup>†</sup> email address: [qxin2002@impcas.ac.cn](mailto:qxin2002@impcas.ac.cn), [hey@impcas.ac.cn](mailto:hey@impcas.ac.cn)

## MATERIALS AND METHODS

The CAFe is the pre-validation device for CiADS and is structured as shown in Fig. 1. In CAFe, the beam is mainly accelerated in the RF superconducting cavity and the energy of the exiting beam is determined by the parameters of the RF superconducting section. In this paper, we use AVAS to map the superconducting section of CAFe to achieve a process that gives the accelerator operating parameters directly through simulations and changes the beam energy.

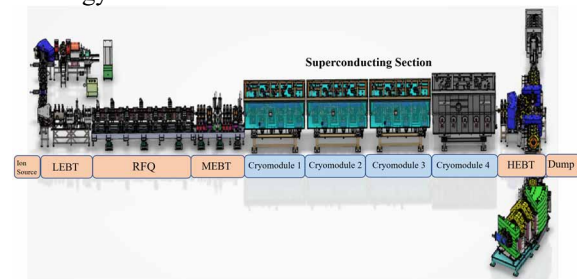


Figure 1: CAFe structure schematic.

The superconducting section of CAFe contains four cryomodules (Cryomodules 1-4), the exact composition of which is shown in Fig. 2. The first three cryomodules contain six solenoids and six RF cavities each, and the last cryomodule contains five solenoids and five RF cavities. The operating parameters of the solenoids are the current of the solenoid magnets and the operating parameters of the RF cavities contain the RF field amplitude and the RF field phase. Therefore, the superconducting section of CAFe has a total of 69 operating parameters. If these 69 operating parameters can be given directly by simulation when the beam energy needs to be changed, stable beam transmission can be achieved quickly.

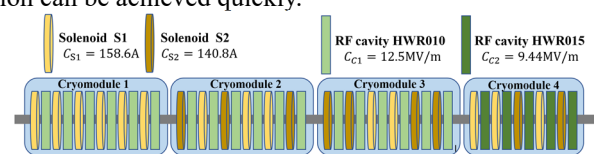


Figure 2: Cryomodule composition diagram.

These three types of parameters contain two types of mapping relationships, one for magnitude, including solenoid current and RF field amplitude, both of which are linearly related to the magnitude of the electromagnetic field (EMF) in the corresponding element, which is controlled in AVAS by adjusting the magnification of the reference electromagnetic field. Therefore, it is necessary to determine the proportionality constants between the reference EMF and the real EMF per unit current (or per unit RF field

amplitude) in the simulation program in order to obtain the values of current and RF field amplitude in the accelerator. The equation is as follows:

$$I_s = C_s K \quad (1)$$

$$E_{pk} = C_c K \quad (2)$$

where  $C$  is the amplification of the reference EMF in the simulation program,  $I_s$  is the solenoid current value and  $E_{pk}$  is the RF field amplitude. Another type of mapping relationship is the mapping of phases, which is the key part of establishing the mapping. The electric field in an RF cavity is:

$$E = E_0 \cos(\varphi_0 + \omega t) \quad (3)$$

The mapping of phases is the determination of the phase difference  $\Delta\varphi$  between  $\varphi_0$  (denoted as  $\varphi_v$ ) in the simulation program and  $\varphi_0$  (denoted as  $\varphi_{RF}$ ) in the RF cavity. The equation for mapping the phase of the numerical simulation to the phase of the real accelerator is

$$\varphi_{RF} = \varphi_v + \Delta\varphi + n \times 360 \quad (4)$$

AVAS determines the phase of the RF cavity by scan-phase. Eq. (5) is the way the RF cavity electric field is calculated in AVAS

$$E = E_0 \cos(\varphi_0 + \omega(t - t_0)) \quad (5)$$

The relationship between Eq. (5) and Eq. (4) is shown in Eq. (6):

$$\varphi_v = \varphi_0 - \omega t_0 \quad (6)$$

In addition, the electric field in the RF cavity can be calculated in AVAS using Eq. (7). This allows AVAS to skip the scan-phase process and simulate using the real phase of accelerator operation, giving simulation results that are closer to the real accelerator.

$$E = E_0 \cos(\varphi_v + \omega t) \quad (7)$$

In summary, the design of AVAS ensures a bi-directional mapping between the numerically simulated phase and the real accelerator phase.

## RESULTS AND DISCUSSION

The goal of the experiment was to increase the energy of the beam (Composed of  $^{40}\text{Ar}^{12+}$ ) to 186.6 MeV by adjusting the operating parameters of the CAFe superconducting section. Firstly, simulate the beam propagation in the CAFe superconducting segment using AVAS. The simulated parameters in AVAS were repeatedly adjusted so that the beam was accelerated to 186.6 MeV in the program. subsequently, the operating parameters of the CAFe superconducting section were obtained based on the mapping of the simulated parameters to the real accelerator operating parameters (Eq. (1-2), (4)).

The CAFe superconducting section contains two solenoids, denoted S1 ( $C_{s1} = 158.6$ ) and S2 ( $C_{s2} = 140.8$ ), and two RF cavities, denoted HWR010 ( $C_{c1} = 12.5$ ) and HWR015 ( $C_{c2} = 9.44$ ), and the phases of each cavity are independent, as shown in Fig. 2. All parameters in the experiment, including the 27 mapped parameters, 69 simulated parameters and the 69 operational parameters calculated from the simulated and mapped parameters are shown in Table 1 and Table 2, the unit of  $E_{pk}$  in the table is MV/m.

Table 1 includes the field amplification factor  $K$  of the solenoid in the simulation and the solenoid current  $I_s$  (A) calculated through Eq. (1). Table 2 includes the field amplification factor  $K$  and phase  $\varphi_v$  used in the simulations, and the operating parameters of the accelerator, including the RF field amplitude  $E_{pk}$  and phase  $\varphi_{RF}$ , can be calculated using Eq. (2) and Eq. (4). The last three RF cavities in CM4 are switched off.

The beam energy was measured by a TOF (Time Of Flight) located at the end of the CAFe linear section. The distance between the two oscilloscopes in the experiment is  $L = 0.6132\text{m}$ , and the measured beam time of flight  $\Delta t = 20.453\text{ns}$ , according to Eq. (8), the energy of the beam can be calculated as 187.5 MeV.

$$E_k = \left( \frac{1}{\sqrt{1 - \left(\frac{L}{\Delta t c}\right)^2}} \right) E_0 \quad (8)$$

where  $c$  is the speed of light and  $E_0$  is the rest energy of the  $^{40}\text{Ar}^{12+}$ , which is 37218.6 MeV.

In summary, AVAS provided parameters suitable for accelerator operation through simulations. In the actual test, the energy of the beam was 187.5 MeV, with a relative error of 0.48% from the simulated energy (186.6 MeV). Subsequently, only minor adjustments to the RF field amplitude or phase of the last RF cavity are required to achieve the required beam energy, avoiding re-scan-phase, simplifying the beam energy switching process in real accelerators, and quickly achieving stable beam transmission.

Table 1: Mapping of Solenoid Currents to Simulation Parameters in CAFe

CM1 Solenoid						
	S1	S1	S1	S1	S1	S1
$K$	0.8	0.78	0.81	0.88	0.75	0.98
$I_s$ (A)	126.9	123.7	128.5	139.6	119.0	155.4
CM2 Solenoid						
	S2	S1	S2	S1	S1	S2
$K$	0.87	0.95	0.47	1.05	0.9	0.9
$I_s$ (A)	122.5	150.7	66.0	166.5	142.7	126.7
CM3 Solenoid						
	S2	S2	S1	S1	S2	S2
$K$	0.9	0.84	0.87	0.95	0.82	0.92
$I_s$ (A)	126.7	118.3	138.0	150.7	115.5	129.5
CM4 Solenoid						
	S1	S1	S2	S1	S2	-
$K$	1.0	0.99	0.98	0.95	0.78	-
$I_s$ (A)	159.0	157.0	138.0	150.7	109.8	-

Table 2: Mapping of CAFe RF Cavity Operating Parameters to Simulation Parameters

CM1 Cavity						
	1-1	1-2	1-3	1-4	1-5	1-6
$K$	1.28	1.2	1.8	1.6	1.5	1.9
$E_{pk}(\text{MV/m})$	16	15	22.5	20	18.8	23.8
$\Delta\varphi(\text{deg})$	116	148	44	83	107	-36
$\varphi_v(\text{deg})$	-171	-140	100	42	45	93
$\varphi_{RF}(\text{deg})$	-55	8	144	124	152	56
CM2 Cavity						
	2-1	2-2	2-3	2-4	2-5	2-6
$K$	2	1.86	2	2.2	2.4	2
$E_{pk}(\text{MV/m})$	25	23.2	25	27.5	30.0	25.0
$\Delta\varphi(\text{deg})$	-146	-139	103	171	-77	-76
$\varphi_v(\text{deg})$	147	7.2	-45	-30	17	137
$\varphi_{RF}(\text{deg})$	0.8	-132	59	141	-60	61
CM3 Cavity						
	3-1	3-2	3-3	3-4	3-5	3-6
$K$	2.1	2	2.3	2.24	1.76	2
$E_{pk}(\text{MV/m})$	26.2	25	28.7	28	22.0	25
$\Delta\varphi(\text{deg})$	-143	-117	-50	-96	-15	41
$\varphi_v(\text{deg})$	-174	98	46	46	86	107
$\varphi_{RF}(\text{deg})$	42	-19	-4	-50	71	148
CM4 Cavity						
	4-1	4-2	4-3	4-4	4-5	-
$K$	2.90	1.22	0	0	0	-
$E_{pk}(\text{MV/m})$	27.4	11.5	0	0	0	-
$\Delta\varphi(\text{deg})$	145	149	-37	-74	-	-
$\varphi_v(\text{deg})$	111	10	-	-	-	-
$\varphi_{RF}(\text{deg})$	-104	159	-	-	-	-

## CONCLUSION

This paper describes the process of mapping the operating parameters of the CAFe superconducting section to the AVAS simulation parameters. After the mapping is completed, control of the CAFe beam energy is achieved. In the future, further information will be used, such as information from sensors in accelerators and historical data, to establish more mapping relationships between numerical simulations and real accelerators, in order to achieve complete reconstruction of real accelerators in computers.

## REFERENCES

- [1] Jin C, "Development and Application of Linear Accelerator Simulation Program", Lanzhou, Institute of Modern Physics, Chinese Academy of Sciences, 2021.
- [2] China Initiative Accelerator Driven System [EB/OL]. <http://ciads.impcas.ac.cn/p/zhuangzhigoucheng>.
- [3] Alex Friedman, David P. Grote, and Irving Haber, "Three - dimensional particle simulation of heavy - ion fusion beams",

*Physics of Fluids B: Plasma Physics*, vol. 4, no. 7, pp. 2203-10, 1992. doi:10.1063/1.860024

- [4] Chao J, Li-Juan Y, Xiao-Ying Z *et al.*, "Improvement of Linear Accelerator Numerical Simulation Algorithm Based on Symmetry Principle", *Nuclear Physics Review*.
- [5] Hofmann I. and Boine-Frankenheim O., "Grid dependent noise and entropy growth in anisotropic 3d particle-in-cell simulation of high intensity beams", *Physical Review Special Topics - Accelerators and Beams*, vol. 17, no. 12, p. 124201, 2014.
- [6] Yi C, "Research on Key Technologies of Machine Protection System of café", Lanzhou, Institute of Modern Physics, Chinese Academy of Sciences, 2021.

# MULTIPOLE FIELD OPTIMIZATION OF X-BAND HIGH GRADIENT STRUCTURE

B. Feng<sup>†</sup>, Q. Gao<sup>\*</sup>, J. Shi, H. Zha, X. Lin, H. Chen, Department of Engineering Physics  
Tsinghua University, Beijing, China

## Abstract

The X-band constant gradient acceleration structure plays a crucial role in the VIGAS project. However, the presence of a multipole field component in the structure's coupler leads to an increase in ray bandwidth and a decrease in yield, ultimately affecting the quality of the generated rays. Through calculations, it has been determined that the quadrupole field component is particularly prominent in the original structure, accounting for 29.5% of the fundamental mode strength. Therefore, it is necessary to modify the cavity structure of the coupler. By altering the shape of the cavity to two staggered circles, the objective of reducing the quadrupole field is achieved. The optimized quadrupole field component now accounts for approximately 0.3% of the fundamental mode strength. Subsequently, the non-resonant perturbation method was employed to simulate and experimentally measure the magnitude of the multipole field component in the actual acceleration cavity.

## INTRODUCTION

In 2021, Tsinghua University introduced the Very Compact ICS Gamma-ray Source project, known as the VIGAS project. The primary objective of the VIGAS project is to develop the world's first compact quasi-monochromatic gamma-ray source operating in the megaelectronvolt range. The gamma-ray energy generated by this project can be continuously adjusted within the range of 0.2 to 4 MeV.

The accelerator structure utilized in the project is based on the X-band technology and comprises an input coupler and an output coupler positioned at its ends. However, the inclusion of these couplers disrupts the circular symmetry of the accelerator structure, resulting in the emergence of multipole fields within the electromagnetic field. These multipole fields, present within the accelerator structure, have the potential to increase the beam emittance. Consequently, this may have an impact on the beam dynamics, ultimately affecting the bandwidth and yield of the produced gamma rays [1].

To analyze the beam dynamics, comprehensive simulations were conducted for the entire accelerator structure. These simulations took into account three-dimensional field distributions for the various components, specifically focusing on comparing the effects of one-dimensional and three-dimensional field distributions within the X-band accelerator structure. The results demonstrate that the emittance, which characterizes the size of the beam, increases by approximately 14% in the presence of three-dimensional field distributions, compared to the case of one-

dimensional field distributions. This indicates that the presence of multipole fields indeed leads to an increase in the emittance.

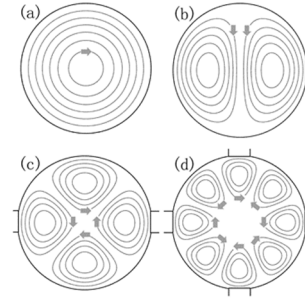


Figure 1: Different drilling situation in the cavity and the distribution of the multi-pole magnetic field.

The emergence of multipole fields within the couplers is a result of the symmetry breaking of the cavity, as shown in Fig. 1 [2]. In the absence of any deviations from perfect circular symmetry, the occurrence of multipole fields can be avoided. However, the introduction of a hole in the cavity wall gives rise to the generation of multipole fields, with the dipole field being the most dominant component. In the case of a pair of symmetric double holes, the quadrupole field becomes the strongest component of the multipole fields. When there are four symmetric holes, the octupole field emerges as the most significant component.

In the existing X-band accelerator structure's couplers, two symmetric holes are present, resulting in the quadrupole field being the most prominent among the multipole fields. It constitutes approximately 30% of the intensity of the fundamental mode. Hence, it becomes crucial to suppress the quadrupole field component effectively.

## OPTIMIZATION

The most effective method to suppress the quadrupole field component is by introducing two additional holes in the vertical direction of the previously symmetrical double holes, forming a symmetric four-hole structure. This modification effectively mitigates the quadrupole field. However, the process of punching additional holes has a considerable impact on the structure. Therefore, a compromise approach was adopted. The entire cavity of the coupler was transformed from a circular structure to two staggered circular structures, creating a racetrack-type structure, as shown in Fig. 2. This approach provides a satisfactory solution to reduce the quadrupole field.

<sup>†</sup> fby22@mails.tsinghua.edu.cn

<sup>\*</sup> gaoq08thu@tsinghua.edu.cn

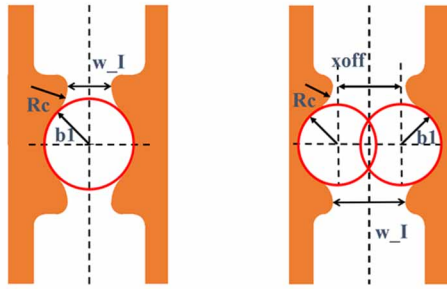


Figure 2: Schematic diagram of coupler structure optimization.

The modified structure of the coupler resembles a symmetrical four-hole structure, which effectively suppresses the quadrupole field without the need for additional drilling. However, the changes in the coupler structure result in an increase in the surface magnetic field. The maximum value of the surface magnetic field occurs at the chamfer on both sides of the feed inlet. To prevent excessive surface magnetic field, it becomes necessary to adjust the size of the chamfer at this location. Additionally, the structural modifications introduce a mismatch between the coupler and the accelerating cavity, necessitating a rematching process.

By conducting parameter scanning, the optimized parameters for the modified structure are obtained, as presented in Table 1. These optimized parameters ensure improved performance and alignment between the coupler and the accelerating cavity.

Table 1: Coupler Optimization Structural Parameters

Parameters	Value [mm]
Rc	4.0
xoff	7.0
b1	5.891
w_I	9.173

By utilizing the optimized parameters in simulation calculations, it is determined that the strength of the quadrupole field component in the input coupler of the X-band acceleration structure is reduced to 0.28% of the fundamental mode strength. The variation of the tangential magnetic field within the entire cavity of the coupler, both before and after optimization, is shown in Fig. 3.

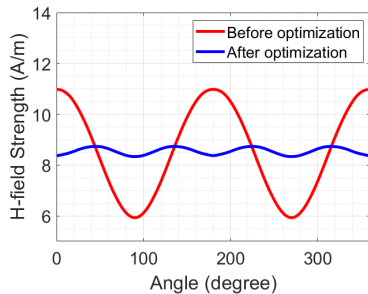


Figure 3: Simulation distribution of tangential magnetic field on  $r = 2$  mm at the cavity of X-band accelerating structure coupler.

## MEASURE

The non-resonant perturbation method is employed to measure the quadrupole field in the X-band acceleration structure [3]. This method involves introducing a perturbation object into the acceleration structure and measuring the reflection coefficient S11 at the input port. By analyzing the S11 measurement, the electromagnetic field at the location of the perturbation object within the acceleration cavity can be obtained. One of the advantages of the non-resonant perturbation method is its ability to measure the electromagnetic field of traveling wave acceleration structures accurately. It enables precise tuning and analysis of the acceleration structure.

Furthermore, the non-resonant perturbation method ensures minimal contact between the measurement system and the interior of the acceleration structure. This eliminates any potential impact on the internal components of the structure. The measurements conducted in this study specifically focus on the coupler structures prior to optimization.

### Simulation

In the unoptimized coupler model, a copper material perturbation object is introduced to simulate the actual scenario. The perturbation object is moved along a circular path centered around the coupler's center, and the reflection coefficient of the coupler's input port is simulated at each position of the perturbation object. By calculating the difference in reflection coefficients between the perturbed and non-perturbed cases, it is possible to assess the electromagnetic field at the location of the perturbation object. Therefore, by analyzing the difference in reflection coefficients, the magnitude of the multipole field component can be determined. The measured data resulting from these calculations are presented in Fig. 4.

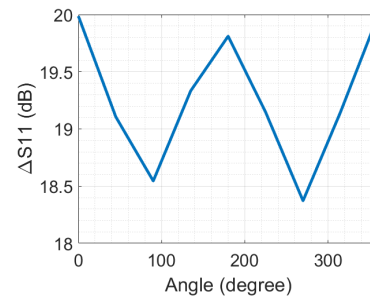


Figure 4: Simulation results of the relationship between the difference in reflection coefficient and the position of the perturbation object.

### Experiments

During the actual measurement process, a pair of eccentric original plates was designed and fabricated to securely position the perturbation object. The purpose of these plates is to ensure that the perturbation body remains in a fixed position throughout the measurement. The design and arrangement of the eccentric original plates can be observed in Fig. 5.



Figure 5: Eccentric disc and fitting between disc and coupler hole.

Throughout the measurement process, the eccentric position of the perturbation object is continuously rotated, and the reflection coefficients are individually measured at different positions. A comparison is then made between the measurement results with the perturbation object and the results without it. By analyzing the relationship between the difference in reflection coefficients and the eccentricity position, valuable insights into the impact of the perturbation object can be obtained. This relationship is visually depicted in Fig. 6.

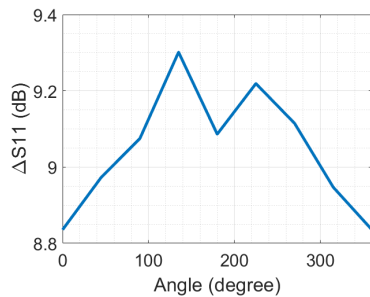


Figure 6: Experiment results of the relationship between the difference in reflection coefficient and the position of the perturbation object.

Through analysis, it has been discovered that the magnitude of the quadrupole field obtained through simulation is approximately 0.0382, while the magnitude of the quadrupole field component obtained through experimentation is around 0.0054. These values exhibit noticeable differences between the simulation and experimental results. The disparities can be attributed to various factors, such as variations in the models and parameters employed in the simulation and experimental setups. Further discussion and analysis are necessary to comprehensively understand and reconcile these disparities.

## CONCLUSION

The optimization of the X-band acceleration structure has successfully suppressed the strength of the multipole field in the coupler. The strength of the quadrupole field component, which initially accounted for approximately 30% of the fundamental mode strength, has been reduced to just 0.28% after the optimization process.

The non-resonant perturbation method has been employed to measure the electromagnetic field within the X-band acceleration structure, both through simulation and

experimental approaches. This method has provided initial insights into the multipole field within the coupler. However, there exist certain differences between the experimental and simulation results, indicating the need for further analysis and calculations to fully understand and reconcile these discrepancies.

## REFERENCES

- [1] H. Chen, Y. Du, L. Yan, J. Shi, W. Huang and C. Tang, "Optimization of the Compact Gamma-ray Source Based on Inverse Compton Scattering Design", 2018 IEEE Advanced Accelerator Concepts Workshop (AAC), Breckenridge, CO, USA, 2018, pp. 1-5, doi:10.1109/AAC.2018.8659417.
- [2] Chae, M. S., et al. "Emittance growth due to multipole transverse magnetic modes in an rf gun." *Physical Review Special Topics-Accelerators and Beams* 14.10 (2011): 104203.
- [3] S. Molloy et al., "Bead-pull Test Bench for Studying Accelerating Structures at RHUL", in *Proc. IPAC'11*, San Sebastian, Spain, Sep. 2011, paper MOPC049, pp. 187-189.

# DESIGN OF A LARGE MOMENTUM ACCEPTANCE GANTRY BASED ON AG-CCT FOR LIGHTWEIGHT PROTON THERAPY FACILITY\*

Yicheng Liao, Wei Wang, Xu Liu, Ruiying Luo, Bin Qin<sup>†</sup>  
State Key Laboratory of Advanced Electromagnetic Technology,  
Huazhong University of Science and Technology, Wuhan, China

## Abstract

Superconducting (SC) gantry can be applied to proton therapy with significantly reduced footprint and weight. However, the relatively lower ramping limit of the SC magnetic field becomes a bottle-neck for fast energy change and beam delivery. Designing a large momentum acceptance (LMA) beam optics can mitigate this issue, which would, meanwhile, bring potential applications for advanced treatment schemes with high beam transmission. In this contribution, we present the design of an LMA gantry using strong focusing AG-CCT SC magnets and symmetrical achromatic lattice. A fast degrader is combined in this design so that the gantry can perform rapid energy switches during the treatment. The AG-CCT design process and beam transport simulation are all performed with our homemade integrated code CSPT, which has interfaces to Geant-4 and Opera, and can reach a maximum speed-up ratio of 450 by applying parallel computation technique. The multi-particle tracking result proves that the gantry has a large momentum acceptance of ~20%.

## INTRODUCTION

Hadron therapy is known to have superior physical characteristics, namely Bragg-Peak. It decreases the deposit dose to surrounded normal tissues and thus holds the potential of reducing the toxicity of organs at risk. Gantry, as an attractive tool in particle therapy, can further expand the ability of conformal treatment by irradiating the beam from different angles. However, the relatively large magnet rigidity, with respect to that of electrons in photon therapy, leads to massive facility size and weight. Most of the gantries running for proton therapy weigh over 100 tons with their length exceeding 10 m [1]. The figure would be much larger when it comes to carbon-ion facilities. Therefore, a cost-effective hadron therapy facility with a smaller gantry is one of the major interests of hospitals and research centers.

Utilizing superconducting (SC) technology enables the magnet to excite a higher magnetic field, which, in consequence, can make the gantry significantly lighter. The main drawback of the SC magnets is their slow ramping rate. The momentum modulation process in the steps of  $\Delta p/p = 1\% \sim 2\%$  is performed with a ramping time of 0.1 ~ 2.0 s per step, corresponding to the momentum of the beam [2]. Designing a gantry lattice with large momentum acceptance (LMA) can mitigate this issue so that the field of

magnets maintains while the beam with various momentum can still be transported to the iso-center. This contribution presents the design of an LMA gantry for proton therapy using alternating gradient canted cosine theta (AG-CCT) magnets. The beam lattice with a fast degrader component and a compact nozzle design is introduced in the paper. For the convenience of the gantry design, a simulation toolkit based on parallel computation technology is developed. A preliminary design of the AG-CCT magnet is displayed at the end.

## OPTICS DESIGN OF THE LMA GANTRY

The overview of the LMA gantry is presented in Fig. 1, which is a cyclotron-based design. A fast degrader component is placed in the middle of the gantry for momentum modulation. The degrader adopts a pair of high-density graphite wedge for continuous momentum modulation, and 2  $B_4C$  blocks for step modulation, since the low Z material can suppress the growth of beam emittance. Linear motors could be equipped for fast energy switches. Two copper collimators lie in sequence, right after the degrader, for emittance restriction. At this stage, only one set of collimator configuration is applied to form a beam with the emittance of  $10\pi$ mm mrad for the following beamline. The Monte Carlo (MC) simulation suggests that the overall transmission efficiency at the nominal energy 70 MeV is about 0.91%, which is about 53% higher than the traditional multi-wedges degrader.

On either side of the degrader component are the 2 bending sections, among which only the second bending section is demanded to have a large momentum acceptance of >16% to ensure a sufficient range of momentum variation with a fixed field of the SC magnet. Considering such a large momentum offset, high-order aberration should be taken into account. AG-CCT is introduced in the design as a main achromatic method [3], and its magnetic field is symmetrically arranged. Due to its flexibility of combining the dipole with multipole fields, the quantity of the magnet in the gantry is reduced. A strong alternating quadrupole field is embedded in the magnet for restricting the beam of different nominal momentum within the bore. Weak sextupole is added for high-order achromaticity. The optics design and optimization process is carried out on COSY Infinity [4]. The optics result of the second bending section is presented in Fig. 2, a stable rounded beam spot is formed at the iso-center, which proves that the gantry is capable of delivering the beam with a momentum range of -9.5%~+10.5%. The main restriction of the momentum acceptance is the good

\* Work supported by the National Natural Science Foundation of China under Grant 11975107, 12205111.

<sup>†</sup> bin.qin@mail.hust.edu.cn

Content from this work may be used under the terms of the CC BY 4.0 licence (© 2023). Any distribution of this work must maintain attribution to the author(s), title of the work, publisher, and DOI

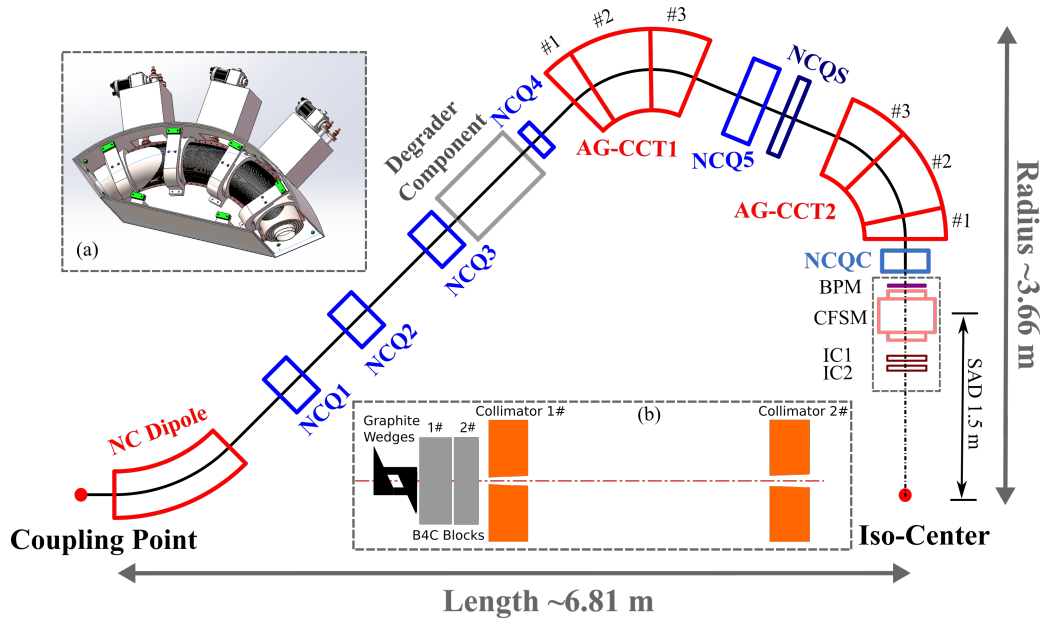


Figure 1: The overview of the LMA gantry. (a) The AG-CCT magnet model; (b) The layout the degrader component.

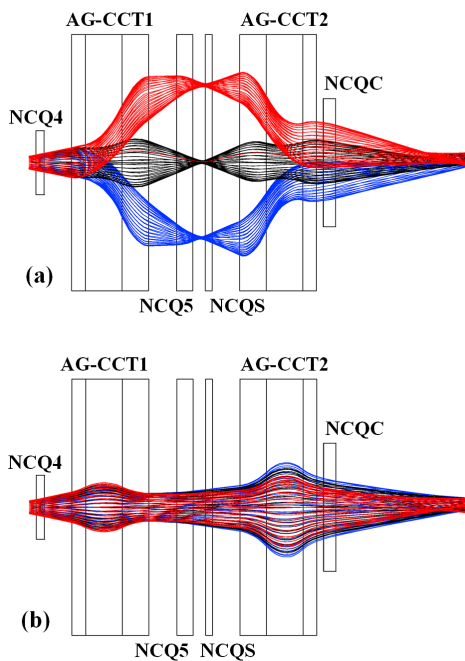


Figure 2: Beam envelope of the second bending section, (a) in the horizontal plane; (b) in the vertical plane. The red, black and blue lines in the figure represent the particle trajectories with the momentum offset of -9.5%, 0%, +10.5%, respectively. The black boxes denote the boundaries of the magnets.

field region (GFR) of the AG-CCT magnet, which is set to 90 mm in this contribution. A compact nozzle component, with a combined-function scanning magnet CFSM, is right after the second bending section, and the SAD is set to 1.5 m in this design.

TUPB014

112

## TOOLKIT FOR GANTRY DESIGN

The field shape of the AG-CCT magnet is greatly affected by the winding geometry, and can hardly be abstracted to a transfer map. The beam tracking with a realistic field offers the best accuracy, which, however, often involves interaction between electromagnetic simulation software and beam optics software. For the convenience of gantry design, we developed a lattice design toolkit using C++, named CSPT [5]. The structure of the toolkit is shown in Fig. 3.

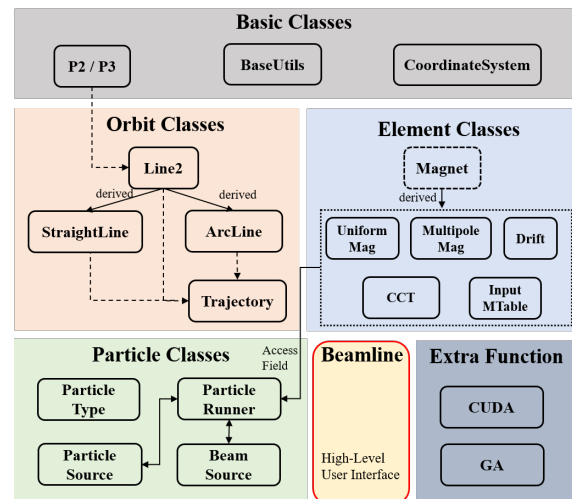


Figure 3: The structure of the CSPT toolkit. Each rectangle with round corners represents a C++ class in the toolkit.

The toolkit is capable of dealing with beam tracking with various initial distributions in the electromagnetic field. The toolkit provides basic optical elements such as dipole, quadrupole and combined-function magnets. The geometry of the CCT magnet can be defined by a winding path

function, and its magnetic field can be calculated with the Biot-Savart law. The toolkit provides interfaces to Geant4 and Opera, so that the simulation can be carried out with input electromagnetic field and complicated beam distribution after a series of particle-matter interactions. Parallel computation technology is applied in the toolkit for fast simulation. The GPU parallel performs a maximum speed-up of 457 times faster than the single thread CPU calculation, exchanged with merely a 0.32% relative error increase.

## AG-CCT MAGNET DESIGN

Due to the large bore aperture of the magnet for LMA beam delivery, the field pattern of the AG-CCT bending magnet can't be taken as cylindrical distribution in approximation. But the relation between the curved winding geometry and toroidal field pattern is complicated. In this contribution, simply the field derivatives are applied to define the field pattern, which also is consistent with the Taylor expansion for particle motion around the nominal trajectory in the transfer map. Ref. [6] discusses the relationship between the winding path of the CCT magnet and its derivative field, which is integrated into our magnet design procedure.

The design of the winding path needs iterative optimization because there are inherent fields that depend only on the geometrical parameters and the current of the magnet. The final derivative field of the AG-CCT magnet is demonstrated in Fig. 4. The integrated harmonic is limited below 5 units, and the main tilt angle of the magnet is set to 40° for a sharp fringe field ramp. A thin iron shield is used in the magnet design to ease the overshooting of the fringe field.

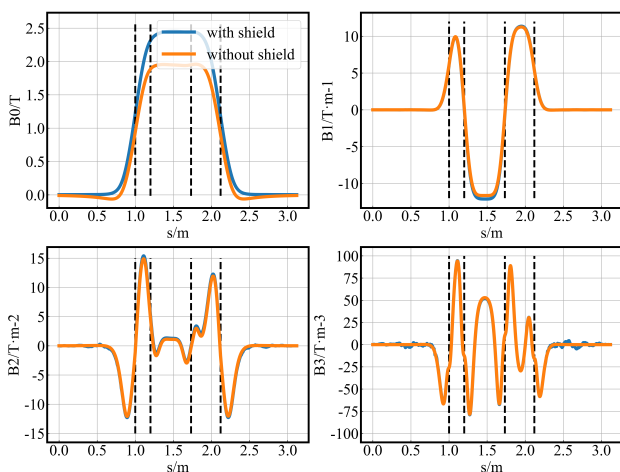


Figure 4: The distribution of the derivative field along the magnet. The black dashed lines in the figure represent the boundaries of each AG section.

## CONCLUSION

Proton therapy has attracted much attention worldwide. Gantries utilizing SC magnets are in demand for more cost-

effective and robust treatment facilities. In this contribution, a systematic design of the LMA gantry with AG-CCT SC Table 1: Integrated Derivative Fields of the AG-CCT Magnet

Order	Section 1#	Section 2#	Section 3#
B0	10000.000	10000.000	10000.000
B1	3247.147	3587.687	3567.178
B2	1.035	4.739	3.428
B3	1.945	2.334	1.103
B4	2.262	0.377	1.058
B5	0.535	0.497	0.345

magnets is proposed. Benefiting from the strong alternating focusing characteristic of the AG-CCT magnet and symmetrical achromatic lattice design, the LMA gantry achieves a large momentum acceptance of -9.5%~+10.5%. For such a large momentum range, in combination with a fast degrader component, the transmission of the lattice at the iso-center is significantly raised, which improves the efficiency of treatment and would bring potential advantages for advanced treatment schemes. A homemade toolkit CSPT is developed for LMA gantry and CCT magnet design. With interfaces to Geant4 and Opera, the toolkit can conduct more realistic multi-physics simulations. More detailed studies, such as the quench protection design of the SC magnet and error analysis, are still ongoing before the LMA gantry comes to the manufacturing stage.

## REFERENCES

- [1] E. Pedroni *et al.*, "The PSI Gantry 2: a second generation proton scanning gantry", *Zeitschrift für Medizinische Physik*, vol. 14, No. 1, p. 25-34, 2004. doi:10.1078/0939-3889-00194
- [2] A. Gerbershagen *et al.*, "The advantages and challenges of superconducting magnets in particle therapy", *Suprocond. Sci. Technol.*, vol. 29, p. 083001, 2016. doi:10.1088/0953-2048/29/8/083001
- [3] L. B. Brouwer, "Canted-Cosine-Theta superconducting accelerator magnets for high energy physics and ion beam cancer therapy", Ph.D. thesis, University of California, Berkeley, American, 2015.
- [4] K. Makino *et al.*, "COSY INFINITY Version 9", *Nucl. Instr. Methods. Phys. Res. Sect. A*, vol. 558, no. , p. 346-350, Mar. 2006. doi:10.1016/j.nima.2005.11.109
- [5] Y. Liao *et al.*, "CSPT: A GPU-Accelerated Lattice Design Toolkit Especially for CCT", presented at the 23rd Int. Conf. on Cyclotrons and their Applications, Beijing, China, Dec. 2022, paper THPO004, unpublished.
- [6] D. Veres *et al.*, "A new algorithm for optimizing the field quality of curved CCT magnets", *IEEE Trans. Appl. Supercond.*, vol. 32, no. 5, p. 4900914, Aug. 2022. doi:10.1109/TASC.2022.3162389

# RESEARCH ON FIRST HARMONIC SHIMMING METHOD OF CYCLOTRON BASED ON LEAST NORM SQUARE SOLUTION

J. Lu<sup>†</sup>, S. An, T. Bian, China Institute of Atomic Energy, Beijing 102413, China

## Abstract

The magnetic field measurement of cyclotron and the shimming of isochronous magnetic field are one of the important links in cyclotron. Due to the influence of factors such as processing errors, installation errors, and inhomogeneity of the magnetic properties of magnet materials, the main magnetic field of the cyclotron will usually deviate from the required isochronous magnetic field and contain a certain amplitude of the first harmonic magnetic field. The existence of the first harmonic magnetic field will rapidly increase the transverse oscillation amplitude and cyclic emittance of the particles, eventually causing beam loss. In order to improve the beam quality of the cyclotron, the shimming technology of the first harmonic magnetic field is essential. In this paper, through the finite element simulation calculation of the main magnet of the cyclotron, a quantitative algorithm for the first harmonic shimming based on the least norm square solution is proposed. At present, this method is being prepared for apply to the magnetic field shimming of the 10MeV high-current proton cyclotron of the CIAE.

## Introduction

Due to the influence of internal defects of iron materials, machining errors and other factors, the magnetic field of the cyclotron usually contains the first harmonic component. During a particle moves in a non-ideal magnetic field, it will be subjected to an additional external force. The lateral oscillation of the particle caused by the external force is a forced oscillation, which will increase the amplitude of the lateral oscillation. When certain conditions are met, it will also cause resonance and cause the particle loss. When constructing a cyclotron, the first harmonic component of the magnetic field must be eliminated, so as to avoid the influence of forced oscillation on the lateral motion of particles and improve the quality of the beam.

The traditional first harmonic shim method is based on the Hard-edge mode method. The hard-edge approximation can be used on transforming the field error to the shape change. However, the accuracy of the calculation results is relatively low. Since a conservative strategy with scaling factor should be adopted to avoid over-shimming and oscillations [1]. For high-current cyclotrons, in order to achieve the physical goal of high-current, the first harmonic component of the magnetic field must be precisely eliminated [2].

In this paper, a magnetic field shimming algorithm based on a multiple linear regression model is proposed to achieve quantitative and accurate shimming of the first harmonic component of the magnetic field.

\* Work supported by CIAE

<sup>†</sup> email address: 359037465@qq.com.

## Principle of Shimming Algorithm

The research on the shimming algorithm and calculation method proposed in this paper is carried out on the basis of the simulation calculation of the compact cyclotron model shown in Fig. 1, through the software Opera-3d. Compared with the magnetic field distribution calculated by the TOSCA solver in the software and the actual measured magnetic field distribution, the error is within  $\pm 0.5\%$  [3].

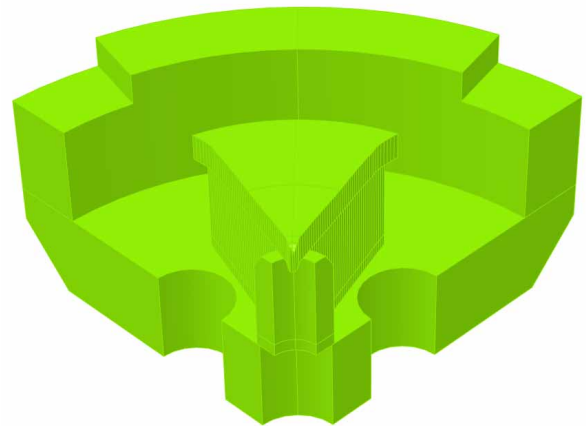


Figure 1: 10MeV cyclotron 1/4 model of CIAE.

The first harmonic magnetic field component of the compact cyclotron can be calculated by Fourier analysis, and the amplitude and phase of the first harmonic along the radial direction can be obtained by Eq. (1):

$$B(r, \theta) = B_0(r, \theta) + \sum_0^{\infty} b_{rk} \cos(k\theta + \beta_{rk}) \quad (1)$$

where  $B_0(r, \theta)$  is the perfect magnetic field,  $b_{rk}$  is the harmonic amplitude,  $k$  is the harmonic coefficient,  $\beta_{rk}$  is the initial phase. The principle of shimming the first harmonic is: without changing the average magnetic field of the cyclotron, artificially introduce a reverse first harmonic to offset the first harmonic component of the original magnetic field. As shown in Fig. 2, in order not to change the average magnetic field, cutting at one pole must be supplemented at the other pole, but in the actual shimming process, the magnetic pole shimming can only be done by cutting. Fortunately, compared to the isochronous error of the magnetic field, the first harmonic magnetic field is a small amount, so the shimming of the first harmonic magnetic field can be included in the shimming process of the isochronous magnetic field, so as to solve the problem of the first harmonic shimming.

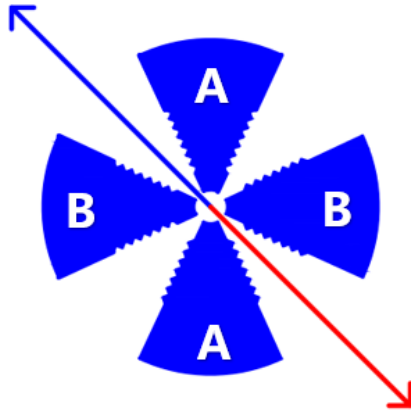


Figure 2: The blue arrow indicates the original first harmonic component of the magnetic field, and the red arrow indicates the artificially introduced reverse first harmonic through magnetic pole shimming, thereby eliminating magnetic field errors.

The shimming method proposed in this paper adopts the asymmetrical cutting method of the magnetic poles to shimming the first harmonic magnetic field. If the cyclotron has  $m$  shimming points in the radial direction, the four magnetic poles correspond to  $4 \times m$  shimming amounts. The shimming amount at any shimming point can be expressed by  $X_k^P$  (P: The Pth pole, k: The kth shimming point). Then the total shimming amount of the cyclotron can be expressed by column matrix:  $X = [X_1^1, X_2^1, \dots, X_m^1, \dots, X_m^4]^T$ . If there are  $n$  magnetic field measurement points in the radial direction, the phase decomposition of the first harmonic magnetic field is performed to obtain two components  $\beta \sin \phi$  and  $\beta \cos \phi$ , then the first harmonic component of the magnetic field can be further expressed as:  $\beta = [\beta_1 \sin \phi_1, \dots, \beta_n \sin \phi_n, \beta_1 \cos \phi_1, \dots, \beta_n \cos \phi_n]^T$ . Among them,  $\beta_1$  represents the amplitude of the first harmonic at the first magnetic field measurement point  $r_1$ , and  $\sin \phi_1$  and  $\cos \phi_1$  represent the phase of the first harmonic at  $r_1$ .

The shimming equation of the first harmonic magnetic field can be expressed as:

$$\beta = A \cdot X + \varepsilon \quad (2)$$

where,  $A$  represents the shimming matrix, which is a correlation regression matrix of order  $2n \times 4m$ ,  $\varepsilon$  is a random disturbance vector, and its mathematical expectation value is zero. The magnetic field error matrix  $b$  is obtained by Fourier analysis of the measured magnetic field, and the magnetic pole shimming amount matrix  $X$  is the shimming amount required at each shimming point in order to eliminate the magnetic field error, which is the unknown quantity to be solved. Equation (2) can be solved only by obtaining the shimming matrix  $A$ .

Shimming matrix  $A$  can be pre-calculated with Eq. (3) by comparing the field difference using an array of unit cutting patches. For example, when cutting an unit triangular patch at  $R_1$  on a pole, as shown in Fig. 3. We have:  $X = [1, 0, 0, \dots, 0]^T$ . The first harmonic magnetic field introduced after cutting:  $\beta = [\beta_1, \beta_2, \dots, \beta_{2n}]$ , the calculation results are shown in Fig. 3,  $A_1 =$

$[A_{11}, A_{21}, \dots, A_{2n-1}]^T$  is calculated by  $A_{k1} = \beta_k$ . Repeat the above process to find all the elements of the padding matrix.

$$\beta_i = A_{i1} \cdot X_1 + A_{i2} \cdot X_2 + \dots + A_{i \cdot 4m} \cdot X_{4m} \quad (3)$$

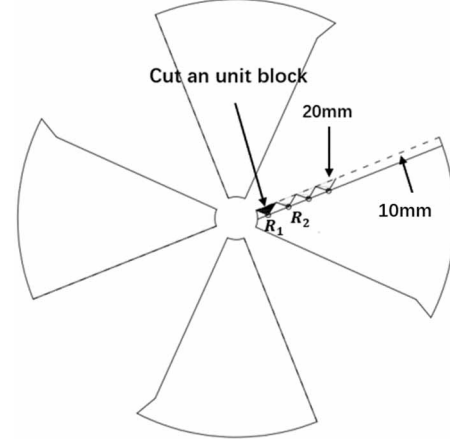


Figure 3: Schematic diagram of cutting to calculate shimming matrix.

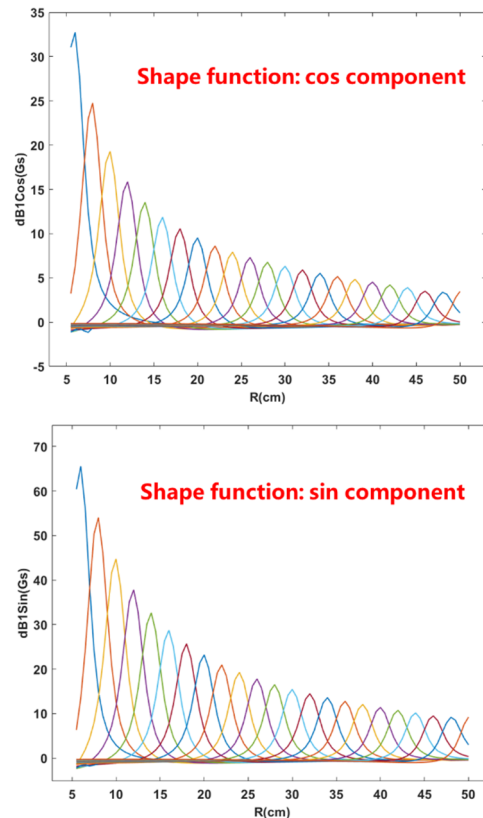


Figure 4: The first harmonic shape function calculated by TOSCA simulation.

We only need to perform finite element simulation calculations on the first magnetic pole to obtain the first harmonic magnetic field introduced by cutting unit shimming blocks at each shimming point. Figure 4 shows the shape function of the first harmonic magnetic field of a single pole obtained by finite element calculation. The magnitude of the first harmonic magnetic field introduced by cutting unit shimming blocks on different magnetic

poles is the same. The phase of the first harmonic is related to the azimuth angle, and the phase difference of the first harmonic magnetic field caused by the cutting of adjacent magnetic poles is  $90^\circ$ . Therefore, as long as the first harmonic magnetic field shape function of one magnetic pole is obtained, the first harmonic magnetic field shape functions of the other three magnetic poles can be obtained.

After obtaining the shimming matrix  $A$ , the shimming Eq. (2) can be written in the following form to solve:

$$X = (A^T A)^{-1} A^T \beta \quad (4)$$

In general, the spacing of the shimming points in the radial direction is twice the spacing of the magnetic field measurement points, and the number of elements of the magnetic field error vector  $b$  is greater than the number of elements of the shimming amount vector  $X$ . Equation (4) is an underdetermined system of equations, and the shimming vector  $X$  can be obtained by solving the method of least norm square solution.

## CONCLUSION

In our study, using the first harmonic magnetic field shimming method based on the multiple linear regression model can realize quantitative and accurate shimming of the first harmonic error of the magnetic field, and the

shimming magnetic field error can be on the order of  $10^{-3}$ . The method is based on a multiple linear regression model of independent magnetic pole shimming effects, which provides a good basis for magnet shimming. The premise is that the area of the shimming block to be cut is much smaller than the area of the magnetic pole, and then the multiple linear regression model can be used. Before integrating the shimming procedure, an appropriate radial cut step size should be chosen to avoid oscillations in the least squares fit.

## REFERENCES

- [1] B. Qin *et al.*, "An improved matrix method for magnet shimming in compact cyclotrons", *Nuclear Inst & Methods in Physics Research A*, vol. 620, no. 2-3, pp.121-127, 2010. doi:10.1016/j.nima.2010.03.135
- [2] T. Zhang *et al.*, "Study and Practice of Shimming Method to First Harmonic in Compact Cyclotron", Annual Report of China Institute of Atomic Energy, 000(001), 2006. doi:CNKI:SUN:YNXB.0.2006-00-017
- [3] C. Baumgarten *et al.*, "Isochronism of the ACCEL 250 MeV medical proton cyclotron", *Nuclear Inst & Methods in Physics Research A*, vol. 570, no. 1, 2007. doi:10.1016/j.nima.2006.09.112

# HIGH-FIDELITY MODELING AND TRANSMISSION OPTIMIZATION FOR THE BEAMLINE OF HUST-PTF \*

Yu Chen, Bin Qin<sup>†</sup>, Xu Liu, Wei Wang, Chengyong Liu

State Key Laboratory of Advanced Electromagnetic Engineering and Technology,  
Huazhong University of Science and Technology, Wuhan, China

## Abstract

A superconducting cyclotron-based proton therapy facility is under construction at Huazhong University of Science and Technology (HUST-PTF). In previous works, the vacuum chamber's shape and the tail effect of the energy spectrum are not considered when calculating the transmission efficiency of the beamline. This study proposes a high-fidelity modeling and optimization method for the HUST-PTF beamline based on Monte Carlo simulation using BDSIM. The modeling procedure of the beamline based on BDSIM is briefly introduced. Then verification of the optical parameters are performed on the gantry sections, and the transmission efficiency of the gantry is optimized by analyzing the unexpected beam loss. After optimization, the transmission efficiency at each energy setting point is calculated. The simulation results show that (1) the proposed optimization method improves the gantry's transmission efficiency from 92.4% to 95.6%; (2) the transmission efficiency calculated by high-fidelity modeling is more accurate than previous simulations because the beam-matter interaction and practical vacuum chamber geometry are considered.

## INTRODUCTION

Huazhong University of Science and Technology is building a superconducting cyclotron-based proton therapy facility, and all magnet designs and installations have now been completed. Previous works have focused on the beamline's design [1], but evaluating the beamline's working state still using separated codes used in the design process may be unsuitable. The more realistic conditions should be considered. For beam tuning, it is of engineering significance to build a high-fidelity model to evaluate the operating state of the beamline and as a surrogate model.

The Refs. [2, 3] use beam delivery simulation software (BDSIM) to conduct seamless simulation on proton therapy systems for radiation protection. Their works consider the beam-matter interaction and practical vacuum chamber geometry. Inspired by their works, this study proposes a high-fidelity modeling and transmission optimization method with the HUST-PTF Beamline as a case study.

The remainder of this study is organized as follows: the model setup and the methodology are briefly introduced in Section II; the results are presented in Section III; and Section VI provides the study's conclusion.

\* Work supported by the National Natural Science Foundation of China (11975107), and the National Key Research and Development Program of China (No. 2016YFC0105305).

<sup>†</sup> bin.qin@hust.edu.cn

## THE MODEL SETUP AND METHODOLOGY

The HUST-PTF beamline is built and validated using BDSIM, a Geant4-based Monte Carlo program that simulates the dynamic motion of beam transport considering the particle-matter interaction and the vacuum chamber geometry [4]. As shown in Fig. 1, the HUST-PTF beamline includes three sections: (i). The energy selection section (ESS) modulates the beam energy and quality. (ii). The periodic transport section transmits the particles to each coupling point efficiently. (iii). The gantry section is to achieve multi-angle treatment. In addition, the physics list "g4qbbc", which includes pure hadronic parts consisting of elastic, inelastic, and capture processes, is used to simulate the physical process during the treatment.

The primary idea behind optimizing transmission efficiency is to analyze the beam loss process and use the gained insights to guide the constraints of the Transport code [5]. This approach achieves the desired results without resorting to complex algorithms. In the next section, this study will present a detailed account of how this study optimized the transmission efficiency of the gantry in the HUST-PTF beamline using this method.

## THE RESULTS

To illustrate the consistency of the high-fidelity model constructed by BDSIM with the present design, the optical parameters need to be verified. Because the optical design does not include the energy modulation process, the beamline is divided into three segments for optical parameters verification according to the collimators' position (line1: from the start to Col#2, line2: from Col#2 to the coupling point; Gantry: from coupling point to iso center).

The optical parameters of line1 and line2 based on BDSIM-model bear almost no difference from the previous optical design, and the transmission efficiency (line1: 100%, line2: 95.8%) satisfy the design requirements of  $\geq 95\%$ . However, the optical parameters of the gantry section, whose transmission efficiency is 92.4% ( $\leq 95\%$ ) and isn't capable of meeting expectations, exhibit some dissimilarities from the previous design, as illustrated in Fig. 2.

From Fig. 2, it can be seen that after the beam enters the first dipole, its x-direction envelope is too large, causing its peripheral particles to hit the beam pipe, thus leading to beam loss, which is the reason why the  $\beta_x$  calculated by BDSIM is small than that calculated by MAD-X codes [6].

Therefore, it is necessary to optimize the transmission efficiency of the gantry section. Based on the above analysis,

Content from this work may be used under the terms of the CC BY 4.0 licence (© 2023). Any distribution of this work must maintain attribution to the author(s), title of the work, publisher, and DOI

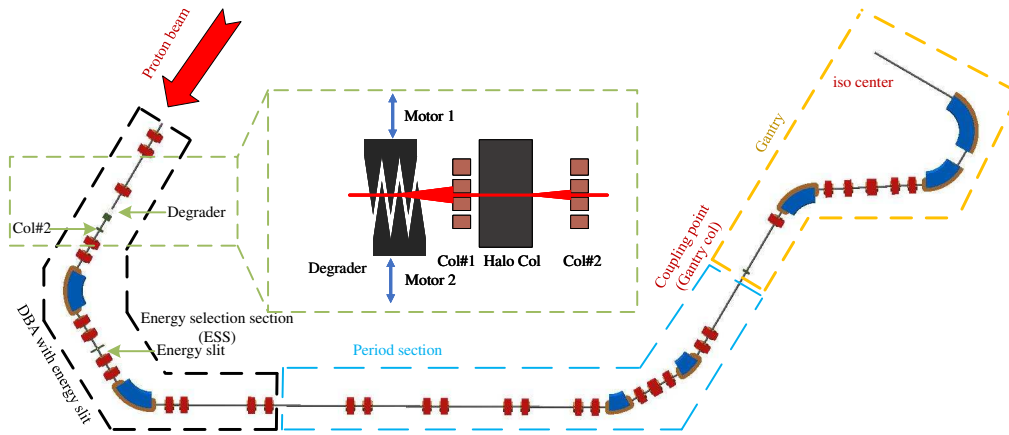


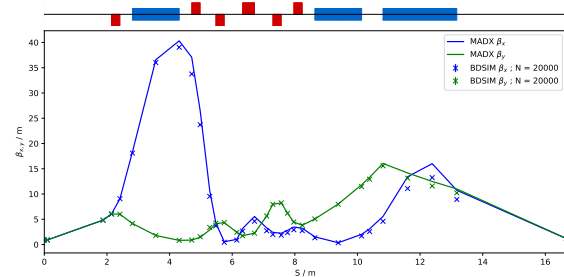
Figure 1: The overall layout of the HUST-PTF beamline based on BDSIM. The ESS is from the beginning to the double-bend achromatic (DBA) entrance. The Period section is from the entrance of DBA to the coupling point. The remaining part is the gantry section. In addition, there are names of typical elements in the figure, which is convenient for evaluating the beam quality after the beam passes through these elements.

Table 1: Transmission Efficiency Under Different Conditions

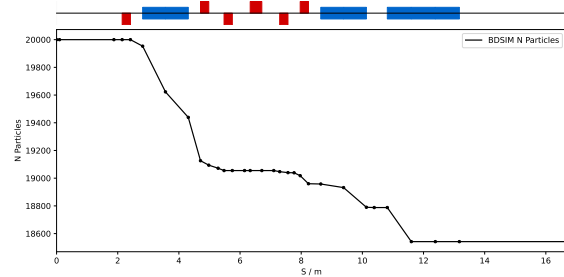
Type	Conditions	Transmission efficiency
Previous restrictions	=18mm	92.4%
Option 1	=15mm	94.2%
Option 2	=14.5mm	94.6%
Option 3	=14.42mm	95.6%
Option 4	=14.41mm	93.4%

a new set of magnets' parameters consisting of six normal quadrupole coefficients can be attained by adjusting envelope conditions, specifically within the x-direction, at the exit of the first magnet. This shall be achieved by employing Transport code matching while ensuring adherence to the established image optics conditions in the previous works [7]. The transmission efficiency under different conditions is shown in Table 1. As shown in Table 1, the highest transmission efficiency is obtained by option 3, which will be adopted to replace the previous magnets' parameters. The optical parameters under the optimized magnets' parameters are shown in Fig. 3. From Fig. 3, it can be concluded that compared with the result in Fig. 2a, the  $\beta_x$  calculated by BDSIM in Fig. 3a is closer to the result of MAD-X code, indicating that the collision at the first dipole has been mitigated after optimization.

After optimization, this study estimates the transmission efficiency of the HUST-PTF beamline under the new magnets' parameters based on the constructed high-fidelity model and the specific settings (lengths of graphite wedge at each energy point and the distance of energy slit at  $\frac{\Delta P}{P} = 0.3\%(1\sigma)$ ), and compares the results with the previous works [8], as shown in Fig. 4. From Fig. 4, it can be concluded that the current results are consistent with the results of the previous work in the high-energy range, but the



(a)  $\beta_x$  and  $\beta_y$



(b) beam transport loss process

Figure 2: Comparison results of optical parameters and beam transport loss process of the Gantry before optimization.

discrepancy becomes larger as the energy setting decreases. This is due to the fact that as the energy setting decreases, the tail effect of the energy spectrum in the energy modulation process becomes more severe, while the previous work assumes beam energy distribution after the degrader as a Gaussian distribution when using Turtle code [9] for calculating transmission efficiency. In addition, the effect of the vacuum chamber's shape on the beam transport is not considered.

To further verify the correctness of the above analysis, Table 2 lists the particle transmission efficiency at typical

Table 2: Transmission Efficiency of Beam Transport Satisfying the Condition  $\frac{\Delta P}{P} < 0.6\%$

Element	70 MeV		230 MeV	
	Transmission efficiency ( $\frac{\Delta P}{P} < 0.6\%$ )	Transmission efficiency	Transmission efficiency ( $\frac{\Delta P}{P} < 0.6\%$ )	Transmission efficiency
Deg	8.2513%	66.4667%	82.5043%	94.2335%
Col#2	0.0546%	0.4571%	14.3113%	20.3937%
Energy slit	0.0481%	0.0495%	13.4451%	13.9387%
Coupling point	0.0472%	0.0478%	13.3852%	13.4515%
iso center	0.0446%	0.0456%	13.2052%	13.2715%

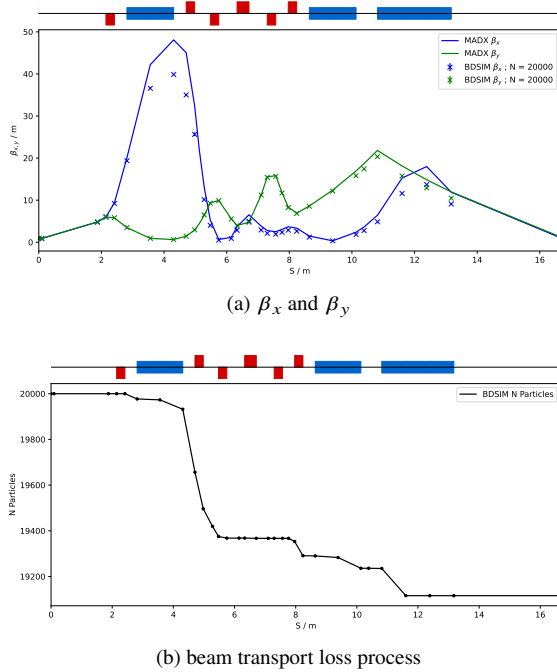


Figure 3: Comparison results of optical parameters and beam transport loss process of the Gantry after optimization.

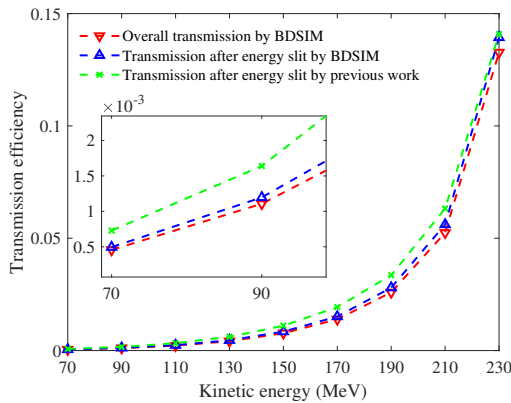


Figure 4: The transmission efficiency at each energy setting

elements under the condition ( $\frac{\Delta P}{P} < 0.6\%$   $2\sigma$ ). From Table 2, it can be seen that: (i). The transmission efficiency (0.0546%) at 70 MeV that meets the condition after passing

through Col#2 is already lower than that (0.0729%) previously calculated by Turtle code. (ii). With the premise that downstream beamline transmission efficiency is high (>95%), the beamline actually transports particles that meet the  $\frac{\Delta P}{P} < 0.6\%$  after passing through Col#2.

## THE CONCLUSION AND FUTURE WORK

In summary, this study proposes high-fidelity modeling and transmission optimization method with the HUST-PTF beamline as a case study. This study utilized a high-fidelity model, considering the vacuum chamber's shape and the tail effect of the energy spectrum, to achieve start-to-end simulation and calculate the transmission efficiency of the beamline at each energy setting. In addition, this study modifies the constraints of Transport code and improves transmission efficiency by analyzing the beam loss process, which is simple and efficient. Our next step is to verify the model's realism through experiments and use the built model data to get a surrogate model to accelerate calculations.

## REFERENCES

- [1] B. Qin *et al.*, "Design and development of the beamline for a proton therapy system", *Nucl. Sci. Tech.*, vol. 32, p. 138, 2021.
- [2] Ramoisaux E *et al.*, "Self-consistent numerical evaluation of concrete shielding activation for proton therapy systems", *Eur Phys J Plus.*, vol. 137, p. 889, 2022.
- [3] Hernalsteens C *et al.*, "A novel approach to seamless simulations of compact hadron therapy systems for self-consistent evaluation of dosimetric and radiation protection quantities", *Eur Phys Lett.*, vol. 132, p. 50004, 2021.
- [4] L. Nevay *et al.*, "BDSIM: An accelerator tracking code with particle-matter interaction", *Comput. Phys. Commun.*, vol. 252, p. 107200, 2020.
- [5] U. Rohrer, PSI graphic transport framework, 2006.
- [6] Methodical Accelerator Design (MAD-X)
- [7] B. Qin *et al.*, "Design of Gantry Beamline for HUST Proton Therapy Facility", *IEEE Trans. Appl. Supercond.*, vol. 28, pp. 1-5, 2018.
- [8] W. Chen *et al.*, "Transmission calculation and intensity suppression for a proton therapy system", *Nucl. Instrum. Methods Phys. Res., Sect. A*, vol. 881, pp. 82-87, 2018.
- [9] U. Rohrer, PSI graphic turtle framework, 2006.

# CALIBRATION EXPERIMENT OF EQUIVALENT AREA OF INDUCTION COIL FOR MAGNETIC FIELD MEASUREMENT OF SUPERCONDUCTING CYCLOTRON

X. Chen<sup>†</sup>, S. An, T. Bian, L. Ling, J. Lu, F. Wang, China Institute of Atomic Energy, Beijing, China

## Abstract

China Institute of Atomic Energy's 250MeV superconducting cyclotron (CYCIAE-250) uses the induction coil method to measure the magnetic field in its airgap. To ensure the precision of magnetic field measurement, area of the induction coil needs to be calibrated. This paper designs a set of coil calibration technique based on flipping coil method. The uniform magnetic field needed for calibration is provided by a permanent magnet with good static performance, its field is measured through high-precision nuclear magnetic resonance (NMR) probe. Then the induction coil will then be installed at the same position of the NMR probe. During the calibration process, induction coil is rotated 180 degrees and magnetic flux through it will be recorded by a high-speed digital integrator. Corresponding equipment is also designed to finish this task. This Paper describes this magnetic field measurement method, corresponding magnetic measurement equipment, calibration process of the induction coil and calibrated area of the coil.

## BACKGROUND

Magnetic Field measurement and shimming is one essential part of cyclotron. There are three main methods of field measurement: hall probe, induction coil and nuclear magnetic resonance [1]. China Institute of Atomic Energy's 250MeV superconducting cyclotron (CYCIAE-250), uses induction coil as field measurement device, which requires the precise area of induction coil.

Calibration method for induction coils used in CYCIAE-230 and other cyclotrons only considers the start point and end point of voltage integral data and can be influenced by nonlinear noise [2-5]. To improve the accuracy of calibration, this article designs a new calibration method and equipment, and then describes the calibration result of the equivalent area of induction coil used for CYCIAE-250.

## CALIBRATION METHOD

According to Faraday law of electromagnetic induction, change of magnetic flux through a close circuit will create an induced electromotive force (EMF), of which the amplitude is proportional to the change rate of magnetic flux and the winding number of the circuit:

$$E = -n \cdot \frac{d\Phi}{dt} = -n \cdot \frac{d}{dt} \int \vec{B} \cdot d\vec{S} \quad (1)$$

<sup>†</sup> email address: 962180915@qq.com

The induction coil used for CYCIAE-250 has a small radius and a large winding number, and is connected to digital integrator with twisted pair. The resistance or induction coil and twisted pair's resistance can be neglected, thus the relation between Voltage on the integrator and field through the coil can be described as:

$$V = E = -nS \cdot \frac{dB}{dt} \quad (2)$$

$$B = -\frac{1}{nS} \int V \cdot dt \quad (3)$$

According to Eq. (3), difference of magnet field between two points in the magnetic field can be calculated by recording the voltage produced by induction coil with fast digital integrator. Accordingly, by changing the magnetic field through the coil at a given amount, the equivalent area of coil can be calibrated according to following equation:

$$nS = \frac{1}{\Delta B} \left| \int_{t_1}^{t_2} V \cdot dt \right| \quad (4)$$

## Clearing up Linear Drift

When using digital integrator to record induction voltage and its integral value, drift caused by electrical noise must be cleared up [2, 4, 5]. High order cumulant of noise tend to be cancelled out after integration and can be neglected, only the average value of noise voltage will cause a linear drift to the integration result. As a result, real value of coil's equivalent area can be described as:

$$nS = \frac{1}{\Delta B} \left| \int_{t_1}^{t_2} V \cdot dt - V_{off} \cdot T \right| \quad (5)$$

Among the expression, nS is equivalent area of coil,  $V_{off}$  is the average value of noise, and T is the integration time.

## Calibration Method

A permanent magnet is used to create a constant uniform magnetic field needed for calibration, together with a set of positioning equipment to locate the coil at the centre of magnetic field. First step of calibration is to calibrate the field of permanent magnet with nuclear magnetic resonance (NMR) probe.

NMR probe measures magnetic field through the coupling of hydrogen's nuclear spin (proton spin) and external magnetic field. When applying a external magnetic field, proton spin will precess in the direction of magnetic field. Protons absorb electromagnetic waves at precession frequency and become excited, creating a loss

of incident electromagnetic waves [6]. Field intensity can be determined by this resonance frequency and the magnetogyric ratio of proton.

The calibration procedure of induction coil is as follows:

- Locate NMR probe at the centre of permanent magnet and measure magnetic field intensity;
- Remove NMR probe, then locate induction coil at the same position
- Initialize digital integrator and begin recording data, which contains two steps: (1) Hold still the coil and record drift voltage; (2) Rotate the coil in 180 degrees and record voltage integral with integrator. There is a measuring equipment to ensure the accuracy of rotation.
- Repeat the measurement process multiple times and calculate the equivalent area of induction coil.

## CALIBRATION EXPERIMENT

We calibrated two induction coils of same parameter, one actually used for magnetic field measurement of CYCIAE-250 (coil 1), one as backup device (coil 2). According to calibration procedure, we first measured the precise field intensity at the center of permanent magnet is measured, the value is 1.021624T, denoted as  $B_0$ , as shown in Fig. 1.



Figure 1: Field intensity measured by NMR probe.

The next step is to locate the induction coil and calibrate its equivalent area. Several tests were first conducted to figure out the appropriate gain of digital integrator in order to improve signal to noise ratio (SNR). We finally choose a gain of 40 times for the integrator.

### Calibration of Coil 2

We conducted the calibration experiment twice at two separate gain settings of the integrator: one at gain 20 and one at gain 40. In each calibration experiment, Voltage integral data was measured 10 times, including 5 times clockwise and 5 times counterclockwise. In each measurement, we keep the coil still for about 2.5 second, and then rotate the coil in 3 second, the total integral time is 6 second, total voltage integral was denoted as  $I_0$ .

First 2 second of data is used to calculate drift time. We use least square method and calculate integral data's slope under the condition of zero intercept, denoted as  $V_{off}$ , the equivalent area of coil can be calculated by following equation:

$$nS = \frac{1}{2B_0} |I_0 - V_{off}T| \quad (6)$$

During data handling process, we notice some bad data caused by misoperation of integrator and no overrange phenomenon. the calculate result is shown in Fig. 2.

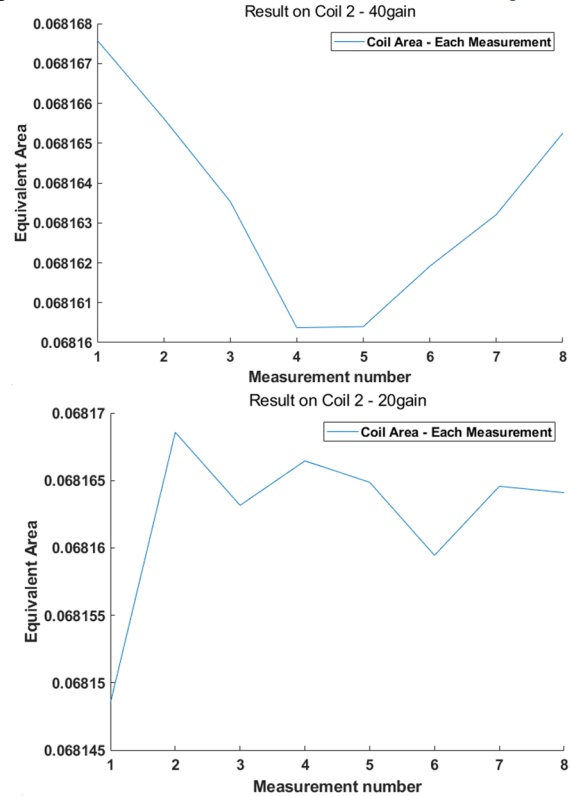


Figure 2: Calculated result of equivalent area of coil 2.

In the case of 20 times gain, one record differs significantly from others and is excluded from final averaging. Average area of coil 2 is described in Table 1 together with that of coil 1.

### Overrange Analysis

By using high gain setting, the SNR of integrator can be improved. However, the integrator has a finite range of 10V, if the multiplied voltage exceeds range, it will be recorded as 10V, causing a mismatch in voltage data record and voltage integral record. To determine whether setting gain to 40 will cause data overrange or not, we calculated the gradient of voltage integrals, and compares it with induced voltage data. In practice, aforementioned difference in voltage and integral is also influenced by noise, so we compare result under gain 20 and gain 40. If only the result under gain 40 is significantly higher, than that under gain 20, we can determine that the recorded voltage data is overrange.

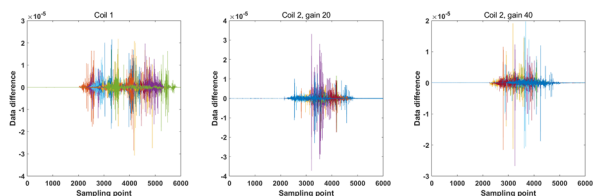


Figure 3: Difference in integral's gradient and voltage data.

As is shown in Fig. 3, calculation result shows similar difference in integral's gradient and voltage data under two different gain settings. We also checked the difference of the sum of induced voltage data and voltage integral, and the result does not exceed  $\pm 1.2 \times 10^{-7}$ .

### Calibration of Coil 1

As the experiment and data handling show, choosing a gain of 40 times didn't cause recorded value to be overrange, and calculated area matches well, we only use voltage integral data in the gain of 40 times to calculate the equivalent area of coil 1, the result shows in Fig. 4.

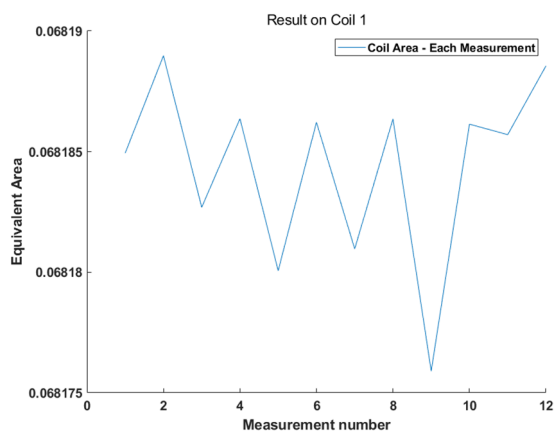


Figure 4: Calculated result of equivalent area of coil 1.

Record with number 9 differs significantly and is excluded from calculating average area. Final calculation result shows in Table 1.

Table 1: Average Area of Two Coils

Coil number	Coil 1	Coil 2, 20 gain	Coil2, 40 gain
Equivalent area(m <sup>2</sup> )	0.06818520	0.0681645	0.0681635

According to experiment results, the consistency of coil area in different gain settings is good, difference in calculated area of coil 2 is less than 20 ppm. Further analysis of data overrange also shows that induced voltage keeps below range, thus we choose calibration result under the gain of 40 times as final calibrated area of coils.

### CONCLUSION

In order to calibrate the equivalent area of induction coil used for magnetic measurement and shimming system of CYCIAE-250, this article designed a new calibration method and equipment. Calibration experiment is

conducted successfully according to this new method, and the precise equivalent area of two induction coil is measured.

### REFERENCES

- [1] K. N. Henrichsen, "Classification of magnetic measurement methods," in *CERN Accelerator School*, Montreux, Switzerland, 16–20 March 1992 (CERN, Montreux, 1992), pp. 70–83. doi:10.5170/CERN-1992-005.70
- [2] M. Li, J. Zhong, T. Cui, and T. Zhang, "Application and Development of a Method to Shim the Isochronous Field in Small Cyclotrons," *IEEE Transactions on Applied Superconductivity*, vol. 26, no. 4, pp. 1-4, June 2016. doi: 10.1109/TASC.2016.2535238
- [3] M. Li *et al.*, "Field Mapping System Design for the Superconducting Cyclotron CYCIAE-230," *IEEE Transactions on Applied Superconductivity*, vol. 28, no. 3, pp. 1-4, April 2018, doi: 10.1109/TASC.2018.2789447
- [4] M. Buzio, "Fabrication and calibration of search coils," in *CERN Accelerator School CAS 2009: Specialised Course on Magnets*, Bruges, Belgium, 16–25 June 2009 (CERN, Bruges, 2009), pp. 387-421. doi:10.5170/CERN-2010-004.387
- [5] P. Miller *et al.*, "Magnetic Field Measurements in the MSU 500 MeV Superconducting Cyclotron," *IEEE Transactions on Nuclear Science*, vol. 26, no. 2, pp. 2111-2113, April 1979, doi: 10.1109/TNS.1979.4329817
- [6] J. M. Pendlebury *et al.*, "Precision field averaging NMR magnetometer for low and high fields, using flowing water." *Review of Scientific Instruments*, vol. 50.5, pp 535-540, 1979. doi: 10.1063/1.1135904

# THE DESIGN OF NONLINEAR REGENERATIVE EXTRACTION IN 250MeV PROTON SUPERCONDUCTING SYNCHROCYCLOTRON

Pengtai Lin, Yufei Yang, XinMiao Wan, Zhiqiang Ren, Wenlong Liao, Xiaobao Luo, Zhihui Li<sup>†</sup>,  
The Key Laboratory of Radiation Physics and Technology of Ministry of Education, Institute of  
Nuclear Science and Technology, Sichuan University, Chengdu, China

## Abstract

The objective of this article is to apply the regenerative extraction system to a 250MeV proton superconducting synchrocyclotron. The parameters of the regenerative extraction system are determined by iteratively calculating the appropriate magnetic field and particle trajectory in the region where the magnetic field and particle trajectories interact. This is then combined with the magnetic channel system to achieve the extraction of the beam from the accelerator. In the article, the particle orbit dynamics analysis and the design of relevant parameters for the regenerative extraction system were successfully implemented using Matlab programming. The simulation results showed that the stability in the vertical direction has the greatest impact on the extraction efficiency and determination of the regenerative magnetic field parameters. In order to maximize the particle extraction efficiency, the radial displacement of particles in the last few turns should pass through two identical nodes.

## INTRODUCTION

Proton therapy is an effective treatment for cancer with minimal side effects. In recent years, due to the development of superconducting technology, superconducting synchrocyclotron has compact structure and low design difficulty to meet the needs of medical treatment of cancer. The extraction problem is very important in the design process of superconducting synchrocyclotron, and the common extraction methods include electromagnetic deflection system, target scattering beam and regenerative extraction system [1]. The electromagnetic deflection system utilizes deflecting plates to apply a radial electric field force on particles, causing an increase in their orbit radius. The electromagnetic deflection system is suitable for accelerators with large particle orbit spacing, and the particle orbit spacing in the superconducting synchrocyclotron is small, so the application of the electromagnetic deflection system in the superconducting synchrocyclotron will cause some particles to hit the deflection plate and cause unnecessary losses. The target scattering beam method involves scattering the beam into a magnetic channel using a material with a high atomic number. However, this method generally exhibits low extraction efficiency. The regenerative excitation system generates the required magnetic field by adding iron blocks between the edges of the magnetic poles. The generated magnetic field disturbs the particles and causes an increase in their radial amplitude while maintaining stable operation in the vertical direction, thereby

<sup>†</sup> lizhihui@scu.edu.cn.

achieving the goal of extracting particles from the accelerator [2]. The extraction efficiency of the regenerative excitation system can reach between 50% and 70%, indicating a high level of extraction efficiency. In order to promote the development of proton therapy in China, the Key Laboratory of Radiation Physics and Technology, Ministry of Education, has designed an extraction system for a 250MeV proton superconducting synchrocyclotron. The main parameters of the accelerator are shown in Table 1.

Table 1: The Main Parameters of 250MeV Superconducting Synchrocyclotron

Extraction beam energy	250MeV
Magnetic pole radius	53cm
Central magnetic field	5.57T
Ampere-Turn Number	533A-3000turns
RF Cavity Voltage	20kv
RF frequency ranges	58-85MHz

The regenerative extraction system was initially proposed by Tuck and Teng [2] and further improved by Le Couteur [3,4]. The initial regenerative system is linear regeneration, which is a method of increasing the number of "peeler" and the "regenerator" two local magnetic fields on the magnetic pole edge. As shown in Figure 1 (a), these two local magnetic fields are reduced and increased by linear methods in a linear way. Then the study found that only a single increase in the magnetic pole edge of the magnetic pole could also achieve the resulting effect. As shown in figure 1 (b), where the magnetic field of "regenerator" increases nonlinearly with the radius, the magnetic pole utilization rate of this method is higher.

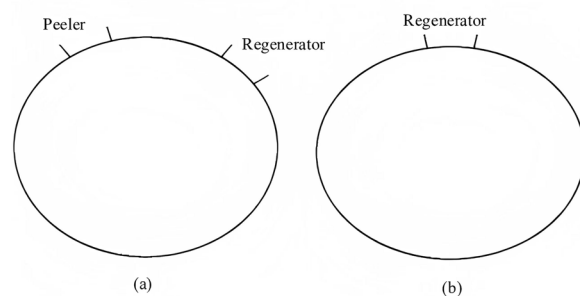


Figure 1: (a) is schematic diagram of linear regenerator extraction, (b) is schematic diagram of nonlinear regenerator extraction.

Appropriate regenerative magnetic field parameters can result in a rapid increase in the radial amplitude of particles while maintaining stability in the vertical direction. When

particles are running near the vicinity of a magnetic field drop-off exponent of  $n=0.2$  ( $vz=2vr$ ), the resonance effect can cause a rapid increase in the vertical displacement of particles, leading to particle loss. Therefore, to avoid the resonance effect, the starting position of the regenerative magnetic field should be located before  $n=0.2$ .

## CALCULATION PRINCIPLE/PHYSICAL MODEL

The parameters of the regenerative extraction system refer to Le Couteur [4]. The distribution of the regenerative magnetic field is:

$$q_0 \frac{r_0}{H_0} H_q = k_1 \rho + k_2 \rho^2 + k_3 \rho^3 + k_4 \rho^4 + k_5 \rho^5 \quad (1)$$

Where,  $\theta_0$  represents the angular width of the regenerative magnetic field region,  $r_0$  represents the starting radius of the regenerated magnetic field,  $H_0$  represents the magnitude of magnetic induction at the starting position of the regenerated magnetic field,  $H_q$  represents the difference between the regenerative magnetic field and  $H_0$ ,  $\rho$  represents the particle's displacement from  $r_0$ ,  $k_1$ ,  $k_2$ ,  $k_3$ ,  $k_4$  and  $k_5$  represents the magnetic field adjustment parameters.

For a complete orbital dynamics analysis, the magnetic field off the central plane needs to be calculated by equations (2), (3) and (4):

$$B_z(r, \theta, z) = B_z(r, \theta) + \frac{1}{2} z^2 \left( \frac{\partial^2}{\partial r^2} + \frac{1}{r} \frac{\partial}{\partial r} + \frac{1}{r^2} \frac{\partial^2}{\partial \theta^2} \right) B_z(r, \theta) + O(z^4) \quad (2)$$

$$B_r(r, \theta, z) = -z \frac{\partial}{\partial r} B_z(r, \theta) + O(z^3) \quad (3)$$

$$B_\theta(r, \theta, z) = -\frac{z}{r} \frac{\partial}{\partial \theta} B_z(r, \theta) + O(z^3) \quad (4)$$

Where,  $z$  represents the displacement of the particle away from the vertical direction of the center plane,  $r$  represents the radial displacement of the particle away from the equilibrium orbit,  $B_z(r, \theta, z)$ ,  $B_r(r, \theta, z)$  and  $B_\theta(r, \theta, z)$  represent the vertical, radial and angular magnetic fields of the desired position in the cylindrical coordinate system,  $B_z(r, \theta)$  represents the vertical magnetic field distribution on the center plane of the magnetic pole.

Programming beam dynamics analysis is based on Runge Kutta numerical calculation method to accurately calculate particle motion information, time  $t$  as an independent variable. The force equation of particles is as follows:

$$\frac{d}{dt} \vec{P} = q e \vec{E} + q e (\vec{v} \times \vec{B}) \quad (5)$$

Where, Vector  $P$  represents the particle momentum, vector  $E$  represents the electric field strength, vector  $v$  represents the particle velocity, vector  $B$  represents the magnetic induction intensity, and  $qe$  represents the amount of charge of the mass particle.

## PARAMETER, SIMULATION RESULTS AND DISCUSSION

After repeated iterative calculation between the regenerated magnetic field and particle orbit dynamics, the regenerated magnetic field parameter is finally determined as (The units used in the formula are the International System of Units).

$$q_0 \frac{r_0}{H_0} H_q = \rho(-0.0495 + 35.5\rho - 800\rho^2 + 10500\rho^3 - 50000\rho^4)$$

When adjusting the parameters of the regenerated magnetic field, the utilization rate of the magnetic pole should be increased as much as possible, and the initial radius of the regenerated magnetic field should be increased as much as possible. When the regenerated magnetic field makes the radial gain of the last circle of particles reach about 1.3cm, the trajectory of the last few circles of particles pass through two nodes and maintain stability in the vertical direction, and the radial gain of the particles makes the first magnetic channel located within the magnetic pole, these requirements are met, indicating that the parameter adjustment of the regenerated magnetic field is completed. The local adjustment of magnetic field can be realized according to the main range of influence of  $k_1$ ,  $k_2$ ,  $k_3$ ,  $k_4$  and  $k_5$ . The simulation results show that maintaining the stability of vertical direction is the most demanding parameter selection.

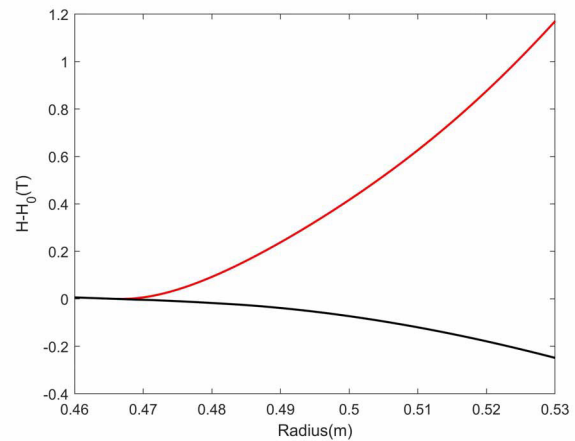


Figure 2: The change of the magnetic field with respect to the radius of  $H_0$ .

Figure 2 describes the change of the main magnetic field and the theoretical regenerated magnetic field with respect to the radius of  $H_0$ . The red and black lines represent the changes in the regenerative field and the main magnetic field with respect to the radius. Due to magnetic leakage at the edge of the magnetic poles, the actual magnetic field needs to conform to the designed field within a region inside the radius where the magnetic channels are located.

### Radial Motion

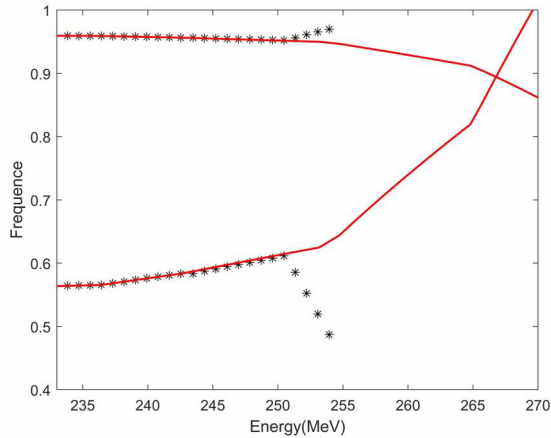


Figure 3: The point and the real line indicate the change in  $v_r$  and  $2v_z$  with the absence of a regenerative magnetic field.

Figure 3 describes the two solid lines intersect at the energy of 266.8MeV, where  $n=0.2$ . When the particle is running close to  $n=0.2$ , the radial amplitude of the resonance effect particle will be converted into the vertical amplitude, resulting in the increase of the vertical amplitude and the particle loss. In order to avoid unnecessary loss of particles, the magnetic field of the regeneration region should be placed before  $n=0.2$ .

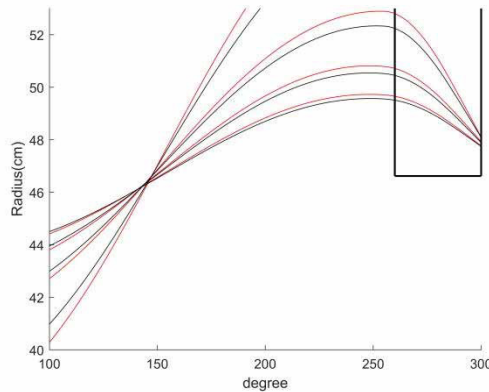


Figure 4: the change of the radius  $r$  with the azimuth  $\theta$ .

Figure 4 describes the trajectory of the radius  $r$  of the last four circles of the two radially unstable orbits changing with the azimuth angle, where the value range is from  $100^\circ$  to  $300^\circ$ , and the vertical displacement of the two radially unstable orbits remains stable. Figure 4 shows that the particle trajectory passes through a node, the node at  $158^\circ$ , the azimuth at  $206^\circ$  the particle radial gain can reach 1.3cm, and the magnetic channel can be placed here.

### Vertical Motion

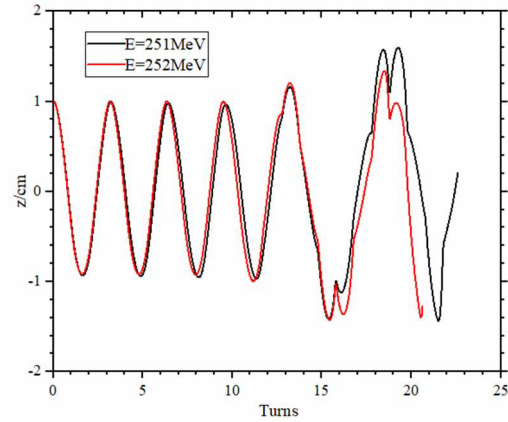


Figure 5: The trajectory of the vertical displacement of particles as the number of runs changes.

Figure 5 describes the trajectory of the vertical displacement of particles with different energies as the number of runs changes. By looking at Figure 5, we can see that the growth factor of the maximum  $z$  value decreases from 1.532 at 251MeV to 1.41 at 252MeV. The higher energy particle have a smaller growth factor because the coupling effect is smaller. The initial values of  $(\rho_0, p_r)$  are different. The simulation results show that the change of the  $(\rho_0, p_r)$  will eventually change the number of rotating cycles for particle into the magnetic channel.

## CONCLUSION

The research method used in this paper can be applied to other energy synchrocyclotron beam extraction. According to the simulation results, if the vertical displacement of the particle beam generated by the used particle source is limited, the extraction efficiency of the beam will be improved accordingly, because the loss of particles in the vertical direction during extraction will be reduced. In addition, the activation caused by the increase of the vertical displacement of particles can be reduced.

## ACKNOWLEDGMENTS

This work was supported by the National Natural Science Foundation of China (Grant Nos. 11375122 and 11875197).

## REFERENCES

- [1] Lembra, and Y. Ya, "Beam extraction methods for synchrocyclotron", *Phys, Usp*, 1963, 6(1): 143.
- [2] J. L. Tuck and L. C. Teng, Institute for nuclear studies 170-inch synchrocyclotron Progress Report III, University of Chicago, 1950.
- [3] Le Couteur, K. J, and S. Lipton, "Non-linear regenerative extraction of synchrocyclotron beams", *The London, Edinburgh, and Dublin Philosophical Magazine and Journal of Science*, 1955, 7(46): 1265.
- [4] Couteur, and K. J. Le, "The regenerative deflector for synchrocyclotrons", *Proc, Phys, Soc, B*, 1951(64): 10

## BEAM DYNAMICS IN SUPERCONDUCTING PROTON LINAC\*

Xin-Miao Wan, Yu-Fei Yang, Zhi-Qiang Ren, Peng-Tai Lin, Wen-Long Liao, Xiao-Bao Luo,  
Xue-Jiang Pu, Zhi-Hui Li<sup>†</sup>

The Key Laboratory of Radiation Physics and Technology of Ministry of Education, Institute of Nuclear Science and Technology, Sichuan University, Chengdu 610065, China.

### Abstract

Beam loss control is a crucial research direction in high-current superconducting linear accelerators (SCL). The research findings include firstly, for continuous beams, when tune depression ( $\eta$ )  $> 0.7$ , zero current periodic phase advance ( $\sigma_{0t}$ ) can partially exceed  $90^\circ$  during transport in solenoid and quadrupole doublet periodic focusing channels. Different results occur when  $\eta < 0.7$ . Secondly, in the solenoid system,  $\sigma_{0t}$  can partially exceed  $90^\circ$  without significant impact on beam quality. In the quadrupole doublet focusing system, the partial breakdown of  $90^\circ$  affects beam quality. Thirdly, Similar conclusions hold for acceleration effects. Fourthly, numerical analysis shows that double-period structures have more stringent design criteria than fully period structures. The double-period structure can cause envelope instability even if  $\sigma_{0t} < 90^\circ$ . Fifthly, the primary factor causing halo is the 2:1 resonance. Additionally, when  $\eta$  is small, higher-order resonances can also cause halo.

### INTRODUCTION

Countries around the world have initiated a series of research projects related to high-power proton superconducting linear accelerators (APT, SNS, J-PARC, CADS, etc.) [1]. The understanding of beam dynamics in high-current SCL has been deepened, leading to the discovery of theories that affect the stability of beam, including envelope instability and particle-core resonance. These findings have been summarized and formulated into a set of fundamental principles for the design of SCL [2]. These principles include ensuring that the  $\sigma_{0t}$  is less than  $90^\circ$  to avoid envelope instability and prevent beam loss [3]. The first principle aims to mitigate envelope instability, while the second principle is derived from studies on halo [4]. In addition, we need to conduct systematic research on the effects of  $\sigma_{0t}$  exceeding  $90^\circ$  in the quasi-periodic focusing structure of the front section of the first acceleration stage in the SCL, as well as the halo in the double-period structure of the cryomodule with a cryostat as a unit [5].

### ENVELOPE INSTABILITY

Based on the transverse motion equation, the RF electromagnetic field at the low-energy end of the linear accelerator exhibits defocusing and axial symmetry. In this study, we used a solenoid (with axial symmetry) and a non-axisymmetric quadrupole doublet as the focusing elements.

The specific parameters of these elements are shown in Fig. 1 for reference in the subsequent discussion.

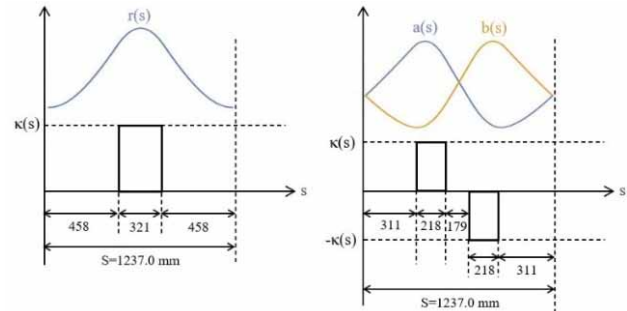


Figure 1: Periodic focusing elements and the corresponding matched beam envelopes. (a) solenoid, (b) quadrupole doublet.

We used *TraceWin* for our simulation and *PARTRAN* for multi-particle simulation and tracking. The K-V distribution and K-V envelope equations were selected for their advantages in analysing the effect of space charge. The initial kinetic energy of the proton beam was 10 MeV, and the initial normalized RMS emittance of the CW beam was  $0.2 \pi \cdot \text{mm} \cdot \text{mrad}$  in both the  $x-x'$  and  $y-y'$  planes. A total of 100,000 particles were simulated. The envelopes where  $X(s)$  and  $Y(s)$  are in the two transverse directions of the periodic focusing channels are described by [6]:

$$X'' + \kappa_x(s) \cdot X - \frac{\varepsilon^2}{X^3} - \frac{2K}{X+Y} = 0 \quad (1)$$

$$Y'' + \kappa_y(s) \cdot Y - \frac{\varepsilon^2}{Y^3} - \frac{2K}{X+Y} = 0 \quad (2)$$

To study the transverse beam dynamics when  $\sigma_{0t}$  partially exceeds  $90^\circ$ , we designed five different focusing schemes for simulating  $\sigma_{0t}$ , as shown in Fig. 2. The maximum  $\sigma_{0t}$  of the beam was set to be  $120^\circ$  (①),  $110^\circ$  (②),  $100^\circ$  (③), and  $90^\circ$  (④) to observe the trend under different acceleration gradients in the presence of an acceleration field. To avoid excessive sensitivity to the focusing parameters, we generally set the minimum value of  $\sigma_{0t}$  to  $40^\circ$  after the beam passes through 80 focusing periods. Furthermore, for the case where the maximum  $\sigma_{0t}$  was  $120^\circ$ , we implemented a control scheme (⑤) to prevent envelope instability in the beam. The maximum  $\sigma_{0t}$  of this control scheme was set to  $88^\circ$ , achieved by reducing the acceleration gradient of the corresponding cavity.

\* Work supported by the National Natural Science Foundation of China (Grant Nos. 11375122 and 11875197)

<sup>†</sup> lizhahui@scu.edu.cn

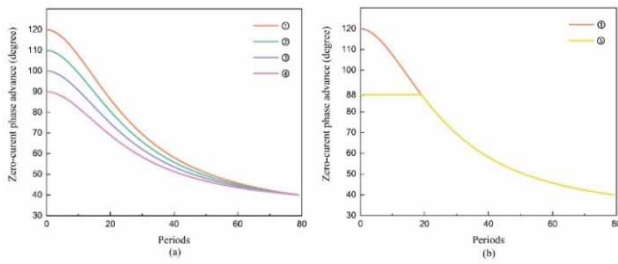


Figure 2:  $\sigma_{0t}$  for the five schemes. (a) Shows the focusing schemes ①-④ and (b) shows the focusing schemes ① and ⑤.

Finally, the  $\varepsilon$  of the output during beam transport was obtained, as shown in Fig. 3.

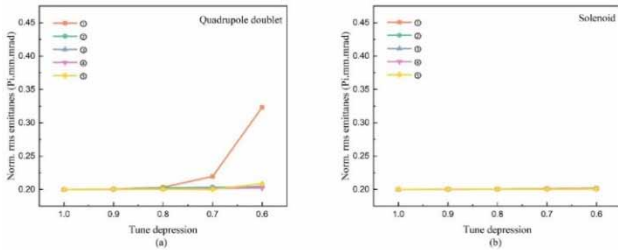


Figure 3: The  $\varepsilon$  when  $\eta$  was equal to 1.0, 0.9, 0.8, 0.7, and 0.6 for different focusing schemes, respectively. (a) shows that when the beams are transported in periodic focusing quadrupole doublet channels, and (b) shows that when beams are transported in a periodic focusing solenoid channel.

In Fig. 3a, it can be observed that when  $\eta = 0.7$  or 0.6, the  $\varepsilon$  value corresponding to focus scheme ① reaches its maximum. Notably, when  $\eta = 0.6$ ,  $\varepsilon$  exceeds 10% of the initial emittance. To further analyse this phenomenon, particle distribution diagrams depicting the transportation of beams in the quadrupole doublet focusing channel under different  $\eta$  values are displayed in Fig. 4.

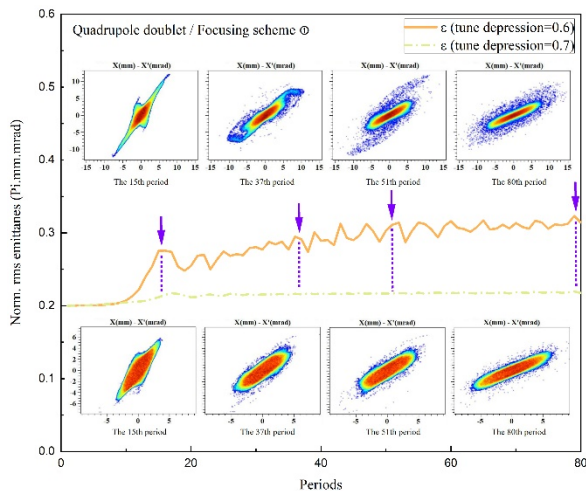


Figure 4: The  $\varepsilon$  and phase space distribution evolution along a quadrupole doublet channel under the focusing scheme ① when  $\eta = 0.6$  and 0.7, respectively. Here, the particle distribution diagrams of the 15th, 37th, 51st, and 80th periods are shown.

Based on Fig. 4, the phase space distribution of particles shows a four-fold structure and envelope instability. The 4th-order resonance occurs before the envelope instability, resulting in an overlapping region between the stopbands associated with these two instabilities. This overlap persists for a significant duration when  $\eta = 0.7$  and 0.6 respectively, seeing of unstable structures in the particle phase-space distribution easier. Moreover, when  $\eta = 0.6$ , the beam requires more time to pass through the stopband. This suggests that the stopband has a prolonged period to attract the beam due to the space-charge effect, leading to further enhancement of the emittance. When the acceleration effect is present, it has been experimentally verified that the observed phenomena and conclusions align with those obtained in the transverse direction. And Fig. 5 shows the emittance when  $\eta$  is equal to 0.6 or 0.7, the  $\varepsilon$  corresponding to ① reaches maximum in quadrupole doublet.

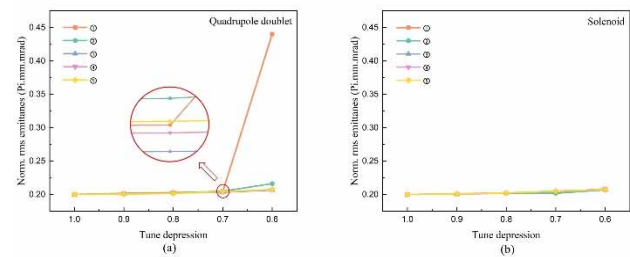


Figure 5: The  $\varepsilon$  during beam transport. (a) the  $\varepsilon$  when beams are focused by quadrupole lattices and (b) the  $\varepsilon$  when beams are focused by solenoid lattices.

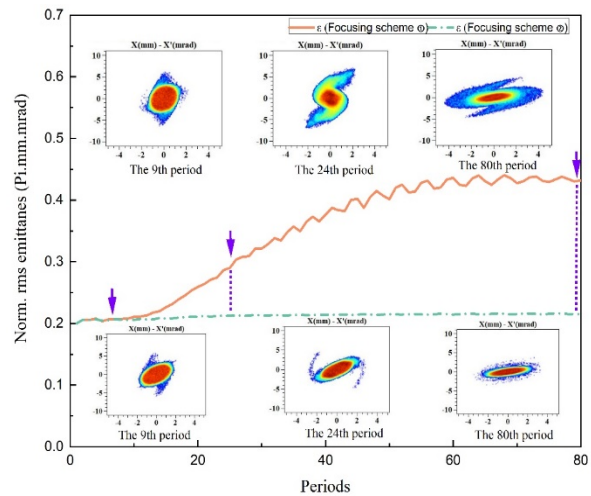


Figure 6: The  $\varepsilon$  of focusing scheme ① and ② and phase space distribution evolution along an acceleration channel that provides focusing strength by quadrupole doublet lattice when  $\eta$  is equal to 0.6. Here, the particle distribution diagrams of the 9th, 24th and 80th periods are shown.

In Fig. 6, it shows the corresponding particle distribution diagrams when the beam passed through 9th, 24th, and 80th periods. By comparing the results obtained by 2D simulation,  $\varepsilon$  keeps mostly consistent with it. It means that results obtained by 2D simulation can extend to 3D simulation.

## HALO FORMATION IN CRYOMODULE

Obviously, in the design of cryomodule, we obtain matched envelope. To analyse the transverse motion of the beam in a double period focusing structure within a cryomodule better, we have designed the following structure as shown in Fig. 7.

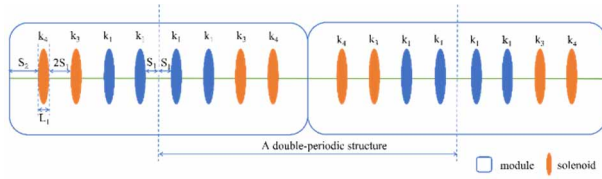


Figure 7: Double period focusing structure.

Poincare maps were computed using a double periodic structure with  $s_1 = 0.25$  m,  $L_1 = 0.23$  m,  $s_2 = 0.63$  m,  $k_1 = 13.0$  m<sup>-2</sup>,  $k_3 = k_4 = 6.0$  m<sup>-2</sup> and a fully periodic structure with focusing parameter  $k_1$  as the focusing unit (slicing at the minimum of the envelope). Meanwhile,  $\varepsilon = \varepsilon_x = \varepsilon_y = 0.2$   $\pi$ .mm.mrad and kinetic energy is approximately 30 MeV. According to particle-core model with test particle with time follows the equation:

$$\frac{d^2x}{ds^2} + k(s)x - \frac{K}{r^2}x = 0 \quad (|x| \leq r)$$

$$\frac{d^2x}{ds^2} + k(s)x - \frac{K}{x} = 0 \quad (|x| > r)$$

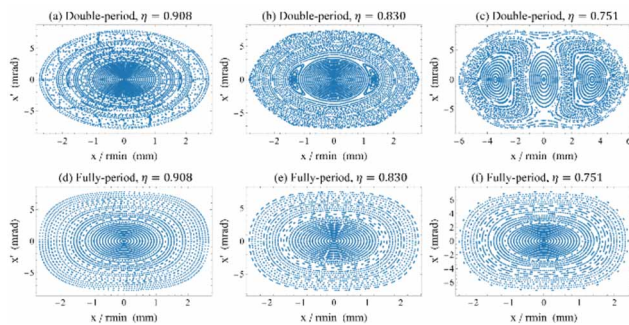


Figure 8: Stroboscopic plot for  $\eta = 0.908$ ,  $\eta = 0.830$ ,  $\eta = 0.751$  when the beam is transported in double-period ((a), (b), (c)) and fully period ((d), (e), (f)) focusing structures respectively.

The Poincare map reflects the frequency ratio between particle and envelope oscillations. Meanwhile, the particle-core model limits the probability of particle loss. Using the double-period structure, as well as the fully periodic structure with  $k_1$  as the period, three sets of  $\eta$  were set: 0.908, 0.830, and 0.751, and the Poincare maps were calculated under each of these conditions. From Fig. 8, it can be seen intuitively that the difference in the frequency ratio between particle and envelope oscillations is significant when the beam is transported in the fully periodic structure and the double-period structure. In the fully periodic structure, the frequency of the matched beam envelope oscillation is consistent with that of the particle oscillation, which is shown as circular-like ellipses on the Poincare map. In this case, we believe that there will be no beam mismatch or

beam halo. However, for the beam transported in the double-period focusing structure, it is obvious that the frequency of particle and envelope oscillations no longer remains consistent as the  $\eta$  decreases. The most significant change is the appearance of a prominent 2:1 resonance in the double-period focusing structure when  $\eta = 0.751$ , and the resonance range at 2:1 is larger at  $\eta = 0.751$  than that at  $\eta = 0.830$ . In conclusion, from the results obtained from numerical simulations, compared with fully periodic focusing structure, the formation of beam halo is more likely to occur during beam transportation in the channel of the double-period focusing structure.

## CONCLUSIONS

This study systematically investigates the envelope instability in quasi-periodic focusing structure and halo phenomena for double-periodic focusing structures in SCL. We explored the beam dynamics when  $\sigma_{0t}$  partially exceeded  $90^\circ$  for quasi-periodic structures for both 2D and 3D simulation. As for double-periodic structure, even for a matched beam, the 2:1 resonance remains a significant cause of halo formation. Furthermore, under the same beam intensity, double-periodic structures are more prone to beam halo formation compared to fully periodic focusing structures.

## ACKNOWLEDGMENTS

This work was supported by the National Natural Science Foundation of China (Grant Nos. 11375122 and 11875197).

## REFERENCES

- [1] Z.H. Li, P. Cheng, and H.P. Geng *et al.*, “Physics design of an accelerator for an accelerator-driven subcritical system”, *Phys. Rev. ST Accel. Beams*, vol.16, p. 080101, 2013. doi: 10.1103/PhysRevSTAB.16.080101
- [2] T. P. Wangler, K. R. Crandall, R. Ryne, and T. S. Wang, “Particle-core model for transverse dynamics of beam halo”, *Phys. Rev. ST Accel. Beams*, vol. 1, p. 084201, 1998. doi:10.1103/PhysRevSTAB.1.084201
- [3] Xin-Miao Wan, Xue-Jiang Pu, Zhi-Qiang Ren, Wei-Hong Huang, Yu-Fei Yang, and Zhi-Hui Li, “Discussion of  $90^\circ$  stopband in low-energy superconducting linear accelerators”, *Nucl. Sci. Tech*, vol. 33, p. 121, 2022. doi:10.1007/s41365-022-01104-z
- [4] F.J. Sacherer, “Rms envelope equations with space charge”, *IEEE T. Nucl. Sci*, vol. 18, pp. 1105–1107, 1971. doi:10.1109/TNS.1971.4326293
- [5] Jean-Michel Lagniel, “Chaotic behaviour and halo formation from 2D space-charge dominated beams”, *Nucl. Instrum. Methods A*, vol. 345, pp. 405-410, 1994. doi:10.1016/0168-9002(94)90490-1
- [6] J.W.G. Thomason, S.A. Fisher, D.J. Adams, M.G. Glover, J. Ranner, and D.J.S. Findlay, “Availability and reliability statistics at ISIS and at other high-power proton accelerators”, *Nucl. Instrum. Methods A*, vol. 1053, p. 168338, 2023. doi:10.1016/j.nima.2023.168338

# THE DESIGN OF A PROTON-HEAVY ION HYBRID SYNCHROTRON UPGRADED FROM XIPAF PROTON RING

H. J. Yao<sup>1,2,3</sup>, X. Y. Liu<sup>1,2,3</sup>, Y. Li<sup>1,2,3</sup>, Z. J. Wang<sup>1,2,3</sup>, S. X. Zheng<sup>1,2,3†</sup>, X. W. Wang<sup>1,2,3</sup>, Z. M. Wang<sup>4</sup>

<sup>1</sup>Key Laboratory of Particle & Radiation Imaging (Tsinghua University), Ministry of Education, Beijing, China

<sup>2</sup>Laboratory for Advanced Radiation Sources and Application, Tsinghua University, Beijing, China

<sup>3</sup>Department of Engineering Physics, Tsinghua University, Beijing, China

<sup>4</sup>State Key Laboratory of Intense Pulsed Radiation Simulation and Effect (Northwest Institute of Nuclear Technology), Xi'an, China

## Abstract

Xi'an 200 MeV Proton Application Facility (XiPAF) has been basically completed at the end of 2020, providing proton beams of 10 to 200 MeV for space radiation effect studies on electronics. To expand its capabilities, XiPAF is undergoing an upgrade to deliver multiple ion species, from proton to Bismuth ion. The upgrade focuses on three aspects. First, the original negative hydrogen linear injector will be remodelled to a proton linac injector. Second, a heavy ion linear injector will be added. Third, the existing proton ring will be retrofitted into a hybrid proton-heavy ion synchrotron. This paper details the considerations and physical designs for upgrading the synchrotron. Within the scope, we discuss the challenges and solutions in transforming a specialized proton synchrotron into a multi-ion accelerator under the constraints of existing plant layout and reuse of existing equipment.

## INTRODUCTION

XiPAF is a dedicated facility for space radiation environment simulation. It has been designed since 2014, and the beam commissioning was completed in a temporary plant at the end of 2020 [1], providing 10 ~ 200 MeV proton beams for irradiation experiments, while the formal plant is also under construction. With the continuous development of space radiation effect studies, new demands have been put forward for the device. Therefore, the XiPAF-Upgrading project was proposed and approved. The requirements and basic principles of XiPAF-Upgrading are:

- Expanding ion species from protons to multiple ions containing protons and heavy ions.
- The size of the upgraded accelerator complex is required to be within the layout of the plant under construction.
- Reuse the original equipment of XiPAF as much as possible to reduce costs.

XiPAF-Upgrading project began design in 2022 and beam commissioning is scheduled to be completed by the end of 2025. The overall layout of XiPAF-Upgrading is shown in Fig. 1. The original H<sup>-</sup> linac injector of XiPAF will be changed to H<sup>+</sup> injector with an energy of 7 MeV. A set of heavy-ion linac injector will be added, the charge-to-mass ratio range of the heavy ions to be accelerated is

1/2~1/6.5, and the energy is 2 MeV/u. The original proton ring will be upgraded to a proton-heavy ion hybrid synchrotron, and two terminals are for proton and heavy ion experiments respectively.

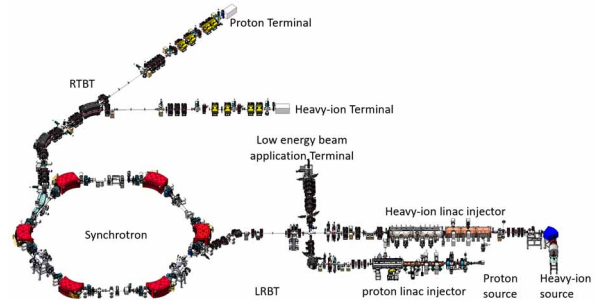


Figure 1: The overall layout of XiPAF-Upgrading.

The main parameter requirements of XiPAF-Upgrading synchrotron are shown in Table 1. The existing equipment needs to be reused, and the size of the synchrotron is limited by the size of the plant (ring circumference  $\leq 40$  m). Under these constraints, the physical design of the proton-heavy ion hybrid synchrotron upgraded from a proton ring is reported.

Table 1: Design Requirements of XiPAF-Upgrading Synchrotron

Ion	Injection Energy [MeV/u]	Extraction Energy [MeV/u]	Particle No. [ppp]
H <sup>+</sup>	7	10~200	1×10 <sup>10</sup>
He <sup>+</sup>	2	4	1×10 <sup>8</sup>
C <sup>4+</sup>	2	9	1×10 <sup>8</sup>
Si <sup>8+</sup>	2	7	1×10 <sup>7</sup>
Ar <sup>11+</sup>	2	4	1×10 <sup>7</sup>
Kr <sup>18+</sup>	2	6	1×10 <sup>7</sup>
Bi <sup>32+</sup>	2	6	1×10 <sup>7</sup>

## LATTICE DESIGN

To upgrade XiPAF proton ring to a proton-heavy ion hybrid synchrotron, two major issues need to be addressed: (1) vacuum; (2) injection. To meet the requirements of the heavy-ion beam lifetime, the vacuum pressure of the synchrotron needs to be upgraded from  $1 \times 10^{-6}$  Pa to  $5 \times 10^{-10}$  Pa. XiPAF proton ring adopts the H<sup>-</sup> stripping injection, to

† zhengsx@tsinghua.edu.cn

inject multi-ions, the multiturn injection scheme needs to be adopted. Therefore, the vacuum system and injection system need to be greatly modified. More equipment installation space is required, that is, the circumference of synchrotron needs to be increased. To reuse the existing dipoles and quadrupoles, the lattice still maintains the original structure of 6 DBFO cells [2], and six straight sections are lengthened. The circumference of the synchrotron is increased from 30.9 m to 39.96 m.

The horizontal tune remains unchanged; if the vertical tune is maintained as the circumference of the synchrotron increases, the strength of the defocusing quadrupoles will decrease to close to zero. Under low current operation, the power supply ripple of the defocusing quadrupole will significantly affect the machine working point, causing beam instability. Therefore, it is necessary to increase the vertical tune to above 2. The injection tune for heavy ions is selected as (1.73, 2.26). For protons with high intensity, at (1.73, 2.26), the space charge effect and lattice nonlinearity will induce coupled resonance  $\nu_x + 2\nu_y = 6$ , resulting in beam loss. Therefore, the injection tune for protons is adjusted to (1.73, 2.11). After the lattice parameters were determined, the influence of the magnetic field errors on closed orbit and dynamic aperture was studied and the detailed results can be found in the Ref. [3].

## INJECTION SYSTEM

To achieve full ions injection, the original negative hydrogen stripping injection scheme needs to be changed to a multiturn injection scheme. The injection system transformation includes:

- Remove the stripping foil equipment and Chicane magnets in the original injection section and add an injection electrostatic septum (ESi).
- Increase the number of bumper magnets (BP1~BP4) from the original two to four to independently adjust the position and angle of the orbit bump at the injection point.
- Redesign an injection magnetic septum (MSi) to meet new injection requirements.

The layout diagram of the injection system is shown in Fig. 2.

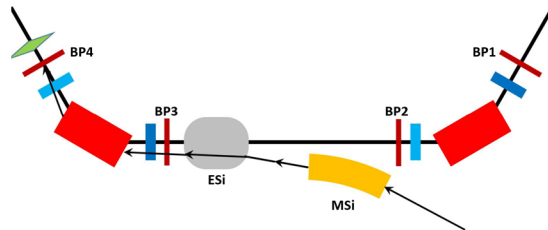


Figure 2: The layout of the injection system.

The main goal of heavy ion injection design is to achieve higher injection efficiency through optimizing the orbit bump curve and the phase space filling, to reduce the influence of beam loss on vacuum. According to the requirements of extraction design, the maximum emittance of each ion after acceleration to the required energy is  $100\pi \text{ mm}\cdot\text{mrad}$ , calculate the allowable emittance after

injection and divide it into three categories for injection optimization: the emittance after injection is  $200\pi \text{ mm}\cdot\text{mrad}$  ( $\text{C}^{4+}$ ),  $170\pi \text{ mm}\cdot\text{mrad}$  ( $\text{Si}^{8+}$ ,  $\text{Kr}^{18+}$ ,  $\text{Bi}^{32+}$ ) and  $120\pi \text{ mm}\cdot\text{mrad}$  ( $\text{He}^+$ ,  $\text{Ar}^{11+}$ ) respectively. The multiturn injection simulation was performed using PyORBIT. After the bump curve optimization, the injection efficiencies of heavy ions have been improved to above 75%, as shown in Table 2.

Table 2: Simulation Results of Multiturn Injection

Ion	Injection Intensity [ $\mu\text{A}$ ]	Injection Efficiency	Particle No. [ppp]
$\text{H}^+$	2000	87%	$7.2 \times 10^{10}$
$\text{He}^+$	35	78%	$3.1 \times 10^9$
$\text{C}^{4+}$	69	86%	$2.3 \times 10^9$
$\text{Si}^{8+}$	25	76%	$3.4 \times 10^8$
$\text{Ar}^{11+}$	32	75%	$2.5 \times 10^8$
$\text{Kr}^{18+}$	40	75%	$2.6 \times 10^8$
$\text{Bi}^{32+}$	20	78%	$7.5 \times 10^7$

Limited by Liouville's theorem, the injection gain of XiPAF-Upgrading synchrotron using multiturn injection is lower than that of the XiPAF using stripping injection. By increasing the proton beam intensity before injection, the particle number after injection can reach the same level as XiPAF. For example, the beam intensity before injection is 8 mA, and the number of particles after injection is  $2.5 \times 10^{11}$ , but the beam loss is serious during the subsequent capture and acceleration process, and the total efficiency is only 5%.

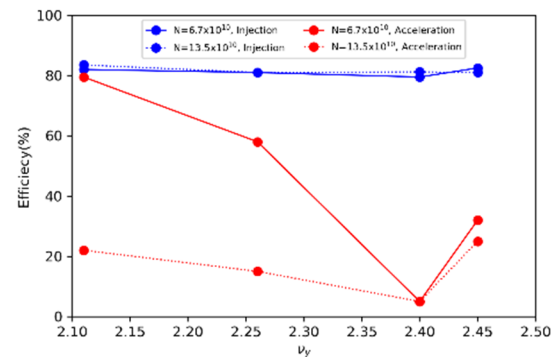


Figure 3: Proton injection and acceleration efficiency varies with vertical tune.

The above problem was studied, and it is found that the main source of beam loss is the transverse coupled resonance  $\nu_x + 2\nu_y = 6$ . Scan the vertical tune and calculate the injection efficiency and acceleration efficiency as shown in Fig. 3. The injection efficiency is almost same under different tune and different stored particle numbers, but the acceleration efficiency is obviously different. When  $\nu_y$  is 2.26, the resonance crossing will occur induced by space charge. The vertical emittance increases sharply, resulting in serious beam loss in vertical direction. To obtain higher acceleration efficiency, the working point is selected as (1.73, 2.11) and the number of particles after injection should not be too high, as shown in Table 2.

## CAPTURE AND ACCELERATION

For XiPAF-Upgrading synchrotron, the capture and acceleration parameters of the proton remain the original XiPAF design. In the case of reusing existing equipment as much as possible, it is necessary to design the parameters of heavy ions. The revolution frequency of heavy ions is 0.49 ~ 1.04 MHz, and the operating frequency range of the existing RF system is 1 ~ 6 MHz. To reuse the existing equipment, the harmonic number is selected to be 2 for heavy ion capture and acceleration.

Table 3: Acceleration Parameters and Results of XiPAF-Upgrading Synchrotron

Ion	RF Voltage [V]	Max. Phase [°]	Efficiency [%]
H <sup>+</sup>	600	8	47.2
He <sup>+</sup>	700	6	99.9
C <sup>4+</sup>	550	12	87.9
Si <sup>8+</sup>	650	12	95.9
Ar <sup>11+</sup>	650	6	99.6
Kr <sup>18+</sup>	850	10	96.3
Bi <sup>32+</sup>	1150	10	96.1

The gap voltage and synchronous phase need to be optimized to form a suitable bucket height and area to reduce beam loss during adiabatic capture and acceleration. The design parameters of capture and acceleration and the simulation results for the total efficiency of capture and acceleration are shown in Table 3. Due to the influence of space charge effect, the efficiency of protons is low, and beam loss mainly occurs in the early stage of acceleration. The existing magnetic alloy cavity can be reused, but the power amplifier needs to be upgraded to increase the gap voltage from the original 800 V to above 1200 V.

## EXTRACTION SYSTEM

XiPAF-Upgrading synchrotron still adopts the third-order resonance and transverse radio frequency knockout (RF-KO) method to achieve slow extraction. The layout of the extraction elements is like that of the XiPAF synchrotron [4]. It is necessary to find the optimal value under the existing equipment aperture limitation. Comprehensively consider the beam loss in the last three turns before extraction and the number of particles stored in the ring to determine that the maximum emittance before extraction is  $100\pi$  mm·mrad. The extraction parameters for heavy ions are shown in Table 4.

The trajectories with different momentum dispersions in the last three turns are shown in Fig. 4, the trajectories of particle with the negative momentum dispersion obviously exceed the existing aperture limitation at two chromatic sextupoles (SC02, SC04), resulting in serious beam loss. To improve the extraction efficiency, the existing two chromatic sextupoles cannot be reused, and need to be redesigned to increase the aperture.

The extraction energy range of protons is 10 ~ 200 MeV, so the extraction parameter design is divided into two cases: low energy (10 ~ 60 MeV) and high energy (60 ~

200 MeV). In the case of high energy extraction, the design parameters can be like those of heavy ions and will not be discussed. Under the condition of low energy and high intensity, the influence of space charge force is great. If the same horizontal tune as the heavy ion is adopted, many particles will be extracted during the turning on of resonant sextupoles. Therefore, for low energy slow extraction, a design scheme of setting the horizontal tune below the third-order resonance line is proposed. Take 10 MeV as an example, the extraction parameters are listed in Table 4.

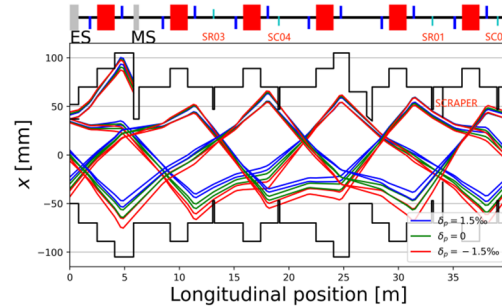


Figure 4: The trajectories in last three turns with different momentum dispersions.

Table 4: Extraction Parameters of XiPAF-Upgrading Synchrotron

Parameters	Heavy ion	Proton (200 MeV)	Proton (10 MeV)
Tune $\nu_x / \nu_y$	1.678/2.26	1.678/2.11	1.661/2.11
Corrected Chromaticity	-0.3/-3.3	-1.34/-1.1	-1.2/-1.2
Triangle Area [ $\mu\text{m}^2$ ]	113	108	63

The beam simulation during the extraction phase was carried out using SynTrack, an upgraded version of LiTrack [5]. The space charge effects are considered for proton. The simulation results show that the extraction efficiency of heavy ions and high energy protons is higher than 90%, and the efficiency of 10 MeV protons is 75%. Combined with the results of Table 2 and Table 3, the number of particles extracted from the synchrotron meets the requirements of Table 1 and has sufficient margin.

## CONCLUSION

Under the condition of limiting the ring circumference and reusing the existing equipment as much as possible, the physical design of XiPAF-Upgrading synchrotron has been completed. The extraction energy for the proton is 10 ~ 200 MeV, and 4 ~ 9 MeV/u for the heavy ions. The number of particles meets the design requirements. The design of ultra-high vacuum system of XiPAF-Upgrading synchrotron with a vacuum pressure of  $5 \times 10^{-10}$  Pa is a challenge and has been completed and will be reported soon elsewhere.

## REFERENCES

- [1] H. J. Yao *et al.*, “Beam commissioning of XiPAF synchrotron”, in *Proc. 12th Int. Particle Accelerator Conf. (IPAC’21)*, Campinas, Brazil, 2021, pp. 639-642. doi:10.18429/JACoW-IPAC2021-MOPAB189
- [2] G. R. Li *et al.*, “Design of a compact ring for proton radiation applications”, *Chinese Phys. C*, vol. 41, p. 017001, 2017. doi:10.1088/1674-1137/41/1/017001
- [3] X. Y. Liu *et al.*, “Lattice considerations for synchrotron of XiPAF-Upgrading project”, in *Proc. 14th Int. Particle Accelerator Conf. (IPAC’23)*, Venezia, Italy, 2023, pp. 3801-3803. doi:10.18429/JACoW-IPAC2023-WEPM136
- [4] H. J. Yao *et al.*, “RF-knockout slow extraction design for XiPAF synchrotron”, in *Proc. 57th ICFA Advanced Beam Dynamics Workshop on High-Intensity and High-Brightness Hadron Beams (HB’16)*, Malmö, Sweden, Jul. 2016, pp. 52-54. doi:10.18429/JACoW-HB2016-MOPR005
- [5] H. J. Yao *et al.*, “A high-performance code for beam dynamics simulation of synchrotrons”, in *Proc. IPAC’19*, Melbourne, Australia, 2019, pp. 3170-3173. doi:10.18429/JACoW-IPAC2019-WEPTS033

# ELECTRON COOLING FOR FUTURE HIGH-ENERGY HADRON ACCELERATORS\*

H. Zhao<sup>†</sup>

Institute of Modern Physics, CAS, Lanzhou 730000, China

## Abstract

Electron cooling is an important method to reduce the emittance and momentum spread of hadron beams, and it has been successfully applied in several facilities around the world. In 2019, the world's first RF-based electron cooler (LEReC) was commissioned at BNL for the RHIC BES-II project, and the integrated luminosity of RHIC is finally doubled. In addition, electron cooling is also a must for the future Electron-Ion Collider (BNL EIC). However, the high energy requirement of the electron beam (150 MeV) is far beyond what all present coolers can achieve (<4.3 MeV). For that, an electron ring cooler with strong radiation damping is proposed and designed, in which the non-magnetized and dispersive cooling techniques are applied. In this paper, I will introduce the physical design and some important considerations of the ring cooler.

## INTRODUCTION

Electron cooling is a powerful method to shrink the size and momentum spread of the stored ion beams for accumulation and high-precision experiments. Since it was first proposed by G. I. Budker in 1967, this technique has been widely applied and developed in many heavy ion accelerators around the world [1, 2]. With the development of particle accelerators and the higher requirements for experimental physics, beam cooling with much higher energy electron beam is demanded.

Up to now, all electron coolers built around the world are based on dc electron beams, which are accelerated by electrostatic fields. The highest-energy electron cooling system with 4.3 MeV electrons has been successfully constructed and operated at Fermi National Accelerator Laboratory in 2005 [3]. Recently, the world's first rf-based electron cooler is successfully commissioned at BNL and the cooling of gold beams in RHIC by 1.6 MeV and 2.0 MeV electron was successfully achieved [4]. It provides the possibility to use similar approach to develop high-energy electron coolers in the future.

Brookhaven National Laboratory (BNL) is designing an Electron-Ion Collider (EIC), which will be a new discovery machine that opens new frontiers for the researches in nuclear physics and quantum chromodynamics [5]. In order to maintain the high luminosity during long collision runs, it is desirable to cool the hadron beam (275 GeV proton) to counteract the emittance growth caused by intrabeam scattering (IBS) [6]. However, the conventional coolers and the

rf-based coolers are no longer suitable for such high energy beam cooling in EIC. In fact, various proposals and new cooling schemes have been proposed, but the technical and experimental demonstrations are still lacking. In this paper, we present a design of electron storage ring cooler with bunched electron beam for the EIC [7].

## EIC COOLING DEMANDS

For the EIC, the most demanding case is to cool the proton beam at the energy of 275 GeV. During the long collision stores, the emittance growth of proton beam due to IBS is the dominant limitation for the luminosity. The requirement for the hadron beam cooling is mainly to counteract the IBS heating effect. The evolution of the 275 GeV proton beam emittance caused by IBS is shown in Fig. 1. It shows that the IBS heating effect for the flattened proton beam is dominated by the horizontal and longitudinal planes. As a result, vertical cooling is not needed for EIC. So, one can effectively use horizontal dispersion to redistribute the cooling rates between the longitudinal and horizontal planes, and achieve required cooling performance.

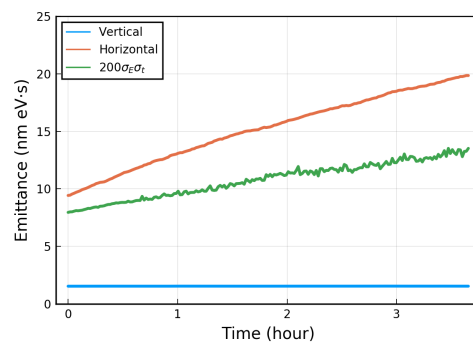


Figure 1: Emittance growth of the 275 GeV proton beam caused by IBS in EIC.

## RING COOLER DESIGN

### Overview

The electron storage ring has a race track shape, with the cooling section located in one long straight section and wigglers in the other. The ring is mirror symmetric around the center of the cooling section, and the top view of the ring is shown in Fig. 2. The cooling section has a length of 170 m and it fits into the straight section of the hadron ring. There are four arcs with radius of 3.42 m, each of them has 10 dipoles and a 90 degree phase advance per cell. The wiggler section is also mirror symmetric with four pairs of wigglers in each half. In our setup, the alternating horizontal and

\* Work supported by the National Natural Science Foundation of China (No. 12275323)

<sup>†</sup> hezhao@impcas.ac.cn

vertical wigglers are used, and the wiggler poles are shaped as combined function sector dipoles. The optics of the ring cooler is shown in Fig. 3, and the parameters of the ring are list in Table 1.

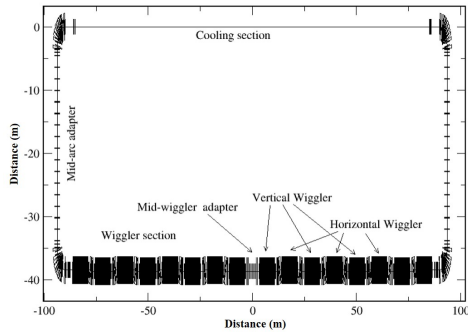


Figure 2: Layout of the ring cooler.

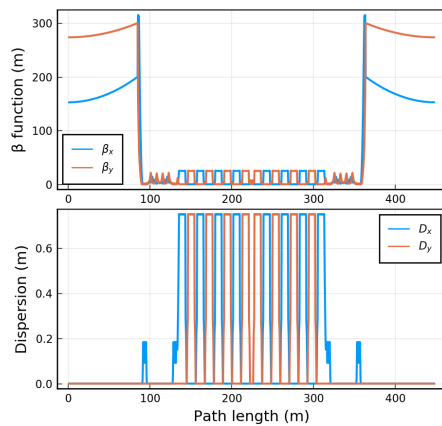


Figure 3: Optics of the ring cooler.

Because of the edge focusing of the dipoles, the wigglers and bending dipoles will create a large chromaticity. As a consequence, the required strong sextupoles strongly affects the dynamic aperture. In order to reduce the strength of the sextupoles, the sextupoles are placed inside the wiggler magnets, where a small dispersion is available throughout the length of the magnet. Also, since the edge focusing is only in one plane, a large ratio between horizontal and vertical beta functions can be maintained, making the chromaticity compensation more effective.

Considering IBS effect, the increase of the transverse emittance which is proportional to  $H = \gamma D^2 + 2\alpha DD' + \beta D'^2$ , must be minimized. The beta function in wiggle plane is chosen to be 25 m, which makes the  $D'^2$  term of the  $H$  function two orders of magnitude bigger than the other terms. Therefore, the dispersion in the wiggler section doesn't have to be small as long as  $D'$  is kept small. We set the dispersion function in wiggler section to 75 cm, which works well for both chromaticity correction and dynamic aperture.

### Beam Parameters

In the ring cooler, the cooling performance is directly determined by the electron beam quality. Based on the lattice

Table 1: Parameters of the Ring Cooler

Circumference [m]	449.079
Length of cooling section [m]	170
Average $\beta$ function in cooling section [m]	170/280
Dispersion in arc [cm]	18.5
Wiggler field [T]	1.88
Length of wiggler [m]	7.44
Bend radius of wiggler [m]	0.246
Poles in wiggler	158
Wiggler period [cm]	4.8
$\beta$ function in wiggler [m]	25
Max. Dispersion in wiggler [cm]	75
Number of wiggler magnets	16
Tune ( $Q_x/Q_y$ )	59.92/59.85
Chromaticity before correction ( $x/y$ )	-117.8/-114.4
Momentum compaction factor $\alpha$	$-3.21 \times 10^{-3}$
Natural emittance ( $x/y$ ) [nm]	3.1/3.1
Natural momentum spread	$2.6 \times 10^{-4}$

design, the equilibrium electron beam parameters can be calculated by considering the radiation damping, quantum excitation, the IBS effect and the Beam-Beam Scattering (BBS) effect. The differential equation of the emittance of electron beam is given by

$$\frac{d\epsilon}{dt} = (-2\lambda_{damp} + \lambda_{IBS} + \lambda_{BBS})\epsilon + C_q \quad (1)$$

where  $\lambda_{damp}$  is the radiation damping rate,  $C_q$  is the factor of quantum excitation,  $\lambda_{IBS}$  and  $\lambda_{BBS}$  are the heating rates from IBS and BBS, respectively. The equation of momentum spread has the same form as Eq. (1). It is known that the heating rates from IBS  $\lambda_{IBS}$  and BBS  $\lambda_{BBS}$  depend on beam parameters dynamically. In order to get the equilibrium beam parameters in the ring cooler, a simulation code was developed which allows to perform turn-by-turn tracking.

In the simulation, the radiation damping rates are calculated from the radiation integrals based on the optics of the ring [8]. The factor of quantum excitation can be obtained by  $C_q = 2\lambda_{damp}\epsilon_{nat}$ , where  $\epsilon_{nat}$  is the natural emittance of electron beam. The Bjorken-Mtingwa IBS model with horizontal and vertical dispersion is used in the code [9]. As of BBS, we derived a new formula using the full Landau collision integral that allows for different temperatures in all three dimensions [10–12]. Considering all above effects, the evolution of the electron beam in the ring cooler with two sets of arbitrary initial parameters is shown in Fig. 4. After several thousand turns, the electron beam converges to an equilibrium state, which is the final e-beam parameters for hadron beam cooling.

### Dispersive Cooling

At high energy, the horizontal angular spread of electron beam in the rest frame is much larger than in the longitudinal plane, which makes the horizontal cooling much slower than the longitudinal cooling. Here, we introduce the dispersions both for the hadron and electron beams to increase

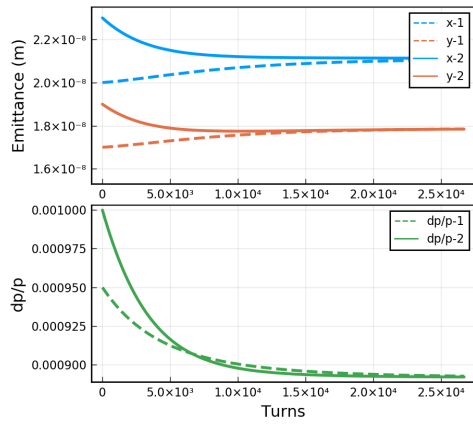


Figure 4: Evolution of the electron beam parameters in the ring cooler with two sets of arbitrary initial parameters.

the horizontal cooling rate at the expense of the longitudinal cooling [13]. As we known, dispersion on ions couples the horizontal coordinate with the longitudinal momentum, thus the cooling effect on momentum spread can be transferred to the horizontal plane. Figure 5 shows an example of the dispersive cooling, in which a dispersion and a transverse gradient are necessary. Even though the change of beam density caused by dispersion will reduce the cooling rates in all three dimensions, the horizontal cooling rate still can be enhanced by the coupling effect, as long as the dispersion is not too large.

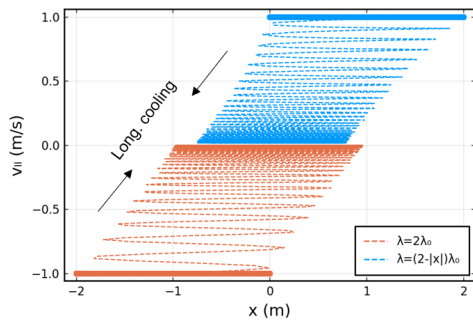


Figure 5: Schematic demonstration of dispersive cooling, in which a dispersion and a transverse gradient are necessary.

### Other Effects

In the ring cooler design, there are also some important effects need to be investigated, such as the beam dynamics, beam lifetime, dynamic aperture, instabilities and so on. These studies are not presented here, and the details can be found in Ref. [7]. In summary, the final electron beam parameters are summarized in Table 2.

## COOLING SIMULATION

Based on the simulation code TRACKIT [14], the cooling process is performed with the electron beam parameters list in Table 2. Figure 6 shows the evolution of the hadron beam transverse and longitudinal emittance with cooling. When

Table 2: E-beam Parameters in the Ring Cooler

Beam energy [MeV]	149.8
Number of electrons per bunch	$3 \times 10^{11}$
Peak current [A]	48.3
Number of bunches	135
Average current [A]	4.4
RMS emittance (x/y) [nm]	21/18
RMS Momentum spread	$8.9 \times 10^{-4}$
RMS Bunch length [cm]	12
Required RF voltage [kV]	6.1
Synchrotron tune $Q_s$	$1.63 \times 10^{-3}$
Max. space charge (x/y)	0.19/0.21
Damping rates (x/y/s) [ $s^{-1}$ ]	32/32/64
IBS rates (x/y/s) [ $s^{-1}$ ]	54/53/68
BBS rates (x/y/s) [ $s^{-1}$ ]	-0.4/1.0/49
Dynamic aperture (x/y/s)	$6\sigma/6\sigma/13\sigma$
Momentum aperture	0.79%
Quantum lifetime [hour]	2.8
Touschek lifetime [s]	<55

there is no dispersion, it shows that there is almost no transverse cooling but a strong longitudinal cooling, which is due to the large difference in cooling gradients. By applying the dispersion both for the proton and electron beam in the cooling section with  $D_i = 2.5$  m and  $D_e = 2$  m, the proton beam can be cooled more effectively in the horizontal plane. With cooling, the proton beam emittance is essentially unchanged within two hours, which satisfies the requirement in the EIC.

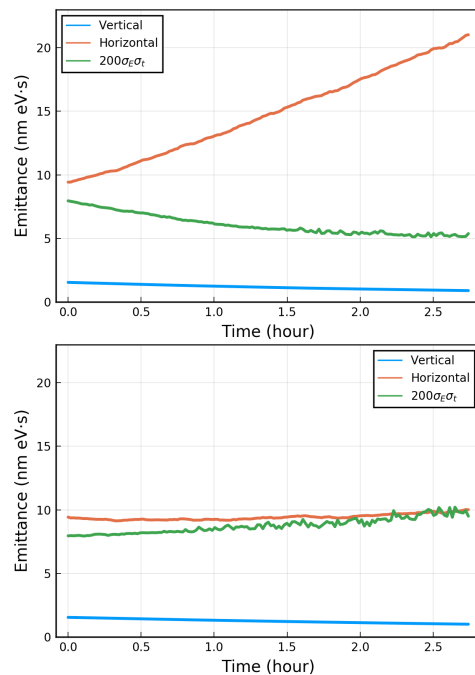


Figure 6: The evolution of the hadron beam emittance during cooling. (Upper plot:  $D_i = 0$  m,  $D_e = 0$  m, Bottom plot:  $D_i = 2.5$  m,  $D_e = 2$  m)

## CONCLUSION

The hadron beam cooling at high energy is an important part of the EIC. In this paper, we present a possible design of such high-energy ring-based electron cooler using bunched electron beam. The electron beam can continuously cool the hadrons while electrons are being cooled by the radiation damping in the storage ring. This approach strongly depends on the design of electron ring which is described here in detail. Based on such ring cooler design, the cooling performance on the hadron beam is simulated, in which the dispersions of the ion and electron beams in the cooling section are effectively employed to redistribute the cooling rate between the longitudinal and horizontal planes. Although there are still some challenges, it appears that the ring-based electron cooler concept offers a viable path for cooling of protons at the top energy in the EIC.

## REFERENCES

- [1] Budker, Gersh Itskovich, "An effective method of damping particle oscillations in proton and antiproton storage rings", *Soviet Atomic Energy*, vol. 22, no. 5, pp. 438–440, 1967.
- [2] Poth, Helmut, "Applications of electron cooling in atomic, nuclear and high-energy physics", *Nature*, vol. 345, no. 6274, pp. 399–405, 1990.
- [3] Nagaitsev, Sergei, *et al.*, "Experimental demonstration of relativistic electron cooling", *Physical review letters*, vol. 96, no. 4, p. 044801, 2006.
- [4] Fedotov, A. V., *et al.*, "Experimental demonstration of hadron beam cooling using radio-frequency accelerated electron bunches." *Physical Review Letters* vol. 124, no. 8, p. 084801, 2020.
- [5] EIC: Colliding Electrons with Ions at Brookhaven Lab. <https://www.bnl.gov/eic/eRHIC.php>
- [6] Montag, Christoph, "eRHIC design overview", No. BNL-212130-2019-COPA. Brookhaven National Lab.(BNL), Upton, NY (United States), 2019.
- [7] H. Zhao, *et al.* "Ring-based electron cooler for high energy beam cooling", *Physical Review Accelerators and Beams*, vol. 24, no. 4, p. 043501, 2021.
- [8] S. Y. Lee, "Accelerator physics", *World scientific publishing*, 2018.
- [9] Nagaitsev, Sergei. "Intrabeam scattering formulas for fast numerical evaluation", *Physical Review Special Topics-Accelerators and Beams*, vol. 8, no. 6, p. 064403, 2005.
- [10] E. M. Lifschitz and L. P. Pitajewski, "Physical kinetics", Textbook of theoretical physics, 10, 1983.
- [11] R. D. Hazeltine, "Coulomb collision operator", *Tech. Rep.*, University of Texas, Austin, 2006. [http://w3fusion.ph.utexas.edu/ifs/ifsreports/1140\\_Hazeltine.pdf](http://w3fusion.ph.utexas.edu/ifs/ifsreports/1140_Hazeltine.pdf)
- [12] H. Zhao and M. Blaskiewicz, "Electron Heating by Ions in Cooling Rings", in *Proc. of North American Particle Accelerator Conference (NAPAC'19)*, Lansing, MI, USA, September 1-6, 2019.
- [13] H. Zhao and M. Blaskiewicz, "Rate redistribution in dispersive electron cooling", *Physical Review Accelerators and Beams*, vol. 24, no. 8, p. 083502, 2021.
- [14] Code available at <https://github.com/hezhao1670/ECool-TRACKIT>.

# INFLUENCE OF TRANSVERSE DISTRIBUTION OF ELECTRON BEAM ON THE DISTRIBUTION OF PROTON BEAM IN THE PROCESS OF ELECTRON COOLING\*

Xiaodong Yang<sup>†</sup>, Institute of Modern Physics, CAS, Lanzhou, China

## Abstract

The electron cooling process of 20 GeV proton beam in EicC was simulated for the eight transverse distribution of electron beam with the help of electron cooling simulation code. The transverse cooling time was obtained in the different transverse distribution of electron beam. The final transverse distribution of proton beam was demonstrated. The simulated results reveal that the transverse distribution of electron beam influences the distribution of proton beam in the process of electron cooling. In the future, this idea was expected to apply to the longitudinal distribution of electron beam. The longitudinal distribution of proton beam was attempted to be controlled by the longitudinally modulated electron beam. As a result, the peak current and longitudinal distribution of proton beam will be controlled by the electron beam. The loss of proton beams will be reduced, and the stored lifetime of proton beam in the storage ring will be extended. The intensity of the proton beam will be maintained for a longer time.

## INTRODUCTION

The electron cooling process of 20 GeV proton beam in EicC was simulated in cases of variety of parameters [1].

The transverse electron cooling time [2] not only depends on the lattice parameters of the storage ring, the Betatron function, dispersion of the cooling section, such as energy, initial emittance and momentum spread of proton beam, but also on the construction parameters of electron cooling device, the strength of magnetic field, the parallelism of magnetic field in the cooling section, the effective cooling length, and the parameters of electron beam, such as radius, density and transverse temperature of electron beam. These parameters are determined by the storage ring and the technology limitation, on the other hand, they are influenced and restricted each other.

As mentioned in the reference [3, 4], As a result of electron cooling, the core of beam distribution is cooled much faster than the tails, producing a denser core. To account for a core collapse of ion distribution. The core directly impacts luminosity in a collider.

From the experiments results from LEReC BNL [5], Application of electron cooling directly at the collision energy of the hadron beams brings some challenges. Of special concern is control of the ion beam distribution under cooling in order not to overcool the beam core. As a result, most of the ions experienced linear part of the friction force without overcooling of ion beam distribution. Providing

transverse cooling appeared to be more beneficial for collider operations compared to the longitudinal cooling. This is because longitudinal cooling led to higher peak currents of ions, affecting the ion beam's lifetime due to the space-charge effects.

## MOTIVATION

High intensity proton beam and short bunch length was expected to store in a collider with long lifetime and less loss. In order to increase the lifetime of proton beam and decrease the loss, longitudinally modulated electron beam [6, 7] will be attempted to suppress the intra-beam scattering. The traditional DC electron beam in the electron cooler will be modulated into shorter electron bunch with different longitudinal distribution. The stronger cooling was expected in the tail of proton beam and the weaker cooling was performed in the core of proton beam. The proton loss will be decreased and the lifetime will be increased. The intensity of proton beam in the collider will be kept and maintained for longer time.

## ELECTRON BEAM DISTRIBUTION

The distribution of electron beam was uniform in the transverse direction in the traditional simulation of electron cooling. The electron density was uniform in the radial direction.

In order to investigate the influence of transverse distribution of electron beam on the distribution of ion beam in the process of electron cooling, eight kinds of electron beam profiles were attempted in the simulation shown in Fig. 1.

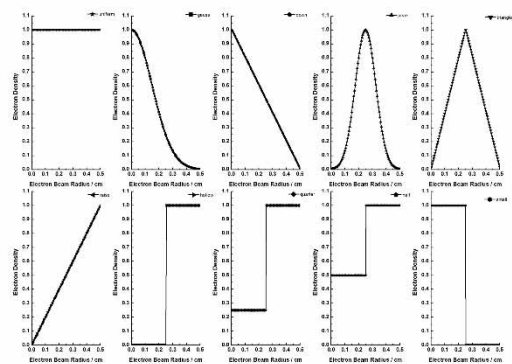


Figure 1: The transverse distribution of electron beam.

Due to the distribution of electron beam in the transverse direction was axial symmetry, only half distribution was described in the simulation.

\* Work supported by NSFC No. 12275325, 12275323, 12205346.

<sup>†</sup> email address yangxd@impcas.ac.cn.

Content from this work may be used under the terms of the CC BY 4.0 licence (© 2023). Any distribution of this work must maintain attribution to the author(s), title of the work, publisher, and DOI

Half, half of Gaussian distribution, the electron density presents one complete gauss shape in the radial direction.

Peak, two Gaussian distribution, the electron density appears two complete gauss shapes in the radial direction.

Uniform, solid beam, the electron density presents uniform in the radial direction.

Hollow, the electron density is zero in the half central region, and the electron density is uniform in the edge region.

Raise, the electron density increases with radial coordinate from the centre of electron beam.

Down, the electron density decreases with radial coordinate from the centre of electron beam.

Triangle, similar as hollow beam, the electron density emerges two triangles in the radial direction. The electron density increases with radial coordinate from the centre of electron beam in the central half part, and decrease with radial coordinate in the edge part.

Small, smaller radius beam, the electron density is uniform in the central half part, and no electrons in the half edge part.

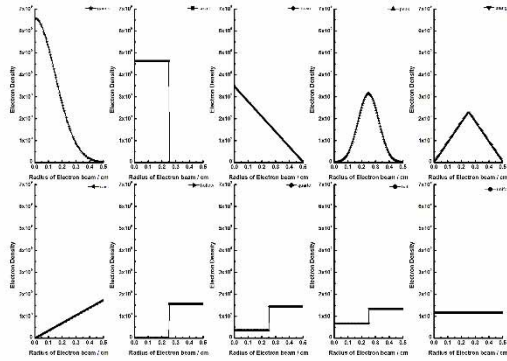


Figure 2: The radial density distribution of electron beam.

During the simulation of hollow beam, the proton beam was not cooled due to zero electron density in the central part of electron beam. Two compromise distributions were considered for the hollow electron beam.

Half, the electron density is one second in the half central region, and the electron density is uniform in the edge half region.

Quarter, the electron density is one fourth in the half central region, and the electron density is uniform in the edge half region.

In order to compare the cooling results, the electron beam current is set as the same in the different transverse distributions. As a result, the electron density is not same at the different radial position. The radial density distribution of electron beam was present in Fig. 2.

### SIMULATION OF COOLING

The transverse cooling time under the different transverse distribution of electron beam is shown in Fig. 3.

The electron density is higher in the central region. Where the electron density is higher, the cooling is stronger, and the cooling time is shorter.

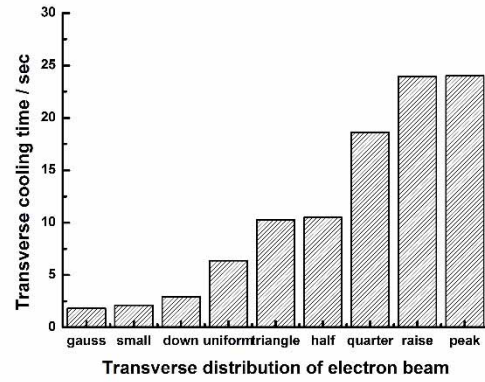


Figure 3: The transverse cooling time under the different transverse distribution of electron beam.

The protons experience the varying strength cooling in the different region. The cooling force was stronger in the region with higher electron density, the cooling force was weaker in the region with lower electron density. No cooling was experienced in the electron empty region. But the effect of intra-beam scattering will expand the proton beam and final distribution becomes wide.

### DISTRIBUTION OF PROTON BEAM

The transverse full width at half maximum of proton beam after electron cooling is demonstrated in Fig. 4.

The proton experienced the stronger cooling in the central region. Where the electron density is higher, the cooling is stronger, and the width of proton beam is narrower.

In the case of hollow beam, the proton beam was not cooled due to zero electron density in the central part of electron beam. The effect of intra-beam scattering will expand the proton beam and final distribution becomes wider.

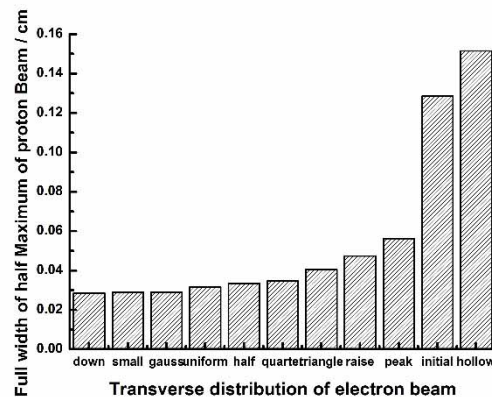


Figure 4: The transverse full width at half maximum of proton beam after electron cooling.

The final transverse distribution of proton beam under the cooling of the different transverse distribution of electron beam was illustrated in the Fig. 5.

As a result, the final distribution of proton beam present the different width because the proton was cooled by the diverse electron density in the different region in the same period.

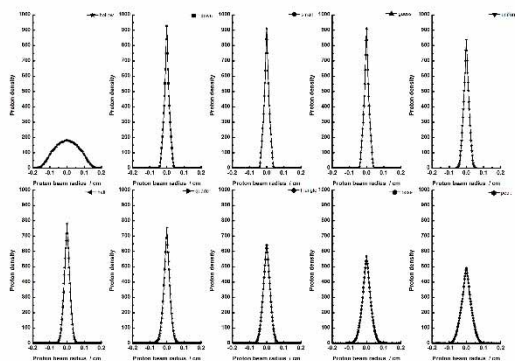


Figure 5: The final transverse distribution of proton beam after cooling.

## RESULTS AND DISCUSSION

The distribution of proton beam has been influenced by the transverse distribution of electron beam in the process of electron cooling from the simulation results. This idea will be extended to the longitudinal direction. The proton beam bunch with Gaussian distribution was expected to be cooled by the different distributions of electron bunches in the longitudinal direction [8, 9]. The longitudinal distribution of proton beam was expected to be controlled by this method in the process of electron cooling. The peak current of proton beam will be decreased and the lifetime of proton beam will be extended. The intensity of proton beam will be maintained.

Differences exist between transverse and longitudinal distribution of electron beam. The transverse distribution of electron beam is axial symmetry. Due to the actions of electric field of space charge in the electron beam and magnetic field, the drift velocity of electron is not same in the different radial position. In the centre of electron beam, the drift velocity is minimum. The relative velocity between proton and electron is also small too. The cooling force is varying in the different radius.

The electron beam is direct current, the longitudinal distribution is uniform. This is the distinction between the transverse and longitudinal direction.

The longitudinal distribution of electron beam is uniform in the traditional electron cooling. The ion beam is coasting beam.

Due to the lack of the setting of longitudinal distributions of proton and electron beams in the existing simulation code, the longitudinal distribution of proton was not presented in the results.

## SUMMARY

The influence of transverse distribution of electron beam on the transverse distribution of proton beam in the process of electron cooling was presented in the paper. In order to obtain the influence of longitudinal distribution of electron beam on the longitudinal distribution of proton beam in the process of electron cooling, the necessary improvement was needed in the electron cooling simulation code. The

input of longitudinal distribution of electron beam should be added. The longitudinal distribution of proton beam with the time in the process of electron cooling should be output in the simulation. The final information of the longitudinal distribution of proton beam should be provided.

In the future work, the simulation code will be modified, and the setting of longitudinal distributions of proton and electron beams will be added in the simulation. The longitudinal distribution of proton beam will be demonstrated in the process of electron cooling. The final longitudinal distribution of proton beam will be obtained after electron cooling.

In the future high energy electron cooling, the electron beam was produced by the RF accelerator, and the electron beam will be not direct current, it will be consisted by pulsed electron bunches. The ion beam will not be coasting beam, it will be multi-bunch configuration in the storage ring.

The cooling process in the longitudinal direction should be investigated furtherly.

## ACKNOWLEDGEMENTS

The author would like to thank Prof. V. Parkhomchuk for him to provide the simulation code SIMCOOL and useful guidance in the simulation during this work.

## REFERENCES

- [1] X. D. Yang, "Simulation of electron cooling and IBS at EicC", in *12th Workshop on Beam Cooling and Related Topics (COOL2019)*, Novosibirsk, Russia, pp. 77-79. doi:10.18429/JACoW-COOL2019-TUPS01
- [2] X. D. Yang, "Simulation of transverse electron cooling and IBS of 20 GeV proton beam at EicC", in *13th Workshop on Beam Cooling and Related Topics (COOL2021)*, Novosibirsk, Russia, pp. 70-73. doi:10.18429/JACoW-COOL2021-P1002
- [3] A.V. Fedotov, I. Ben-Zvi, Yu. Eidelman, et al., "Simulation of high-energy electron cooling", in *Proceedings of 2005 Particle Accelerator Conference*, Knoxville, Tennessee, USA, pp. 4251-4253.
- [4] A.V. Fedotov, I. Ben-Zvi, Yu. Eidelman, et al., "IBS for ion distribution under electron cooling", in *Proceedings of 2005 Particle Accelerator Conference*, Knoxville, Tennessee, USA, pp. 4263-4265.
- [5] A. V. Fedotov, Z. Altinbas, S. Belomestnykh, et al., "Experimental Demonstration of Hadron Beam Cooling Using Radio-Frequency Accelerated Electron Bunches", *Phys. Rev. Lett.* Vol. 124, p. 084801, 2020. doi:10.1103/PhysRevLett.124.084801
- [6] X. D. Yang, L. J. Mao, J. Li, et al., "Investigation on the suppression of intrabeam scattering in the high intensity heavy ion beam with the help of longitudinal double-bunch of electron", in *13th Symposium on Accelerator Physics (SAP2017)*, Jishou, China, pp. 67-69. doi:10.18429/JACoW-SAP2017-MOPH18
- [7] X. D. Yang, L. J. Mao, J. Li, et al., "Investigation on the suppression of intrabeam scattering in the high intensity heavy ion beam with the help of longitudinal multi-bunch of electron", in *11th Workshop on Beam Cooling and Related Topics (COOL2017)*, Bonn, Germany, pp. 58-60. doi:10.18429/JACoW-COOL2017-TUP14

- [8] M.W. Bruker, S. Benson, A. Hutton, et al., “Demonstration of electron cooling using a pulsed beam from an electrostatic electron cooler”, *Phys. Rev. Accel. Beams*, vol. 24, 012801, 2021. doi:10.1103/PhysRevAccelBeams.24.012801
- [9] He Zhao, Lijun Mao, Jiancheng Yang, et al., “Electron cooling of a bunched ion beam in a storage ring”, *Phys. Rev. Accel. Beams*, vol. 21, p. 023501, 2018. doi:10.1103/PhysRevAccelBeams.21.023501

# DESIGN OF A SYNCHROTRON FOR PROTON FLASH RADIOTHERAPY BASED ON FAST VARIABLE-ENERGY BUNCH SPLITTING\*

Y. Li, H. J. Yao, S. X. Zheng<sup>†</sup>, Q. Z. Xing<sup>‡</sup>, X. W. Wang

Key Laboratory of Particle & Radiation Imaging, Ministry of Education, Beijing, China

<sup>†</sup>also at Laboratory for Advanced Radiation Sources and Application,  
Tsinghua University, Beijing, China

<sup>‡</sup>also at Department of Engineering Physics, Tsinghua University, Beijing, China

## Abstract

Ultra-high dose rate (FLASH) radiotherapy not only guarantees effective tumor treatment but also greatly enhances the protection of normal tissue. Moreover, it is a convenient procedure for tumor patients that has enhanced the benefits provided by medical institutions. Proton FLASH radiotherapy, which combines the Bragg peak effect of proton spatial dose distribution with the unique temporal effect advantage of FLASH, is an attractive tumor treatment approach. To achieve proton FLASH discrete pencil beam scanning in a 1-L volume, taking into account the 5-mm point interval, 9261 points would need to be irradiated within 500 ms, which is beyond the capability of existing medical devices. To meet these requirements, based on a fast cycle synchrotron with a period of 25 Hz, we simultaneously combined variable-energy, fast splitting, and extraction beam bunches, and proposed a scanning method suitable for continuous variable-energy extraction bunches. The proposed technique meet the requirements of proton FLASH discrete pencil beam scanning within a volume of 1 L.

## INTRODUCTION

While ensuring the effect of tumor treatment, FLASH therapy greatly reduces the damage to normal tissue cells [1], and at the same time brings convenience to tumor patients and improves the benefits of medical institutions. Proton FLASH therapy, which combines the Bragg peak effect advantage of spatial dose distribution and the unique time effect advantage of FLASH therapy, is a very attractive tumor therapy. The ultra-high dose rate (>40 Gy/s) and very short treatment time (usually less than 500 ms) in the target area of FLASH therapy impose high requirements on the accelerator outlet beam intensity and energy transformation time. Synchrotron has the advantage of active energy regulation. Using proton synchrotron in FLASH therapy combined with spot scanning irradiation therapy with high beam utilization rate is expected to meet the requirements of dose rate and irradiation time in the target area.

Due to the high requirements of proton FLASH therapy for dose rate and treatment time, only some medical institutions have conducted proton radiotherapy based on small

volume or fixed energy penetration irradiation on cyclotrons. Some preliminary results of these experiments have shown the effect of FLASH therapy, but further research is needed in more functional proton radiotherapy equipment. At present, cyclotrons are mainly used in medical institutions around the world. However, cyclotrons have low energy regulation speed, high beam loss and great influence on beam quality, which is not conducive to the treatment of tumors with large depth distribution. Synchrotron has the advantage of active energy regulation, which can shorten the energy regulation speed and ensure the beam quality, and has certain advantages in the application of FLASH therapy. However, some key problems still need to be solved in the application of proton synchrotron in FLASH therapy.

## KEY ISSUES AND CHALLENGES

Proton FLASH therapy is a kind of ultra-high dose rate radiotherapy. The average dose rate is not less than 40 Gy/s and the total irradiation time is in the order of hundred milliseconds. For the pencil beam scanning method, the average dose rate in the target scanning process can be calculated according to the dose sum of each scanning point and the total scanning time:

$$\dot{D} = \frac{D}{T} = \frac{\sum_{i=1}^n D_i}{\sum_{i=1}^n (T_{del,i} + T_{scan,i}) + \sum_{j=1}^m T_{energyswitch,j}} \quad (1)$$

where,  $\dot{D}$  is the dose rate;  $D$  is the dose sum of each scanning point;  $T$  is the total treatment time; there are  $n$  scanning points and  $m$  energy switching processes;  $D_i$  is the dose of each scanning point;  $T_{del,i}$  and  $T_{scan,i}$  are the beam delivery time and scanning time of each scanning point, respectively; and  $T_{energyswitch,i}$  is the time of each energy switching.

To improve the average dose rate, it is necessary to increase the number of particles reaching the target area during the treatment time, and to shorten the delivery time, energy switching time, and scanning time. In the volume of 1 L, to meet the minimum dose rate requirement of 40 Gy/s for proton flash therapy, the number of particles required for 100 ms was  $3.8 \times 10^{11}$  [2].

At present, medical institutions providing radiation therapy around the world mostly use cyclotrons to extract beams of fixed energy, and irradiate in the target area after energy regulation. Energy regulation with a range shifter

\* Work supported by National Natural Science Foundation of China (No. 12075131).

<sup>†</sup> zhengsx@tsinghua.edu.cn

<sup>‡</sup> xqz@tsinghua.edu.cn

has the problem of producing a large number of secondary particles and large residual radiation. The multi-energy slow extraction method of the synchrotron provides a new idea to solve the above problems. By changing the energy of the particles at the right time during the extraction process, the extracted particles will deposit the dose at different depths in the lesion area due to different energy, so that the dose can be deposited at different depths of the target area without the need of energy reduction device. In order to give full play to the variable energy advantages of the synchrotron, if the multi-energy fast extraction can be realized, it will further shorten the treatment time, if the beam bunch can be divided into several small beam bunches in advance in the ring, it will greatly improve the convenience of multi-energy fast extraction, and at the same time provide the possibility for the application of back-end extraction beam in radiotherapy with three-dimensional point scanning.

To perform spot scan FLASH therapy on a 1 L (10 cm×10 cm×10 cm) tumor within 500 ms, a total of 9261 spots[3] would be scanned with an average scan interval of 54 μs per spot at a dot interval of 5 mm. 21 energy layers are required, and the switching time between adjacent energy layers is required to be <25 ms. In order to shorten the time interval of point scanning during flash therapy, we used square wave pulse voltage to split the bunch in the synchrotron. By adjusting the pulse voltage to control the number of particles in the small beam cluster, we avoided the waiting time to turn off the beam according to the dose feedback on the target. In the follow-up study, we improved the beam bunch splitting method to meet the requirements of point scanning interval of FLASH therapy. In order to shorten the time to adjust the energy, the energy is adjusted by a square wave pulse voltage in the time interval of generating small beam bunches, and finally the variable energy beam splitting is realized. Combined with the oblique scanning method for continuous variable energy beam splitting, the variable energy scanning irradiation can be realized, so as to meet the requirement of variable energy during FLASH therapy.

## DESIGN OF A SYNCHROTRON

To reduce the required number of particles in a synchrotron duty cycle, a 25-Hz fast-cycle synchrotron with a period of 40 ms can be used. This allows for multiple cycles in a single FLASH treatment time (e.g., 500 ms), thereby reducing the need to store a high number of particles in one cycle. The rising stage of the main magnet of the fast cycle synchrotron generally produces a sinusoidal magnetic field waveform, and there is no platform for fixed energy extraction, as Fig. 1 shows. In one working cycle, half of the period of 40 ms is used for demagnetization. To make full use of the cycle, the time interval of the scanning points is increased as much as possible. To provide more time for beam splitting, it is necessary to combine the beam splitting and extraction process with the rise and fall of the magnetic field to realize the continuous variable-energy beam splitting and extraction process.

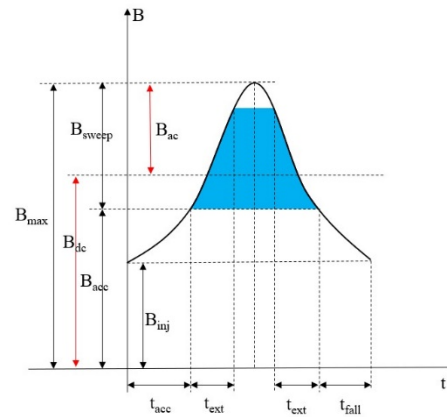


Figure 1: The intensity waveform curve of the main magnet.

In a fast cycle of 40 ms, the rising stage of the main magnet lasts for 20 ms. The waveform expression of the main magnet strength is as follows:

$$B = B_{dc} + B_{ac} = \frac{(B_{max} - B_{inj})}{2} \sin(2\pi f(t - t_0)) + \frac{(B_{max} + B_{inj})}{2} \quad (2)$$

$B_{dc}$  represents the DC part of the main magnet waveform,  $B_{ac}$  represents the sinusoidal part of the main magnet waveform,  $B_{max}$  represents the maximum value of the main magnet waveform,  $B_{inj}$  represents the strength of the magnetic field corresponding to the injected energy, and  $f$  is the frequency of the sinusoidal waveform. For a fast cycle synchrotron with a period of 40 ms,  $f$  can be set as 25 Hz, and  $t$  is the time.  $t_0$  represents the amount of translation of the sinusoidal waveform on the time axis, which is negative when translated to the right and positive when translated to the left. Generally, the strength of the main magnet at  $t = 0$  is minimized, i.e., the sinusoidal waveform is translated to the right on the time axis by a 1/4 cycle.

Figure 2 shows the waveform distribution of the barrier bucket. V2 and V4 form a pair of potential well voltages that are used to constrain the particles of the main beam bunch. A low V2 amplitude is set to ensure that some particles overflow from the main beam bunch area to the left. The particles entering the left phase area increase their momentum dispersion under the action of the larger voltage of V1, accelerating the phase shift speed in the left phase area. The momentum dispersion of particles on the left side does not change within the phase range covered by the V3 voltage. The protruding part of V3 on the left side prevents the momentum dispersion of the overflow particles from being substantially deviated due to the change in the energy of the main beam bunch. After the particles overflow to the left, the kicker is applied in a certain phase range to kick these particles out of the circulating beam. This is combined with the back-end electrostatic septum (ES), magnetic septum (MS), and other extraction devices to realize the extraction of this part of the particle beam. The single-turn phase shift of the particle beam in the longitudinal direction is determined as follows:

$$V_{\phi} = 2\pi\eta\delta. \quad (3)$$

V1 can effectively improve the phase shift speed by increasing the momentum dispersion of particles entering the

left region. In a short time (tens of  $\mu\text{s}$ ), the particle phase shift can cover the phase region kicked out by the kicker, so that the particles can fill the phase region again, thus ensuring the continuity of the split beam bunch. In this process, V3 remains open, and the split beam is carried out in the process of energy switching. The time interval of the kicker kicking out the bunch is the time required for particles to make up for the kicker kicking them out of the phase area. If the required number of turns is  $n$  and the period is  $T$ , then the time interval of the kicker kicking out the bunch is:

$$t = n \cdot T_0 = \frac{\phi}{2\pi\eta\delta} \cdot T_0 = \frac{T_{\text{kicker}} \cdot 2\pi}{2\pi\eta\delta} \cdot T_0 = \frac{T_{\text{kicker}}}{\eta\delta} \quad (4)$$

where,  $T_{\text{kicker}}$  is the pulse duration of the kicker, which together with  $\eta$  and  $\delta$  determines the time interval required for kicking out the bunch.

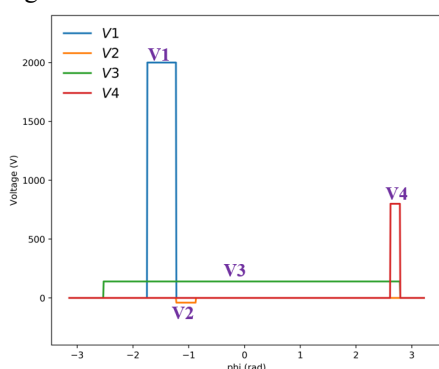


Figure 2: The waveform distribution of the barrier bucket.

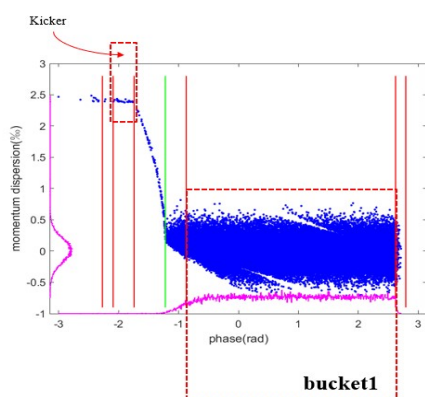


Figure 3: The longitudinal phase space of the bunch to be extracted.

The longitudinal phase space during the rapid bunch splitting process is shown in Fig. 3. The momentum dispersion range of the beam before bunch splitting is  $\pm 0.6\%$ . During the bunch splitting process, the particles enter the left side from the bucket1 region, and the momentum dispersion of the particles increases to  $2.5\%$  under the action of V1. At  $T_{\text{kicker}} = 30 \text{ ns}$ , the time interval for kicking out the bunch is  $t = 20 \mu\text{s}$ , that is, the fast splitting of bunches can be realized.

The extraction process takes "kicker + electrostatic deflector + Lambertson magnet" to complete as Fig.4 shows.

kicker first acts on particles of a specific phase to realize the pre-separation of the particles to be extracted and the circulating beam. Kicked particles enter the diaphragm of the electrostatic deflector and are deflected by the electrostatic deflector into the Lambertson magnet, thus entering the transport line for transmission to the target station.

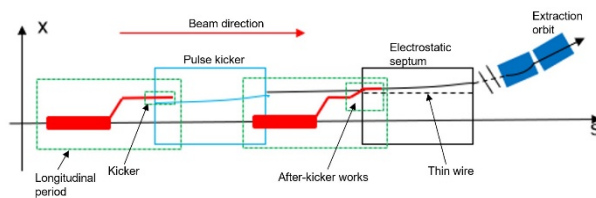


Figure 4: The schematic diagram of the extraction process.

A fast cycle synchrotron based on the existing component layout of the XiPAF (Xi'an 200 MeV Proton Application Facility) can be combined with the rapid variable-energy bunch splitting and extraction methods described above to achieve improved outcomes. The key parameters of synchrotron scheme design are shown in Table 1.

Table 1: The Key Parameters of the Synchrotron

Parameter	Value	Parameter	Value
Ion type	Proton	Magnetic Rigidity	0.38~2.43T·m
Circumference	30.9m	Particle Number	$\geq 3.88e11$
Energy (Min.)	7 MeV	Energy (Max.)	70~250MeV
Frequency (Min.)	1.2MHz	Frequency (Max.)	6.0MHz
Operating Frequency	25Hz	Time per Cycle	40ms

## CONCLUSION

Aiming at the needs and challenges faced by the application of proton synchrotron in the pencil beam scanning FLASH therapy scenario, this paper proposes to alternate the fast beam bunch splitting and extraction processes in the continuous energy transformation process of the fast-cycle synchrotron, so as to realize the beam bunch with continuous energy sweeping at the exit of the accelerator, so as to shorten the energy transformation time during the pencil beam scanning therapy, improve the dose rate on the target, and finally meet the requirements of the FLASH therapy for dose rate and total treatment time.

## REFERENCES

- [1] J. Bourhis, W.J. Sozzi, P.G. Jorge, et al., "Treatment of a first patient with FLASH-radiotherapy". *Radiother. Oncol.* vol. 139, p. 18-22, 2019. doi: 10.1016/j.radonc.2019.06.019
- [2] S. Jolly, H. Owen, M. Schippers, et al., "Technical challenges for FLASH proton therapy". *Phys. Med.* vol. 78, p. 71-82, 2020. doi: 10.1016/j.ejmp.2020.08.005
- [3] E. Kanouta, J.G. Johansen, G. Kertzscher, et al., Time structure of pencil beam scanning proton FLASH beams measured with scintillator detectors and compared with log files. *Med. Phys.* vol. 49, p. 1932-1943, 2022. doi: 10.1002/mp.15486

# NEW PROGRESS OF THE MINIATURIZED MICROWAVE ION SOURCE AT PEKING UNIVERSITY\*

S. X. Peng<sup>1, †</sup>, T. H. Ma<sup>1</sup>, W. B. Wu<sup>1</sup>, B. J. Cui<sup>1</sup>, A. L. Zhang<sup>2</sup>, Y. X. Jiang<sup>1</sup>, Z. Y. Guo<sup>1</sup>, J. E. Chen<sup>1</sup>  
<sup>1</sup>State Key Laboratory of Nuclear Physics and Technology & Institute of Heavy Ion Physics, Peking University, Beijing, China

<sup>2</sup>State Key Laboratory of Particle Detection and Electronics, Department of Modern Physics, University of Science and Technology of China, Hefei 230026, China

## Abstract

The generation of plasma in a microwave ion source involves confining electrons using a static magnetic field and energizing them with an electromagnetic field that transmitted into the plasma chamber. However, according to electromagnetics theory, there is always a cut-off size in circular wave guides for a given frequency. For a 2.45 GHz microwave, this dimension is 72 mm, which should theoretically prevent transmission of the microwave into the discharge chamber and no plasma can be generated. Since 2006 Peking University (PKU) has successfully developed a series of permanent magnet 2.45 GHz microwave ion sources (PKU PMECRs) with a discharge chamber less than 50 mm, capable of delivering tens of mA beams for accelerators. To explain this anomalous phenomenon, a hybrid discharge heating (HDH) mode that combines surface wave plasma (SWP) and electron cyclotron heating (ECH) has been proposed. This HDH mode not only successfully explains PKU PMECRs, but also predicts that the optimized inner diameter of the plasma chamber is 24 mm, which is confirmed by experiments involving different liners in the miniaturized microwave ion source.

## INTRODUCTION

Microwave ion sources (MISs) operating at 2.45 GHz have found widespread use in scientific research, industry, agriculture, and medical science due to their high intensity, low emittance, high stability, simple structure, low cost, and long lifetime [1]. For example, tens even hundred milliamperes H<sup>+</sup>, D<sup>+</sup>, etc. ion beams have been obtained by 2.45 GHz ECR sources, such as CEA/Saclay, PKU [2][3]. Their rms emittance is about 0.2  $\pi$ -mm-mrad. Through long term operation test, CEA/Saclay has made a record with 103 hours CW beam operation with no spark or plasma fault occurred in 2001. In 2016, PKU group improved this non-spark record up to 300 hours. Up to now, no new long term CW beam operation result can be found in the world.

Recently, there has been growing interest in high current miniaturized microwave ion sources (MMISs) for use in compact equipment such as neutron generators, ion thrusters, and ion implanters [4-6]. Despite impressive performance exhibited by MMISs generating overdense plasma ( $n > 10 n_{\text{cutoff}}$ ) over the past few decades [7,8], theoretical

studies on the breakdown mechanism of MMISs remain perplexing. Conventional microwave transmission theory suggests that the chamber diameter of a 2.45 GHz MIS should be larger than the cutoff size of a 2.45 GHz microwave [9], implying that microwaves cannot penetrate into the plasma chamber of MMISs with a diameter smaller than 72 mm.

In our previous work, a novel HDH mode is put forward to understand the complex mechanism of the MMISs [10]. The HDH mode believes that the initial stage of plasma establishment is based on SWPs and the plasma maintenance is based on ECH. In this paper, we will present the HDH mode in details. Meanwhile, the optimized inner diameter of the plasma chamber will be investigated systematically.

## THE MINIATURIZED MICROWAVE ION SOURCE

The MMIS of PKU is composed of microwave window, plasma chamber, permanent magnet rings, and extraction system. A schematic diagram of the source body of the MMIS is presented in Figure 1. The 2.45 GHz microwave of TEM mode produced by microwave generator is transmitted through coaxial line, then transformed to TE<sub>10</sub> mode in the coaxial-waveguide transition by a N-type connector and transformed to TE<sub>11</sub> mode in circular microwave window and finally injected into the plasma chamber. The microwave window is composed of 3 alumina layers with the diameter of 27 mm. A piece of BN is placed behind the microwave window, which faces plasma to protect the alumina from the backbombed electrons. The dimension of plasma chamber is  $\Phi 30$  mm  $\times$  40 mm. The mirror magnetic field is produced by a set of permanent magnets surrounded plasma chamber. The diameter of the chamber can be changed by inserting liners with different inner diameters. In addition, three NdFeB permanent magnet rings are installed around the plasma chamber to provide a magnetic field for the plasma confinement. The magnetic field distribution is presented in Figure 2, it can be found that the axial magnetic field is a magnetic-mirror field with  $B_{\text{max}} > 875$  Gs. A 50 kV three-electrode extraction system consisting of a plasma electrode, suppressor electrode and ground electrode is used for beam extraction.

\* Work supported by the National Natural Science Foundation of China (Grant Nos. 12205019, 12147144, and 11975036).

<sup>†</sup> sxpeng@pku.edu.cn

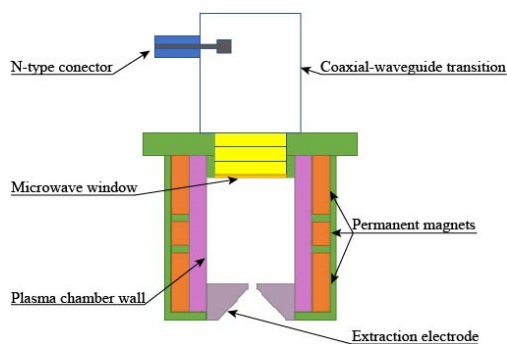


Figure 1: Schematic diagram of the source body of the miniaturized microwave ion source at PKU.

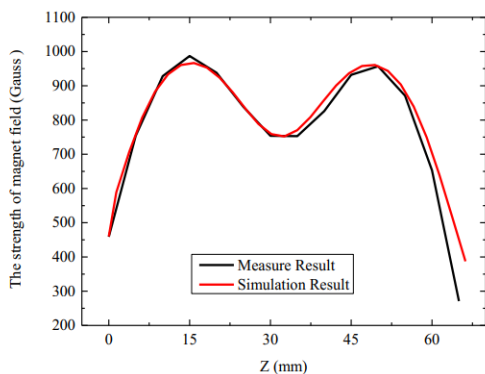


Figure 2: The axial magnetic field distribution of the MMIS.

### SIMULATION OF HDH MODEL

The HDH mode believes that the initial stage of plasma establishment is based on SWPs and the plasma maintenance is based on electron cyclotron resonance. In this work, the numerical simulation of the hybrid discharge mode is made using the Ø30 mm MMIS at PKU based on COMSOL Multiphysics, plotted in Figure 3. The temporal behaviour of the plasma density and hot electron temperature up to the steady state condition are calculated and presented. In our simulation, the gas pressure of hydrogen in the plasma chamber is 10 Pa, and the microwave power supplied on the microwave window is 100 W.

As presented in Figure 4, the electron density increases dramatically with the elapse of time, while the electron temperature gradually increases with the elapse of time and reaches the highest value of 36 eV at  $2.5 \times 10^{-7}$  s, then gradually decreases and finally reaches a certain stable value [10].

Furthermore, at the stage of stable plasma, the plasma properties are analysed in pure ECH or SWPs. As shown in Figures 5 and 6, the electron density increases as the inner diameter increases from 20 mm to 30 mm in the mode of pure ECH. What stands out is that in the mode of SWP without the confinement of magnetic field, however, the electron density can reach the maximum when the inner diameter is 24 mm and then decreases as the inner diameter decreases or increases. The simulation of stable plasma in

MMIS points out the possibility of further miniaturization of MMIS.

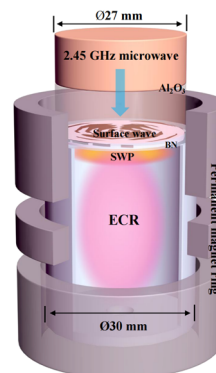


Figure 3: Schematic diagram of the HDH mode for MMIS.

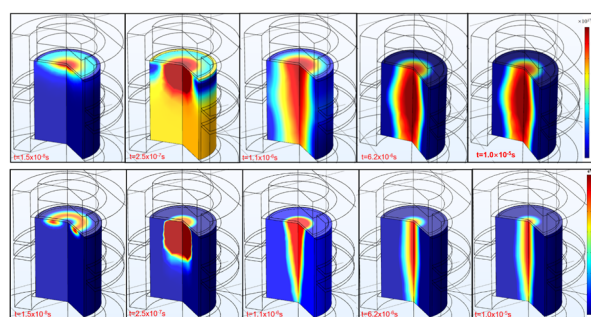


Figure 4: Profiles of the electron density (up) and electron temperature (down) at different time steps [8].

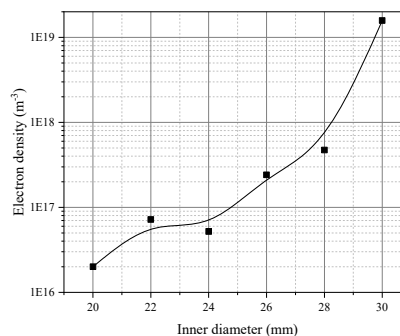


Figure 5: Dependence of electron density on inner diameter with pure ECH mode.

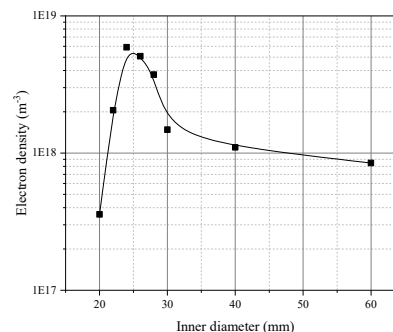


Figure 6: Dependence of electron density on inner diameter with pure SWPs which means no confinement by magnetic field.

## EXPERIMENT RESULTS

According to the simulation results, 4 stainless steel liners with different inner diameters are inserted into the plasma chamber of the MMIS. The dependence of high voltage load on pressure, with different liners, is shown in Figure 7. As the pressure increases, the changed point of pressure describes the high voltage load starts to have a rapid growth and the maximum point is the pressure related to the maximum of high voltage load. With the different liners, the high voltage loads have the same changing trend. The dependence of maximum point and change point on the inner diameter is shown in Figure 8.

Among the four liners, the MMIS with the inner diameter of 24 mm can produce the highest high voltage load above 40 mA which is the higher than ones with other liners. This experiment result confirms the stable plasma of simulation, which means in stage of the plasma maintenance, SWPs is important to produce overdense plasma in MMIS.

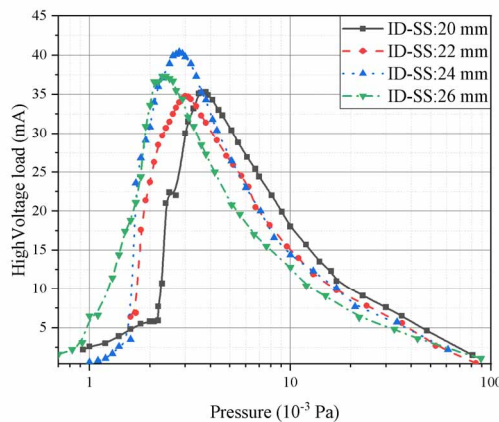


Figure 7: Dependence of hydrogen beam current on pressure with different chamber diameters.

## DISCUSSION AND OUTLOOK

In this work, the HDH mechanism is proposed and studied based on the MMIS at PKU. The spatial and temporal evolution and stable discharge of the electron temperature and electron density have been investigated. The changing trends of electron density with increasing inner diameters in pure ECH mode and pure SWP mode are compared. Preliminary experiments indicate that the MMIS has even better performance than the traditional PMECR at PKU and the optimized diameter of plasma chamber is 24 mm. All of these results have illustrated the rationality of the HDH mode. This work, we believe, is helpful to the comprehension and miniaturization of MISs.

## ACKNOWLEDGEMENTS

This work is supported by National Natural Science Foundation of China (Grant Nos. 12205019, 12147144 and 11975036). The support from State Key Laboratory of Nuclear Physics and Technology, Peking University is appreciated.

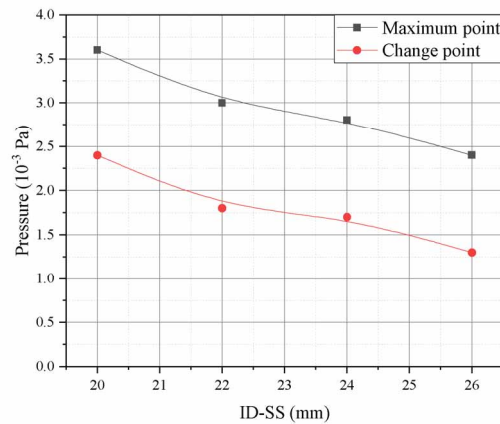


Figure 8: Dependence of maximum point and change point on the inner diameter of liners.

## REFERENCES

- [1] S. Gammino, *et al.*, “Review on high current 2.45 GHz electron cyclotron resonance sources”, *Rev. Sci. Instrum.* vol. 81, p. 02B313, 2010. doi.org/10.1063/1.3266145
- [2] R. Gobin, *et al.*, Saclay high intensity light ion source status. *Proc. Of EPAC 2002*, Paris, France, pp.1712-1714
- [3] S. X. Peng, *et al.*, New progress on beam availability and reliability of PKU high intensity CW proton ECR ion source. *Chin. Phys. B*, **26(2)** (2017): 025206. doi: 10.1088/1674-1056/26/2/025206
- [4] J. H. Vainionpaa, *et al.*, “High yield neutron generators using the DD reaction”, *AIP Conf. Proc.* vol. 1525, p118, 2013. doi.org/10.1063/1.4802303
- [5] Y. J. Ke, *et al.*, 2017 “Analysis of the primary experimental results on a 5 cm diameter ECR ion thruster”, *Plasma Sci. Technol.* vol. 19, p. 095503, 2017. doi.org/10.1088/2058-6272/aa6d4c/meta
- [6] Y. X. Jiang, *et al.*, “A miniaturized ECR plasma flood gun for wafer charge neutralization”, *Rev. Sci. Instrum.* vol. 91, p. 033319, 2020. doi.org/10.1063/1.5128522
- [7] Q. Ji. “Compact Permanent Magnet Microwave-Driven Neutron Generator”, *AIP Conf. Proc.* vol. 1336, p. 528, 2011. doi.org/10.1063/1.3586156
- [8] J. M. Wen, *et al.*, “A miniaturized 2.45 GHz ECR ion source at Peking University”, *Chin. Phys. B* vol. 27, p. 055204, 2017. doi.org/ 10.1088/1674-1056/27/5/055204/meta
- [9] O. A. Popov, *et al.*, “Electron cyclotron resonance plasmas excited by rectangular and circular microwave modes”, *J. Vat. Sci. Technol. A* vol. 8, p.2909, 1990. doi.org/10.1116/1.576648
- [10] W. B Wu, *et al.*, “Theoretical and experimental study of the overdense plasma generation in a miniaturized microwave ion source”, *J. Appl. Phys.* vol. 132, p.083305, 2022. doi.org/10.1063/5.0098645

# WAKEFIELD STUDIES FOR THE STEP STRUCTURE AND THE SKIN DEPTH OF COATED DIELECTRIC TUBES

H. Liu<sup>†1</sup>, Shanghai Institute of Applied Physics, Chinese Academy of Sciences Shanghai, China  
 J. J. Guo, Zhangjiang Laboratory, Shanghai, China  
 Y. M. Wen, S. Chen, B. Liu, H. X. Deng,  
 Shanghai Advanced Research Institute Chinese Academy of Sciences, Shanghai, China  
<sup>1</sup>also at Shanghai Advanced Research Institute Chinese Academy of Sciences, Shanghai, China

## Abstract

Wakefield issues are always important in free electron laser (FEL) facilities. Since the wakefield in free electron laser facilities usually leads to a decrease of FEL performance, the research of the wakefield impacts is of great significance. Step structures are almost ubiquitous in the overall undulator section of an FEL facility, which always generate critical wakefields. In this paper, we systematically analyse and summarize the wakefield characteristics of step structures including the step-in and the step-out. In addition, the skin depth issue of the wakefield is still controversial. We study the skin depth of the wakefield field in the vacuum chamber of the kicker in the Shanghai high-repetition-rate XFEL and extreme light facility (SHINE), which is made of the dielectric tube. We proposed the conception of “effective skin depth” from two different perspectives and wrote simulation codes to calculate the “effective skin depth”. We hope these methods could provide new mentalities for related research in the future.

## INTRODUCTION

FEL lasing performance largely depends on the quality of electron bunches [1]. While the wakefield generated by the electron bunch always destroys its phase space, which leads to a decrease of lasing performance [2-4]. Since there are many different types of devices the inner apertures of chambers in different devices are always different. The connection of chambers with different apertures is called step structure. In our research before [5, 6], we found that the wakefield generated in step structures is an important component of the total wakefield of an FEL facility. The step structure wakefield even contributes half of the total wakefield. Therefore, the study of the step structure wakefield is important for FEL. There are currently some studies on the step structure wakefield, but there is still a lack of systematic summary of the characteristics of this kind of wakefield. In this paper, we calculate and analyse the step structure wakefield in different situation and initially list its characteristics comprehensively.

In our study of the wakefield in the kicker of the SHINE, we found that the skin depth issue in wakefield calculations

is still unsolved. Different teams presented different perspectives. In this paper, we proposed the conception of “effective skin depth” from the perspective of the accumulation of free charges and the attenuation of the surface current. We calculate the effective skin depth using our own simulation code. The results demonstrate the feasibility of the development of this conception in the future.

## WAKEFIELDS OF THE STEP STRUCTURE

The step structure includes two types of structures, the step-in and the step-out. The former means the structure whose aperture varies from large to small while the latter is the opposite structure to step-in. There are two connection types of step structures, the saltatory type is called the “hard connection” and the “soft connection” means a gradual change of aperture. Although there are some research about the step structure wakefield, some questions are still unsolved. In this section, we will answer these questions based on our simulation results (simulation code: ECHO2D [7]).

### Short Bunch Situation

In our research before, we always ignore the effect of step-in wakefield since its value is much smaller than that of step-out wakefield. Taking the situation in the SHINE as an example, we calculated wakefields of a step-in and a step-out with soft (taper) and hard connection schemes. The parameters are listed in Table 1 and the simulation results are shown in Figure 1.

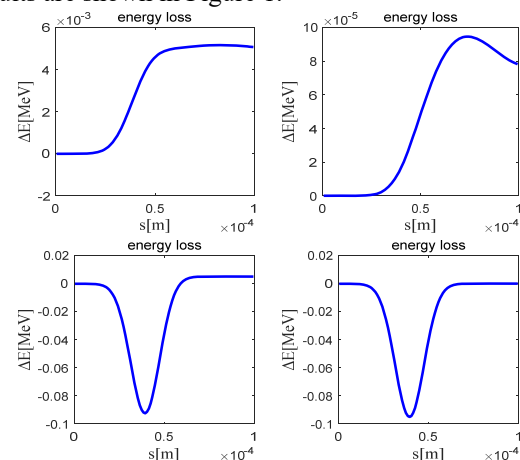


Figure 1: Simulation results of step structure wakefields in short bunch situation.

\* Work supported by the CAS Project for Young Scientists in Basic Research (YSBR-042), the National Natural Science Foundation of China (12125508, 11935020), Program of Shanghai Academic/Technology Research Leader (21XD1404100), and Shanghai Pilot Program for Basic Research – Chinese Academy of Sciences, Shanghai Branch (JCYJ-SHFY-2021-010).

<sup>†</sup> email address

liuhe@sairi.ac.cn.

Table 1: Parameters of Wakefield Simulation

Aperture 1 [mm]	Aperture 2 [mm]	Bunch length [GeV]	Charge [pC]
14	24	8	100

Figures in the first row are step-in wakefields and the second row contains step-out wakefields. The first column is soft connection, and the second column is hard connection. As shown in Figure 1, the step-out wakefield is almost unchanged in different connection schemes, while the step-in wakefield shows a significant growth in soft connection scheme. However, step-in wakefields are consistently inappreciable compared with step-out wakefields. In most FEL facilities, the bunch length is usually short enough that the step-in wakefields could be ignored.

To understand the characteristics of step structure wakefields, we referred to L. Palumbo's theory about step structures [8].

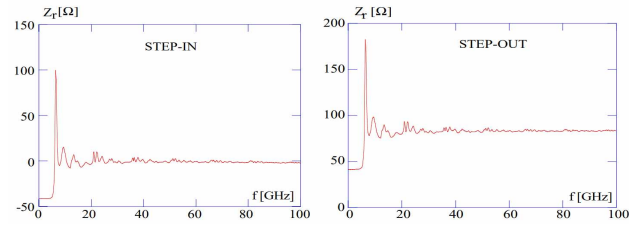


Figure 2: Impedance spectrum of step-in and step-out [8].

As we all know, the wakefield is the inverse Fourier transform of the impedance, so the larger impedance means the stronger wakefield and they have opposite signs. According to Figure 2, we could analyse the reason of step structure wakefield variation. In short bunch situation, the main part of the impedance comes from the high frequency part in the spectrum. Thus, the step-out wakefield is a negative number just like the most wakefields, while the step-in wakefield is positive due to the negative impedance. In soft connection scheme, the low frequency of impedance is growing with the slope decreasing. Then, the step-in wakefield is getting stronger and the step-out wakefield is getting weaker. The value of this variation is very small, so it is obvious for the step-in wakefield but not for the step-out wakefield.

### Long Bunch Situation

When the bunch length becomes extremely long, the conclusion could be quite different from the short bunch situation. We calculated wakefields in the same structure but generated by a long bunch (rms=260mm, Q=670pC). The results are shown in Figure 3.

The correspondence between the wakefield and structure is the same as Figure 2. It is obvious that in long bunch situation, the value of the step-in wakefield and the step-out wakefield in soft connection scheme is almost the same. This is expectable according to Figure 2. In long bunch situation, the low frequency part becomes the key part of the impedance. When the frequency is approaching to zero, the impedances of step-in and step-out become almost opposite numbers. Thus, when the slope of connection part

is getting smaller, the sum of their wakefields is getting closer to zero.

Note that the step-in wakefield is always positive in all simulation results. It seems that the electron bunch has gained energy at this position. This does not conform to the law of conservation of energy. In Palumbo's theory, the energy loss of an ultra-short bunch caused by step-out and step-in is given by the following equation:

$$q^2 k^{out} \sim 2U(a < r < b),$$

$$q^2 k^{in} \sim 0, \quad (1)$$

while the energy loss of an extremely long bunch caused by a long tapering step structure is given as:

$$q^2 k^{out} \sim U(a < r < b),$$

$$q^2 k^{in} \sim -U(a < r < b). \quad (2)$$

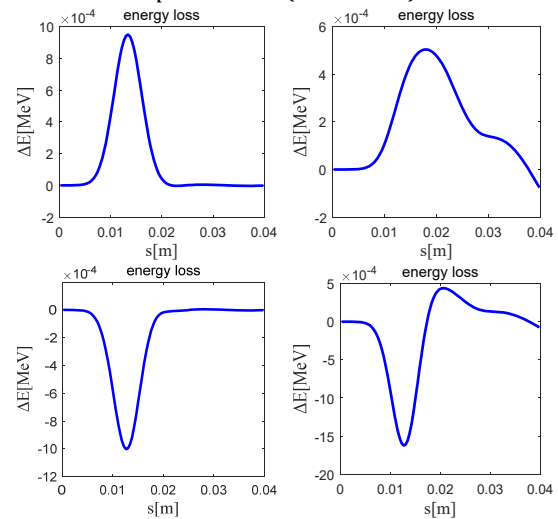


Figure 3: Simulation results of step structure wakefields in long bunch situation.

According to Eq. (1), when the high frequency part dominates, the wakefield of step-in could be ignored. While if the low frequency part dominates, as shown in Eq. (2), the wakefield value of step-in is equivalent to that of step-out. Under this circumstance, the effect of step-in wakefield should not be ignored anymore and its physical implication needs to be explained. Actually, the energy lost by the electron bunch at the position of step-out will not immediately dissipated but diffuses into the cavity space. We believe that the positive wakefield of the step-in structure means that the energy loss at the step-out structure will be partially returned through the step-in structure. We summarize the wakefield characteristics of the step structure as follows:

- The wakefield of step-in is positive, which means an energy compensation. This part of energy comes from the energy lost by the electron bunch itself at the position of step-out.
- In the case of ultra-short bunch and hard connections, the wakefield of step-in is extremely small. It is several orders of magnitude smaller than that of step-out.
- As the electron bunch becomes longer and the slope of the step structure becomes smaller, the low-frequency part of the impedance spectrum increases,

resulting in a larger step-in wakefield and a smaller step-out wakefield. Ultimately, the absolute values of the two gradually approach. For a infinitely long bunch and an infinitely flat slopes, the sum of the wakefields of step-in and step-out is 0.

- The length of the electron bunch is the main factor that dominates the high and low frequency proportion of the impedance spectrum of the step structure.
- The value of the wakefield discussed above refers to the total wakefield from the beginning to the end of the step structure. In the case of ultra-short beam clusters, although the total wakefield cannot be obviously changed by a tapering connection, it can be distributed across the entire slope, which is helpful in weakening the thermal effect of the wakefield.

## SKIN DEPTH ISSUES OF THE WAKEFIELD

The kicker in the SHINE employs a metal coated dielectric tube as its vacuum chamber. In order to better transmit the field, the coating thickness should be as thin as possible, while to avoid the wakefield of the dielectric tube, the coating thickness should be thick enough. Under the common requirements of both aspects, we recommend that setting the coating thickness as the skin depth is the best scheme. For a single frequency electromagnetic field, solving skin depth is never a problem. But in the wakefield issue, the skin depth of a multifrequency mixed field is hard to define and calculate. To find a suitable coating solution, we proposed the conception of “effective skin depth” from the perspectives of the accumulation of free charges and the attenuation of the surface current.

### Effective Skin Depth 1: Accumulation of Free Charges

Assuming that the electromagnetic field enters the conductor perpendicular to the surface of the conductor. If only under the action of the electric field force and the Lorentz force, the electrons in the conductor will move deeply. At this time remainder residual positive charges will be generated on the surface, resulting in a charge force that attracts electrons towards the surface. As more and more electrons move towards the depth, this amount of charge gradually increases. Finally, the electrons achieve equilibrium under the combined action of the electromagnetic field and charge force, as illustrated in Figure 4.

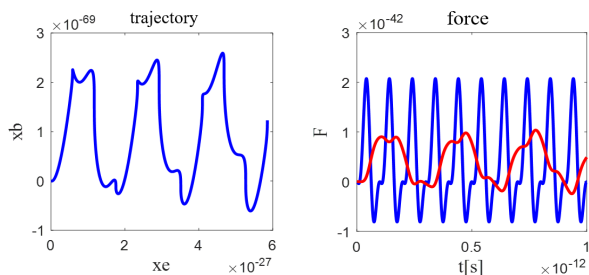


Figure 4: The trajectory and force of electron motion reaching equilibrium state

We calculated the attenuation total charge density at the equilibrium state as shown in Figure 5. Take the depth where the charge density attenuates to 1/e as the effective skin depth  $\delta_{eff}$ , we got  $\delta_{eff} = 162\text{ mm}$ .

### Effective Skin Depth 2: Attenuation of The Surface Current

Actually, charge accumulation may not occur at all frequencies of electromagnetic fields, as evidenced by the decay function of free charge density within a conductor:

$$\rho(t) = \rho_0 e^{-\frac{\sigma}{\epsilon} t} \quad (3)$$

When the attenuation characteristic time  $\tau \ll \omega^{-1}$ , charges will attenuate before accumulating. In the impedance spectrum of kicker's quasi coating material titanium, the curve almost comes to zero when the frequency exceeds 10THz [9,10] while  $\tau \approx 10^{-17}\text{ s}$ . Thus, we have to calculate the effective skin depth from a new perspective. Considering the transvers motion of electrons along the conductor surface, we could calculate the surface current and figure out effective skin depth. We wrote a code and simulated electron motion under multi frequency superposition field. The result of surface current distribution is shown in Figure 5. Equally, we found the position where surface current attenuates to 1/e and the effective skin depth, in this situation, is 272mm.

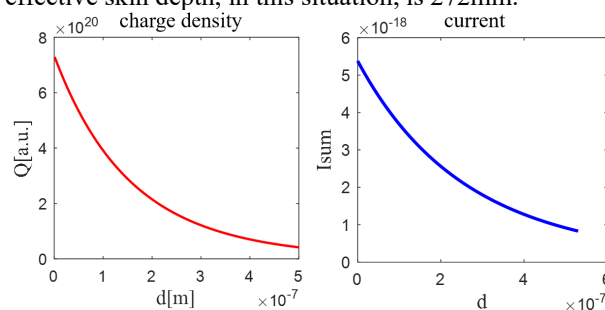


Figure 5: Attenuation curve of total charge density (left) and surface current distribution under multi frequency superposition field (right)

## CONCLUSION

We systematically summarized the wakefield characteristics of the step structure. The conclusion could be helpful for related research. In addition, we proposed the conception of “effective skin depth” from two different perspectives. Although the simulation code is rough, we believe these methods could provide new mentalities for related research in the future.

## REFERENCES

- [1] H Deng, and M Zhang. “Review of Electron Beam Manipulation by using Corrugated Device for Light Sources”[C], 2014.
- [2] Minghao, Song, Kai, and *et al.*, “Wakefield issue and its impact on X-ray photon pulse in the SXFEL test facility”[J]. *Nuclear Instruments & Methods in Physics Research*, 2016.
- [3] Song M H, Feng C, Huang D Z, and *et al.*, “Wakefields studies for the SXFEL user facility”[J]. *Nuclear Science and Techniques*, 2017, 28(7).

- [4] H. Liu, H. X. Yang, N. S. Huang, and *et al.*, “Measurement of undulator section wakefield at the SXFEL test facility”. *Nuclear Instruments and Methods in Physics Research Section A: Accelerators, Spectrometers, Detectors and Associated Equipment*, 2021.
- [5] H. Liu, H. X. Yang, H. X. Deng, and *et al.*, “Calculation of undulator section wakefield at the SHINE”. *Proc. SPIE 12169*, Eighth Symposium on Novel Photoelectronic Detection Technology and Applications, 121691B, 2022
- [6] H. Liu, J. Y. Yan, J. J. Guo, and *et al.*, “Wakefield Calculations of the Undulator Section in FEL-I at the SHINE”, *Proc. FEL'22*, Trieste, Italy, Aug. 2022.
- [7] I. Zagorodnov, K. Bane, and G. Stupakov, “Calculation of wakefields in 2D rectangular structures”. *Physical Review Special Topics - Accelerators and Beams*, 2015, 18(10):152-4.
- [8] L. Palumbo, V. G. Vaccaro, and M. Zobov. “Wake Fields and Impedance”, *Physics*, 2003:39-79.
- [9] Stupakov G, Bane K L F, Emma P, and *et al.*, “Resistive wall wakefields of short bunches at cryogenic temperatures”[J]. *Physical Review Special Topics - Accelerators and Beams*, 2015, 18(3).
- [10] Bane K, and Stupakov G. Erratum, “Using surface impedance for calculating wakefields in flat geometry”, *Phys. Rev. ST Accel. Beams*, vol. 18, p. 034401, 2015

# HEATING ESTIMATION OF UNDULATOR VACUUM CHAMBER AT S<sup>3</sup>FEL

Huaiqian Yi<sup>1</sup>, Xiaofan Wang<sup>1\*</sup>, Weiqing Zhang<sup>1,2†</sup>, Xueming Yang<sup>1,2,3</sup>

<sup>1</sup>Institute of Advanced Science Facilities, Shenzhen 518107, China

<sup>2</sup>Dalian Institute of Chemical Physics, Dalian 116023, China

<sup>3</sup>Southern University of Science and Technology, Shenzhen 518055, China

## Abstract

Heating of the vacuum chambers are unavoidable when electron beams pass through the chamber channels at relativistic speeds. In the undulator vacuum chambers, such effects might lead to temperature increase of the magnets and eventually cause degradations in the FEL lasing process. Thus, in this paper, the heating of the undulator vacuum chambers at Shenzhen superconducting soft x-ray free-electron laser due to wake field effects and spontaneous synchrotron radiation are estimated using an analytical approach. For the wake field effects, the contribution from finite conductivity of the vacuum chamber material and from the inner surface roughness are considered. An electron beam profile from a start-to-end simulation is used to calculate the total wake field and the induced heat. For the synchrotron radiation, a simple analytical expression is used.

## INTRODUCTION

At Shenzhen superconducting soft x-ray free-electron laser (S<sup>3</sup>FEL) [1], electron beams from the injector system are accelerated in a single superconducting linac and transported to the undulator lines through the beam distribution system (BDS). At the end of the BDS, the typical electron beam parameters are given in Table 1. The maximum designed repetition rate of the electron bunches is 1MHz.

Table 1: Electron Beam Parameters

Beam Parameters	Value	Unit
Electron Energy	2.5	GeV
Slice Energy Spread	190	keV
Electron Bunch Charge	100	pC
Slice Emittance	0.5	mm·mrad
Rms Bunch Length	25	μm

When electron beams pass the vacuum chambers of the beam lines, heat will be deposited in the chamber walls due to electrons losing energy when interacting with their own wake fields.

The heating problems may become prominent for vacuum chambers in the undulators since the chamber transverse dimensions are small compared to other parts along the beam lines, and the wake field effects are stronger. In

addition, spontaneous synchrotron radiation is generated and absorbed by the chamber walls.

The vacuum chambers within the undulators at S<sup>3</sup>FEL are made of extruded aluminium with an elliptical cross-section, as shown in Fig. 1. The full height and width of the chamber cavity are 6 mm and 15 mm, respectively. The two circular holes adjacent to the chamber are for the water-cooling system, while the two outermost holes are space designed for correction coils.

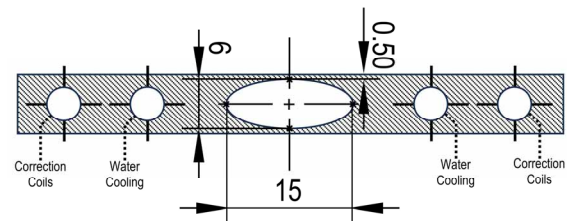


Figure 1: Cross-section of the vacuum chamber geometry.

If excessive heat in the vacuum chambers is not removed efficiently by the cooling system, the temperature gradient within the permanent magnet blocks will be affected and the magnetic field distributions and undulator K values will be modified. This will result in a negative impact on the FEL lasing process.

Under such considerations, the heat load projected on the vacuum chambers by the two heat sources mentioned above is estimated analytically in this paper. The results will serve as supplementary information to aid the design of the cooling system.

## WAKE FIELD EFFECTS

The wake fields due to wall resistivity and the roughness of the inner surface of the vacuum chamber are considered in this work. Wake fields generated by single or periodic structures or other effects are ignored. A simplified approach is taken in the current calculations, where the longitudinal distributions of the electron beams is assumed to be unchanged as they travel down the undulator lines.

### Calculation of the Wake Fields

The analytical approach first involves the calculation of resistive wall and roughness induced surface impedance and thereafter the longitudinal beam impedance  $Z$ . The latter depends on the cross-section shape of the vacuum chamber, and in this work, both round and flat plate

\* wangxf@mail.iasf.ac.cn

† weiqingzhang@dicp.ac.cn

approximation of the chamber cross-section is assumed. The analytical expressions for coupling of the impedances due to resistance and wall roughness for round and flat geometries derived in [2] is used. An appropriate analytical model for elliptical shaped chamber is not yet available, but numerical calculations have shown that the beam impedances computed for elliptical cross-section shapes are very similar to those calculated using a flat plate model [3].

The resistive wall surface impedance, denoted as  $\zeta_{rw}$ , is given by [2]:

$$\zeta_{rw}(k) = (1 - i) \sqrt{\frac{k(1 - ik\tau_c)}{2Z_0\sigma_c}}, \quad (1)$$

where  $k$  is the wavenumber of the Fourier transform of the wake field,  $Z_0 = 377 \Omega$  is the impedance of vacuum,  $\sigma_c$  is and  $\tau_c$  are the dc conductivity and the relaxation time of the metallic walls. The surface impedance due to roughness, denoted by  $\zeta_{rs}$ , is given as [4]:

$$\zeta_{rs}(k) = \frac{1}{4}kh^2\kappa^{\frac{3}{2}} \left( \frac{\sqrt{2k + \kappa} - i\sqrt{2k - \kappa}}{\sqrt{4k^2 - \kappa^2}} \right). \quad (2)$$

The roughness model assumes sinusoidal corrugation of the round pipes or of the flat plate model where the radius (or the half height of flat plate)  $r$  vary according to  $r = a - h \cdot \cos(\kappa z)$ . For the model to be valid it is required that the period ( $\lambda_{ro} = 2\pi/\kappa$ ) and the amplitude of the corrugation is small compared to the radius, i.e.,  $\kappa a \gg 2\pi$  and  $h \ll a$ , and that the corrugation is shallow ( $h \ll 2\pi/\kappa$ ). The impedances given in Eq. (1) and Eq. (2) are defined for  $k \geq 0$ . For  $k < 0$ , the complex conjugate should be taken, i.e.,  $\zeta(-k) = \zeta^*(k)$  [5].

For a round vacuum chamber, the coupled beam impedance contains the contribution from both  $\zeta_{rw}$  and  $\zeta_{rs}$ , and is given by [2, 6]:

$$Z_r(k) = \frac{Z_0}{2\pi a} \left( \frac{1}{\zeta_{rw}(k) + \zeta_{ro}(k)} - \frac{ika}{2} \right)^{-1}, \quad (3)$$

while for the flat plate model, the coupled beam impedance is [2, 7]:

$$Z_{fp}(k) = \frac{Z_0}{2\pi a} \cdot \int_{-\infty}^{\infty} \text{sech}(q) \left( \frac{\cosh(q)}{\zeta_{rw}(k) + \zeta_{ro}(k)} - \frac{ika}{q} \sinh(q) \right)^{-1} dq, \quad (4)$$

where  $q$  is the frequency component of another Fourier transform.

With the beam impedance known, the wake field of a single electron can be calculated with the inverse Fourier transform:

$$W_\delta(s) = \frac{c}{2\pi} \int_{-\infty}^{\infty} Z_{tot}(k) e^{-iks} dk, \quad (5)$$

where  $s$  is the distance behind the electron that invoked the wake field. Considering an electron beam that has a certain longitudinal distribution  $f(s)$  (with unit C/m), the

wake field along the beam longitudinal position can be calculated with the convolution:

$$W_f(s) = - \int_0^\infty W_\delta(s') f(s - s') ds'. \quad (6)$$

Using a typical electron beam longitudinal profile that is obtained from start-to-end simulation, the total wake field is computed according to Eq. (1-6). The integrations presented in these equations are performed numerically by selecting sufficiently small integration steps. As given in Fig. 1, the chamber radius or half height  $a$  is set to 3 mm. The aluminium conductivity and relaxation time are taken to be  $\sigma_c = 3.5 \times 10^7 \Omega^{-1} \text{m}^{-1}$  and  $\tau_c = 8$  fs, respectively.

While the resistivity induced wake is well determined by the geometry and material of the chamber, the parameters for the roughness wake is uncertain due to the manufacturing process. However, practical experience suggested that the roughness surface thickness local maxima and minima difference is around 200 nm, which corresponds to  $h = 100$  nm. The determination of the roughness oscillation wavelength is even more ambiguous, thus, the wake fields generated along the beam with different  $h$  and  $\lambda_{ro}$  values for the flat plate pipe model are compared in Fig. 2.

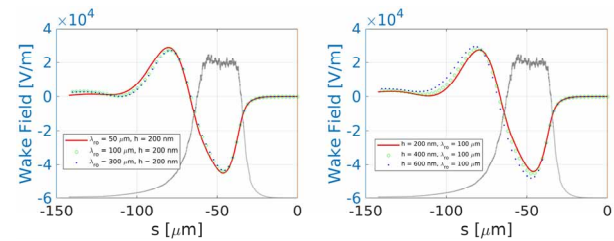


Figure 2 Electron beam wake field calculated using the round pipe model, for different surface roughness amplitudes (left) and for different corrugation wavelength (right). The beam profile is shown in grey.

It can be seen that variations of the roughness parameters have very limited influences on the total wake field and, consequently, on the amount of heat generated. Similar behaviours are also observed for the round model. Hence, the values for the roughness parameters are used in calculations hereafter are  $h = 200$  nm and  $\lambda_{ro} = 100 \mu\text{m}$ .

Based on these parameters, a comparison of the wake field calculated with round and flat model, and their corresponding effects on the electron beam longitudinal energy distribution, after passing 10 undulator segments (i.e., travelling a distance of  $\sim 40$  meters), are shown in Fig. 3. In calculation of the beam energy change, the longitudinal distribution of the beam is assumed to stay unchanged. The advantage of choosing longer horizontal width of the vacuum chamber is thus clear since the flat plate model predicts lower influence on the beam energy as compared to the round pipe model.

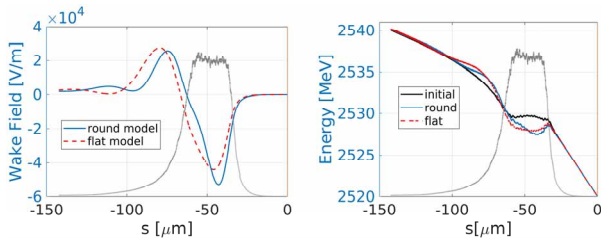


Figure 3 Wake field calculated using the round pipe model and flat plate model (left), and their corresponding influences on the electron beam energy distribution (right). The beam profile is shown in grey.

### Heating due to Wake Fields

The wake fields computed with both geometry models are then used to estimate the heating power.

Taking an electron located at position  $s$  within the beam that travels a length  $L$  in the vacuum chamber, the energy loss per meter travelled for this electron is:

$$\delta_w^E(s) = \frac{W_f(s) \cdot L \cdot e}{L} = W_f(s) \cdot e, \quad (7)$$

where  $e$  is the charge of the electron. Then after travelling one meter in the vacuum chamber, the energy loss of the entire electron beam is:

$$\Delta E_B^{rw+rs} = \int_0^{l_B} \delta_w^E(s') \frac{f(s')}{e} ds'. \quad (8)$$

Finally, taking into account the repetition rate of the electron beams that pass the undulator lines, the heat generation rate per unit length (with the unit W/m) is calculated according to:

$$\frac{dP^{rw+rs}}{dz} = -\Delta E_B^{rw+rs} \cdot f_{rep}. \quad (9)$$

The total wake field is computed using both round and flat plate models and the heating estimation is summarized in Table 2. The flat plate model predicts slightly higher heat generation rate but is still the favourable geometry choice since it induces less energy variation along the electron beam.

Table 2 Wake Field Induced Heat Generation Rate Per Unit Length

Model	Round Pipe	Flat Plate
$dP^{rw+rs}/dz$ [W/m]	2.0487	2.2722

### SYNCHROTRON RADIATION

Synchrotron radiation emitted by relativistic electron beams in the undulators may be absorbed by the chamber walls. The total synchrotron radiation power after passing through a length  $L_u$  is calculated with [8]:

$$P^{sr} = e\gamma^2 \frac{\langle I \rangle}{12\pi\epsilon_0} \left(\frac{2\pi}{\lambda_u}\right)^2 K^2 L_u, \quad (10)$$

where  $\gamma$  is the Lorentz factor,  $\lambda_u$  is the undulator period,  $K$  is the undulator parameter and  $\langle I \rangle$  is the average current of the electron beams calculated by:

$$\langle I \rangle = Q_B f_{rep}. \quad (11)$$

$Q_B$  is the charge of each electron beam. Assuming conservatively that half the power will be absorbed by the vacuum chamber, the heat generation rate per unit length due to synchrotron radiation is then given by:

$$\frac{dP^{sr}}{dz} = 0.5 \frac{P^{sr}}{L_u}. \quad (12)$$

The typical undulator parameter  $K$  values at S<sup>3</sup>FEL ranges from 1 to 5. Considering the case where 15 nm radiation is generated with an undulator period of 0.043 m, the corresponding undulator  $K$  value is 5.6034. In this case, the synchrotron radiation related heat generation calculated according to Eq. (10) and Eq. (12) is 0.38537 W/m.

### CONCLUSION

In this paper, the heat generation rates in the S<sup>3</sup>FEL undulator vacuum chambers are estimated. The electron beam longitudinal profile in the undulator is obtained from a start-to-end simulation and is used to compute the contributions wake field effects. The synchrotron radiation deposited power is calculated conservatively using an analytical expression. The estimated total heating power is approximately 2.6 W/m and should be easily compensated with the cooling water system.

### ACKNOWLEDGEMENTS

The authors thank Wei Wei (IASF) for providing the vacuum chamber geometry shown the vacuum in Fig. 1. This work is supported by the Shenzhen Science and Technology Program (Grant No. RCBS20210609104332002), the Scientific Instrument Developing Project of Chinese Academy of Sciences (Grant No. GJJSTD20190002) and the National Natural Science Foundation of China (22288201).

### REFERENCES

- [1] X. Wang *et al.*, “Physical design for Shenzhen superconducting soft x-ray free-electron laser (S<sup>3</sup>FEL)”, in *Proc. IPAC’23*, Venice, Italy, 2023, paper TUPL043. <https://doi.org/10.18429/JACoW-14th International Particle Accelerator Conference-TUPL043>
- [2] K. Bane and G. Stupakov, “Roughness Tolerance Studies for the Undulator Beam Pipe Chamber of LCLS-II”, SLAC National Accelerator Laboratory, CA, USA, Rep. LCLS-II-TN-14-06, May 2014. <https://doi.org/10.48550/arXiv.1405.0330>
- [3] K. Fujita, “Impedance computation of cryogenic vacuum chambers using boundary element method”, *Phys. Rev. Accel. Beams.*, vol. 25, no. 6, p. 64601, June 2014. <https://doi.org/10.1103/PhysRevAccel-Beams.25.064601>
- [4] K. Bane and G. Stupakov, “Impedance of a beam tube with small corrugations”, in *Proc. Linac2000*, Monterey, CA, USA, Aug. 2000, pp. 92-94.

<https://doi.org/10.48550/arXiv.physics/0008205>

- [5] G. Stupakov and S. Reiche, “Surface roughness wakefield in FEL undulator”, in *Proc. FEL2013*, New York, NY, USA, Aug. 2013, pp. 127-131.  
<https://accelconf.web.cern.ch/FEL2013/papers/mopso73.pdf>
- [6] G. Stupakov, “Surface impedance and synchronous modes”, in *AIP Conference Proceedings*, vol. 496, no. 1, pp. 341-350, 1999.

<https://doi.org/10.1063/1.1301898>

- [7] H. Henke and O. Napoly, “Wake fields between two parallel resistive plates”, in *Proc. EPAC90*, Nice, France, 1990, pp. 1046-1048.  
[https://accelconf.web.cern.ch/e90/PDF/EPAC1990\\_1046.PDF](https://accelconf.web.cern.ch/e90/PDF/EPAC1990_1046.PDF)
- [8] K.J. Kim et al., “Synchrotron radiation and free-electron lasers”. Cambridge university press, 2017.

# RECENT PROGRESS OF THE BEAM BACKGROUND EXPERIMENT IN THE BEPCII\*

B. Wang<sup>†1</sup>, H.Y. Shi<sup>1</sup>, H.C. Shi<sup>2</sup>, C.H. Yu<sup>1</sup>

<sup>1</sup> Key Laboratory of Particle Acceleration Physics and Technology,  
Institute of High Energy Physics, Chinese Academy of Sciences, Beijing, China

<sup>2</sup> Zhejiang University, Hangzhou 310027, People's Republic of China

## Abstract

The Beijing Electron Positron Collider II will upgrade to extend the beam energy and the luminosity by increasing the beam current and slightly compressing the beam size, where the beam energy will be extended from 2.3 GeV to 2.8 GeV and the peak luminosity will be up to  $1.1 \times 10^{33} \text{cm}^{-2} \text{s}^{-1}$  at the optimizing beam energy of 2.35 GeV. The BEPCII upgrade is expected to result in challenging levels of beam related background in the interaction region. An precise simulating and mitigating beam background is necessary to protect the BESIII detector and increase the beam current and peak luminosity. The beam related background at BEPCII is mainly from the Touschek effect and the beam gas effect, this paper presents the recent progress of the beam background simulation and experiment.

## INTRODUCTION

The Beijing Electron Positron Collider II (BEPCII) [1] is a two-ring electron positron collider which has operated successfully for over 10 years and collected more than  $40 \text{fb}^{-1}$  data sets in the  $\tau$ -charm energy range. A series of significant experimental observations have been reported based on these data sets [2]. In 2019, BESIII collaboration has reported the future physics programme (also called “white paper”) which contains a detailed survey of important topics in  $\tau$ -charm physics and hadron physics [3]. However, the age of BEPCII becomes an important issue, such as main drift chamber (MDC). Due to the beam-induced with a hit rate up to  $2 \text{kHz/cm}^2$ , the cell gains of the inner chamber drops dramatically (about 39% drop for the first layer cells in 2017) and furthermore lead to a degradation of the spatial resolution and reconstruction efficiency [3]. In addition, the peak luminosity of BEPCII is optimized at 1.89 GeV, the evaluated peak luminosity at 2.35 GeV is only  $0.35 \times 10^{33} \text{cm}^{-2} \text{s}^{-1}$ . Therefore, an upgrade is required for BEPCII to collect more data sets in this energy region, especially at center-of-mass energies larger than 4 GeV [4]. The peaking luminosity at 2.35 GeV will increase to  $1.1 \times 10^{33} \text{cm}^{-2} \text{s}^{-1}$  with high beam current and small beam size. However, the resulting high beam background must be controlled within a safe range.

In the beginning of BEPCII, ten collimators with fixed aperture were installed on both the electron and positron rings. Three horizontal movable collimators were installed at 8.2 m, 11 m upstream, and 11 m downstream from IP

on the electron ring, and a horizontal movable collimator was installed at 8.2 m upstream from IP on the positron ring. Simulations of beam-gas effect [5], Touschek effect [6], SR [7] and movable collimators [8] were separately studied to predict the background rate in BESIII. These collimators obviously mitigated the beam background and played an important role in the stable operation of the BEPCII machine in its initial stage. Each movable collimator has a pair of movable jaws which is able to adjust their aperture independently. Due to the high beam current and small beam size of BEPCII upgrade project, it is necessary to reexamine beam background simulation and experiments.

## BEAM BACKGROUND SIMULATION AND EXPERIMENT IN 2021

The beam background at BEPCII consists of luminosity-related background and beam-related background, where the first one is generated by beam-beam interaction and can be simulated with an acceptable precise, the second one is highly dependent on beam parameters and the storage ring. The dominant sources of beam-related background can be parameterized by:

$$O_{\text{SingleBeam}} = S_{\text{tous}} \cdot \frac{I_t \cdot I_b}{\sigma_x \sigma_y \sigma_z} + S_{\text{gas}} \cdot I_t \cdot P(I_t) + S_{\text{const}}, \quad (1)$$

where  $O_{\text{SingleBeam}}$  is the total background rate of single beam and can be described by the dark current or count rate of the machine-detector interface (MDI). The first term (the Touschek background) is proportional to bunch current ( $I_b$ ) and beam current ( $I_t$ ), and inversely proportional to beam size ( $\sigma_{x,y,z}$ ). The second term (beam-gas background) is proportional to beam current and vacuum pressure. Generally, the residual gas mainly comes from the interactions between synchrotron radiation (SR) photons and the inner wall of beam pipe, so the vacuum pressure depends on the beam current. The third term is the constant background from cosmic rays and electronic noise, independent of the beam condition and can be presented by a constant term.

The beam-related background simulation is based on the framework which includes generators for lost particles, SAD [9] for tracking the particles in the collider ring, and Geant4 [10] and Geant4-based software framework of the BESIII offline software system (BOSS) [11] for simulating the detector's responses and MDI. The beam background experiment was performed for validating the simulation result. The “data/MC” ratio, which is the ratios of the background

\* Work supported by the National Natural Science Foundation of China (NSFC), under Contract No. 11905225

<sup>†</sup> corresponding author: wangbin@ihep.ac.cn

Content from this work may be used under the terms of the CC BY 4.0 licence (© 2023). Any distribution of this work must maintain attribution to the author(s), title of the work, publisher, and DOI

rate between experimental measurements and simulating prediction, is used to evaluate the difference between them.

We performed a separate measurement of the main two beam-related beam background components in 2021. Figure 1 shows the distribution of the count rate in the first layer of the MDC versus the bunch current for both electron and positron beams, where the nominal total beam current is set to 450 mA, the bunch current and bunch number are scanned from 3.8 mA to 8 mA and 118 to 56, respectively. According to Eq. 1, the Touschek background is calculated from the slope in the linear fit and the intercept of the fit denotes the beam-gas and constant background. Figure 2 shows the separated beam background in all layers of the MDC. The results show that the Touschek background is dominant in all layers, and the beam-gas constitutes a small portion, especially in the outer layers. Figure 3 shows the “data/MC” ratios of the background rate between experiments and MC simulations, the result reveals that the simulating Touschek background is larger than that in the experimental measurement by one to two orders of magnitude. It means that more optimizations for simulation and experiment, such as collimator simulation, particle tracking, and the interactions of MDI materials in simulation, are necessary for future work.

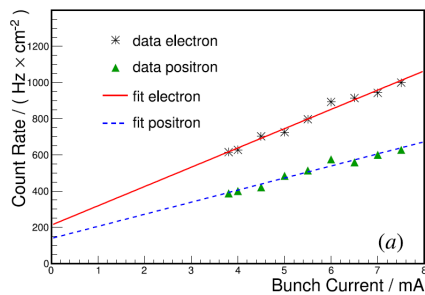


Figure 1: The distribution of the count rate in the first layer of the MDC with respect to the bunch current for both electron and positron beams, where the beam current is set to 450 mA.

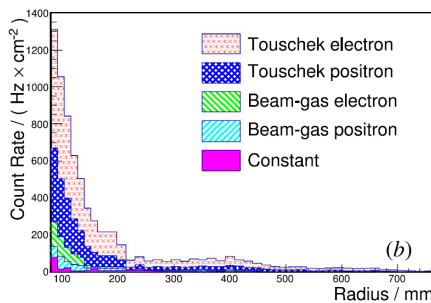


Figure 2: The distribution of the accumulated count rate of separate background sources in all MDC layers, where the bunch current is set to 6 mA.

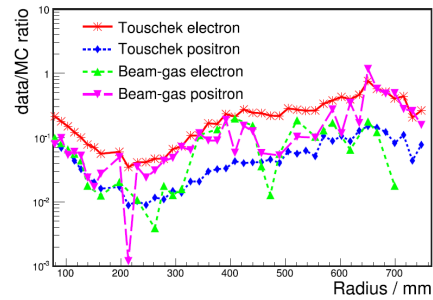


Figure 3: Data/MC ratios with respect to the radius of all MDC layers for both electron and positron beams for the Touschek and beam-gas effects.

## MOVABLE COLLIMATOR EXPERIMENT IN 2022 AND 2023

We have conducted several tests on these movable collimators in the last decade. Changing the aperture of these collimators will increase the vacuum pressure and worsen the operation status. So it is necessary to perform a feasibility test for changing the aperture of these collimators. In 2022, we perform the feasibility experiment and irradiation dose of these collimators. The results show that changing the aperture of collimators can suddenly but not dramatically increase the vacuum pressure and decrease the lifetime of beam. While the vacuum pressure and lifetime will recover in a few seconds. It indicates that more detailed collimator experiments can be conducted in the next beam background experiment.

The following movable collimator experiment is conducted in 2023:

1. Baseline beam background experiment. To compare with the experiment results collected in 2021, a series of baseline beam background experiment is performed for different aperture of these movable collimators. We also set the nominal single beam current to 450 mA and four bunch number, which are 60, 75, 82, and 90.
2. Aperture scan. We independently scan the aperture of the inner and outer jaw for all four movable collimators on both electron and positron ring. The aperture settings with minimum dark current are assumed to be the “best settings” for further beam background experiment.
3. Baseline beam background experiment with best settings of movable collimators.
4. Beam background experiment with different aperture settings. We collect the experimental data by changing the aperture of each movable collimators.
5. Beam background experiment with different beam current.

Figure 4 shows the overall plots for the beam background experiment in 2023. 01 to 17 denotes the different experiment item, where 01 and 11 denote the baseline beam background experiment before collimator movements for electron

and positron rings, respectively. 02 and 03 denote the aperture scan of the outer and inner jaw of the movable collimator at 8.2 m upstream from IP on the electron ring. 04 and 05 denote the aperture scan of the outer and inner jaw of the movable collimator at 11.0 m upstream from IP on the electron ring. 06 and 07 denote the aperture scan of the outer and inner jaw of the movable collimator at 8.2 m downstream from IP on the electron ring. 08 and 14 denote the baseline beam background experiment with the best settings of the movable collimator movements on the electron ring, 09 and 15 denote the beam background experiment with different aperture settings for electron and positron rings, respectively. 10 and 16 denote the beam background experiment with different beam current. 12 and 13 denote the aperture scan of the outer and inner jaw of the movable collimator at 8.2 m upstream from IP on the positron ring. 17 denotes the normal data taking with the best settings of all movable collimator movements.

The further data analysis is ongoing. The preliminary result shows that the movable collimator upstream from IP obviously effect the beam background, while the collimator downstream from IP has not obviously effect the beam background. The collimator in positron ring is much more effective than that of electron ring. It is worth noting that the beam lifetimes and the luminosities for different aperture settings are almost unchanged. We also perform an additional validation for the best settings of these movable collimator in the normal collider, which the beam current is up to 900 mA. By comparing the dark current with and without the best settings of these movable collimator, the dark current is decreased from 11  $\mu\text{A}$  to 6  $\mu\text{A}$  (about 40%). This obvious decrease of the beam background will provide a important support for the top-up injection in the next machine running, as well as the beam background evaluation of the BEPCII upgrade project.

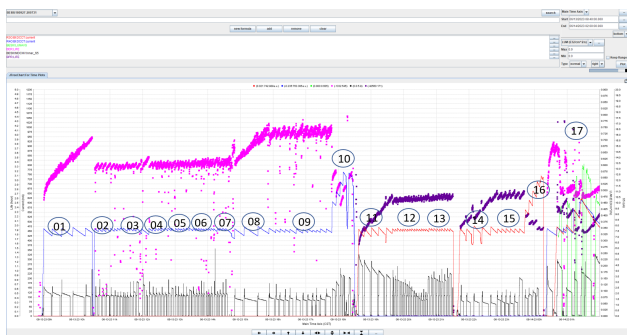


Figure 4: The beam background experiment in 2023, where the pink and purple points are the lifetime of electron beam and positron beam, respectively. the green, black, red and blue curve are the peak luminosity, dark current, electron beam current, positron beam current, respectively.

## CONCLUSION

In summary, we reported the recent progress of beam background experiments and simulations at BEPCII. The

Touschek background is dominant in the beam-related background according to results of experiment and simulation. A comparison between experiment and simulation for Touschek background shows a discrepancy of one to two orders of magnitude. A series of movable collimators experiment is conducted. The collimator at downstream from IP is expected to be no significant effect with the beam background, while the collimator at 8.2 m upstream from IP obviously effect the beam background. The best settings of the aperture of all collimators is calculated and obviously mitigated the beam background. Further data analysis for these data sets is necessary for comparing with the simulating result and evaluating the beam background for the BEPCII upgrade project. An additional data taking with the best setting of these movable collimators is performed, the dark current is decreased from 11  $\mu\text{A}$  to 6  $\mu\text{A}$  (about 40%) with 900 mA beam current and the beam lifetime and peak luminosity are no obviously changed. The obvious mitigation of beam background will play an important role of the future data taking of BEPCII and the evaluation of the beam background of the BEPCII upgrade.

## REFERENCES

- [1] J.Q. Wang, L. Ma, and C. Zhang, “The BEPCII: Status and early commissioning”, in *2007 IEEE Particle Accelerator Conference, PAC*, pp. 53-57, 2007.
- [2] R.L. Workman *et al.*, “Particle Data Group”, *Prog. Theor. Exp. Phys.*, p. 083C01 2022, (2022)
- [3] M. Ablikim, *et al.*, “BESIII Collaboration, Future Physics Programme of BESIII”, *Chinese Physics C*, vol. 44, p. 040001, 2020.
- [4] H. Geng, W. Liu, *et al.*, “Lattice design for BEPCII upgrade”, in *Proc. IPAC21*, Campinas, SP, Brazil, pp. 3756-3758, 2021.
- [5] D. Jin, L. Feng, *et al.*, “Monte Carlo simulation of BEPCII/BESIII backgrounds beam-gas interactions”, *HEP & NP* vol. 28, no. 11, 2004, (in Chinese).
- [6] D. Jin, Y. Guo, *et al.*, “Monte Carlo simulation of BEPCII/BESIII backgrounds Touschek effect”, *HEP & NP*, vol. 30, no. 5, 2006, (in Chinese).
- [7] N. Zhou, D. Jin, *et al.*, “Monte Carlo simulation of BEPCII beam-related background-synchrotron radiation”, *HEP & NP*, vol. 28, no. 3, 2004, (in Chinese).
- [8] T. Luo, D. Jin, *et al.*, “Application of movable collimators to the BEPC”, *Chinese Physics C*, vol. 34, pp. 1742–1748, 2010.
- [9] SAD, Website and software repository. <http://acc-physics.kek.jp/SAD/index.html>; <https://github.com/KatsOide/SAD>
- [10] J. Allison, K. Amako, *et al.*, “Recent developments in geant4”, *Nucl. Instrum. Meth. A*, vol. 835, pp. 186–225, 2016.
- [11] W.D. Li, *et al.*, “The BESIII offline software”, in *Proceeding of CHEP2006*, Mumbai, India, pp. 13-17, 2006.
- [12] H.C. Shi, B. Wang, H.Y. Shi *et al.*, “Beam background simulation and experiment at BEPCII”, *Nucl. Instr. Meth. A*, vol. 1050, p. 168174, 2023.

14<sup>th</sup> Symp. Accel. Phys.  
ISBN: 978-3-95450-265-3

SAP2023, Xichang, China

JACoW Publishing  
doi:10.18429/JACoW-SAP2023

## List of Authors

**Bold** papercodes indicate primary authors; ~~strike through~~/black papercodes indicate no submission received

<b>– A –</b>		<b>– G –</b>	
An, S.	<del>MOCYA01</del> , <del>TUPB005</del> , <del>TUPB015</del> , <del>TUPB017</del>	Gao, Q.	<del>MOPB008</del> , <del>TUPB013</del>
<b>– B –</b>		Geng, H.	<del>MOPB019</del>
Bai, Z.H.	<del>MOPB009</del> , <del>MOPB010</del> , <del>MOPB017</del>	Gong, L.Y.	<del>TUPB001</del> , <del>TUPB038</del>
Bian, T.J.	<del>MOIBA01</del> , <del>MOCYA01</del> , <del>TUPB005</del> , <del>TUPB015</del> , <del>TUPB017</del>	Gu, Q.	<del>MOPB020</del>
<b>– C –</b>		Gu, W.H.	<del>MOPB008</del>
Chao, A.	<del>MOPB037</del> , <del>MOPB039</del>	Guan, F.P.	<del>MOCYA01</del> , <del>TUPB005</del>
Chen, F.G.	<del>TUPB020</del>	Guan, J.B.	<del>MOPB035</del>
Chen, H.B.	<del>MOIAA01</del> , <del>MOPB008</del> , <del>TUCYA01</del> , <del>TUPB013</del>	Guo, J.J.	<del>TUPB029</del>
Chen, J.E.	<del>TUPB027</del>	Guo, R.	<del>TUPB020</del>
Chen, L.J.	<del>MOPB003</del>	Guo, Y.Y.	<del>TUPB030</del>
Chen, L.W.	<del>MOIAA01</del>	Guo, Z.Y.	<del>TUPB027</del>
Chen, M.	<del>TUAA01</del>	<b>– H –</b>	
Chen, Q.S.	<del>MOPB034</del>	Hao, H.F.	<del>TUPB020</del>
Chen, S.	<del>TUPB029</del>	He, J.H.	<del>MOPB031</del> , <del>MOPB035</del>
Chen, W.L.	<del>MOAA01</del> , <del>TUPB003</del> , <del>TUPB007</del>	He, T.H.	<del>MOPB030</del>
Chen, X.Y.	<del>TUPB017</del>	He, T.L.	<del>MOPB009</del> , <del>MOPB010</del>
Chen, X.Z.	<del>TUXA02</del>	He, X.	<del>MOBA01</del>
Chen, Y.	<del>MOPB031</del> , <del>MOPB035</del>	He, Y.	<del>MOAA01</del> , <del>TUPB001</del> , <del>TUPB003</del> , <del>TUPB012</del>
Chen, Y.C.	<del>TUPB016</del>	He, Z.-F.	<del>MOPB005</del>
Chu, Y.M.	<del>TUPB007</del>	Huang, G.	<del>MOAA01</del>
Chu, Z.C.	<del>MOIBA01</del>	Huang, L.	<del>TUPB023</del>
Cui, B.J.	<del>TUPB027</del>	Huang, P.W.	<del>MOIAA01</del> , <del>TUCYA01</del>
<b>– D –</b>		Huang, R.	<del>MOPB003</del>
Dai, Y.X.	<del>MOPB019</del>	Huang, S.	<del>MOPB011</del> , <del>MOPB013</del> , <del>TUIAA01</del>
Dai, Z.Y.	<del>MOPB035</del>	Huang, W.-H.	<del>MOIAA01</del> , <del>MOPB039</del> , <del>TUCYA01</del>
Deng, H.X.	<del>TUPB029</del>	Huang, X.Y.	<del>TUPB034</del>
Deng, X.J.	<del>MOIAA01</del> , <del>MOPB037</del> , <del>MOPB039</del>	Huang, Y.L.	<del>TUPB003</del>
Dong, Z.	<del>MOPB023</del> , <del>MOPB024</del>	Hui, Z.	<del>MOPB035</del>
Dou, W.P.	<del>MOAA01</del> , <del>TUPB001</del>	<b>– J –</b>	
Du, C.C.	<del>TUPB028</del>	Ji, H.F.	<del>TUPB030</del> , <del>WEXA01</del>
Du, Y.C.	<del>MOIAA01</del> , <del>TUCYA01</del>	Ji, L.Y.	<del>MOCYA01</del> , <del>TUPB005</del>
Duan, Z.	<del>MOPB019</del>	Jia, D.Y.	<del>TUPB022</del>
<b>– F –</b>		Jia, H.	<del>MOAA01</del> , <del>TUPB003</del> , <del>TUPB022</del>
Fan, K.	<del>MOPB001</del> , <del>MOPB016</del>	Jia, H.Y.	<del>MOPB013</del> , <del>TUIAA01</del>
Fan, S.J.	<del>MOPB002</del>	Jia, Q.K.	<del>MOPB003</del>
Fang, P.Z.	<del>TUPB006</del>	Jiang, B.C.	<del>WEAA02</del>
Feng, B.Y.	<del>TUPB013</del>	Jiang, Y.X.	<del>TUPB027</del>
Feng, C.	<del>MOBA03</del> , <del>MOPB026</del>	Jiao, Y.	<del>MOBA04</del> , <del>TUPB030</del> , <del>TUPB034</del> , <del>WEAA03</del> , <del>WEXA01</del>
Feng, C.	<del>TUPB012</del>	Jin, C.	<del>TUPB012</del>
Feng, G.Y.	<del>MOPB009</del> , <del>MOPB017</del> , <del>WEAA01</del>	<b>– L –</b>	
Fu, W.	<del>MOIBA01</del>	Le, H.	<del>MOIBA01</del>
		Li, C.	<del>MOPB020</del>
		Li, C.L.	<del>MOPB036</del>
		Li, C.X.	<del>TUPB001</del>

Li, D.Z.	MOPB024	Luo, X.B.	TUPB009, TUPB018, TUPB019
Li, H.H.	MOPB031, MOPB035	– M –	
Li, H.Y.	MOPB008	Ma, T.H.	TUPB027
Li, J.	TUPB008	Ma, W.J.	TUAA02
Li, J.T.	MOPB006, MOPB025, MOPB028	Meng, C.	M0BA04, WEXA01
Li, J.Y.	M0BA04	Miao, L.	TUPB020
Li, N.	TUPB030, WEXA01	– N –	
Li, R.K.	M0IAA01, TUCYA01	Nie, Y.	MOPB035
Li, S.Y.	MOPB018	– O –	
Li, W.M.	MOPB009	Ohmi, K.	MOCXA02
Li, W.W.	MOPB009, MOPB010	– P –	
Li, X.M.	MOPB026, MOPB029	Pan, Z.	M0IAA01, MOPB037, MOPB039
Li, X.X.	TUPB037	Pei, S.	M0IBA01
Li, Y.	TUPB006, TUPB021, TUPB026	Peng, S.X.	TUPB027
Li, Z.	TUPB009, TUPB010, TUPB018, TUPB019	Peng, Y.M.	WEXA01
Li, Z.H.	MOPB019	Pu, X.J.	TUPB009, TUPB019
Li, Z.Z.	M0IAA01, MOPB037, MOPB039	– Q –	
Liang, Y.F.	MOPB026, MOPB029	Qi, H.	MOPB016
Liao, W.L.	TUPB009, TUPB018, TUPB019	Qi, X.	TUPB012
Liao, Y.C.	TUPB014	Qiao, P.	TUPB020
Lin, C.	TUAA02	Qin, B.	TUPB014, TUPB016
Lin, C.T.	MOCXA02, MOPB014	Qin, Y.S.	M0AA01, TUPB003
Lin, P.T.	TUPB009, TUPB010, TUPB018, TUPB019	– R –	
Lin, X.	TUPB013	Ren, Z.Q.	TUPB009, TUPB010, TUPB018, TUPB019
Ling, L.	TUPB017	– S –	
Liu, B.	TUPB029	Shao, Z.X.	MOPB023, MOPB024
Liu, C.L.	TUPB016	Shi, H.C.	MOPB035
Liu, H.	TUPB029	Shi, H.Y.	TUPB035
Liu, H.Y.	M0AA02	Shi, J.R.	M0IAA01, MOPB008, TUCYA01, TUPB013
Liu, J.	TUIBA02	Shi, J.S.	M0BA01
Liu, J.Y.	M0IBA01	Shi, X.Y.	MOPB021
Liu, L.X.	MOPB035	Song, Y.	MOPB001
Liu, P.F.	TUPB020	Su, C.G.	TUPB036
Liu, S.H.	M0AA01	Su, M.Y.	MOPB019
Liu, T.	MOPB027, WEBA01	Sun, J.T.	MOPB026, MOPB029
Liu, T.	MOPB018	Sun, L.P.	M0AA01
Liu, W.B.	MOPB019	Sun, Z.	MOPB015
Liu, X.	TUPB014, TUPB016	– T –	
Liu, X.	M0IAA01	Tan, J.J.	MOPB017
Liu, X.Y.	TUPB006, TUPB021	Tang, C.-X.	M0IAA01, MOPB037, MOPB039, TUCYA01
Liu, Y.D.	M0BA02	Tang, J.Y.	MOPB018
Liu, YX.	MOPB027	Tang, J.Z.	MOPB004
Liu, Z.	MOPB001, MOPB016	Tian, S.K.	MOPB006, MOPB028, TUPB028
Liu, Z.Q.	MOPB011	Tsai, C.-Y.	M0IAA02, MOPB001, MOPB016
Liu, Z.S.	MOPB035	– W –	
Lu, J.R.	TUPB015, TUPB017	Wan, J.	WEAA03
Lu, X.H.	MOPB019, WEXA01		
Lu, Y.	MOPB036		
Luo, Q.	MOPB018		
Luo, R.Y.	MOPB034, TUPB014		

Wan, W.	<b>MOPB005</b> , MOPB020	Yang, J.Y.	<b>TUIBA01</b>
Wan, X.M.	TUPB009, TUPB010, TUPB018, <b>TUPB019</b> <b>TUPB035</b>	Yang, X.D.	<b>TUPB025</b>
Wang, B.	MOIBA01	Yang, X.M.	MOPB029, TUPB033, MOPB026
Wang, C.	TUPB017	Yang, Y.F.	TUPB009, <b>TUPB010</b> , TUPB018, TUPB019
Wang, F.	MOIAA01	Yang, Y.Z.	<b>TUPB032</b>
Wang, H.	MOPB035	Yang, Y.Z.	TUPB006, <b>TUPB021</b> ,
Wang, J.	MOPB001, MOPB016	Yao, H.J.	TUPB026
Wang, J.	MOPB024	Yi, H.	MOPB026, MOPB029, <b>TUPB033</b>
Wang, J.Q.	TUPB028	Yi, M.Y.	<b>TUPB002</b>
Wang, K.	MOPB036	Yin, Z.G.	MOIBA01
Wang, K.D.	<b>MOPB038</b> , TUA002, TUPB008	Yin, Z.Y.	MOIBA01
Wang, L.	MOPB009, MOPB024	Yu, C.H.	TUPB035
Wang, L.	<b>MOCYA02</b>	Yu, P.Y.	<b>TUPB020</b>
Wang, L.	<b>MOPB032</b>	Yu, Y.	MOPB026, MOPB029
Wang, N.	<b>MOPB006</b> , MOPB014, MOPB028, TUPB028	Yuan, Y.S.	<b>TUPB004</b>
Wang, Q.	TUA002	Yue, S.	MOPB006, <b>MOPB028</b>
Wang, T.	<b>MOPB007</b>	– Z –	
Wang, W.	<b>TUBA01</b>	Zeng, L.	MOPB026, MOPB029
Wang, W.	TUPB014, TUPB016	Zeng, M.	MOPB021, <b>TUXA01</b>
Wang, X.F.	<b>MOPB026</b> , MOPB029, <b>TUYA02</b> , TUPB033	Zha, H.	MOPB008, TUPB013
Wang, X.W.	TUPB006, TUPB021, TUPB026	Zhang, A.L.	TUPB027
Wang, Y.X.	MOPB036	Zhang, H.	MOBA01
Wang, Z.	MOPB026	Zhang, L.H.	<b>MOPB018</b>
Wang, Z.J.	MOAA01, TUPB001, TUPB002, TUPB007, TUPB012, TUPB022, TUPB036	Zhang, Q.L.	<b>MOPB036</b>
Wang, Z.J.	TUPB006, TUPB021	Zhang, S.P.	MOIBA01
Wang, Z.M.	TUPB006, TUPB021	Zhang, T.	MOPB023, MOPB024
Wei, B.F.	<b>MOPB017</b>	Zhang, T.J.	<b>MOIBA01</b>
Wei, S.M.	MOCYA01, TUPB005	Zhang, W.Q.	MOPB029, TUPB033, MOPB026
Wei, Y.	TUPB034	Zhang, X.	<b>TUPB031</b>
Wen, Y.M.	TUPB029	Zhang, X.	<b>TUPB011</b>
Wu, D.	TUCXA01	Zhang, X.-Y.	TUCYA01
Wu, W.B.	TUPB027	Zhang, Y.	MOCXA02, MOPB014, MOPB019
– X –		Zhao, H.	<b>TUPB024</b>
Xie, H.D.	TUPB005	Zhao, J.	MOAA01
Xin, T.	<b>MOPB015</b> , MOPB019	Zhao, J.R.	TUA002
Xing, Q.Z.	TUPB026	Zhao, M.H.	MOPB005
Xiong, Y.	TUPB006	Zhao, Y.L.	MOPB019, <b>WEXA01</b>
Xu, H.	MOPB010	Zhao, Y.Y.	TUA002
Xu, H.	MOPB030	Zheng, L.M.	TUCYA01
Xu, H.S.	<b>MOCXA01</b> , MOPB014, MOPB021, TUPB028	Zheng, S.X.	TUPB006, TUPB021, TUPB026
Xu, J.Y.	<b>MOPB014</b>	Zheng, X.	TUPB005
Xu, X.	<b>TUYA01</b>	Zhong, J.H.	MOPB035
Xu, Y.	<b>MOPB001</b>	Zhou, H.	MOIBA01
– Y –		Zhou, K.	MOPB030, <b>WEBA02</b>
Yan, L.X.	MOIAA01	Zhou, W.	MOPB035
Yan, X.Q.	TUA002, TUPB008	Zhou, Z.	MOPB030, TUCXA01
Yang, J.C.	<b>MOAA03</b> , MOCYA02	Zhou, Z.R.	MOPB024
		Zhu, K.	TUA002, TUPB008
		Zhu, X.F.	MOIBA01
		Zou, Y.	<b>MOPB031</b> , MOPB035

## Institutes List

### CAEP/IAE

Miangang, Sichuan, People's Republic of China

- Chen, L.J.
- He, T.H.
- Wu, D.
- Xu, H.
- Zhou, K.
- Zhou, Z.

### CAEP/IFP

Mainyang, Sichuan, People's Republic of China

- He, X.
- Shi, J.S.
- Zhang, H.

### Chongqing University

Shapingba, People's Republic of China

- Jiang, B.C.

### CIAE

Beijing, People's Republic of China

- An, S.
- Bian, T.J.
- Chen, X.Y.
- Chu, Z.C.
- Fu, W.
- Guan, F.P.
- Ji, L.Y.
- Le, H.
- Ling, L.
- Liu, J.Y.
- Lu, J.R.
- Pei, S.
- Wang, C.
- Wang, F.
- Wei, S.M.
- Xie, H.D.
- Yin, Z.G.
- Zhang, S.P.
- Zhang, T.J.
- Zhang, X.
- Zheng, X.
- Zhou, H.
- Zhu, X.F.

### CIRP

Xiaodian District, People's Republic of China

- Chen, F.G.
- Guo, R.
- Hao, H.F.
- Liu, P.F.
- Miao, L.
- Qiao, P.
- Yu, P.Y.

### DICP

Dalian, Liaoning, People's Republic of China

- Li, X.M.
- Sun, J.T.
- Yang, J.Y.

- Yang, X.M.
- Yu, Y.
- Zhang, W.Q.

### FRIB

East Lansing, Michigan, USA

- Yin, Z.Y.

### HUST

Wuhan, People's Republic of China

- Chen, Q.S.
- Chen, Y.C.
- Fan, K.
- Liao, Y.C.
- Liu, C.L.
- Liu, X.
- Liu, Z.
- Luo, R.Y.
- Qi, H.
- Qin, B.
- Song, Y.
- Tsai, C.-Y.
- Wang, J.
- Wang, W.
- Xu, Y.

### IAS

Wuhan City, People's Republic of China

- Chen, Y.
- Dai, Z.Y.
- Guan, J.B.
- He, J.H.
- Hui, Z.
- Li, H.H.
- Liu, L.X.
- Liu, Z.S.
- Nie, Y.
- Wang, J.
- Zhong, J.H.
- Zhou, W.
- Zou, Y.

### IASF

Shenzhen, Guangdong, People's Republic of China

- Liang, Y.F.
- Lin, C.T.
- Yang, X.M.
- Yi, H.
- Zeng, L.
- Zhang, W.Q.

### IHEP

Beijing, People's Republic of China

- Du, C.C.
- Duan, Z.
- Geng, H.
- Guo, Y.Y.
- Huang, X.Y.
- Ji, H.F.
- Jiao, Y.
- Li, D.Z.
- Li, J.T.

- Li, J.Y.
- Li, N.
- Liu, W.B.
- Liu, Y.D.
- Meng, C.
- Peng, Y.M.
- Shi, H.Y.
- Shi, X.Y.
- Sun, Z.
- Tian, S.K.
- Wan, J.
- Wang, B.
- Wang, J.Q.
- Wang, J.
- Wang, N.
- Wei, Y.
- Xin, T.
- Xu, H.S.
- Xu, J.Y.
- Yu, C.H.
- Yue, S.
- Zeng, M.
- Zhang, Y.
- Zhao, Y.L.

#### IHEP CSNS

Guangdong Province, People's Republic of China

- Huang, L.
- Liu, H.Y.
- Lu, X.H.
- Yuan, Y.S.

#### IMP/CAS

Lanzhou, People's Republic of China

- Chen, W.L.
- Chu, Y.M.
- Dou, W.P.
- Feng, C.
- Gong, L.Y.
- He, Y.
- Huang, G.
- Huang, Y.L.
- Jia, D.Y.
- Jia, H.
- Jin, C.
- Li, C.X.
- Li, X.X.
- Liu, J.
- Liu, S.H.
- Qi, X.
- Qin, Y.S.
- Su, C.G.
- Sun, L.P.
- Wang, L.
- Wang, Z.J.
- Yang, J.C.
- Yang, X.D.
- Yi, M.Y.
- Zhao, H.
- Zhao, J.

Institute of Advanced Science Facilities  
Shenzhen, People's Republic of China

- Wang, X.F.

#### KEK

Ibaraki, Japan

- Ohmi, K.

#### NINT

Shannxi, People's Republic of China

- Wang, Z.M.

#### PKU

Beijing, People's Republic of China

- Chen, J.E.
- Cui, B.J.
- Guo, Z.Y.
- Huang, S.
- Jia, H.Y.
- Jiang, Y.X.
- Li, J.
- Lin, C.
- Liu, Z.Q.
- Ma, T.H.
- Ma, W.J.
- Peng, S.X.
- Wang, K.D.
- Wang, Q.
- Wang, T.
- Wu, W.B.
- Yan, X.Q.
- Zhang, X.
- Zhao, J.R.
- Zhao, Y.Y.
- Zhu, K.

#### Rejected

Tanzania

- Chen, X.Z.

#### SARI-CAS

Pudong, Shanghai, People's Republic of China

- Chen, S.
- Deng, H.X.
- Feng, C.
- Li, C.L.
- Liu, B.
- Liu, T.
- Wang, K.
- Wang, Z.
- Wen, Y.M.
- Zhang, Q.L.

#### SCU

Chengdu, People's Republic of China

- Li, Z.
- Liao, W.L.
- Lin, P.T.
- Luo, X.B.
- Pu, X.J.
- Ren, Z.Q.
- Wan, X.M.
- Yang, Y.F.

#### Shanghai Institute of Optics and Fine Mechanics

Shanghai, People's Republic of China

- Wang, W.

**Shanghai Jiao Tong University**

Shanghai, People's Republic of China  
• [Chen, M.](#)

**ShanghaiTech University**

Shanghai, People's Republic of China  
• [Li, C.](#)  
• [Wan, W.](#)

**SINAP**

Shanghai, People's Republic of China  
• [He, Z.-F.](#)  
• [Liu, H.](#)  
• [Liu, YX.](#)  
• [Wang, K.](#)  
• [Zhao, M.H.](#)

**SLAC**

Menlo Park, California, USA  
• [Chao, A.](#)  
• [Xu, X.](#)

**SSRF**

Shanghai, People's Republic of China  
• [Gu, Q.](#)

**Tsinghua University**

Beijing, People's Republic of China  
• [Wang, L.](#)

**TUB**

Beijing, People's Republic of China  
• [Chao, A.](#)  
• [Chen, H.B.](#)  
• [Chen, L.W.](#)  
• [Deng, X.J.](#)  
• [Du, Y.C.](#)  
• [Fan, S.J.](#)  
• [Fang, P.Z.](#)  
• [Feng, B.Y.](#)  
• [Gao, Q.](#)  
• [Gu, W.H.](#)  
• [Huang, P.W.](#)  
• [Huang, W.-H.](#)  
• [Li, H.Y.](#)  
• [Li, R.K.](#)  
• [Li, Y.](#)  
• [Li, Z.Z.](#)  
• [Lin, X.](#)  
• [Liu, X.Y.](#)  
• [Liu, X.](#)  
• [Pan, Z.](#)  
• [Shi, J.R.](#)  
• [Tang, C.-X.](#)  
• [Tang, J.Z.](#)  
• [Wang, H.](#)  
• [Wang, X.W.](#)  
• [Wang, Z.J.](#)  
• [Xing, Q.Z.](#)  
• [Xiong, Y.](#)  
• [Yan, L.X.](#)  
• [Yang, Y.Z.](#)  
• [Yao, H.J.](#)

- [Zha, H.](#)
- [Zhang, X.-Y.](#)
- [Zheng, L.M.](#)
- [Zheng, S.X.](#)

**UCAS**

Beijing, People's Republic of China  
• [Dai, YX.](#)  
• [Li, Z.H.](#)  
• [Liu, W.B.](#)  
• [Su, M.Y.](#)  
• [Wang, YX.](#)  
• [Zhang, Y.](#)

**University of Chinese Academy of Sciences**

Beijing, People's Republic of China  
• [Wang, L.](#)  
• [Yue, S.](#)

**USTC**

Hefei, Anhui, People's Republic of China  
• [Dong, Z.](#)  
• [Shao, Z.X.](#)  
• [Zhang, A.L.](#)  
• [Zhang, T.](#)

**USTC/NSRL**

Hefei, Anhui, People's Republic of China  
• [Bai, Z.H.](#)  
• [Feng, G.Y.](#)  
• [He, T.L.](#)  
• [Huang, R.](#)  
• [Jia, Q.K.](#)  
• [Li, S.Y.](#)  
• [Li, W.M.](#)  
• [Li, W.W.](#)  
• [Liu, T.](#)  
• [Luo, Q.](#)  
• [Tan, J.J.](#)  
• [Wang, L.](#)  
• [Wei, B.F.](#)  
• [Xu, H.](#)  
• [Zhou, Z.R.](#)

**USTC/SNST**

Hefei, Anhui, People's Republic of China  
• [Tang, J.Y.](#)  
• [Zhang, L.H.](#)

**Zhangjiang Lab**

Shanghai, People's Republic of China  
• [Guo, J.J.](#)  
• [Lu, Y.](#)

**Zhejiang University, Institute for Fusion Theory and Simulation**

Hangzhou, People's Republic of China  
• [Shi, H.C.](#)

## Participants List

### — A —

**An, ShiZhong**  
China Institute of Atomic Energy

### — B —

**Bian, Tianjian**  
China Institute of Atomic Energy

### — C —

**Cai, Chengying**  
Huazhong University of Science  
and Technology

**Chen, Xiaolong**  
Institute of Modern Physics,  
Chinese Academy of Sciences

**Chen, Xinyu**  
China Institution of Atomic Energy

**Chen, Yu**  
Huazhong University of Science  
and Technology

**Chen, Xizhuan**  
SIOM, CAS

**Chen, Min**  
Shanghai Jiao Tong University

**Chen, Qijian**  
LZU

**Chu, Yimeng**  
Institute of Modern Physics,  
Chinese Academy of Sciences

**Cui, Bujian**  
Peking University

### — D —

**Dai, Zeyi**  
Wuhan University

**Ding, Jingxin**  
LZU

**Dou, WeiPing**  
IMP

**Du, Yingchao**  
Tsinghua University

**Duan, Zhe**  
IHEP

### — F —

**Feng, Chao**  
Shanghai Advanced Research Institute, CAS

**Feng, Boyuan**  
TUB

**Fu, Wei**  
China Institute of Atomic Energy

### — G —

**Guo, Yuanyuan**  
IHEP

### — H —

**He, Tao**  
Institute of Advanced Science Facilities

**He, Tianhui**  
IAE of CAEP

**He, Tianlong**  
USTC

**He, Yuan**  
IMP

**He, Zi-Feng**  
Shanghai Institute of Applied Physics,  
Chinese Academy of Sciences

**Hu, Tongning**  
Huazhong University of Science  
and Technology

**Hu, Fangjun**  
TUB

**Huang, Nanshun**  
zjlab

**Huang, Pengwei**  
Tsinghua University

**Huang, Ruixuan**  
University of Science and  
Technology of China

**Huang, Senlin**  
Peking University

**Huang, Xiyang**  
Institute of High Energy Physics

**Huang, Yuejing**  
University of Science and  
Technology of China

**Huang, Wenhui**  
TUB

**Huang, Guirong**  
IMP

### — J —

**Jia, Duanyang**  
Institute of Modern Physics,  
Chinese Academy of Sciences

**Jia, Haoyan**  
Peking University

**Jiang, Bocheng**  
Chongqing University

### — L —

**Li, Chuang**  
ShanghaiTech University

**Li, Jie**  
Peking university

**Li, Jingyi**  
IHEP

**Li, Jintao**  
IHEP

**Li, Tianyi**  
Peking University

**Li, Zhongyi**  
Institute of Modern Physics,  
Chinese Academy of Sciences

**Li, Renkai**  
TUB

**Li, An**  
TUB

**Li, Changliang**  
SARI

**Li, Haohu**  
Wuhan University

**Li, Hongyuy**  
TUB

**Liao, Wenlong**  
Sichuan University Institute of  
Nuclear Science and Technology

**Liao, Yicheng**  
Huazhong University of Science  
and Technology

**Lin, Chen**  
Peking University

**Lin, Chuntao**  
Institute of Advanced Science Facilities,  
Shenzhen

**Lin, Cong**  
Lanzhou University

**Lin, Huan**  
LZU

**Liu, Ao**  
ShanghaiTech University

**Liu, Chengyong**  
Huazhong University of Science  
and Technology

**Liu, Gangwen**  
University of Science and  
Technology of China

**Liu, Guoting**  
Lanzhou University

**Liu, Hanyang**  
IHEP

**Liu, Jie**  
Institute of Modern Physics,  
Chinese Academy of Sciences

**Liu, Juntao**  
Peking University

**Liu, Tao**  
SARI, CAS

**Liu, Weibin**  
Institute of High Energy Physics

**Liu, Yudong**  
Institute of High Energy Physic, CAS

**Liu, Zhongqi**  
Peking University

**Liu, Zipeng**  
ZJLab

**Lu, Xiaohan**  
IHEP

**Lu, JinRong**  
China Institute of Atomic Energy

**Luo, Ruiying**  
Huazhong University of Science  
and Technology

**Luo, Xiaobao**  
Sichuan University

**Lv, Peng**  
Tsinghua University

— M —

**Mao, Lijun**  
Institute of Modern Physics, CAS

**Meng, Cai**  
IHEP

— N —

**Nie, Yuancun**  
Wuhan University

— P —

**Pan, Zhilong**  
TUB

**Peng, Shixiang**  
Peking University

— Q —

**Qi, Hong**  
Huazhong University of Science  
and Technology

**Qi, Xin**  
Institute of Modern Physics,  
Chinese Academy of Science

**Qin, Bin**  
Huazhong University of Science  
and Technology

**Qiu, Jing**  
LZU

— S —

**Shao, Jiahang**  
Institute of Advanced Science Facilities,  
Shenzhen

**Shao, Zhuoxia**  
University of Science and  
Technology of China

**Shi, Xueyan**  
IHEP

**Su, Chunguang**  
Institute of Modern Physics,  
Chinese Academy of Sciences

**Su, Xingkang**  
LZU

**Sun, KunXiang**  
IMP

**Sun, Zheng Sun**  
Institution of High Energy Physics, IHEP

— T —

**Tang, Jiazhen**  
Tsinghua University Accelerator  
Laboratory

**Tian, Saik**  
IHEP

— W —

**Wan, Weishi**  
ShanghaiTech University

**Wang, Bin**  
IHEP

**Wang, Haimeng**  
Huazhong University of Science  
and Technology

**Wang, Kedong**  
Peking University

**Wang, Lei**  
Institute of Modern Physics

**Wang, Lin**  
USTC

**Wang, Na**  
IHEP

**Wang, Tianyi**  
Peking University

**Wang, Xiaofan**  
Institute of Advanced Science Facilities,  
Shenzhen

**Wang, Yiwei**  
Institute of high energy physics

**Wang, Zhijun**  
IMP

**Wang, Wentao**  
SIOM, CAS

**Wei, Bingfeng**  
University of Science and  
Technology of China

**Wei, Yelong**  
University of Science and  
Technology of China

**Wu, Jianqiang**  
IMP

— X —

**Xin**, Tianmu  
IHEP

**Xu**, Hongliang  
NSRL, USTC

**Xu**, Gang  
IHEP

**Xu**, Haisheng  
IHEP, CAS

**Xu**, Xinlu  
Peking University

**Xu**, Yang  
Huazhong University of Science  
and Technology

**Xu**, Yuanfang  
University of Science and  
Technology of China

**Xu**, Zhenghao  
ShanghaiTech University

**Xu**, Jingye  
IHEP

— Y —

**Yang**, Penghui  
National Synchrotron Radiation  
Laboratory, USTC

**Yang**, Xiaodong  
Institute of Modern Physics,  
Chinese Academy of Sciences

**Yang**, XiongBin  
IHEP

**Yang**, YuFei  
SiChuan University

**Yang**, Zhou  
Department of Engineering Physics,  
Tsinghua University

**Yao**, Hongjuan  
Tsinghua University

**Yi**, Jiao  
IHEP

**Yi**, Huaiqian  
Institute of Advanced Science Facilities,  
Shenzhen

**Yu**, Peiyan  
China Institute for Radiation Protection

**Yu**, Wentao  
Department of Engineering Physics,  
Tsinghua University

**Yue**, Sen  
IHEP

— Z —

**Zeng**, Ming  
IHEP

**Zhang**, Jinbiao  
Lanzhou University

**Zhang**, Linhao  
University of Science and  
Technology of China

**Zhang**, Xiang  
Peking University

**Zhang**, Yao  
Chongqing University

**Zhang**, Tong  
University of Science and  
Technology of China

**Zhao**, Yu  
IHEP

**Zhao**, Zhouyu  
NSRL/USTC

**Zhao**, He  
Institute of Modern Physics

**Zhou**, Wenming  
Lanzhou University

**Zhou**, Kui  
Institute of Applied Physics, CAEP

**Zhou**, Xingchen  
Lanzhou University

**Zhou**, Yang  
Institute of Modern Physics,  
Chinese Academy of Sciences

**Zhou**, Zhikai  
ShanghaiTech University

**Zhou**, Zheng  
USTC

**Zou**, Ye  
Advanced Light Source Research Center,  
Wuhan University